NIST SPECIAL PUBLICATION **400-94**

Semiconductor Measurement Technology:

Improved Characterization and Evaluation Measurements for HgCdTe Detector Materials, Processes, and Devices Used on the GOES and TIROS Satellites

GOES

D. G. Seiler, J. R. Lowney, W. R. Thurber,
J. J. Kopanski, and G. G. Harman

*T*he National Institute of Standards and Technology was established in 1988 by Congress to "assist industry in the development of technology . . . needed to improve product quality, to modernize manufacturing processes, to ensure product reliability . . . and to facilitate rapid commercialization . . . of products based on new scientific discoveries."

NIST, originally founded as the National Bureau of Standards in 1901, works to strengthen U.S. industry's competitiveness; advance science and engineering; and improve public health, safety, and the environment. One of the agency's basic functions is to develop, maintain, and retain custody of the national standards of measurement, and provide the means and methods for comparing standards used in science, engineering, manufacturing, commerce, industry, and education with the standards adopted or recognized by the Federal Government.

As an agency of the U.S. Commerce Department's Technology Administration, NIST conducts basic and applied research in the physical sciences and engineering and performs related services. The Institute does generic and precompetitive work on new and advanced technologies. NIST's research facilities are located at Gaithersburg, MD 20899, and at Boulder, CO 80303. Major technical operating units and their principal activities are listed below. For more information contact the Public Inquiries Desk, 301-975-3058.

Technology Services
- Manufacturing Technology Centers Program
- Standards Services
- Technology Commercialization
- Measurement Services
- Technology Evaluation and Assessment
- Information Services

Electronics and Electrical Engineering Laboratory
- Microelectronics
- Law Enforcement Standards
- Electricity
- Semiconductor Electronics
- Electromagnetic Fields[1]
- Electromagnetic Technology[1]

Chemical Science and Technology Laboratory
- Biotechnology
- Chemical Engineering[1]
- Chemical Kinetics and Thermodynamics
- Inorganic Analytical Research
- Organic Analytical Research
- Process Measurements
- Surface and Microanalysis Science
- Thermophysics[2]

Physics Laboratory
- Electron and Optical Physics
- Atomic Physics
- Molecular Physics
- Radiometric Physics
- Quantum Metrology
- Ionizing Radiation
- Time and Frequency[1]
- Quantum Physics[1]

Manufacturing Engineering Laboratory
- Precision Engineering
- Automated Production Technology
- Robot Systems
- Factory Automation
- Fabrication Technology

Materials Science and Engineering Laboratory
- Intelligent Processing of Materials
- Ceramics
- Materials Reliability[1]
- Polymers
- Metallurgy
- Reactor Radiation

Building and Fire Research Laboratory
- Structures
- Building Materials
- Building Environment
- Fire Science and Engineering
- Fire Measurement and Research

Computer Systems Laboratory
- Information Systems Engineering
- Systems and Software Technology
- Computer Security
- Systems and Network Architecture
- Advanced Systems

Computing and Applied Mathematics Laboratory
- Applied and Computational Mathematics[2]
- Statistical Engineering[2]
- Scientific Computing Environments[2]
- Computer Services[2]
- Computer Systems and Communications[2]
- Information Systems

[1] At Boulder, CO 80303.
[2] Some elements at Boulder, CO 80303.

Semiconductor Measurement Technology:

Improved Characterization and Evaluation Measurements
for HgCdTe Detector Materials, Processes, and Devices
Used on the GOES and TIROS Satellites

David G. Seiler, Jeremiah R. Lowney, W. Robert Thurber,
Joseph J. Kopanski, and George G. Harman

Semiconductor Electronics Division
Electronics and Electrical Engineering Laboratory
National Institute of Standards and Technology
Gaithersburg, MD 20899-0001

April 1994

National Oceanic and Atmospheric Administration
TIROS Satellites and Satellite Meteorology

.

TABLE OF CONTENTS

LIST OF FIGURES

LIST OF TABLES

Semiconductor Measurement Technology:

Improved Characterization and Evaluation Measurements for HgCdTe Detector Materials, Processes, and Devices Used on the GOES and TIROS Satellites

D. G. Seiler, J. R. Lowney, W. R. Thurber,
J. J. Kopanski, and G. G. Harman

Semiconductor Electronics Division
National Institute of Standards and Technology
Gaithersburg, MD 20899

ABSTRACT

An extensive study was carried out to improve the characterization and evaluation methods used for HgCdTe (mercury-cadmium-telluride) photoconductive infrared detectors used in GOES and TIROS satellites. High-field magnetotransport techniques were used to determine the electrical properties of the detector accumulation layers, which partially control their detectivities. Assessments were made of the quality of the bonding and packaging used in detector fabrication, and a list of recommended practices was produced. The applicability of scanning capacitance microscopy and test structures to detector-array evaluation is discussed, and, finally, recommendations are made for standardized detector calibration. The results of this work have provided new and more refined measurement methods that can be adopted by the detector manufacturers to improve performance and yield.

KEY WORDS: bonding; geostationary environment satellite; infrared detector; IR detector calibration; magnetoresistance; mercury cadmium telluride; packaging; scanning probe microscopy; Shubnikov-de Haas; test structure

1
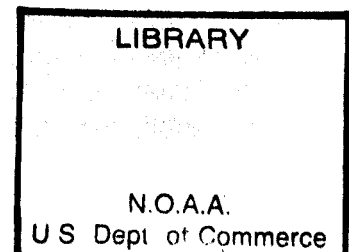
EXECUTIVE SUMMARY

This report summarizes results of extensive studies carried out by the National Institute of Standards and Technology (NIST) for the National Oceanic and Atmospheric Administration (NOAA) on improving characterization and evaluation measurements of HgCdTe infrared detector materials, processes, and devices used for the Geostationary Operational Environmental Satellite (GOES) and the Television and Infrared Operational Satellite (TIROS) systems.

NIST has provided services to NOAA, the National Aeronautics and Space Administration (NASA), ITT Aerospace Communications Division in Fort Wayne, Indiana, and several other detector fabrication companies in areas of detector packaging, bonding, and metallization. Numerous detector committee meetings and briefings were attended by NIST personnel.

The techniques developed by NIST and reported here have the advantage that they can be applied to actual, small-area, commercial detectors being manufactured for the GOES and TIROS Programs. These measurements provide high-quality data which are demonstrated to provide a unique characterization signature for an infrared detector. A physical model of the detector surface layers has been developed relating detector parameters to performance, thus permitting a better understanding and engineering of current detectors as well as future generations. In addition, the techniques developed here provide a diagnostic tool to characterize effects of processing on detector performance, as well as the ability to characterize detector stability and reliability. New processing fabrication procedures being developed can now be much better understood and monitored.

NIST has carried out state-of-the-art applied and fundamental research on two magnetic-field-based characterization measurements needed for the HgCdTe-based infrared photoconductive detectors of the GOES and TIROS Programs. The oscillatory variation in resistance with magnetic field, i.e., the Shubnikov-de Haas (SdH) effect, and the behavior of the dc magnetoresistance are both shown to provide crucial understanding and characterization of the properties (electron concentrations and mobilities) of the two-dimensional electron gas (2DEG) in the accumulation layers produced by the passivation process. The detector performance depends to a great extent upon the type and quality of the passivation process. Ten samples were prepared for low-temperature Shubnikov-de Haas and other measurements for the NIST HgCdTe detector studies.

Shubnikov-de Haas oscillations in the transverse magnetoresistance have been used to characterize accumulation layers of the infrared detectors used in GOES and TIROS weather satellites. Electron densities, cyclotron effective masses, and Dingle temperatures can be obtained from the data for each subband in the 2D electron gas formed by the accumulation layer. A first-principles calculation of the subband energy dispersion relations has been performed in order to compare theory and experiment. The model is needed to extract the electron density from the data because the energy bands are very nonparabolic in narrow-gap HgCdTe. The agreement between predicted and measured masses and Fermi energies was excellent for anodically oxidized layers. Effective masses could not be obtained for other processes because signals were weak and complex. A large number of detectors from each of three suppliers were measured by the SdH effect, and the data were analyzed. Results obtained for devices with type I passivation (anodic oxidation) gave Fourier transforms with large, well-defined peaks from which the carrier density of the accumulation layer was obtained. Detector elements with different passivations, type II and type III, had a weak SdH response. The carrier density of accumulation layers of type II and III detectors were much greater than those for type I detectors. The generally lower mobilities and higher densities of accumulation layers in type II and type III

2

detectors led to their improved performance because of reduced leakage and decreased surface recombination. Angular rotation studies were done on devices from two suppliers to verify that the SdH signal was coming from the two-dimensional accumulation layers. Effective masses and Dingle temperatures were calculated for one or more elements with type I passivation. The values were in good agreement with theoretical calculations.

A new and simpler method to characterize infrared detectors has been developed based on dc magnetoresistance upon which the small-amplitude SdH oscillations are superimposed. Electron density and mobility in the top accumulation layer can be determined from the magnetic-field dependence of the transverse magnetoresistance at high fields. Agreement between densities and mobilities in accumulation layers of type I and type II detectors with Hall measurement data supplied by the manufacturers showed the method was accurate. Measurements were made on a large number of detectors. The results showed variability of the accumulation-layer density by 20% among three elements of a multi-element detector. This method can be applied directly to the fabricated detectors because it requires only two terminals.

A total of six visits were made to three GOES and TIROS infrared detector manufacturers during fiscal years 1992 and 1993. The first visit to each site served to evaluate the production lines and the processes. Later visits were made to help them improve the detector packaging. This included one 2.5-h seminar on wire bonding and reliability of metallurgical systems used in packaging HgCdTe detectors. Over 30 people attended that seminar. For another company, a more informal hour-long presentation was made to 6 or 7 engineers and management personnel. Extra time was later spent in visiting their packaging laboratories. A scanning electron microscope study was made of detectors from one manufacturer that showed several defects (the results of this study were presented at a GOES project review at NASA Goddard, July 10, 1992). This information, with proposed solutions, was also fed back to the manufacturer to help them improve their product. Studies were carried out at NIST and at two detector manufacturing sites to establish the best molecular-cleaning methods that are compatible with normal HgCdTe detector packaging methods. For this work, ultraviolet cleaning equipment was handcarried to detector manufacturers so that tests could be performed there.

Because of the substantial impact of test structures on other semiconductor circuits, the current state-of-the-art applications of test structures to HgCdTe-based IR detectors were comprehensively reviewed. To place these applications in context, the general principles of applying test structures, determined through experience with silicon integrated circuits (ICs) and GaAs monolithic microwave integrated circuits (MMICs), were also reviewed. From these two reviews, principles and ideas were extracted for test-structure applications that could be used to further enhance the manufacturability, yield, and performance of IR detectors. To communicate and encourage application of test structures, the results of the study were presented at the Measurement Techniques for Characterization of MCT Materials, Processes, and Detectors Workshop held in Boston, Massachusetts, during October 1992 and published in *Semiconductor Science and Technology*. A reprint of this paper is included in this report as an appendix.

Scanning capacitance microscopy (SCM) is a new, nondestructive metrology tool that merges a high-sensitivity capacitance sensor with an atomic force microscope (AFM). SCM applications that could be expected to have a large impact on the quality, yield, and manufacturability of IR detectors include: nondestructive diagnosis of material variations within the active regions of detectors, nondestructive prefabrication materials evaluation, and depth profiling of dopants in nanostructures. AFM images were made of some photoconductive detector elements to illustrate the feasibility,

3

potential resolution, and image quality of SCM applied to IR detectors.

NIST staff from the Radiometric Physics Division visited and examined the radiometric calibration programs of the detector suppliers and the system integration contractor where the final radiometric calibrations are performed. NIST recommends that a fundamental calibration program be established that is coordinated between the different manufacturers and assemblers. NIST also recommends that the GOES detectors be calibrated several times before launch to establish a calibration history and base line.

1. INTRODUCTION

A. Background

(1) Infrared Detectors Used on the GOES and TIROS Satellites

The National Oceanic and Atmospheric Administration (NOAA) has the responsibility for producing, launching, and operating a multiple Geostationary Operational Environmental Satellite (GOES) system. The primary purpose of the GOES Program is the continuous and reliable collection of environmental data in support of weather forecasting and related services. The data obtained by the GOES satellites provide information needed for severe storm detection, monitoring, and tracking; wind measurements from cloud motion; sea surface thermal features; precipitation estimates; frost monitoring; rescue operations; and research. The geostationary orbit of these satellites allows continuous observation of a portion of the earth and its atmosphere. Since 1974, these GOES satellites have been used to collect and disseminate environmental data for the United States National Weather Service. At present, there is only one aging satellite, GOES H or (GOES-7), in orbit. The United States National Weather Service now relies heavily on this aging satellite GOES-7 for crucial weather information.

New weather satellites are being produced by a program known as GOES-NEXT, for the next generation of Geostationary Operational Environmental Satellites. A series of five satellites, designated by the letters I-M, are scheduled to be produced. There are significant differences between the GOES I-M series satellites and the earlier series. The GOES D-H satellites had a passive, spin-stabilized, attitude control system. The GOES I-M series of satellites uses a three-axis attitude control system. Unlike the GOES D-H series, the GOES I-M satellites support separate imager and sounder instruments that operate independently and simultaneously perform imaging and sounding operations. These satellites perform a number of functions including visible and infrared imaging (Imager) and atmospheric sounding (i.e., depth profiling of the atmosphere) (Sounder) by using various types of detectors.

The GOES sensors provide two-dimensional cloud and temperature imagery in both visible and infrared spectra, radiometric data that provide the capability to determine the three-dimensional structure of atmospheric temperature and water-vapor distribution, and solar and near-space environmental data. Three different types of detectors are used in each of the Imager and Sounder systems: silicon (Si) photovoltaic detectors for visible radiation, indium-antimonide (InSb) photovoltaic detectors for infrared radiation, and mercury-cadmium-telluride (HgCdTe) photoconductive detectors for various infrared-radiation spectral regions. There are five channels for the Imager. Table 1.1 shows their specifications for detector type, wavelength range, and their purpose. Spectral separation in the Imager is done by fixed dichroic beam splitters, permitting simultaneous sampling of all five spectral channels.

The Sounder instrument has 19 channels. There are four Sounder bands containing Si detectors for the visible, InSb detectors for the shortwave infrared, and HgCdTe detectors for both the midwave and longwave infrared regions. These bands provide information on atmospheric temperature profiling. The visible spectrum and the three infrared bands are separated by dichroic beam splitters. The three infrared bands then pass through three concentric rings of a filter wheel where channel filters provide sequential sampling of the seven longwave, five midwave, and six shortwave channels.

Table 1.1. Imager Channel Functions

	Spectral Channels				
	1	2	3	4	5
Detector Type	Si	InSb	HgCdTe	HgCdTe	HgCdTe
Wavelength (μm)	0.55 to 0.75	3.80 to 4.00	6.50 to 7.00	10.20 to 11.20	11.50 to 12.50
Function	Cloud Cover	Nighttime Clouds	Water Vapor	Surface Temperature	Sea Surface Temperature & Water Vapor

The ternary intermetallic compound $Hg_{1-x}Cd_xTe$ is one of the most important materials used in infrared detectors. These infrared detectors are widely used for military applications and civilian purposes such as in satellites that need spaceborne infrared sensors for remote temperature sensing. Interest also exists in using these detectors for evaluating home and industrial energy loss, medical thermography (i.e., breast cancer detection), astronomical research, spectrophotometers, laser light detection, remote controls for TV sets and VCRs, etc.

The Television and Infrared Observation Satellite (TIROS) also performs meteorology functions using HgCdTe infrared (IR) detectors incorporated into two instruments: the Advanced Very High Resolution Radiometer (AVHRR) and the High Resolution Infrared Radiation Sounder (HIRS). In fact, there are a large number of commercial and defense satellites that incorporate HgCdTe IR detectors in their instruments as illustrated in Table 1.2.

6

Table 1.2. Partial Listing of Spaceborne Infrared Sensor Programs Using Mercury-Cadmium-Telluride Detectors

KNOWN APPLICATION AREA	SATELLITE	INSTRUMENT
Meteorology	DMSP (Defense Meteorological Satellite Program)	OLS (Operational Linescan System)
Communications	ATS (Applications Technology Satellite)	VHRR (Very High Resolution Radiometer)
Meteorology/Oceanography	NIMBUS	CZCS (Coastal Zone Color Scanner) LRIR (Limb Radiance Inversion Radiometer) LIMS (Limb Infrared Monitor of the Atmosphere) HIRS (High Resolution Infrared Radiation Sounder)
Meteorology	TIROS (Television and Infrared Observation Satellite)	AVHRR (Advanced Very High Resolution Radiometer) HIRS (High Resolution Infrared Radiation Sounder)
Meteorology	ITOS (Improved TIROS Operational Satellite)	VHRR (Very High Resolution Radiometer)
Earth Resources	LANDSAT	MSS (Multispectral Scanner System)
Meteorology	NOAA (National Oceanic & Atmospheric Administration)	AVHRR (Advanced Very High Resolution Radiometer)
Earth Resources	SKYLAB	S-192 (Multispectral Scanner)
Earth Resources	ERTS (Earth Resources Technology Satellite)	MSS (Multispectral Scanner System)
Meteorology	GOES (Geostationary Operational Environmental Satellite)	VAS (Visible Infrared Spin-Scan Radiometer Atmospheric Sounder)
Meteorology	SMS (Synchronous Meteorological Satellite)	VISSR (Visible Infrared Spin-Scan Radiometer)
Earth Resources	ERBS (Earth Radiation Budget Satellite)	HALOE (Halogen Occultation Experiment)

(2) Previously Published Report on HgCdTe Detector Reliability Study for the GOES Program

The results of a special assessment carried out by NIST, at the request of NOAA, of the reliability of certain infrared detectors for the Geostationary Operational Environmental Satellite system were summarized in a special report, NISTIR 4687, by D. G. Seiler, G. G. Harman, J. R. Lowney, S. Mayo, and W. S. Liggett, Jr. [1.1]. The data made available by ITT on detector resistances and signals supported the conclusion that degradation of some detector responses had occurred, even when the estimated measurement uncertainty was included. Statistical analysis of the 11-μm detectors confirmed that one detector decreased in signal with time. The existing data available to NIST are not sufficient to identify uniquely the cause of degradation or unstable behavior present in a number of detectors. NIST's physical examination of several detectors by optical and SEM microscopy methods and an examination and analysis of the Detector Measurement Database has yielded several plausible possible mechanisms for the observed degradation. These possible mechanisms are related to the detector fabrication or processing steps and include: incomplete or poor passivation procedures, excess mercury diffusion resulting from the ion-beam milling fabrication step, poor indium electrical contacts produced by the indium-plating fabrication step, and delamination of the ZnS anti-reflection optical coating. Other observed problems were poor wire bonding, use of tin-lead solder to couple the fine gold wire (bonded to the detector) to the package terminal, and use of silicone RTV to stake the bond wires to the edge of the ZnS substrate.

One of the recommendations given at the end of this assessment report suggested that magnetic-field-based measurements such as Hall-effect and Shubnikov-de Haas effect measurements be performed to determine the properties of the accumulation layers produced by the passivation process. The work presented here addresses this recommendation.

(3) Fabrication of Photoconductive HgCdTe Infrared Detectors

Infrared photoconductive detectors are devices that convert electromagnetic radiation to electric signals by direct conversion of incident photons into conducting electrons or holes. The signals can then be processed to obtain information from the intensity and wavelength distribution of the incident radiation. Figure 1.1 shows the principal elements of the HgCdTe GOES detectors [1.2].

There are a number of reasons why $Hg_{1-x}Cd_xTe$ alloys are used. By varying the mole fraction x, the energy gap can be continuously adjusted from below 0.04 to above 1.3 eV, covering the 1- to 25-μm infrared region. Tailor-made materials can thus be grown to respond to preselected wavelengths, providing one the opportunity to make a range of temperature measurements from orbit. Quantum efficiencies approaching 100% for 12- to 16-μm-thick devices are possible. Material having a long carrier lifetime can be produced even at relatively high processing temperatures. The material can also be made quite pure (approaching electrical levels of approximately 1×10^{14} cm^{-3} carriers). In addition, the surfaces can be passivated by any of a large number of approaches, including using ZnS, native (anodic) oxides, sulphides, fluorides, etc. It is important to note that the performance of the detector depends to a great extent upon the type of passivation process.

Important factors that influence the responsivity, impedance, and noise of the photoconductive detectors are the energy gap, doping concentration, electron and hole mobilities, carrier lifetimes, passivation properties, the effects of ion millings, and the contacts. Effects associated with the device contacts and surfaces can cause gross distortions of the detector operating characteristics. The processing details for fabricating contacts to HgCdTe are based largely upon empiricism. A

8

ZnS
antireflective
coating ─

Gold bond
wires ─

┌─ Passivation

┌─ In

HgCdTe

Glue

ZnS
substrate
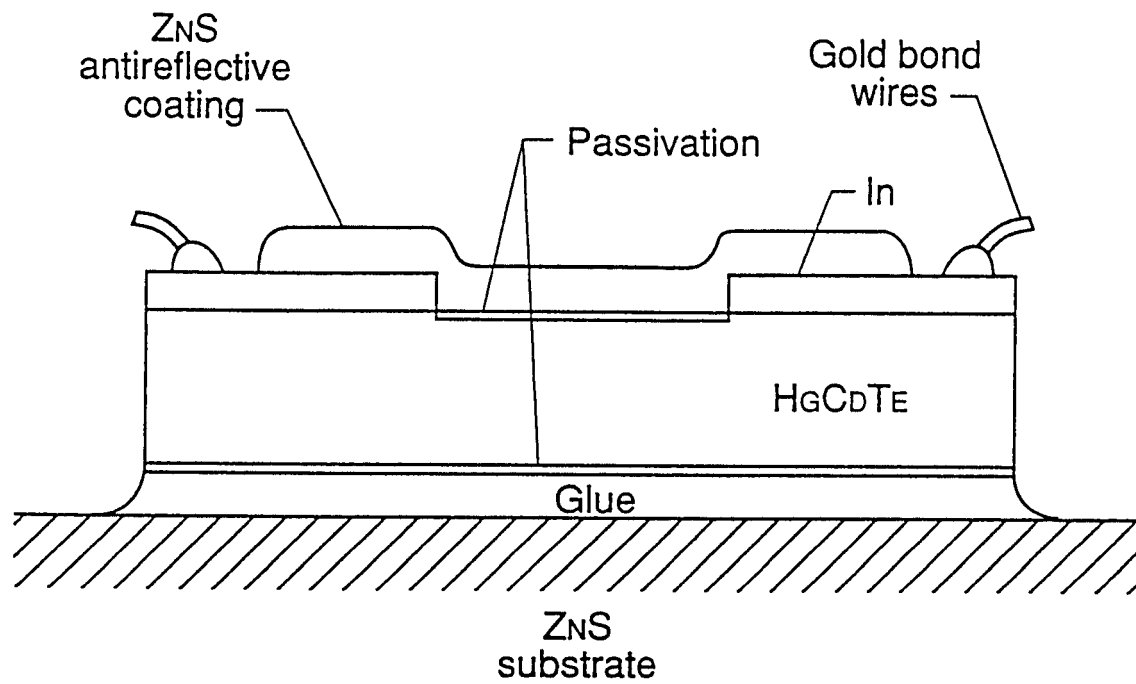
Figure 1.1 Principal components of a HgCdTe GOES detector element [1.2]. For the Imager,
the 7-μm-wavelength detectors have two elements; the 11-μm- and 12-μm-wavelength detectors, four.

fundamental understanding is lacking. Formation of Schottky barriers causes voltage instabilities and problems with reproducibility and reliability.

Passivation is used to produce high carrier densities at the detector surfaces to reduce recombination and noise by repelling minority carriers and filling surface traps. Passivation also serves to stabilize the surfaces. An adequate passivation layer must (1) be a good insulator, (2) adhere sufficiently well to the HgCdTe, (3) be time stable, (4) be stable against the atmosphere (unless a hermetic seal is used), (5) not be attacked by chemicals necessary for making the device, (6) be sufficiently nonporous that atmospheric gases cannot move through it and attack the HgCdTe, and (7) produce an interface which is sufficiently inert electrically so that it does not degrade the operation of the detector. Inhomogeneity or nonuniformity in the relative concentrations of mercury and cadmium, doping concentration level, or defects throughout the wafers can cause problems. Production yields for the high-performance detectors are typically low, on the order of 5 to 10% or even lower.

B. Importance of Work Presented Here

The HgCdTe infrared detectors used in the GOES and TIROS Satellite Programs are essential components of the satellite. The success or failure of the many functions of these satellites depends upon the proper and reliable operation of these detectors. The detectors planned for use must have high reponsivities or detectivities along with low 1/f noise characteristics in order to meet specifications required by NOAA.

These state-of-the-art detectors are not easy to manufacture, and production yields are correspondingly very low. In addition, it may be that "hot" detectors, i.e., those that meet the stringent specifications, are more susceptible to degradation or reliability problems because of the use of newer technologies. It is, thus, imperative that a physically based understanding, rather than just empirically based knowledge, be acquired for the selection, operation, and determination of the limitations and reliability of the detectors.

The GOES detector degradation task force team "struggled" with the question of how to characterize and understand the stability or reliability of the photoconductive detectors. A significant diagnostic technique was found to be lacking. The development of the magnetotransport methods presented here now provides a diagnostic tool to be used.

The HgCdTe industry is very concerned about the following issues that were directly raised by several companies:

- "Why do individual detectors fail? Local characterization techniques are needed. There is no well-understood body of knowledge available for HgCdTe. In wide-gap HgCdTe, one obtains good signatures by photoluminescence methods, but in narrow-gap material, understanding of the issues and characterization methods is lacking."

- "Many issues exist: nonuniform impurity distributions, defects and impurities, complexes, ... We don't know how to analyze the structures we are growing. THE ABILITY TO GROW STRUCTURES HAS OUTGROWN THE ABILITY TO CHARACTERIZE THE MATERIAL. There is a need to develop a good signature by using a particular characterization technique."

- Producing high-performance detectors is still a "trial and error" process using "black magic" and

10

"lots of sweat." Industry has to "build a learning curve" first.

NIST has thus investigated, developed, and performed state-of-the-art applied and fundamental research related to new and improved characterization measurements for HgCdTe-based infrared detectors needed by the GOES and TIROS Programs. NIST has developed a number of magnetic-field-based techniques that have the proven capabilities of providing the necessary understanding and characterization of HgCdTe detectors. These techniques include: (1) variable magnetic field and variable-temperature magnetotransport measurements, and (2) oscillatory magnetoresistance (periodic variation of resistance with magnetic field), i.e., Shubnikov-de Haas measurements. These techniques are capable of determining the necessary information about the properties of the two-dimensional electron gas (2DEG) in the accumulation layers produced by the passivation process and of the bulk HgCdTe. This information includes the concentrations and mobilities of electrons in the 2DEG and bulk, and related properties such as energy gaps and impurity- and defect-level information. These magnetic-field-based measurement results can then be compared with the device parameters so that a direct correlation of materials, processing, and device properties is achieved. This allows the establishment of a database linking the detector parameters to specific aspects of the material properties and the effects of the processing.

NIST is also developing and establishing scanning capacitance microscopy (SCM) as a new tool for contactless, nondestructive characterization of HgCdTe wafers and processing technologies. Nondestructive evaluation techniques are urgently needed for enhancing the yields of the HgCdTe infrared detectors. SCM combines two established NIST technologies: capacitance-voltage characterization of semiconductors and atomic-force microscopy. SCM will provide high spatial resolution mapping of native and process-induced lateral variations in the electrical properties of HgCdTe, including the bulk and accumulation layer regions.

C. Outline and Organization of Report

The following items summarize the content of this report, which is divided into two parts. Part I relates to high-field magnetotransport characterization of detector accumulation layers, while Part II relates to a number of other characterization techniques and issues.

- Section 2 gives extensive, systematic results on the use of quantum magnetotransport measurements (Shubnikov-de Haas oscillations) to characterize GOES and TIROS HgCdTe IR photoconductive detectors. The fundamental theory is presented, as well as the proper physical modeling for the electric subband energies and densities, accumulation-potential wells at the HgCdTe interface, and the subband effective masses and Dingle temperatures.

- Section 3 presents the results of a new technique developed to extract the electron density and mobility in the top accumulation layers. It is based on measurements of the dc magnetoresistance (the background signal on which the Shubnikov-de Haas oscillations are superimposed). This technique is easy to apply and should be easily adopted by the detector manufacturers to improve their quality control of existing detectors as well as to help engineer new, improved detectors.

- Section 4 presents the bonding, metallization, and packaging consulting work done for the GOES and TIROS infrared detectors. An overview, rationale, and accomplishments of the work are given.

11

- Section 5 summarizes NIST work done on reviewing the use of test structures in the semiconductor manufacturing industry, with a particular emphasis on HgCdTe-based IR detectors. This section, along with the detailed results presented in Appendix B, gives a complete review of test structures applied to IR detectors and contains suggestions on how to improve IR detector process control, yield, performance, and reliability through the intelligent application of test structures.

- Section 6 gives a report on the establishment at NIST of scanning capacitance microscopy. SCM has important capabilities to image nanoscale variations in dopant concentration, composition, defects, mobility, and charge distributions within the detector elements.

- Section 7 discusses recommendations for detector calibration.

- Section 8 summarizes and concludes the work presented.

- Section 9 lists the references.

- Appendix A is a reprint of an article, "Heavily Accumulated Surfaces of Mercury Cadmium Telluride Detectors: Theory and Experiment" which reports NIST work on characterizing the GOES detectors [1.3]. These initial results were disseminated to the HgCdTe detector community through a talk and this paper given at the 1992 U.S. Workshop on the Physics and Chemistry of HgCdTe and Other IR Materials. The paper is published in the *Journal of Electronic Materials* in August 1993.

- Appendix B is a reprint of an invited article "Review of Semiconductor Microelectronic Test Structures with Applications to Infrared Detector Materials and Processes," published in June 1993. This paper was given at the 1992 Workshop on Measurement Techniques for Characterization of HgCdTe Materials, Processing, and Detectors and was published in *Semiconductor Science and Technology* in 1993.

- Appendix C is a reprint of an invited article "$Hg_{1-x}Cd_xTe$ Characterization Measurements: Current Practice and Future Needs," was published in *Semiconductor Science and Technology* in 1993.

PART I - HIGH-FIELD MAGNETOTRANSPORT STUDIES

2. CHARACTERIZATION OF GOES AND TIROS HgCdTe IR DETECTORS BY QUANTUM MAGNETOTRANSPORT MEASUREMENTS

A. Review of Shubnikov-de Haas (Oscillatory Magnetoresistance) Effect

The two-terminal resistance of a semiconductor generally rises in a transverse magnetic field, B, and this effect is referred to as transverse magnetoresistance. It can be caused either by macroscopic current bending by the magnetic field or microscopic effects resulting from the admixture of carriers with different mobilities. This nonoscillatory or dc magnetoresistance is discussed in section 3. The magnetoresistance effect discussed here is due to the small Shubnikov-de Haas (SdH) oscillations in resistance that are superimposed on the large dc magnetoresistance background. These oscillations are quantum-mechanical in nature and result from the successive crossing of Landau levels by the Fermi energy. Analysis of these oscillations leads to values for the densities and effective masses of the contributing carriers, and thus this technique can be very useful in characterizing important properties of semiconductors.

Shubnikov-de Haas analyses have been performed on HgCdTe infrared detectors to determine the carrier densities in their accumulation layers [2.1]. The accumulation layers form a two-dimensional (2D) electron gas with several allowed subbands. The bulk, which is three-dimensional (3D) in behavior, does not contribute significantly to these oscillations because of its low carrier density ($\sim 3 \times 10^{14}$ cm^{-3}). This is illustrated for the GOES detectors by the angular dependence of the oscillations in section 2.B.6. Each subband produces its own oscillation, and Fourier transform techniques are then used to separate and identify the components. This technique has been used and extended in this work to characterize the properties of accumulation layers, which have a controlling influence on long-wave infrared detector performance.

The detector sample is mounted in a liquid-helium, variable-temperature cryostat in a superconducting magnet capable of 9 T. The plane of the sample is perpendicular to the field so that the field is perpendicular to both the current and the accumulation layers. The oscillations are very small and must be enhanced by lock-in amplifier techniques. A small ac magnetic field is superimposed on the dc magnetic field, and the ac signal is then measured by a lock-in amplifier that uses a reference signal with twice the frequency of the ac signal. The resultant signal is greatly magnified, and is comparable to a second derivative of the initial signal. This second-derivative-like signal is then Fourier analyzed to obtain subband densities and effective masses. A review of these techniques is given by Seiler et al. [2.2] and Yamada et al. [2.3].

B. Physical Modeling and Fundamental Theory

(1) Theory of Shubnikov-de Haas Effect

The Shubnikov-de Haas effect is a small oscillation in the magnetoresistance of a solid at high magnetic fields. It is due to the redistribution of carriers among the Landau levels, which are the allowed energy levels in the presence of a magnetic field, when one of the Landau levels crosses the Fermi energy. This oscillatory behavior is characteristic of the properties of the conducting electrons, e.g., carrier density, effective mass, and mobility, and can be used as an important characterization

13

tool. It is a much simpler measurement to make on a fabricated detector than the more common Hall-effect measurement because it can be made with only two terminals.

The fundamental theory for the effect has been developed by Ando [2.4], who derived the following equation for the oscillatory magnetoresistance signal in two dimensions:

$$\frac{\Delta\rho}{\rho_o} = - \sum_{S=0}^{n} \sum_{r=0}^{\infty} 2\, A_s(\omega_s,\tau_s,r_s) B_s(\omega_s,T,r_s) C_s(m_s,g_s,r_s)$$

$$\times\, D_s(\omega_s,\tau_s{}',r_s)(-1)^{r_s+1} \cos\left[\frac{2\pi(r_s+1)E_{F,s}}{\hbar\omega_s}\right] J_2((r_s+1)\sigma_s) \quad, \tag{1}$$

where

$$A_s(\omega_s,\tau_s,r_s) = \frac{4(\omega_s\tau_s/(r_s+1))^2}{\left[(r_s+1)^2 + (\omega_s\tau_s)^2\right]^2} \quad, \tag{2}$$

$$B_s(\omega_s,T,r_s) = \left[\frac{2\pi^2(r_s+1)k_BT}{\hbar\omega_s}\right] csch\left[\frac{2\pi^2(r_s+1)k_BT}{\hbar\omega_s}\right] \quad, \tag{3}$$

$$C_s(m_s,g_s,r_s) = \cos\left((r_s+1)\pi m_s g_s/2\right) \quad, \tag{4}$$

$$D_s(\omega_s,\tau_s{}',r_s) = \exp\left(-(r_s+1)\pi/\omega_s\tau_s{}'\right) \quad, \tag{5}$$

$$\sigma_s = \frac{2\pi E_{F,s}B_m}{\hbar\omega_s B} \quad, \tag{6}$$

and where ρ_o is the resistivity at zero magnetic field, $\Delta\rho$ is the oscillatory part of the magnetoresistance at a magnetic field B, s is the subband index, r_s is the harmonic index, ω_s is the cyclotron frequency, τ_s is the scattering lifetime, $\tau_s{}'$ is the Landau-level broadening lifetime, m_s is the cyclotron effective mass, g_s is the effective g-factor, $E_{F,s}$ is the Fermi energy, k_B is Boltzmann's constant, T is the equilibrium lattice temperature, J_2 is the second-order Bessel function, and B_m is the amplitude of the modulating B-field.

14

The term A_s (ω_s, τ_s, r_s) is from Ando's self-consistent solution of magneto-transport and is left out by some authors to simplify eq (1) since A_s is slowly varying with magnetic field. A simplified phenomenological form is also sometimes used:

$$A_s(\omega_s, \tau_s, r_s) \ = \ 2\left[(r_s+1)^2 \ + \ (\omega_s \tau_s)^2\right]^{-1} \tag{7}$$

The term B_s (ω_s, T, r_s) involving temperature accounts for the broadening of the Fermi-Dirac distribution function, which greatly reduces the oscillation amplitude at high temperatures because of the gradual change in Landau-level occupancy as a function of level energy. The effect of spin splitting of the Landau levels is accounted for by the term C_s (m_s, g_s, r_s), which averages $\Delta\rho$ over both spin components. The term D_s (ω_s, τ_s', r_s) accounts for the broadening of the Landau levels due to collisions between the electrons and scattering centers. The τ_s' values are related to the scattering times τ_s for mobility, but differ in value from them because low-angle scattering contributes much more to the Landau-level broadening than to the reduction in mobility. The term $2J_2$ ((r_s+1) σ_s) occurs because the signal is measured with a lock-in amplifier that uses a signal with twice the frequency of the modulating B field to detect the signal.

(2) Fourier Transform Analysis

The first step in extracting useful data from the signal is to obtain its Fourier transform. The cyclotron frequency, ω_s, equals eB/m_s in SI units, and thus the oscillatory term in eq (1) becomes $\cos(2\pi m_s E_{F,s}/\hbar eB)$. It is periodic in $1/B$, and its Fourier transform has peaks corresponding to the $m_s E_{F,s}$ products for each subband. If the subband is parabolic, then $N_s = m_s E_{F,s}/2\pi$, where N_s is the subband carrier density, and the peak positions yield the densities directly. However, HgCdTe is very nonparabolic, especially for long-wavelength detectors, which have small energy gaps, and a model is needed to determine N_s from the peak positions.

All the terms involving B other than the oscillatory one should be removed prior to the taking of the transform. However, it is not possible to do so generally because m_s, τ_s, and τ_s' are not known *a priori*. It turns out that this is not necessary because the oscillations are much more rapid than the variations associated with these terms. Thus, the entire signal is used in the transform.

The Fourier transforms can exhibit quite complicated spectra. Peaks may appear for one or two harmonics ($r=1, 2$) and may be identified because they are multiples of the fundamentals. Generally, the harmonic peaks are much smaller than the fundamental peaks and thus may be ignored. Peaks may be split due to spin-splitting by the high electric field in the accumulation layer, or there may be multiple peaks for each subband because of the two separately passivated surfaces of the detector or variations in density within one surface. Skill is therefore needed in identifying peaks, and the model discussed below helps in interpreting the Fourier transform.

(3) Determination of Effective Masses

The Fourier transform peaks provide the $m_s E_{F,s}$ products for each subband; to proceed further, the values of m_s must be determined. The most direct way to find m_s is to first decompose the signal into its individual oscillatory components by inverse transforming each peak in the Fourier transform.

15

Then one obtains each m_s value from a best fit to the temperature dependence of the amplitude of each elemental oscillation at a fixed B value:

$$\frac{S_s(T)}{S_s(T_o)} = \frac{B_s(\omega_o, T, 0)}{B_s(\omega_o, T_o, 0)} \quad , \tag{8}$$

where $S_s(T)$ is the experimental amplitude of the fundamental signal for subband s, and ω_o is chosen at a field B_o that corresponds to a strong oscillation peak at all temperatures. A nonlinear least-squares fit is made to extract the value of m_s from the data for several temperatures according to the dependence given by eq (8). The total signal is decomposed by taking the inverse Fourier transform of its Fourier transform only between frequencies where the given subband peak is above the background. The remainder of the Fourier transform is set to zero except for the corresponding peak at very high frequency, which is not shown in the figures. This corresponding peak occurs in discrete Fourier transforms because of the equivalence between the evaluation at points k and $n - k$, where n is the number of points. However, if the peaks are not well separated, the decomposition becomes difficult, and several peaks must be included in one to obtain an "average" peak. A small error is also incurred by abruptly terminating a peak when the background is noticeably above zero. This is the main method used in this work.

An alternative method is to use the temperature dependence of the amplitude of the Fourier transform peaks directly. This approach requires the determination of an average B-field to use in the analysis because the Fourier transform involves an integral over $1/B$. Mathematically, the weighted average $1/B$ is given by:

$$<1/B> = \frac{\int_\infty^0 \frac{1}{B} \Delta\rho(B) \cos \frac{2\pi f_s}{B} d(1/B)}{\int_\infty^0 \Delta\rho(B) \cos \frac{2\pi f_s}{B} d(1/B)} \tag{9}$$

where f_s is the peak frequency. In practice, the entire complex transform is used to avoid having to determine the phase of the signal.

As long as the region in $1/B$ over which the integrals in eq (9) vary from zero to their final values is sufficiently small and symmetrical about the determined average B-field, this method should be adequate. The average B-field also must not vary significantly with temperature because only one B-field value can be used in the analysis for a given subband. This method is somewhat easier to implement than the decomposition approach and can be used for closely spaced peaks. However, occasional checks with the decomposition approach should be made to make sure the averaging is working.

After the masses have been found, the Fermi energies are then found from the values of the Fourier transform peaks. Comparison with the model discussed below yields the surface electron density that

16

gives the best agreement between experimental and theoretical values. This analysis depends on the assumption that bulk and surface electron mobilities do not depend on temperature in the measurement range, so that the only temperature dependence occurs in the term $B_s(\omega_s, T, r_s)$ in eq (1). This is usually a good assumption for temperatures between 4 K and 30 K, the temperature range most often used in measurements to extract effective masses.

(4) Model for Subbands

First-principles calculations have been used to determine the accumulation-layer potentials, electron densities, cyclotron effective masses, and Fermi energies of the 2D electron gases produced by the passivation process. For parabolic subbands, the electron densities can be obtained directly from the frequencies of the peaks in the Fourier transform. However, HgCdTe is very nonparabolic because of its small energy gap, and therefore a model is needed to deduce the densities, as stated earlier. The subband Fermi energies can be obtained from the fundamental frequencies once the cyclotron effective masses are determined from the measured temperature dependence of the amplitude of the oscillations. The model then relates these measured quantities to the electron densities.

The work of Nachev [2.5], who has performed the most rigorous analysis of the subband dispersion relations, has been extended to the entire set of allowed subbands for a wide range of electron densities. Initial results of theoretical calculations and a brief comparison to some data have been published, the reprint of which is in Appendix A [1.3]. Nachev has derived the 8×8 matrix Hamiltonian for the conduction band and the heavy-hole, light-hole, and split-off valence bands for both spin directions ($\pm$). He then reduced the Hamiltonian to a second-order differential equation for the wave function $\phi_\pm$ in the direction z-perpendicular to the accumulated surface:

$$\frac{d^2\phi_\pm}{dz^2} = a \frac{d\phi_\pm}{dz} + \left(k^2 - b \right) \phi_\pm \pm \frac{1}{3} c k \phi_\pm \tag{10}$$

where

$$a = \frac{2\alpha^2 + \beta^2}{2\alpha + \beta} \frac{dV(z)}{dz} , \tag{11}$$

$$b = \frac{3\gamma}{P_0^2(2\alpha + \beta)} , \tag{12}$$

$$c = \frac{3(\alpha^2 - \beta^2)}{2\alpha + \beta} \frac{dV(z)}{dz} , \tag{13}$$

and

17

$$\alpha = \frac{1}{E_v(z) - E^\pm} \quad , \tag{14}$$

$$\beta = \frac{1}{E_v(z) - \Delta - E^\pm} \quad , \tag{15}$$

$$\gamma = E_c(z) - E^\pm \quad . \tag{16}$$

In the above equations, k is the wave number in the plane of the surface and refers to the 2D free electron gas; $V(z)$ is the built-in potential in the accumulation layer due to the oxide charge; $E_c(z)$ and $E_v(z)$ are the conduction and valence band energies, respectively, including the effect of the potential; Δ is the split-off band energy separation from the valence band edge; P_0 is a number proportional to the momentum matrix element as given in Kane's band model for HgCdTe [2.7]; and $E^\pm$ are the eigenvalues for the two spin directions.

The wave functions $\phi_\pm(k,z)$ are real, and the actual subband wave functions, ψ, can be computed from them by solving for the eight envelope functions f_n because

$$\Psi(r) = \sum_{n=1}^{8} f_n(z) \, u_n(r) \quad , \tag{17}$$

where $u_n(r)$ denotes the periodic part of the Bloch function at $k=0$. The envelope wave functions of the conduction band, $f_1(z)$ and $f_5(z)$, are found directly in terms of $\phi_\pm(k,z)$:

$$\phi_\pm(k,z) = i \left(\frac{k_+}{k}\right) f_1(z) \pm f_5(z) , \qquad k_+ = k_x + ik_y \quad . \tag{18}$$

The other envelope functions are found from the matrix Hamiltonian in terms of these two envelope functions by direct substitution. The equations for them, which are somewhat lengthy, involve the derivatives of $f_1(z)$ and $f_5(z)$ as well because of the momentum operator in the Hamiltonian. The volumetric electron density can then be computed directly from Ψ and the areal density of the 2D electron gas.

The initial potential is found by solving Poisson's equation for a nonquantized 3D free electron gas. The standard Kane $k \cdot p$ band model [2.7], which treats the coupling of the light-hole and split-off valence bands with the conduction band, is used. Poisson's equation is solved by a nonlinear two-point boundary value method based on finite differences with deferred correction and Newton

iteration. Equation (10) is then solved by integrating the equation from an initial value and slope at the boundary opposite to the accumulation layer, and eigenvalues are found by selecting those solutions that vanish at the surface. As in reference [2.5], the interior boundary, where the conduction-band wave functions go to zero, has been chosen to be at the middle of the energy gap for a given eigenvalue or at a maximum distance of 0.5 μm if the eigenvalue always lies above midgap. Thus, only those states that are effectively bound by the conduction band and constitute a 2D electron gas are accepted. This approximation is based on the assumption that the wave functions decay sufficiently in the energy gap so that those associated with the conduction band can be separated from those associated with the valence band. As the gap becomes very small, this approximation breaks down, and a continuum background of states that traverse the entire thickness of the detector becomes allowed. This is a limitation for gaps smaller than 40 meV and densities greater than 10^{13} cm^{-2}.

Equation (10) is solved for at most 50 k values to construct the dispersion relations for the allowed subbands. A new potential is computed from the calculated wave functions between the surface and 0.1 μm; beyond this point the original bulk potential is used. Were the calculated wave functions beyond 0.1 μm to be used, there would be a difficulty because of the artificial boundary condition at 0.5 μm where the wave functions are forced to be zero. The process is iterated until the input and output potentials agree to within 1%. In order to prevent the potentials from gradually diverging from their original values, they are scaled each time by the ratio of the initially computed areal electron density to that just computed [2.8]. When this factor is between 0.99 and 1.01, convergence is obtained. It was discovered that convergence could be obtained more rapidly, and often only, if the initial potential were modified slightly between the surface and 0.025 μm to take into account the strong differences between the electron density computed initially and quantum-mechanically near the surface in the accumulation layer. The initial potential was thus subsequently scaled by a quadratic function to make it agree better with the shape of the first calculated potential over this range.

Once the self-consistent subband dispersion relations were found, the subband carrier densities, Fermi energies, and cyclotron effective masses at the Fermi energy were computed by performing either a parabolic spline interpolation or linear extrapolation of the computed eigenvalues to the Fermi energy. The spin-averaged cyclotron effective mass, m^*, is obtained from the expression

$$(m^*)^{-1} = \frac{\hbar^{-2}}{2} \sum_{\pm} \left(\frac{1}{k} \frac{dE^{\pm}}{dk} \right) , \qquad (19)$$

evaluated at the Fermi energy, E_f. These quantities now allow one to compute the value of the subband densities from the peaks in the Fourier transform of the SdH data. The frequencies corresponding to the peaks equal $m^* E_f / \hbar e$ for each subband [2.3]. The value of m^* is determined from the measured temperature dependence of the amplitude of the SdH oscillations [2.2]. Thus, one can find the subband density for which the theoretically computed product of $m^* E_f$ has the measured value for each subband. For the case of parabolic subbands, $m^* E_f = \hbar^2 \pi N$, where N is the electron density, and the peak frequencies provide N directly. This relation is referred to as the parabolic approximation, which is used throughout this work except in section 2.D.

Calculations of the subband dispersion relations and related quantities have been made here for the range of areal electron densities between 0.1 and 5.0 $\times$ 10^{12} cm^{-2}. The x-value of the detector was taken to be 0.191, with a corresponding energy gap of 41.1 meV [2.9], which is representative of

19

long-wavelength detectors and equal to that of the detectors reported on in detail below. The bulk electron doping density was assumed to be 3.9×10^{14} cm^{-3}, which was reported for these detectors, along with a bulk mobility of 2.5×10^5 cm^2/Vs at 77 K. Bulk SdH oscillations were not observed because of their low frequency, which implies that they would have been observed only at low magnetic fields where broadening effects greatly reduce their signal strength. The temperature is taken to be 6 K, at which the material is degenerate. As an example, the calculated built-in field and subband dispersion relations for an areal density of 8.9×10^{11} cm^{-2} are shown in figures 2.1a and 2.1b, respectively. The surface potential in figure 2.1a is about three times greater than the energy of the lowest subband edge and over five times the energy gap. The spin splitting is evident in figure 2.1b, and is greatest for the lowest subband. The density of electrons in the spin-up subband is about 15% greater than in the spin-down subband for the lowest four subbands. At the lower densities this percentage decreases somewhat, especially for the higher subbands, while at higher densities it remains nearly the same for all subbands. Note also that the deviation from a parabolic to a nonparabolic, nearly linear dependence of E on k is clear for energies only about 10 meV above the subband edges. The small oscillations in these curves are due to 1% numerical uncertainty in the solutions.

The corresponding electron density in the accumulation layer is shown in figure 2.2a for both the semi-classical result from the initial solution of Poisson's equation and the final quantum-mechanical result from the subbands. The width of the accumulation layer is seen to be about 0.1 μm. The latter density is greatly reduced at the surface because of the boundary condition on the wave functions. It goes to zero discontinuously across the boundary because of the dependence of the wave function on the derivatives of f_1 and f_5, which undergo a discontinuous change from a finite to zero value at the boundary. Therefore, the shape of the potential near the interface is different in the two cases, and the value of electron density obtained quantum-mechanically is less than that of the initial semi-classical solution. The electron densities of the first four subbands are plotted as a function of total density in figure 2.2b. The total density is computed from a sum over only the first four subbands, for which accurate computations can be performed. The error incurred by this approximation is estimated to be less than 1%. The relations are nearly linear with average slopes of 0.673, 0.223, 0.077, and 0.027 for the first (n=0) through fourth (n=3) subband, respectively. The deviations from linearity are less than 1%. This near linearity shows that the shape of the potential distribution is relatively insensitive to the magnitude of the surface potential. This linearity has been observed before experimentally as well, and the values of the experimental slopes are nearly the same as those calculated [2.1].

The subband Fermi energies and cyclotron effective masses are shown in figures 2.3a and 2.3b, respectively, as a function of total density. The Fermi energy in the bulk is computed to be 5.44 meV for an assumed bulk density of 3.9×10^{14} cm^{-3}. The scatter in the mass values is due to the derivative in eq (19). Although the calculated eigenvalues appear relatively smooth in figure 2.1b, they are only accurate to about 1%, and this uncertainty as well as that due to the discreteness of the k-values causes the theoretical masses to have errors of about 5% occasionally. A more refined calculation would lead to better accuracy. The strong variations of the masses with density attest to the nonparabolicity of the dispersion relations, which have an effect on the optimization of device performance. The serpentine shape of the curves is due to the strong curvature of the built-in potential.

In conclusion, the dispersion relations for the 2D subbands in the accumulation layers of HgCdTe detectors have been computed by solving the 8×8 matrix Hamiltonian for a large range of electron

20
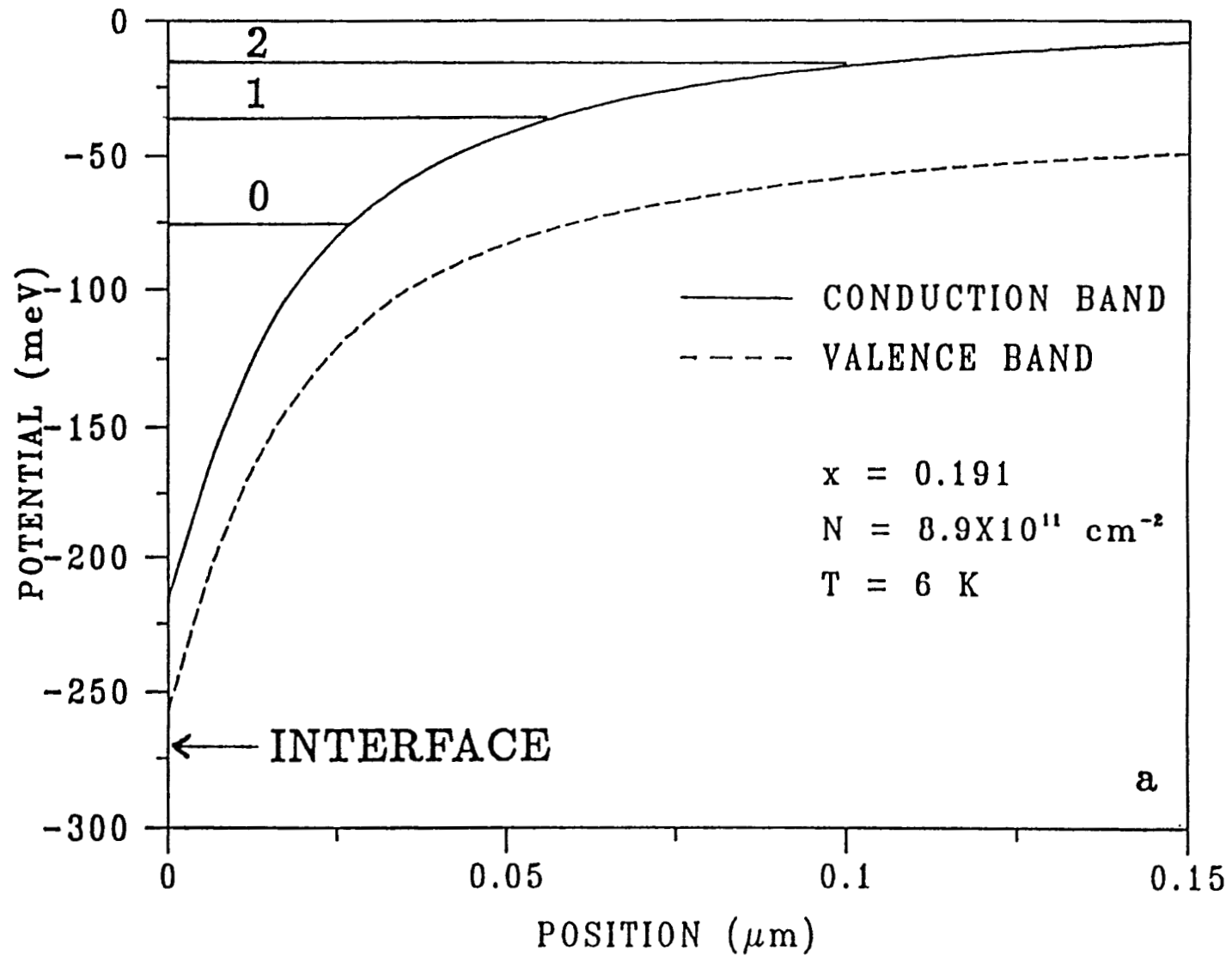
Figure 2.1a Built-in potential for accumulation layer with total electron density of 8.9×10^{11} cm^{-2} and alloy fraction x = 0.191. The horizontal lines are the subband-edge energies for the first three subbands (n=0,1,2).
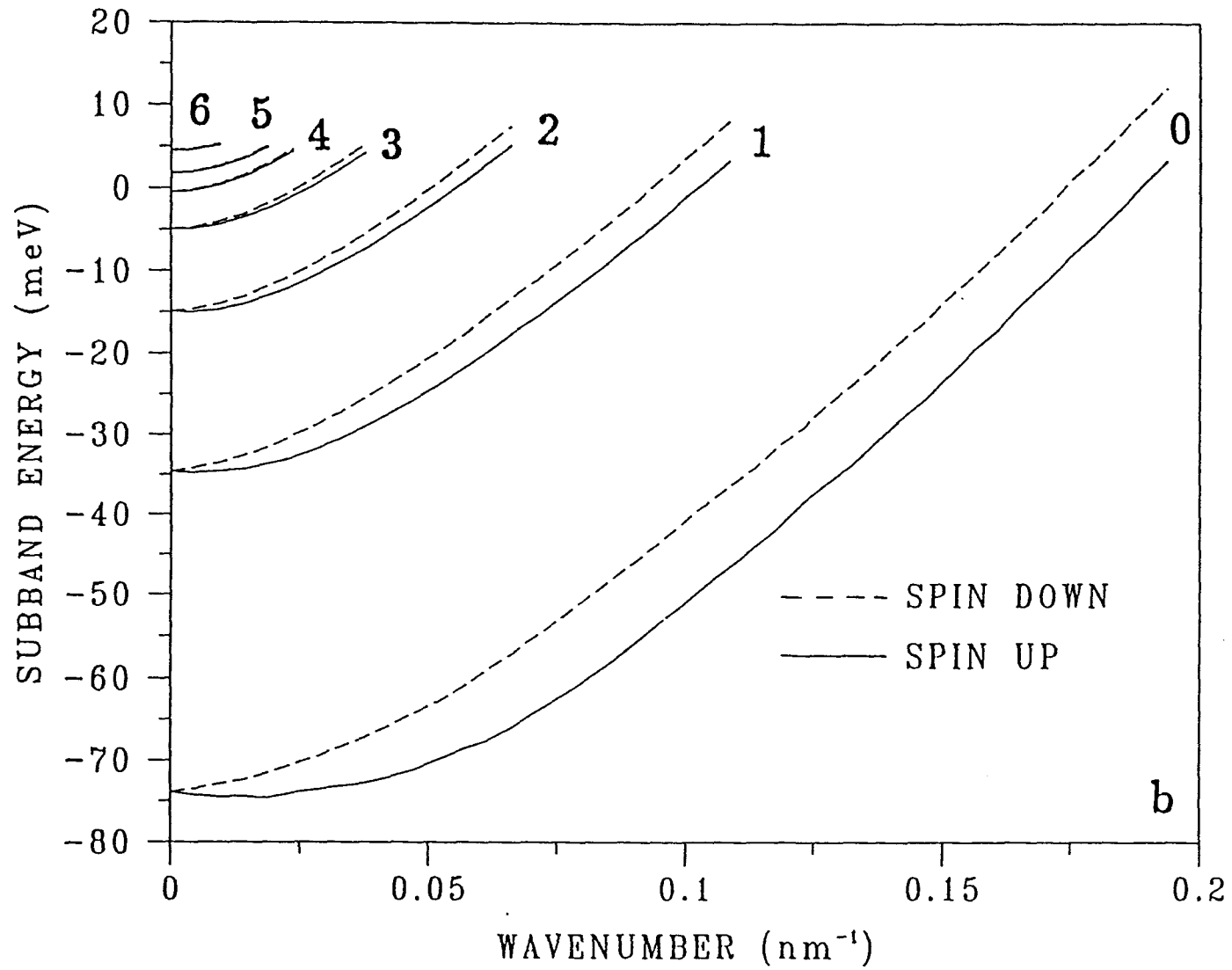
Figure 2.1b "E versus k" dispersion relations for the subbands for this potential, showing spin-splitting. The curves are labeled by subband number from 0 to 6.
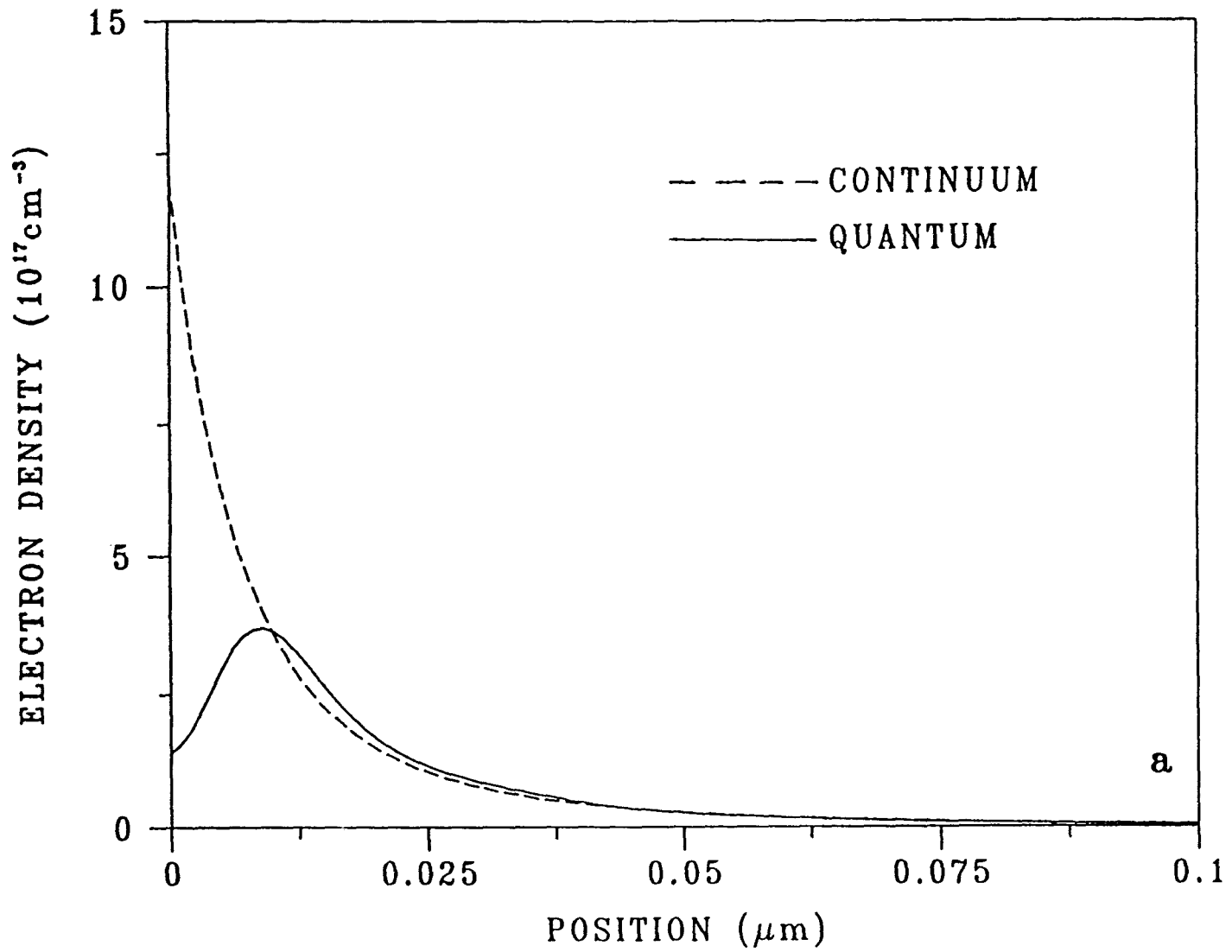
Figure 2.2a Electron density computed by solving Poisson's equation for a charge continuum (dashed) and from full quantum-mechanical calculations (solid) for the case of figure 2.1b.
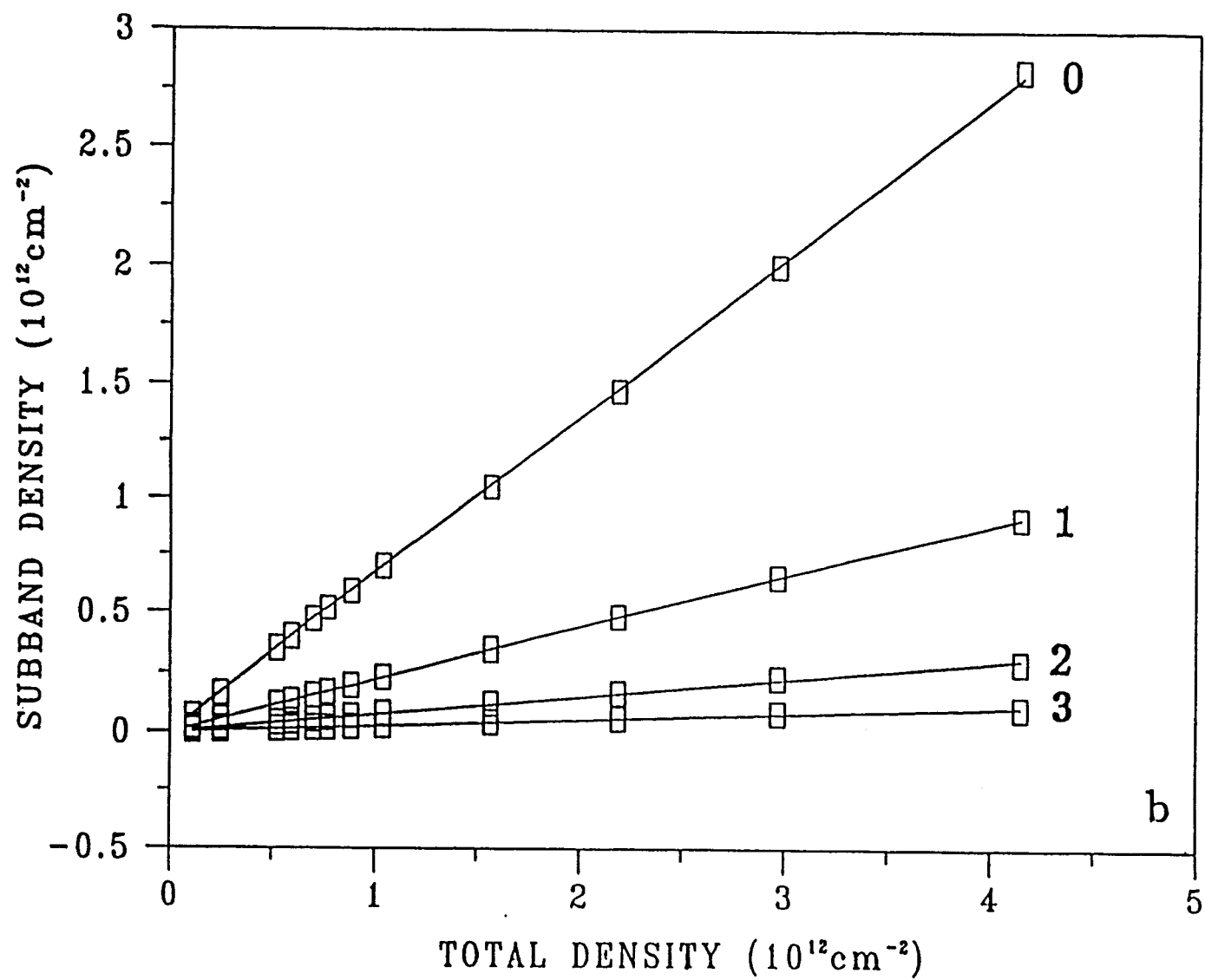
Figure 2.2b Calculated subband densities as a function of total density. Lines are linear least-squares fit. The curves are labeled by subband number from 0 to 3, and x = 0.191.

25
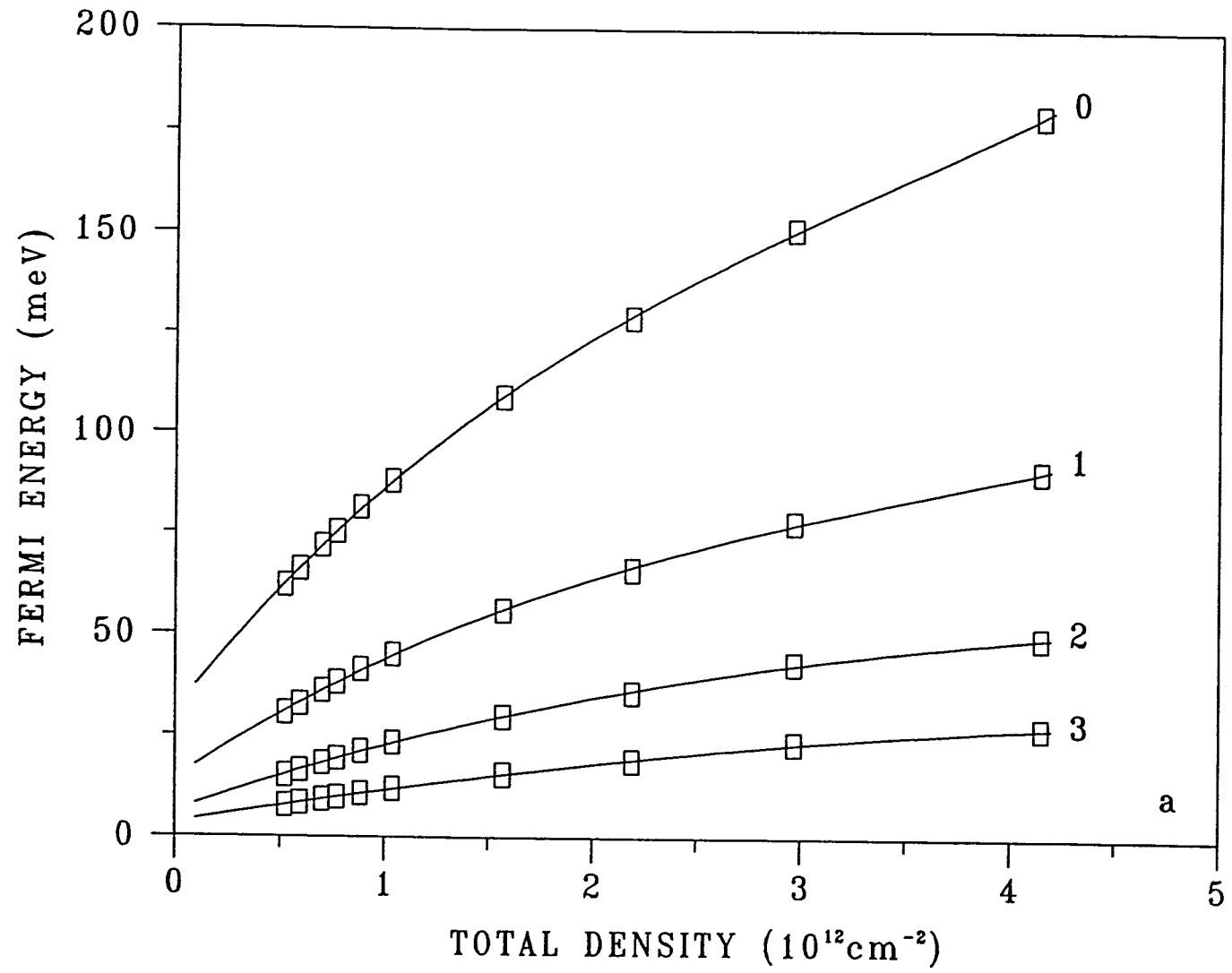
Figure 2.3a Subband Fermi energies as a function of total density, measured from the bottom of each subband.
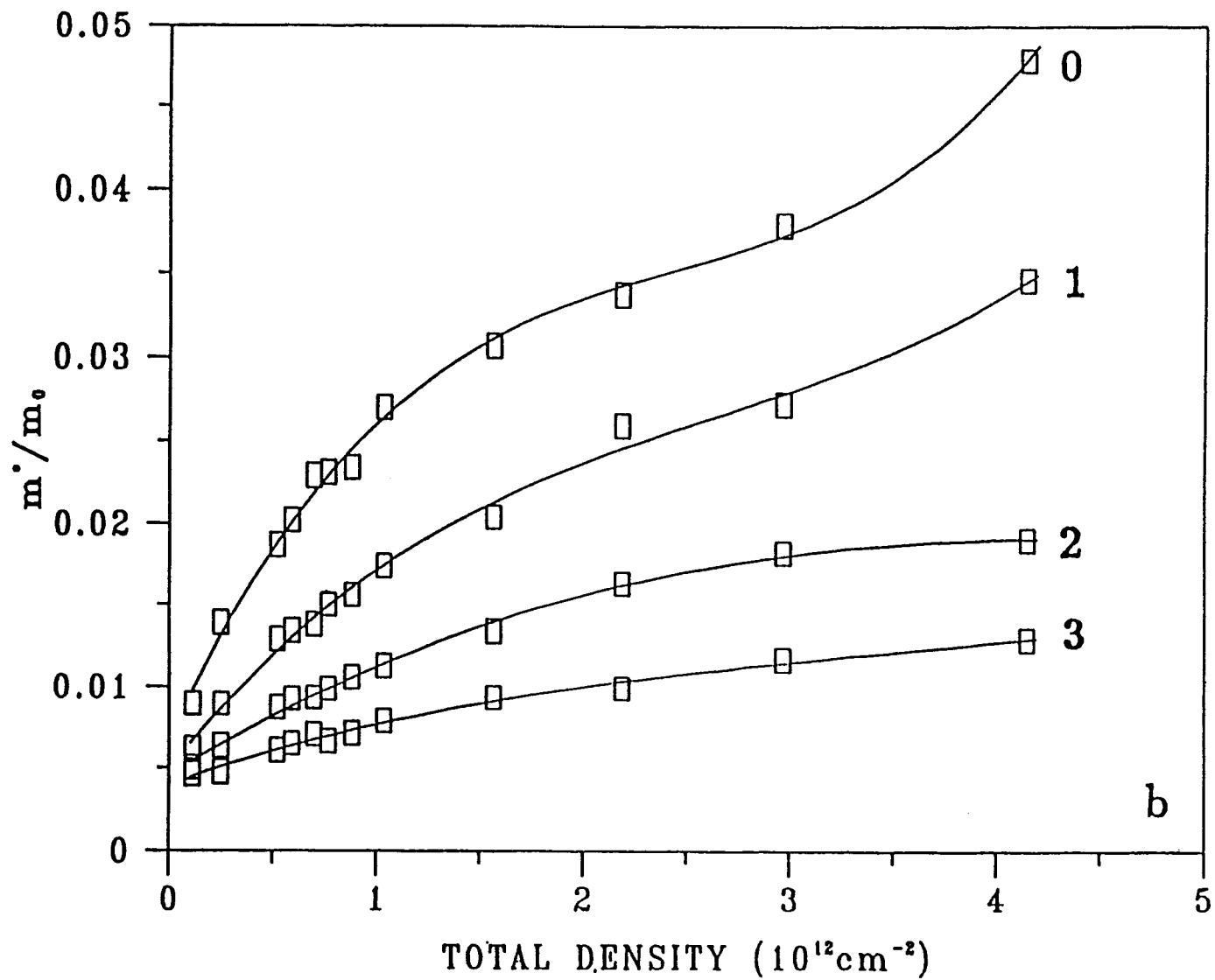
Figure 2.3b Ratio of subband cyclotron effective masses to the free electron mass at the Fermi energy as a function of total density. Lines are cubic least-squares fit. The curves are labeled by subband number from 0 to 3, and x = 0.191.

densities (0.1 to 5 × 10^{12} cm^{-2}). The subband densities, Fermi energies, and cyclotron effective masses have been computed as a function of the total electron density. The results show the effects of strong nonparabolicity. The near linear dependence of the subband densities on total density, which has been observed experimentally, has been confirmed theoretically.

(5) Determination of Dingle Temperatures

The oscillations decay with increasing $1/B$ (decreasing B) because of the scattering of the electrons by the lattice, defects, and impurities, which disrupt the cyclotron orbits and broaden the Landau levels. The term $D_s(\omega_s, \tau_s', r_s)$ in eq (1) contains this effect, which is described by the scattering time τ_s'. This τ_s' differs in value from that of the electron mobility τ, because low-angle scattering has a much smaller effect on τ [2.10,2.11]. However, the scattering mechanisms are the same in both cases, and the Landau-level broadening can at least be correlated to the mobility.

The values for τ_s' for each subband are obtained from the decomposed signals $S_s(B,T_0)$ by dividing out all the terms in eq (1) except $D_s(\omega_s, \tau_s', 0)$, and plotting the absolute result semilogarithmically, as demonstrated later. The slope of the line that is tangent to the peaks of the absolute value of the oscillations gives τ_s' directly. Another parameter, the Dingle temperature $T_{D,s}$, is commonly used instead of τ_s'. It is defined by:

$$T_{D,s} = \frac{\hbar}{2\pi k_B \tau_s'} \quad , \tag{20}$$

and is an equivalent measure of the scattering, with high Dingle temperatures implying low mobilities. The Dingle temperature can only be determined if nearly all the current goes through the top accumulation layer, which occurs at sufficiently high B-fields, so that the signal amplitude does not vary because of current division between the accumulation layers and the bulk.

(6) Dependence of SdH Signal on Angle of B-Field

The equations derived in this section are for the B-field perpendicular to the passivated interface. This configuration gives cyclotron orbits in the plane of the accumulation layer, which maximizes the effect of the field on the 2D electron gas. If the angle θ of the field with respect to the perpendicular is not zero, then only its component in the perpendicular direction relates to cyclotron orbits. Thus, all the terms involving B should be replaced with $B \cos \theta$, and the peak frequencies f_s all vary as $1/\cos \theta$ to compensate.

This dependence of the peak frequencies on θ is a definitive test of whether or not the electrons are behaving as a 2D electron gas. An example of this is shown later for a GOES detector 2D electron gas system. In a 3D system, there is no angular dependence because the cyclotron orbits can occur in any direction. Thus, one can separate 2D and 3D behavior by measuring the angular dependence of the SdH oscillations.

27

C. Results of Measurements on Specific Detectors

(1) Typical Data

Shubnikov-de Haas oscillations can be recorded with either ac or dc techniques. However, for the weak oscillatory structure present in most GOES detectors, the much more sensitive ac method which involves using ac magnetic-field modulation and phase-sensitive detection techniques is chosen for use. Figure 2.4 shows the dc magnetoresistance compared with the signal from the lock-in amplifier obtained by the ac technique. As can be seen in the figure, the dc signal has a large monotonic background which is essentially eliminated by the ac method. Sometimes the ac trace is essentially flat, and no further data manipulation is needed prior to obtaining the Fourier transform. However, frequently the ac response has some gradual background variation, as seen in figure 2.5, which is not related to the SdH oscillations. A varying background gives rise to structure at low frequencies in the Fourier transform which can mask or distort peaks in the region. Background effects are removed from the ac trace by a procedure called centering. For this procedure, the trace is divided into 5 to 20 regions, depending on the nature of the background curvature and oscillation frequency, and the average value of each region is found. Then the average values are connected by a spline fit, and the trace is replotted relative to the fitted background, as seen in figure 2.6. The next step is to spline fit the data to obtain a file, typically 2000 points, equally spaced in inverse magnetic field. The inverse field plot is shown in figure 2.7. The region of oscillations associated with each subband is labeled. This complex spectrum results from several surfaces, each with its own set of subbands, such that the regions are a mixture of oscillations of several frequencies. The final step in the analysis is to do the Fourier transform, as plotted in figure 2.8. From the multitude of peaks, it is apparent that several surfaces of slightly different carrier concentration are present. For a sample this complex, there is some uncertainty in assigning peaks to a particular surface and subband. However, peaks in figure 2.8 were assumed to be associated with subbands 0, 1, 2, and 3 from three surfaces: unprimed, primed, and double-primed.

(2) Results on GOES Detectors

(a) Supplier 1

A typical commercial GOES imager detector consists of four individual detector elements, each with a length of 50 to 100 μm, a width of about 50 μm, and a thickness of 6 to 8 μm. Elements of two detectors from Supplier 1, passivated by the anodic oxidation process (type I), were measured at several temperatures. The Fourier transforms of five elements at 6 K are shown in figure 2.9. In the element code, the supplier number is first, then the passivation type, next the detector number, and finally the letter of the particular element. The results of the three elements from detector 1 (1I1B, 1I1C, 1I1D) are very similar and can be interpreted as two surfaces, probably front and back, with slightly different carrier densities. The subband 0 (first surface) and 0' (second surface) peaks are close together but completely resolved. The peaks for subbands 1 and 1' overlap because the spacing decreases by about a factor of three in going to higher subbands. The 1 peak is seen as a shoulder on the right side of the 1' peak. The two elements of detector 2 differ from each other and from the elements of detector 1. The assignment of peaks to subbands is given in table 2.1, but there is some uncertainty for the elements of detector 2. Carrier densities were calculated by using the parabolic approximation. Effective masses and Dingle temperatures were determined for the dominant subbands in elements 1I1D and 1I2A. (The latter values, given in table 2.1, are considered to have an uncertainty of about 20% from estimates of the residual errors obtained from the goodness of the
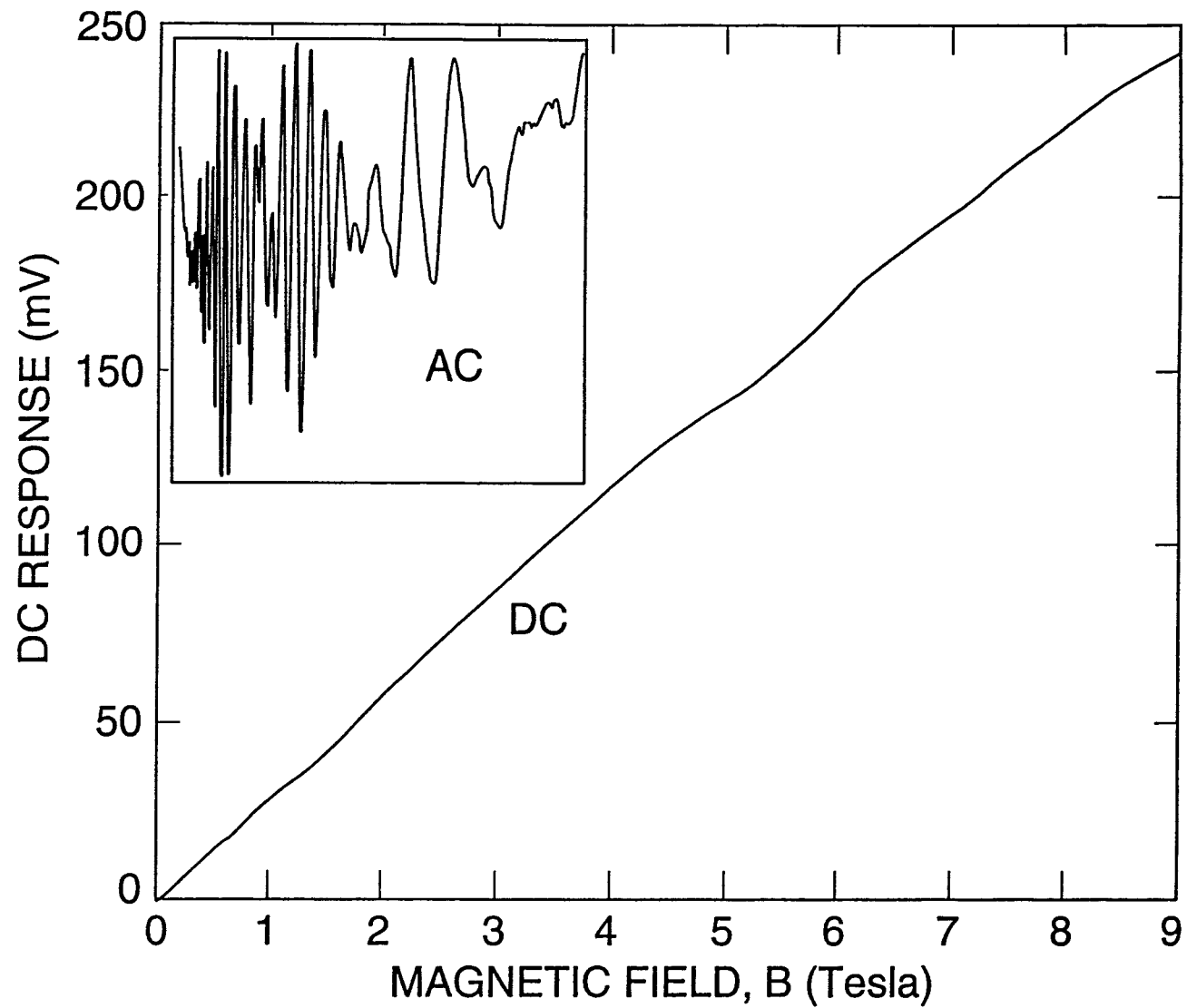
Figure 2.4 The ac and dc signals of the magnetoresistance of a typical detector element, 3I1B. Small wiggles can be seen in the dc trace, but only the ac technique gives results that reveal the rich spectrum of oscillations. The ac and dc traces have the same magnetic field scales; the y-axis of the ac response shows the relative response.
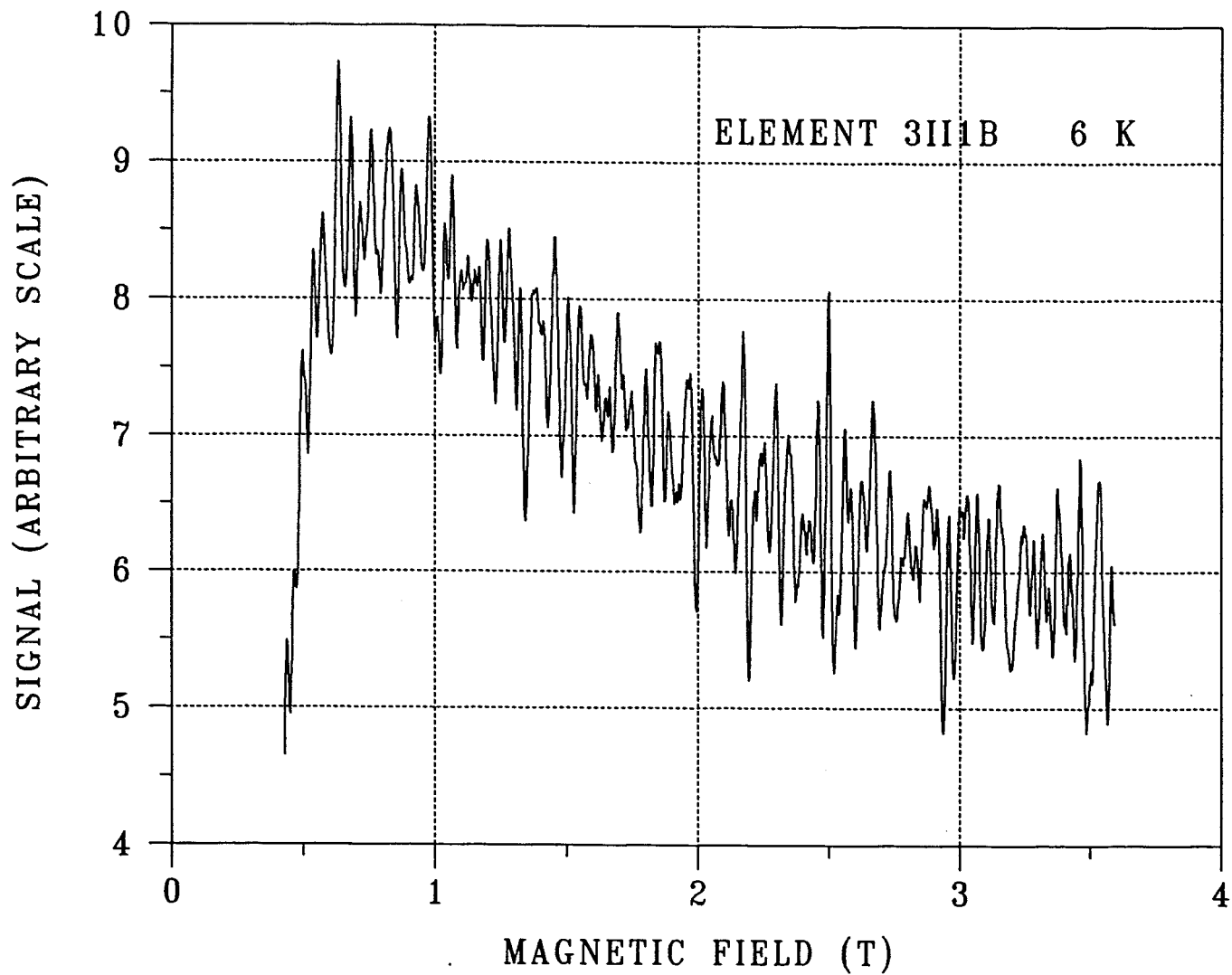
Figure 2.5 AC signal for detector element 3II1B showing the oscillations imposed on a background which initially rises abruptly and then falls slowly. Since this background gives a low-frequency contribution to the Fourier transform, it is desirable to eliminate it before taking the transform.
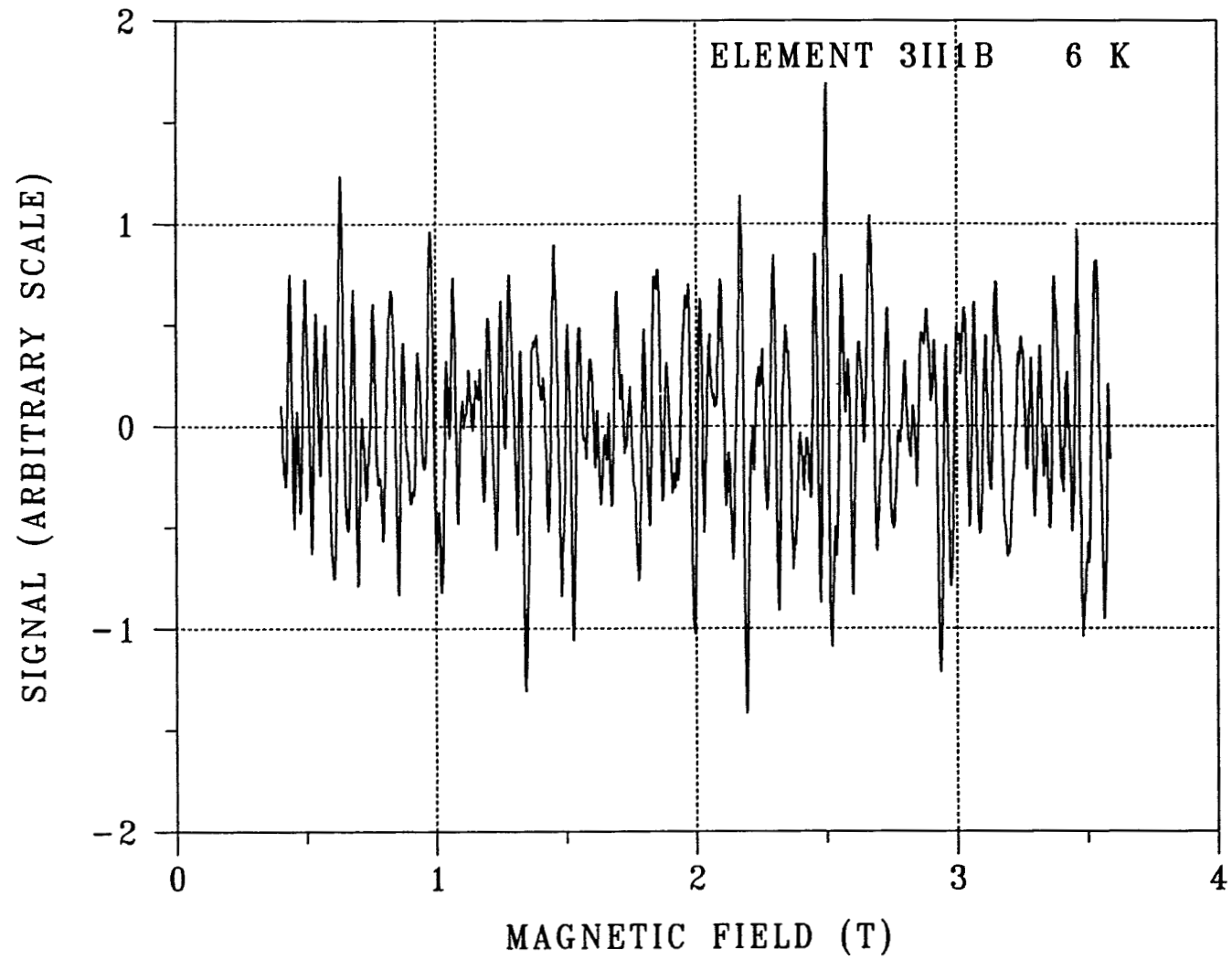
Figure 2.6 The ac signal which has been centered by doing a spline fit to the average value of regions of the original signal and then replotting the signal relative to the fit.
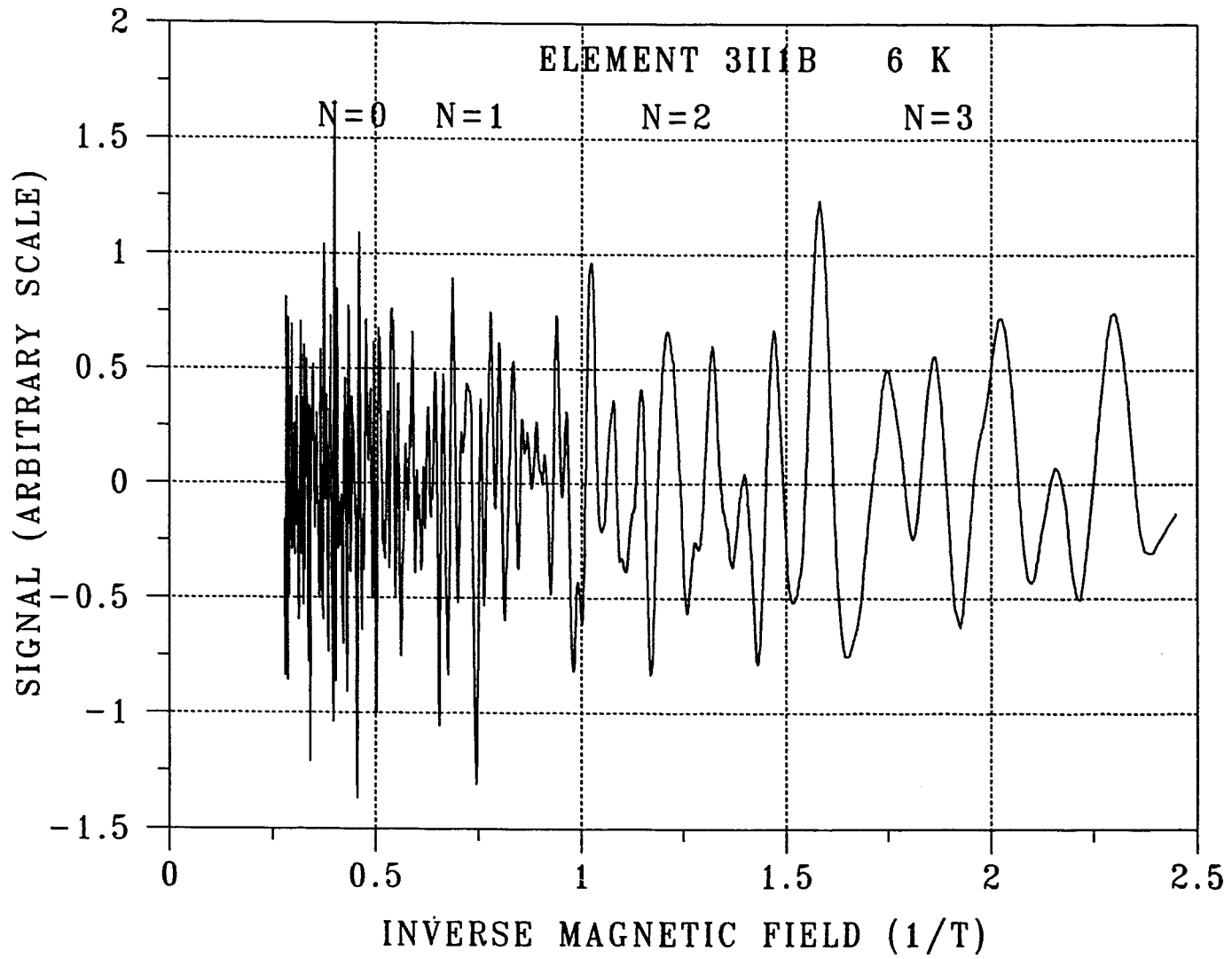
Figure 2.7 The ac signal as a function of inverse magnetic field. This is a necessary step prior to taking the Fourier transform. The oscillations corresponding to the various subbands are labeled.
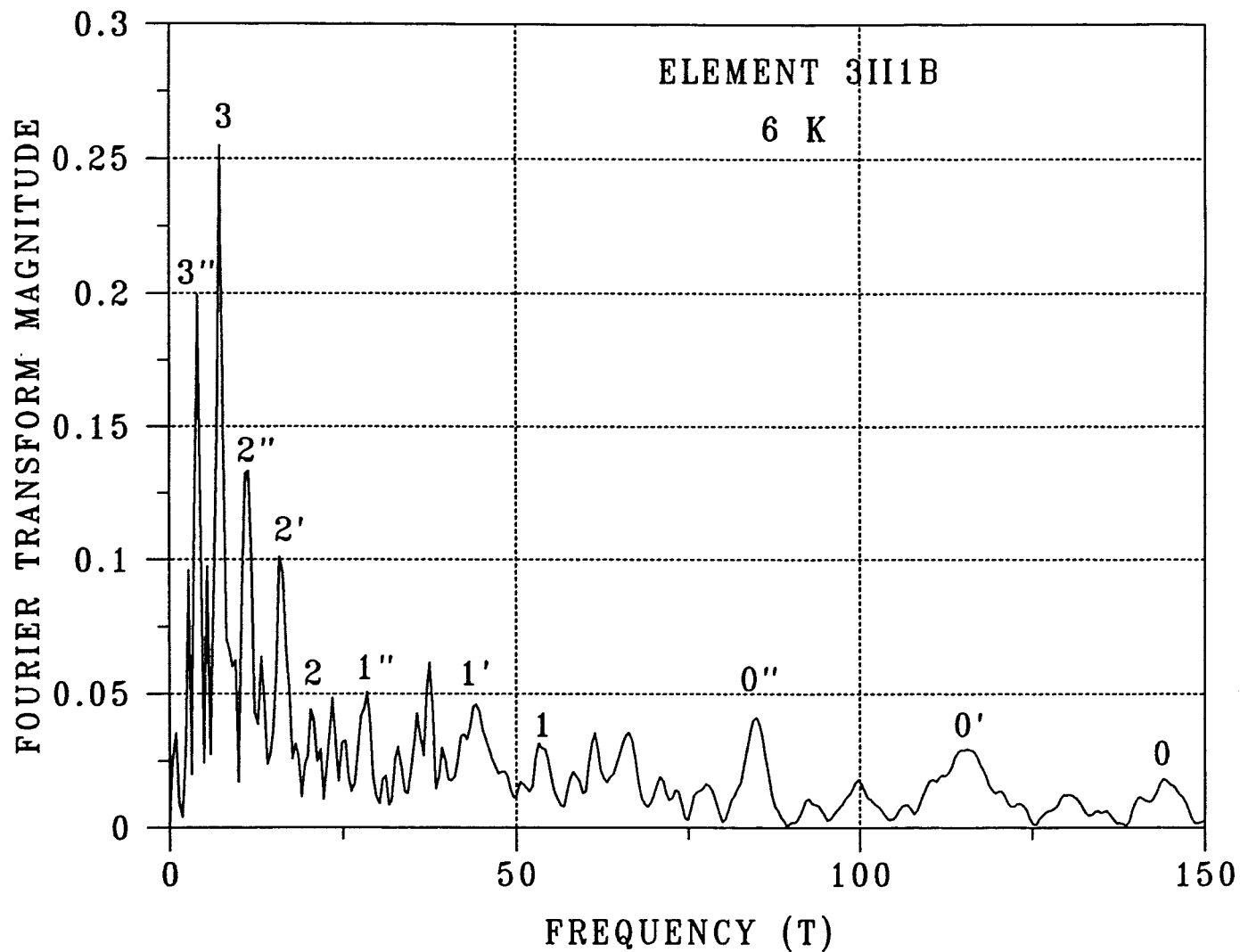
Figure 2.8 Fourier transform of the signal in the previous figure. From the many peaks in the transform, it is apparent that several surfaces are contributing to the SdH signal. Peaks associated with three surfaces - unprimed, primed, and double-primed - are labeled on the figure.
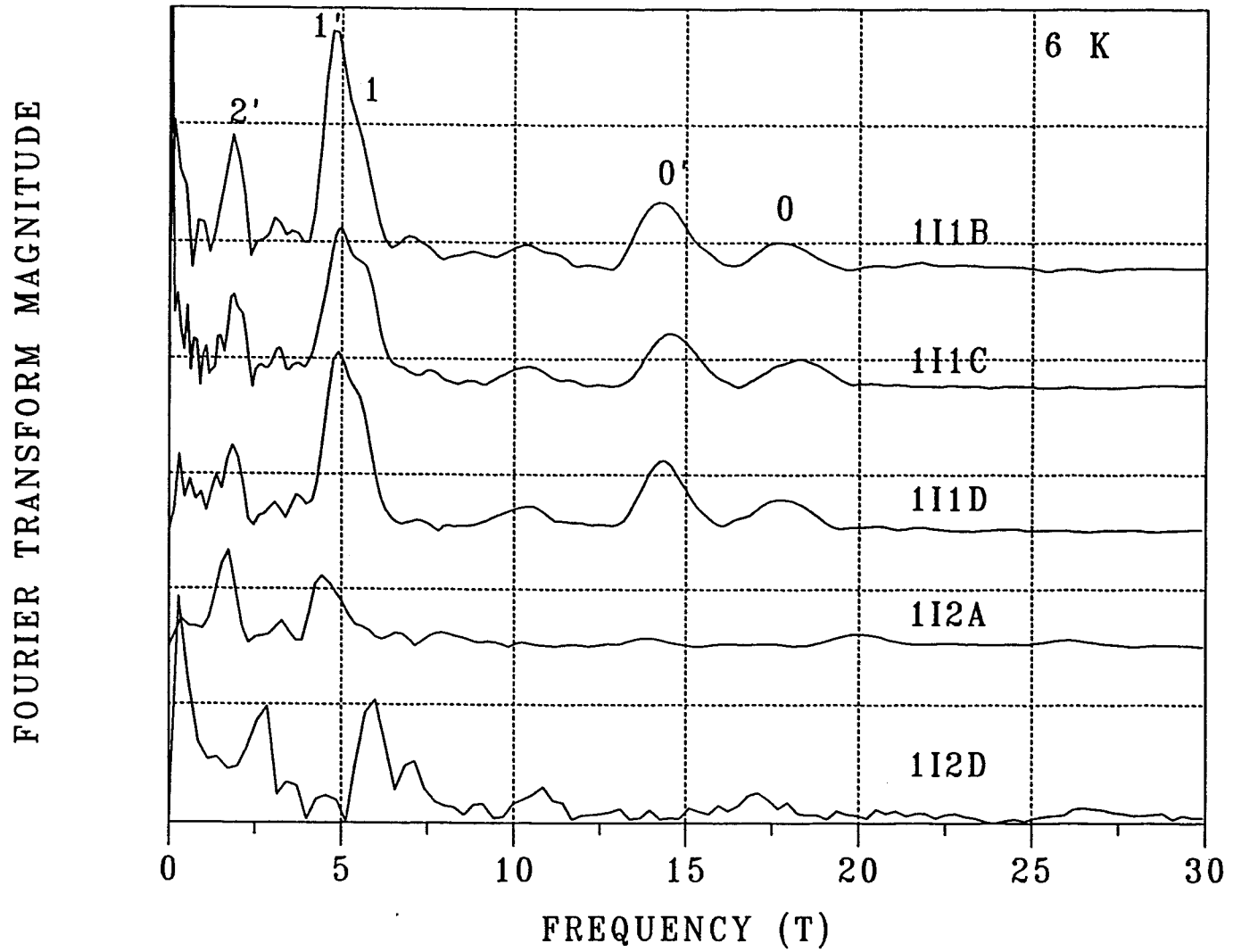
Figure 2.9 Fourier transforms from elements of two different Supplier 1 detectors, 1 and 2. All of the elements of detector 1 are very similar and easy to interpret, but this is not the case for the elements of detector 2.

Table 2.1. Results of Shubnikov-de Haas Analysis for Supplier 1 Detectors

Detector Element	Electric Subband	Frequency (T)	$\underline{m^*}$ E_F m_o (meV)	Carrier Density ($\times 10^{11}$cm^{-2})	m^*/m_o	E_F(meV)	T_D(K)
1I1B	0	17.70	2.050	8.55			
	1	5.33	0.617	2.57			
	2	-		1.30$^+$			
	3	-		0.41$^+$			
	SUM			12.83			
	0'	14.24	1.649	6.88			
	1'	4.86	0.563	2.35			
	2'	1.83	0.212	0.88			
	3'	-		0.33$^+$			
	SUM			10.44			
1I1C	0	18.22	2.110	8.80			
	1	5.66	0.655	2.73			
	2	-		1.34$^+$			
	3	-		0.43$^+$			
	SUM			13.30			
	0'	14.50	1.679	7.00			
	1'	4.94	0.572	2.39			
	2'	1.85	0.214	0.90			
	3'	-		0.34$^+$			
	SUM			10.63			
1I1D	0	17.86	2.068	8.62	0.017	120	48
	1	5.50	0.637	2.66			
	2	-		1.43$^+$			
	3	-		0.45$^+$			
	SUM			14.15			
	0'	14.32	1.658	6.92	0.016	104	40
	1'	4.86	0.563	2.35	0.011	53	31
	2'	1.83	0.212	0.89	0.0063	34	20
	3'	-		0.34$^+$			
	SUM			10.50			

35

Table 2.1 (Continued)

Detector Element	Electric Subband	Frequency (T)	$\underline{m}^* E_F / m_0$ (meV)	Carrier Density ($\times 10^{11}$cm^{-2})	m^*/m_0	E_F(meV)	T_D(K)
1I2A	0	19.86	2.300	9.59	0.021	109	37
	1	7.90	0.915	3.81			
	2	3.18	0.368	1.53			
	3	-		0.49$^+$			
	SUM			15.42			
	0'	13.66	1.582	6.60	0.022	73	34
	1'	4.6	0.533	2.22	0.014	38	17
	2'	1.72	0.199	0.83	0.0093	21	13
	3'	-		0.32$^+$			
	SUM			9.97			
1I2D	0	26.40	3.057	12.75			
	1	10.69	1.238	5.16			
	2	-		2.09$^+$			
	3	-		0.66$^+$			
	SUM			20.66			
	0'	16.94	1.962	8.18		.	
	1'	6.0	0.695	2.90			
	2'	2.77	0.321	1.34			
	3'	-		0.41$^+$			
	SUM			12.83			

$^+$ Calculated estimate based on densities of other subbands

36

fit.) The subband densities are plotted as a function of total density N_t in figure 2.10. The results of the linear fits are: $N_0 = 0.638\ N_t$, $N_1 = 0.225\ N_t$, and $N_2 = 0.077\ N_t$. The subband 3 values were all calculated by using the relationship $N_3 = 0.032\ N_t$. Note that the theoretically calculated values given earlier were 0.673, 0.223, and 0.077, respectively.

(b) Supplier 2

Two detectors of four elements each from Supplier 2 were measured at several temperatures. The back and front surfaces were passivated by different processes (the combination designated type III), with the result that the SdH traces are complex and very difficult to analyze. Oscillations associated with the second process are closely spaced, even at high fields, and continue with the same amplitude to at least 9 T. Traces at 6 K of the four elements of the first detector are shown in figure 2.11. The temperature dependence of element 2III1B is plotted in figure 2.12. The figure shows that the amplitude of the oscillations decreases with increasing temperature as expected. Traces of the four elements of detector 2III2 are shown in figure 2.13. The Fourier transforms for detector 2III1 are plotted in figure 2.14. The identification of peaks associated with particular subbands is difficult. A possible assignment for element 2III1D is shown on the figure and is given in table 2.2a. The Fourier transforms for detector 2III2 are shown in figure 2.15 and are similar to those for detector 2III1. This type of detector is better characterized using the new dc magnetoresistance method presented in section 4.

To determine if the oscillations were indeed coming from the two-dimensional surfaces, a limited rotational study was undertaken, as shown in figure 2.16. The magnetic field is perpendicular to the surface layers at 0° and parallel to them at 90°. The decrease in the response with rotation indicates that the oscillations are associated with the surfaces rather than the bulk. The residual amplitude at 90° is considered to be the noise level.

In order to better understand the detectors of Supplier 2 with their two different passivations, a series of three experimental detectors was prepared by Supplier 2 for SdH studies. Detector 2IV5 had the back surface prepared with the first process passivation, and the front surface was unfinished (designated by type IV). Detector 2I6 had both surfaces passivated by the first process, whereas detector 2III7 had the back surface passivated with the first process and the front surface done with the second process. The SdH response of these three detectors is shown in figure 2.17. The addition of the second process is seen to strongly interfere with the oscillations from the first process at low magnetic fields. The Fourier transforms of these spectra are shown in figure 2.18. The first process peaks are identified and are similar to those seen in detectors from other suppliers with this type of passivation. The n=0 subband has three peaks, indicating that the surface has at least three regions with slightly different carrier densities. The addition of a second surface of the same type gives a response which is similar to that of one surface with only slight changes in peak frequency and relative height. The detector with two surfaces passivated, each of a different passivation, has quite a different behavior. The first process peaks are difficult to identify since they are greatly reduced and appear to have shifted slightly. The only definite front surface peak (second process) is the one labeled 1s. The 0s response is fairly weak and the 2s peak occurs in the region of structure from the other surface.

Effective masses were determined for four of the subbands of detector 2IV5. The values are in good agreement with those found for the Supplier 1 detectors which had similar passivation. The information on carrier density, effective mass, and Dingle temperature is listed in table 2.2b.

37
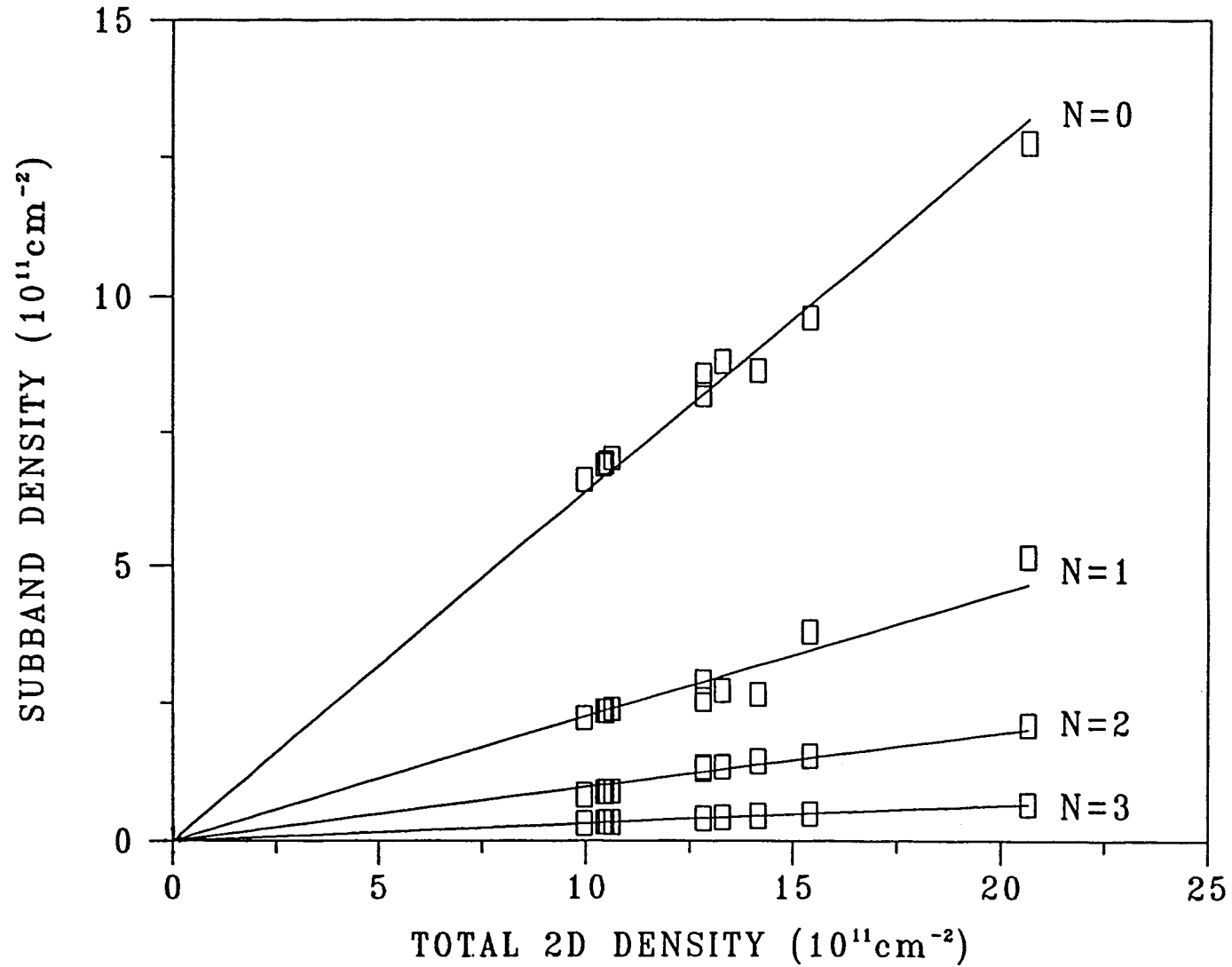
Figure 2.10 Subband carrier density versus total density for the Supplier 1 detector elements in figure 2.9. Each element has two sets of subbands - unprimed and primed - and the values, calculated using the parabolic approximation, are given in table 2.1. The uncertainties in the data are represented by the size of the symbols shown.
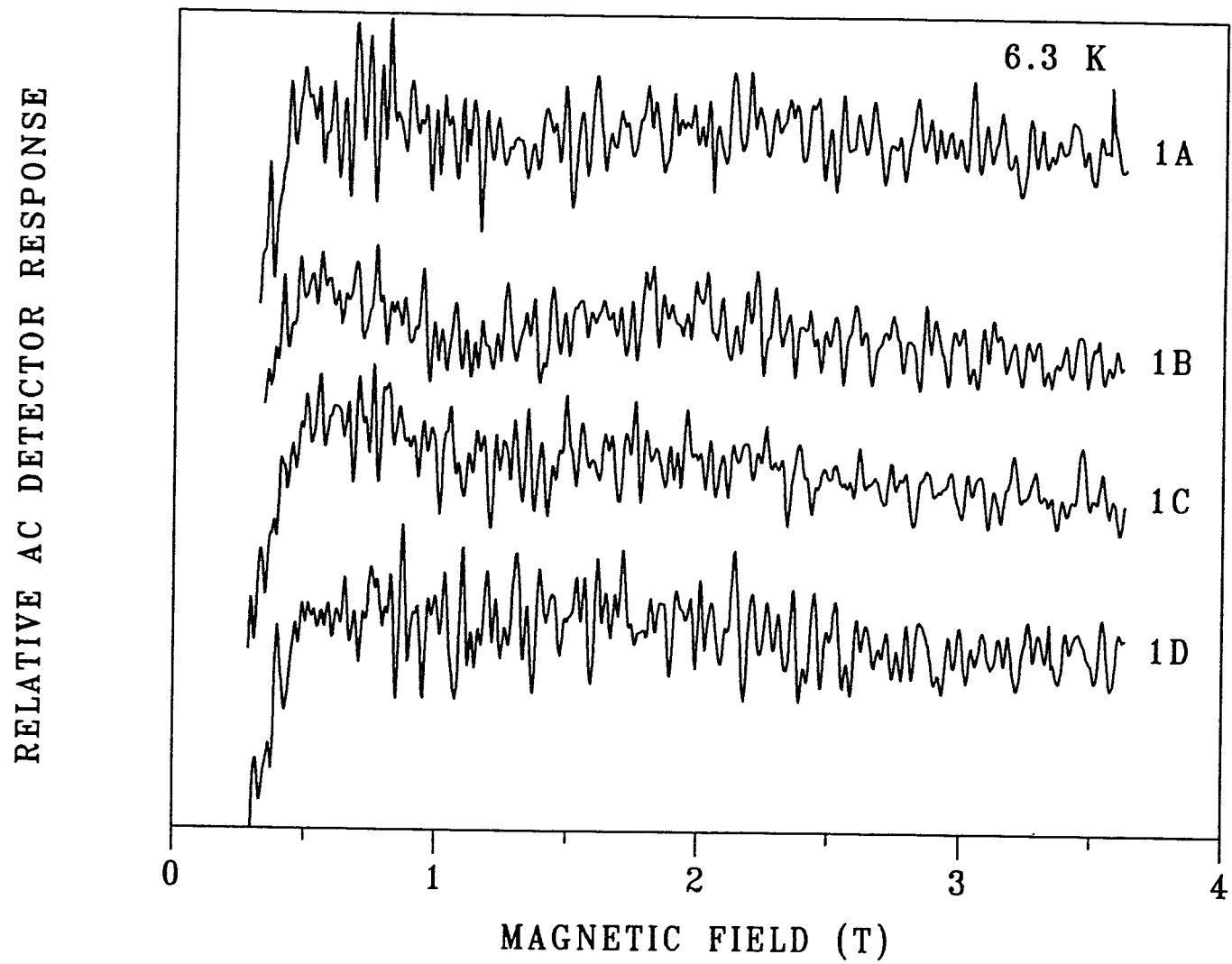
Figure 2.11 SdH traces of four elements of detector 2III1 from Supplier 2. The closely spaced oscillations are characteristic of an accumulation layer produced by a passivation process other than
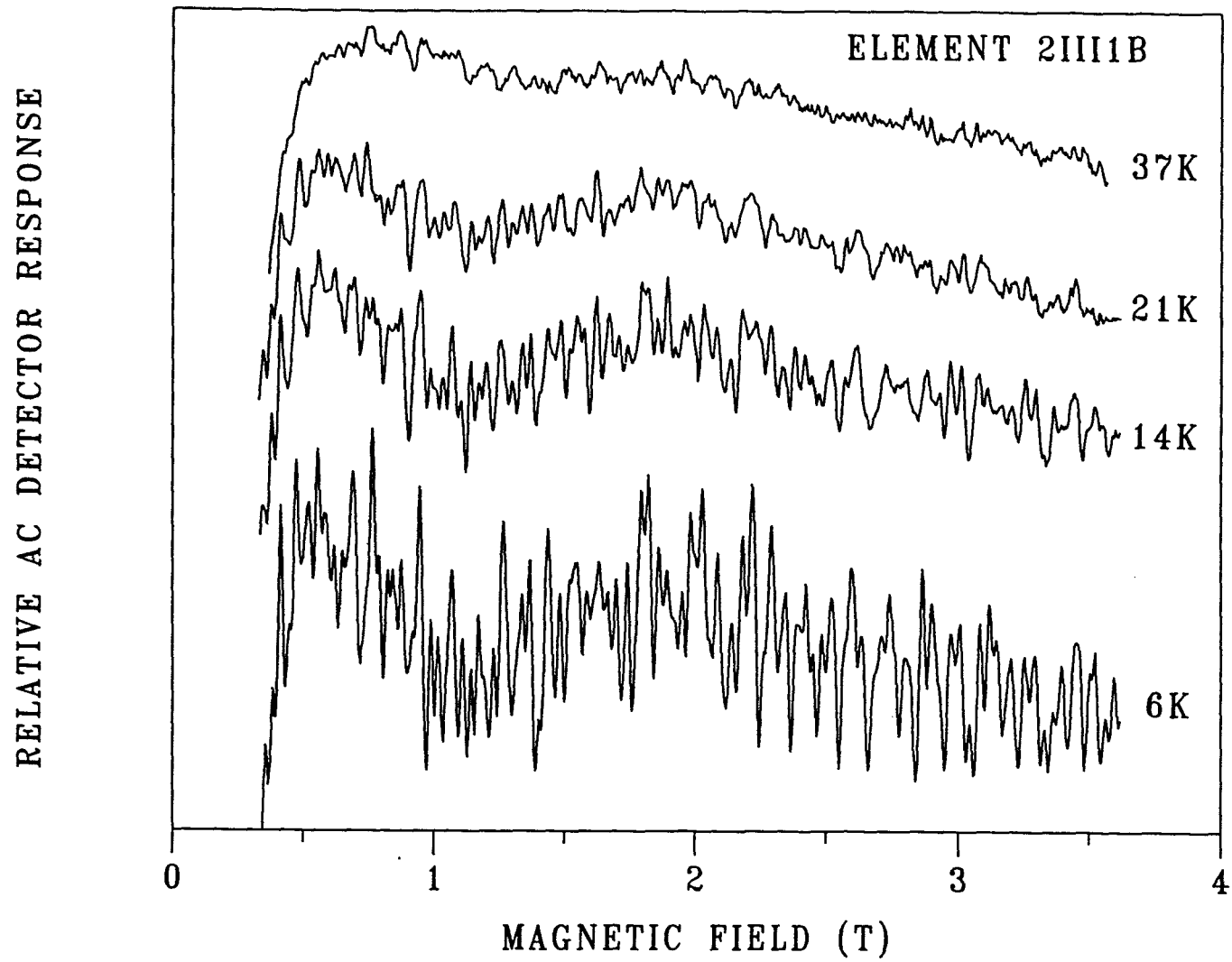
Figure 2.12 Temperature dependence of the SdH oscillations of element 2III1B.
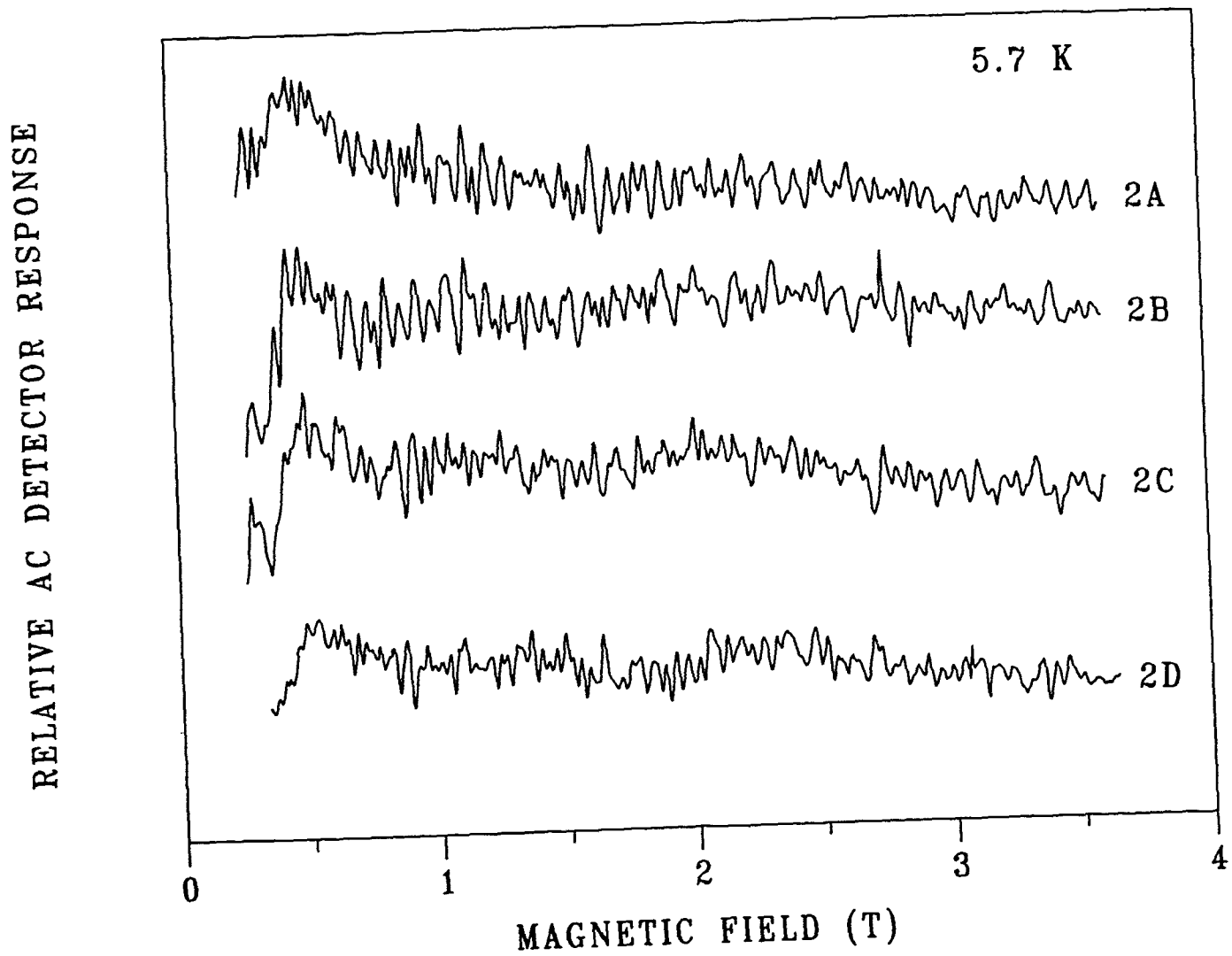
Figure 2.13 Traces of four elements of detector 2III2. The closely spaced oscillations continue to magnetic fields as high as 9 T.
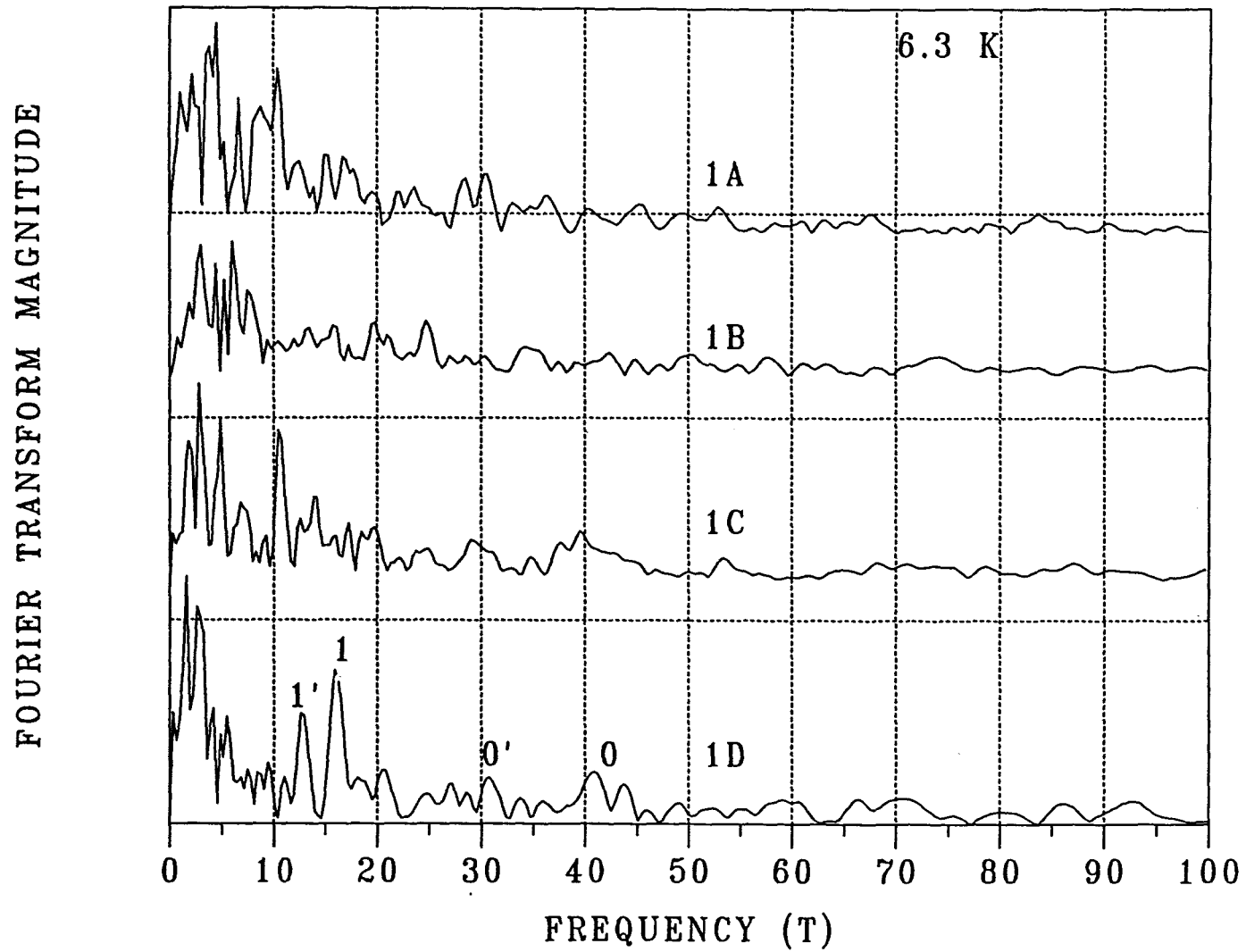
Figure 2.14 Fourier transforms for the elements of detector 2III1. The lack of well-defined, large peaks makes these transforms extremely difficult to interpret.

Table 2.2a. Results of Shubnikov-de Haas Analysis for Supplier 2 Detector

Detector Element	Electric Subband	Frequency (T)	$\frac{m^*E_F}{m_0}$ (meV)	Carrier Density ($\times 10^{11} cm^{-2}$)
2III1D	0	42.0	4.86	20.29
	1	16.05	1.86	7.75
	2	-		3.27[+]
	3	-		1.03[+]
	SUM			32.34
	0'	30.8	3.57	14.88
	1'	12.81	1.48	6.19
	2'	-		2.45[+]
	3'	-		0.78[+]
	SUM			24.30

[+] Calculated estimate based on densities of other subbands
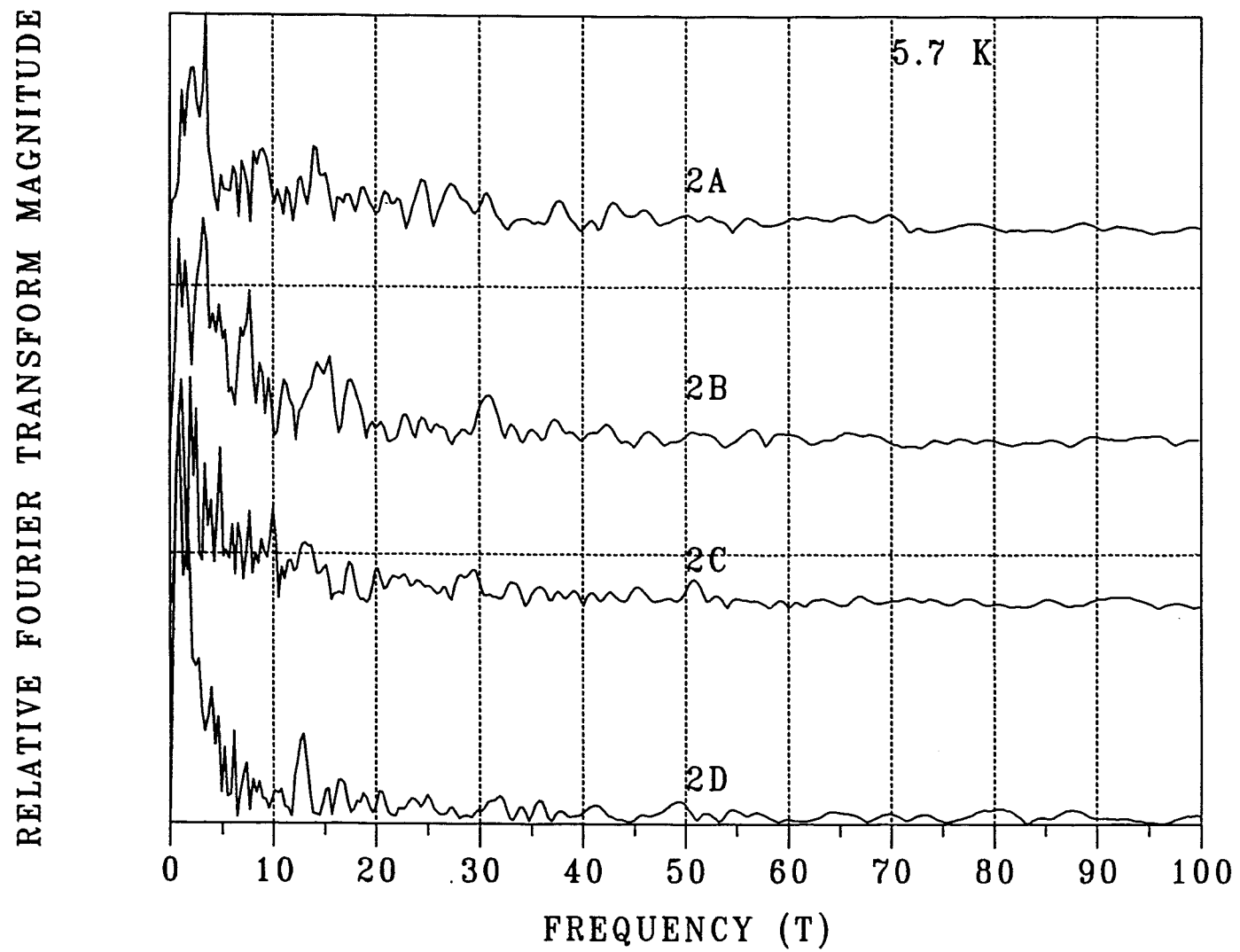
Figure 2.15 Fourier transforms for the elements of detector 2III2.
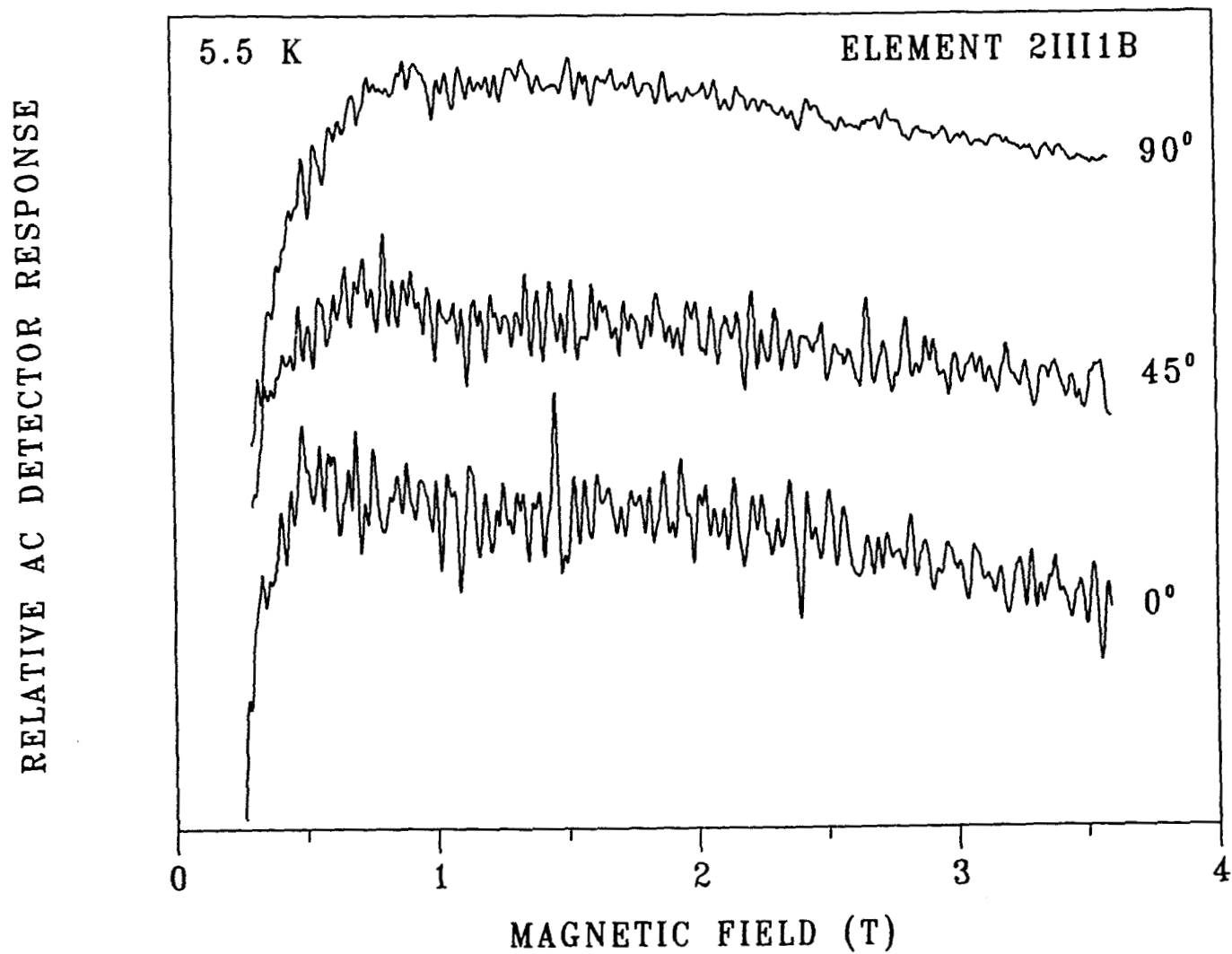
Figure 2.16 Results of rotating element 2III1B in the magnetic field. The greatly diminished response at 90°, when the field is parallel to the surfaces, shows that the SdH oscillations are coming from the two-dimensional surface layers rather than the bulk.
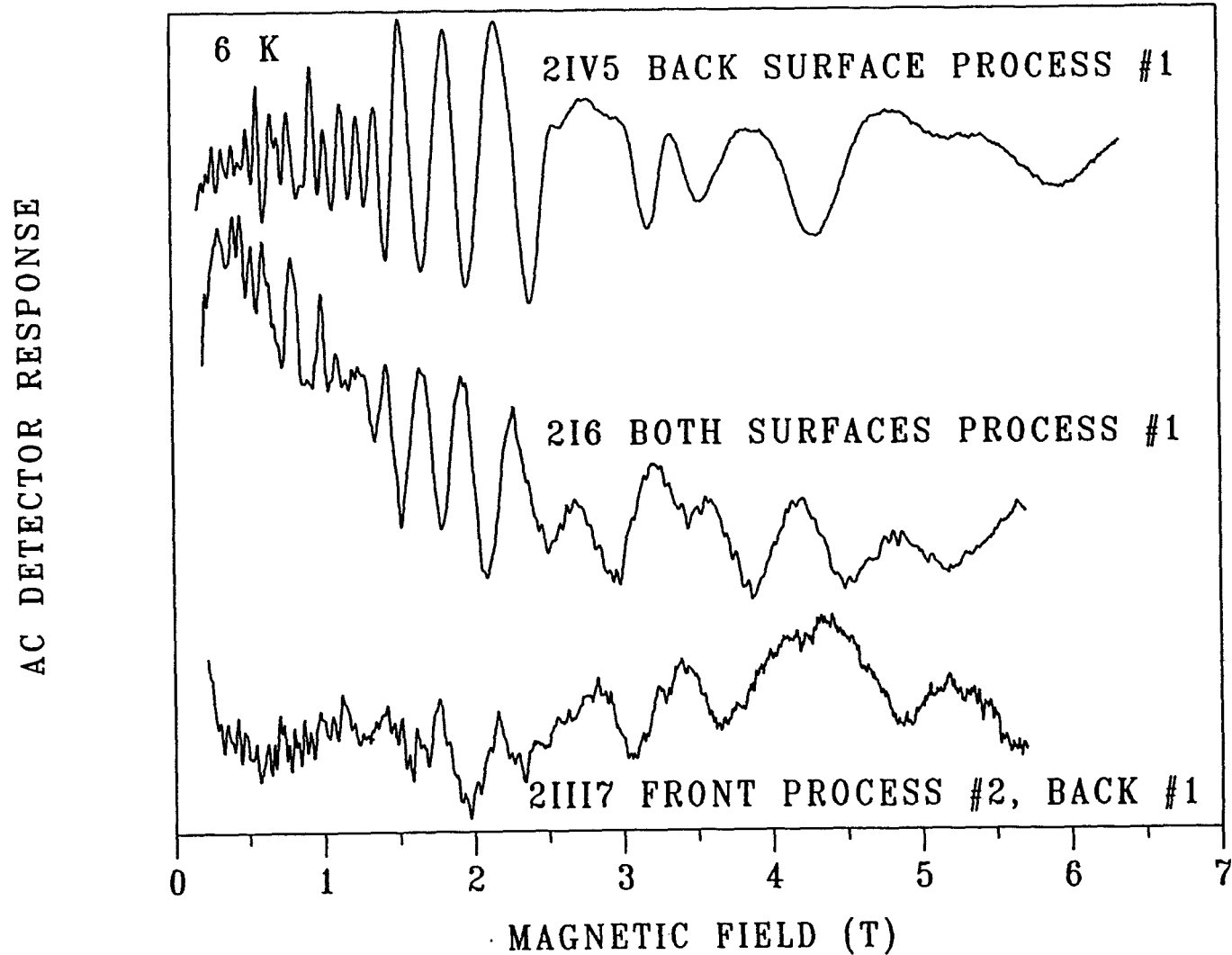
Figure 2.17 Shubnikov-de Haas oscillations from the three Supplier 2 detectors fabricated for diagnostic purposes. The passivation on detector 2III7 is equivalent to that on a commercial detector.
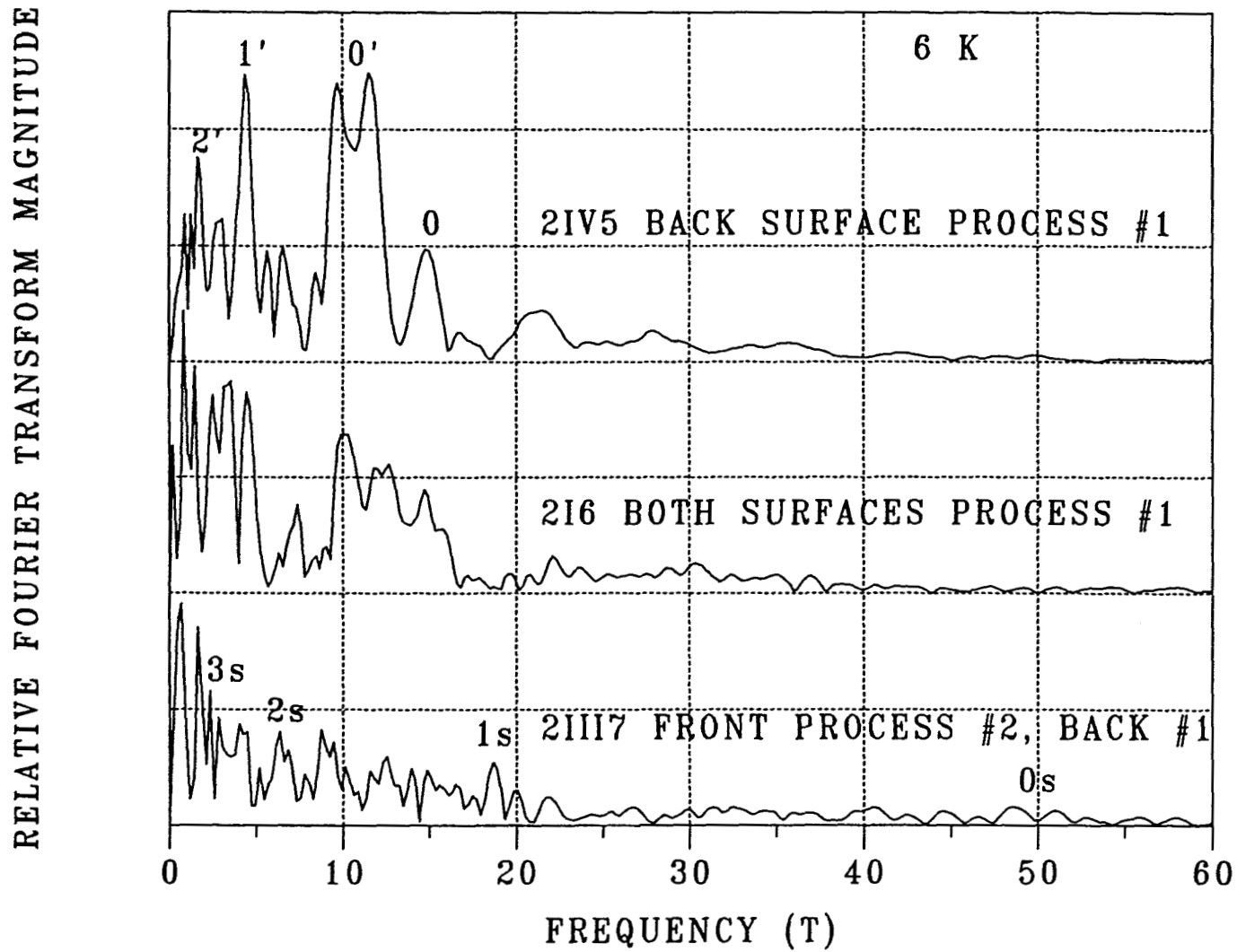
Figure 2.18 Fourier transforms of the SdH response in figure 2.17 for the experimental Supplier 2 detectors. The peaks associated with the first process passivation are difficult to identify in the detector with mixed surfaces.

Table 2.2b. Results of Shubnikov-de Haas Analysis for Supplier 2 Experimental Detectors

Detector Element	Electric Subband	Frequency (T)	$\dfrac{m^*E_F}{m_o}$ (meV)	Carrier Density ($\times 10^{11}$cm^{-2})	m^*/m_o	E_F(meV)	T_D (K)
2IV5	0	14.93	1.729	7.21	0.021	83	34
	1	5.70	0.660	2.75			
	2	-		1.16$^+$			
	3	-		0.37$^+$			
	SUM			11.49			
	0'	11.60	1.343	5.60	0.018	75	35
	1'	4.47	0.518	2.16	0.013	40	16
	2'	1.80	0.208	0.87	0.0076	27	13
	3'	0.66		0.32			
	SUM			8.95			
2III7	0s	49.8	5.767	24.05			
	1s	18.70	2.165	9.03			
	2s	6.37	0.738	3.08		.	
	3s	2.36	0.273	1.14			
	SUM			37.30			

$^+$ Calculated estimate based on densities of other subbands

48

(c) Supplier 3

Figure 2.19 shows the responses of the two types of Supplier 3 detectors. One element has type I (anodic oxidation) passivation, whereas the other element has a different, proprietary, passivation designated here as type II. It is readily apparent that these give very different SdH signatures. The magnitude of the oscillations is much greater for the type I detectors when recorded at the same current and instrument settings. The type I element shows the normal SdH behavior in that a series of oscillations is periodic in inverse magnetic field. For the type II element, the spacing of the oscillations does not show any obvious pattern due to the complicated, high frequency signal, although the Fourier transform does show a set of peaks.

The temperature dependence of a type I device, 3I2A, is shown in figure 2.20. Note that the oscillations at low magnetic field damp out first with increasing temperature. Figure 2.21 shows the Fourier transforms of the temperature traces. The transform peaks broaden somewhat with temperature as evidenced by the decreased resolution of the subband 0 and 0' peaks at 18 K. The temperature dependence of the peak amplitude can be used to obtain the effective mass as discussed elsewhere.

Figure 2.22 shows the Fourier transforms from five Supplier 3 type I detector elements. Elements 3I2A through 3I2D were from one detector and 3I3C was from another detector. Elements 3I2A and 3I2B are seen to be essentially identical, 3I2C and 3I2D have a stronger $n=0$ and $n=1$ surface region with apparent reduction in the other surfaces (denoted by the primes and double primes), and 3I3C shows a new surface region at the expense of the dominant surface (double-primed subbands) of 3I2A through 3I2D. The most probable explanation of these Fourier spectra is related to the geometry of the detector elements. All of the elements have the same active area but the device length, and consequently the resistance, varies from element to element. Elements 3I2A and 3I2B have the same length, 0.0071 cm, and the same Fourier spectra. Element 3I2C is longer, 0.0107 cm, and its spectrum shows a significant amount of the unprimed surface (subbands 0, 1, and 2). Element 3I2D is even longer, 0.0132 cm, and has more of the unprimed surface in its spectrum. It appears that the unprimed surface is the region of the device outside the active area. A coating, or the lack of it, on the non-active regions produces a surface layer with a different carrier density, which in turn gives rise to a different Fourier spectrum. The decrease in the peaks of the long elements, compared to the peaks seen in the short elements, may be due to the effect of series and parallel resistances of the various layers. Element 3I3C from another detector is equivalent in length to 3I2C. It basically has the same number of surfaces, but with the strongest one (see for example, the 0'' peak) in elements 3I2A through 3I2D essentially absent and one new surface region present. All of the major peaks in the transforms are listed in table 2.3.

Figure 2.23 shows SdH traces of a Supplier 3 type II detector element at a series of temperatures. With the many high-frequency oscillations, it is difficult to track a specific oscillation as a function of temperature. The Fourier transforms for the elements of a type II detector are shown in figure 2.24. The assignment of peaks to specific subbands is shown for element 3I1B, and given in table 2.4 for all elements, but the identification is somewhat arbitrary. The unlabeled peaks are associated with other regions of the surfaces.

Experimental subband carrier densities are plotted versus total density in figure 2.25 for the Supplier 3 type I detector elements listed in table 2.3. The linear fits gave: $N_0 = 0.656\ N_t$, $N_1 = 0.225\ N_t$, and $N_2 = 0.087\ N_t$. These compare favorably to the theoretically calculated values given earlier,
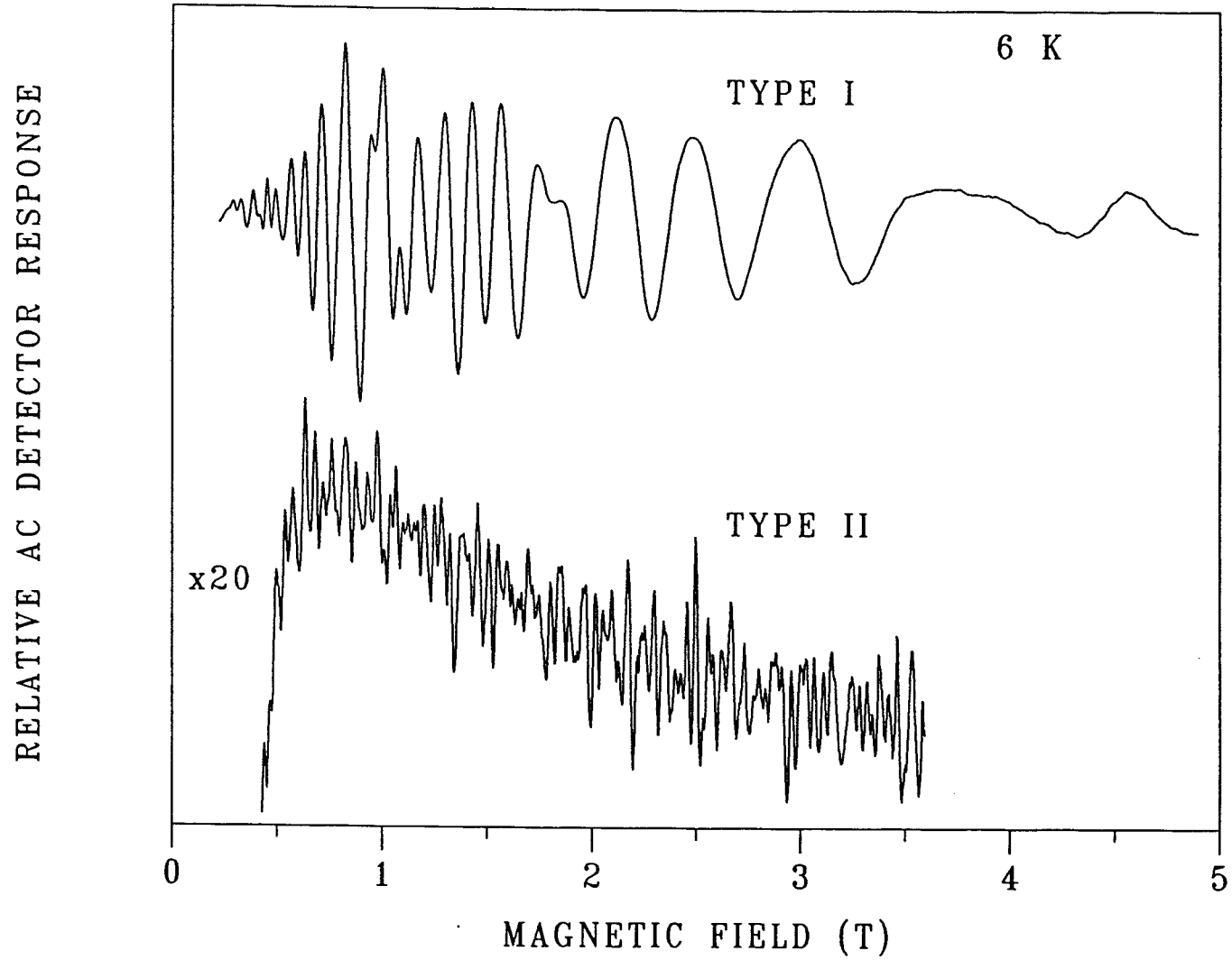
Figure 2.19 Response curves for the two types of Supplier 3 detectors. Type I passivation is anodic oxidation whereas type II passivation is a different process. The SdH oscillation signatures are seen to be radically different. The type II response is much smaller and has been enlarged by a factor of 20.
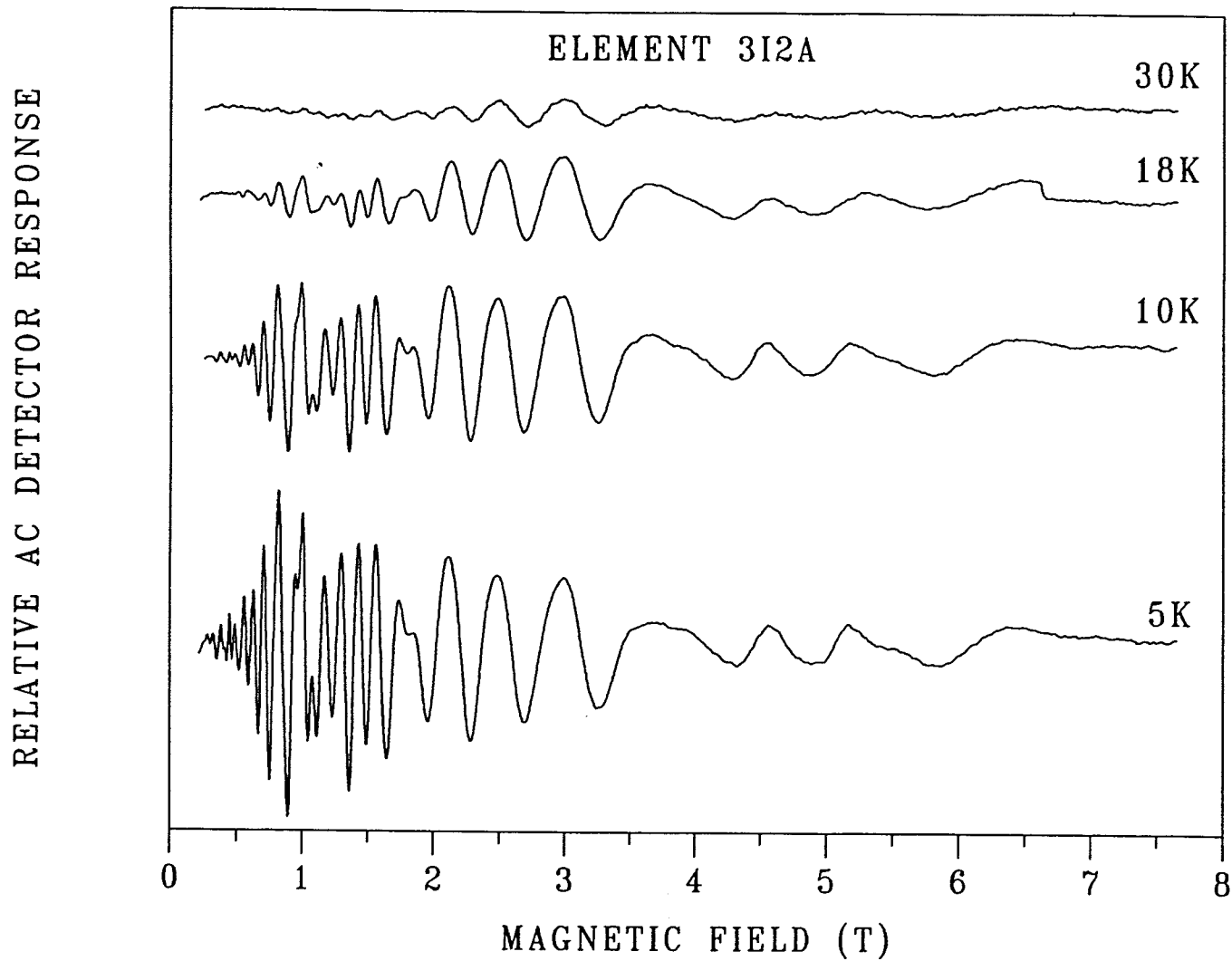
Figure 2.20 Temperature dependence of the SdH response of a Supplier 3 type I element, 3I2A. Note that the oscillations at low magnetic field decay first with increasing temperature.
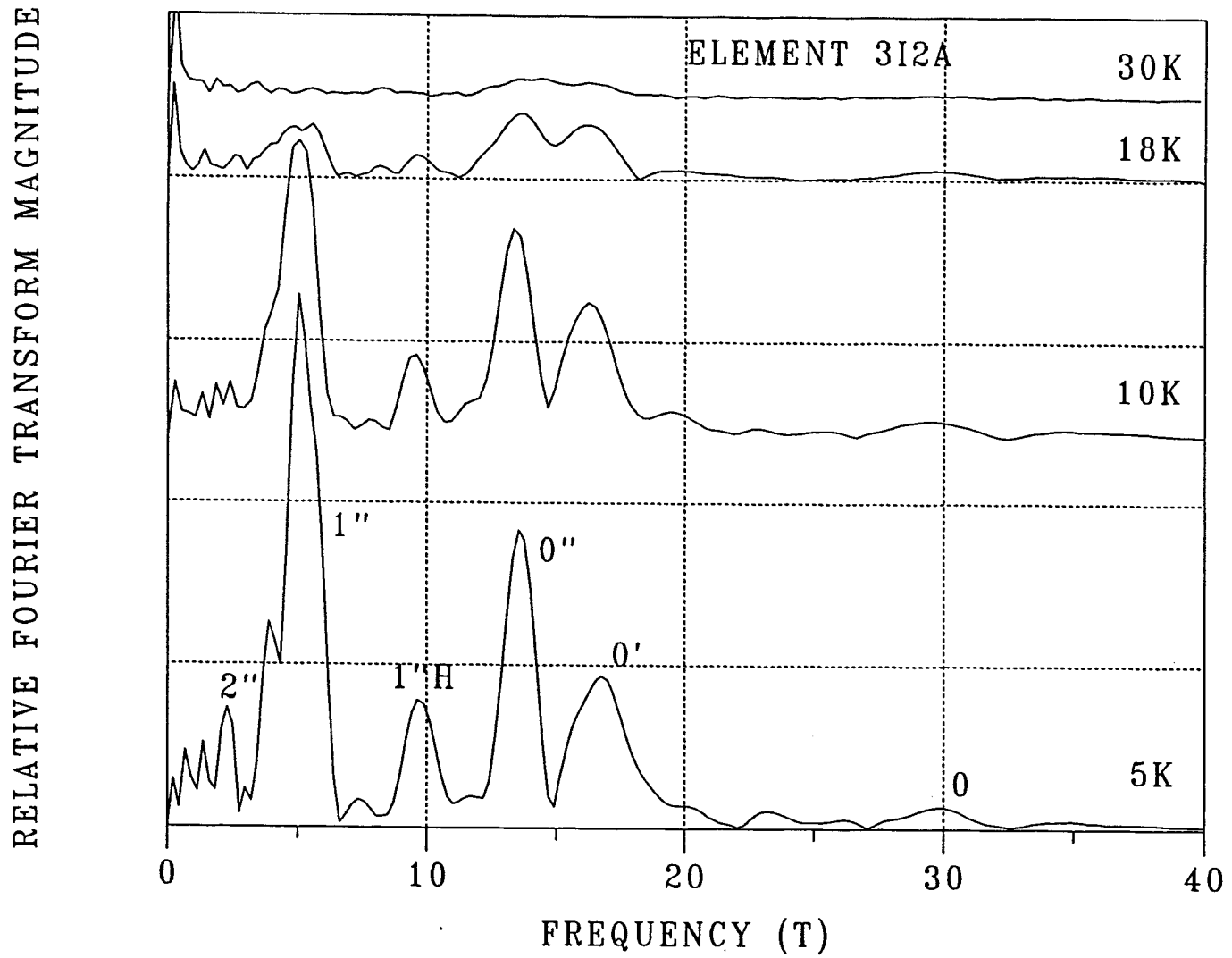
Figure 2.21 Fourier transforms of the temperature data in figure 2.20. The peaks associated with the subbands of two surfaces, primed and unprimed, are labeled.
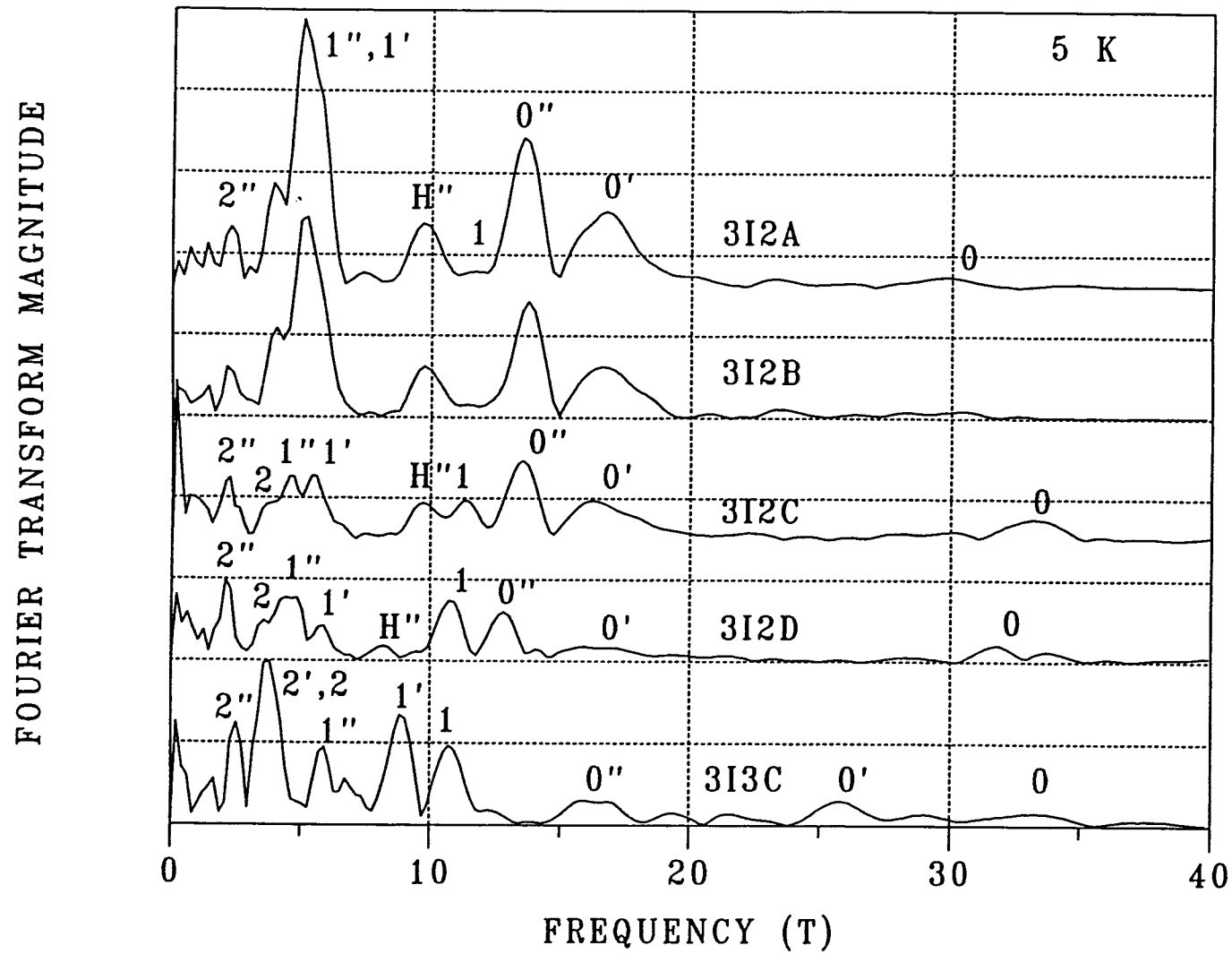
Figure 2.22 Fourier transforms from five type I detector elements from Supplier 3. Devices 3I2A to 3I2D were all the elements on one detector; 3I3C was one of the elements on another detector. Surfaces with the same electron concentration are present in most of the devices, but there are noticeable differences, as discussed in the text.

Table 2.3. Results of Shubnikov-de Haas Analysis for Supplier 3 Type I Detectors

Detector Element	Electric Subband	Frequency (T)	$\frac{m^*}{m_o} E_F$ (meV)	Carrier Density ($\times 10^{11} cm^{-2}$)	m^*/m_o	E_F(meV)	T_D(K)
3I1B	0	11.70	1.355	5.65			
	1	4.17	0.483	2.01			
	2	1.89	0.219	0.91			
	3	-		0.28^+			
	SUM			8.85			
	0'	10.0	1.158	4.83			
	1'	3.33	0.386	1.61			
	2'	1.61	0.186	0.78			
	3'	-		0.24^+			
	SUM			7.46			
3I1C	0	11.00	1.274	5.31			
	1	4.08	0.472	1.97			
	2	1.54	0.178	0.74			
	3	-		0.27^+			
	SUM			8.29			
3I1D	0	10.70	1.239	5.17			
	1	3.94	0.456	1.90			
	2	1.48	0.171	0.72			
	3	-		0.26^+			
	SUM			8.05			
	0'	8.55	0.990	4.13			
	1'	3.03	0.351	1.46			
	2'	1.48	0.171	0.72			
	3'	-		0.21^+			
	SUM			6.52			
3I2A	0'	16.75	1.940	8.09	0.022	88	29
	1'	5.83	0.675	2.82			
	2'	-		1.27^+			
	3'	-		0.40^+			
	SUM			12.58			

Table 2.3 (Continued)

Detector Element	Electric Subband	Frequency (T)	$\frac{m^*}{m_o} E_F$ (meV)	Carrier Density ($\times 10^{11} cm^{-2}$)	m^*/m_o	E_F(meV)	T_D(K)
	0''	13.60	1.575	6.57	0.022	72	28
	1''	5.05	0.585	2.44	0.014	42	23
	2''	2.29	0.265	1.11			
	3''	-		0.33^+			
	SUM			10.45			
3I2B	0'	16.60	1.922	8.02			
	1'	5.5	0.637	2.66			
	2'	2.20	0.255	1.06			
	3'	-		0.39^+			
	SUM			12.13			
	0''	13.74	1.591	6.64			
	1''	5.5	0.637	2.66			
	2''	-		1.08^+			
	3''	-		0.34^+			
	SUM			10.73			
3I2C	0	33.24	3.849	16.05			
	1	11.35	1.314	5.48			
	2	3.7	0.428	1.79			
	3	-		0.77^+			
	SUM			24.09			
	0'	16.23	1.879	7.84			
	1'	5.47	0.633	2.64			
	2'	2.3	0.26	1.11			
	3'	-		0.38^+			
	SUM			11.97			
	0''	13.54	1.568	6.54			
	1''	4.58	0.530	2.21			
	2''	2.1	0.24	1.01			
	3''	-		0.32^+			
	SUM			10.08			

Table 2.3 (Continued)

Detector Element	Electric Subband	Frequency (T)	$\frac{m^*}{m_0}$ E_F (meV)	Carrier Density ($\times 10^{11}$ cm^{-2})	m^*/m_0	E_F(meV)	T_D(K)
3I2D	0	32.2	3.729	15.55			
	1	10.75	1.245	5.19			
	2	3.59	0.416	1.73			
	3	-		0.74$^+$			
	SUM			23.21			
	0'	16.5	1.911	7.97			
	1'	5.80	0.672	2.80			
	2'	-		1.25$^+$			
	3'	-		0.40$^+$			
	SUM			12.42			
	0''	12.81	1.483	6.19			
	1''	4.85	0.562	2.34			
	2''	2.15	0.249	1.04			
	3''	-		0.32$^+$			
	SUM			9.89			
3I3C	0	33.27	3.853	16.07			
	1	10.75	1.245	5.19			
	2	3.85	0.446	1.86		.	
	3	-		0.76$^+$			
	SUM			23.88			
	0'	25.75	2.982	12.44			
	1'	8.87	1.027	4.28			
	2'	3.55	0.411	1.71			
	3'	-		0.61$^+$			
	SUM			19.04			
	0''	16.4	1.899	7.92			
	1''	5.88	0.681	2.84			
	2''	2.52	0.292	1.22			
	3''	-		0.40$^+$			
	SUM			12.38			

$^+$ Calculated estimate based on densities of other subbands
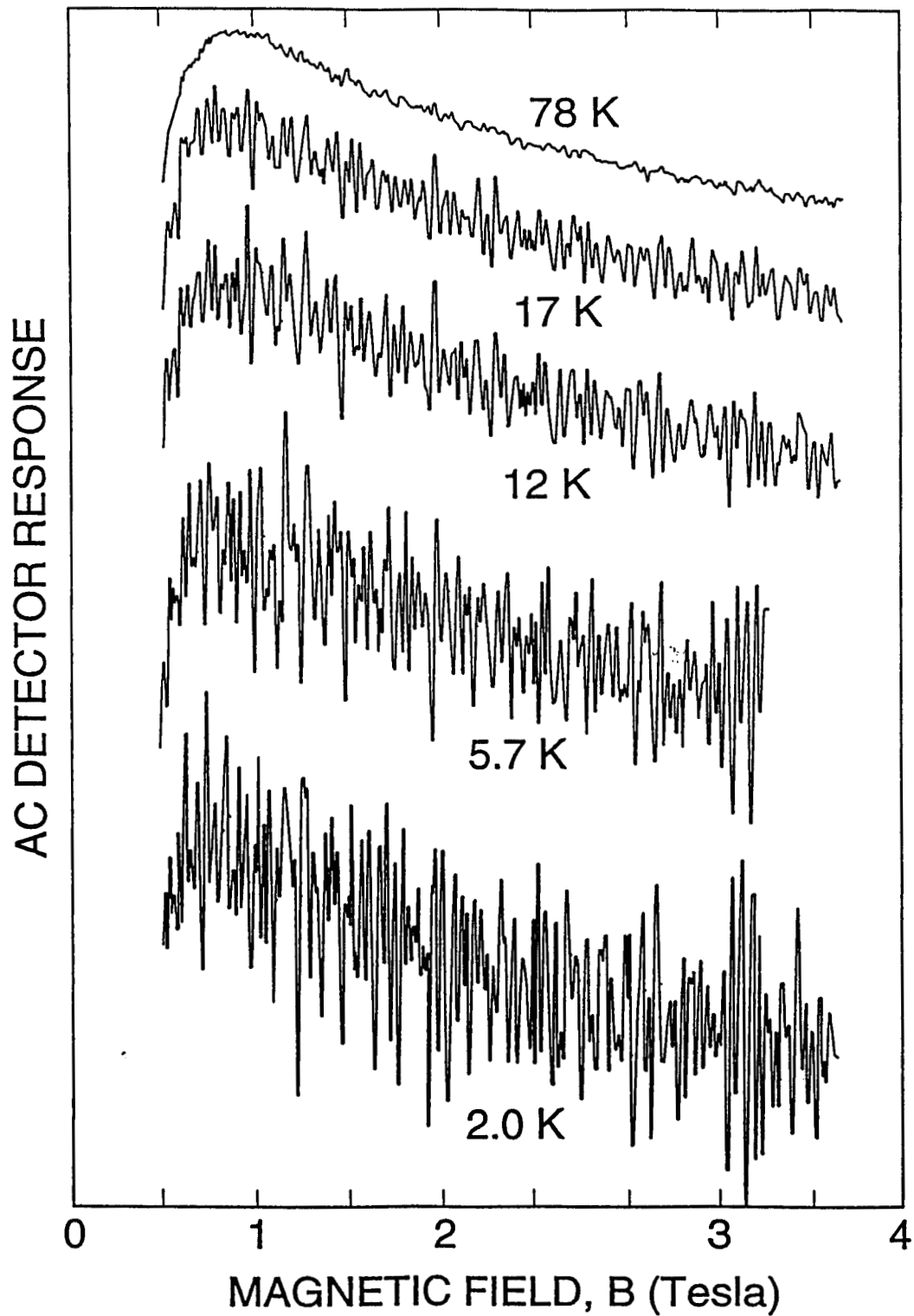
Figure 2.23 Temperature dependence of the response of element 3II1C from a Supplier 3 type II detector. The quiet trace at 78 K suggests that noise is low for these spectra.
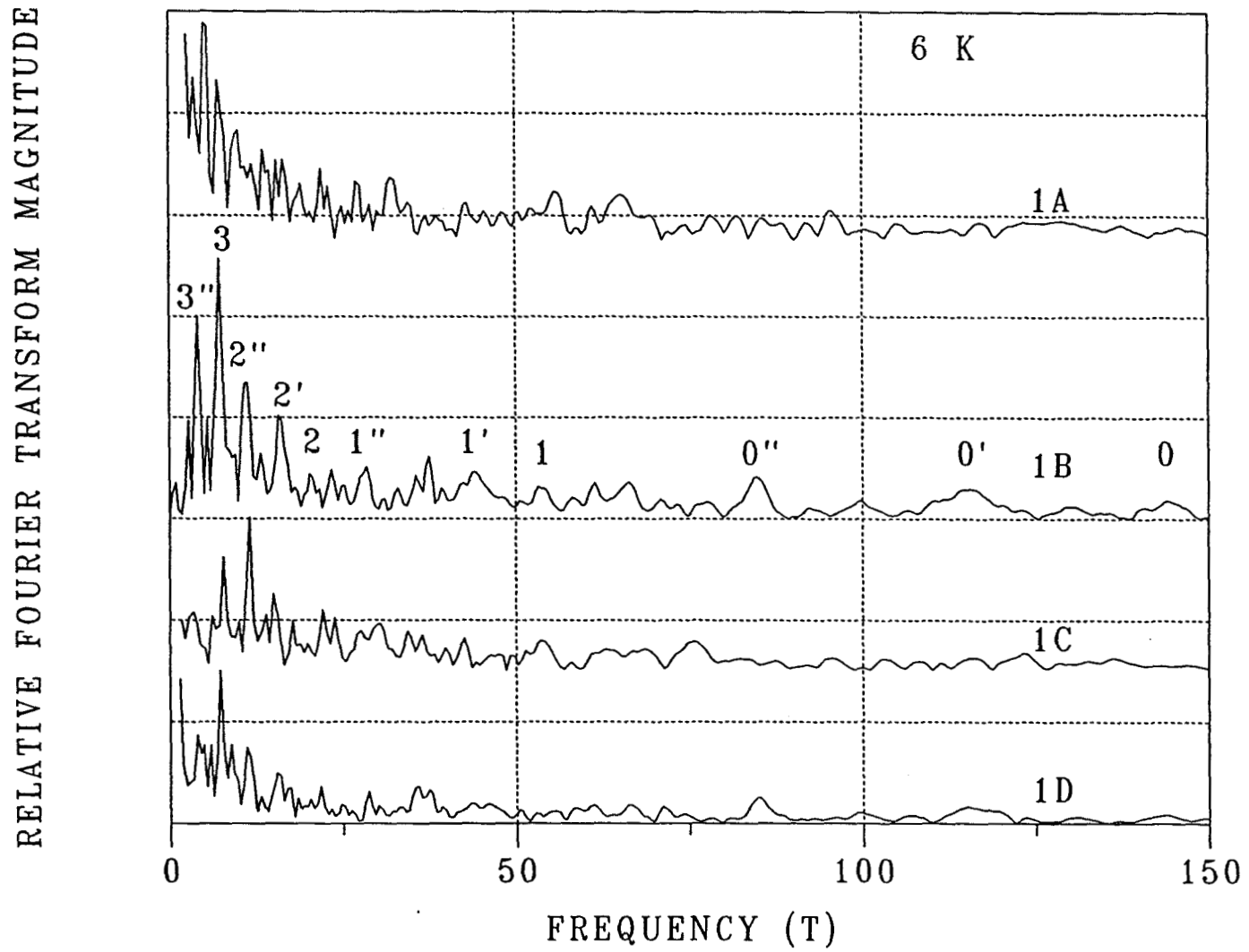
Figure 2.24 Fourier transforms of four elements of a Supplier 3 type II detector. In contrast to the type I devices, the type II have many small peaks extending to high frequencies.

Table 2.4. Results of Shubnikov-de Haas Analysis for Supplier 3 Type II Detectors

Detector Element	Electric Subband	Frequency (T)	$\underline{m^*}\,E_F$ m_0 (meV)	Carrier Density $(\times 10^{11} cm^{-2})$	m^*/m_0	E_F(meV)
3II1A	0	192.6	22.30	93.03		
	1	65.1	7.54	31.44		
	2	22.0	2.55	10.63		
	3	7.0	0.81	3.38		
	SUM			138.48		
	0′	128.9	14.93	62.26		
	1′	43.0	4.98	20.77		
	2′	13.4	1.55	6.47		
	3′	5.2	0.60	2.51		
	SUM			92.01		
	0″	95.4	11.05	46.08		
	1″	32.0	3.71	15.46		
	2″	9.8	1.13	4.73		
	3″	3.5	0.41	1.69		
	SUM			67.96		
3II1B	0	144.0	16.68	69.55		
	1	53.9	6.24	26.03	0.015	416
	2	20.4	2.36	9.85		
	3	7.2	0.83	3.48	0.0081	102
	SUM			108.91		
	0′	115.6	13.39	55.83		
	1′	44.2	5.12	21.35		
	2′	16.0	1.85	7.73		
	3′	5.4	0.63	2.61		
	SUM			87.52		
	0″	84.8	9.82	40.96	0.023	427
	1″	28.4	3.29	13.72		
	2″	11.0	1.27	5.31		
	3″	4.1	0.47	1.98		
	SUM			61.97		

Table 2.4 (Continued)

Detector Element	Electric Subband	Frequency (T)	$\frac{m^*}{m_o} E_F$ (meV)	Carrier Density ($\times 10^{11}$cm^{-2})	m^*/m_o	E_F(meV)
3II1C	0	123.3	14.28	59.55		
	1	39.7	4.60	19.18		
	2	15.0	1.74	7.25		
	3	6.1	0.71	2.95		
	SUM			88.93		
	0'	75.6	8.75	36.51		
	1'	30.0	3.47	14.49		
	2'	11.8	1.37	5.70		
	3'	3.5	0.41	1.69		
	SUM			58.39		
3II1D	0	115.3	13.35	55.69		
	1	36.3	4.20	17.53		
	2	15.5	1.79	7.49		
	3	5.8	0.61	2.80		
	SUM			83.51		
	0'	84.9	9.83	41.01		
	1'	28.6	3.31	13.81		
	2'	11.1	1.29	5.36		
	3'	3.9	0.45	1.88		
	SUM			62.06		
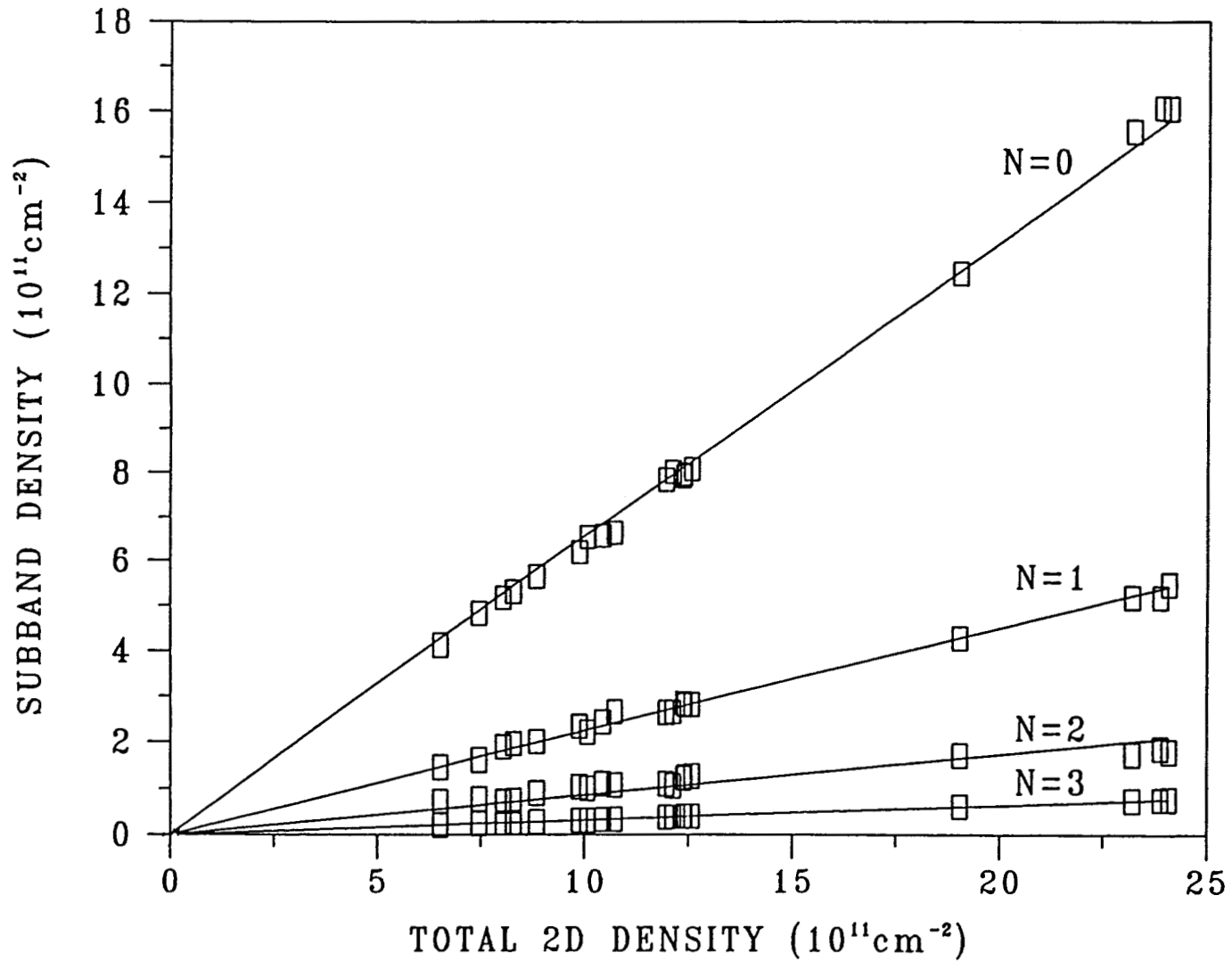
Figure 2.25 Subband carrier density as a function of total density for the Supplier 3 type I detector elements listed in table 2.3. The slopes of the linear fits, given in the text, are in good agreement with those for the Supplier 1 detectors in figure 2.10. The uncertainties in the data are represented by the size of the symbols shown.

0.673, 0.223, and 0.077, respectively. All of the subband 3 values were calculated using N_3 = 0.032 N_t. Figure 2.26 is a subband carrier density plot for the Supplier 2 type III and Supplier 3 type II detector elements given in tables 2.2 and 2.4, respectively. The subbands identified for the Supplier 2 element are considered to be associated with the second passivation process, and the Supplier 3 type II elements had the same alternate passivation on both sides. The results of the linear fits are: N_0 = 0.660 N_t, N_1 = 0.229 N_t, N_2 = 0.083 N_t, and N_3 = 0.029 N_t. Once again, these are in excellent agreement with the theoretically calculated values.

Figure 2.27 shows SdH data for the rotation of element 3I2A from a type I detector with respect to the magnetic field direction. At 0° the field is perpendicular to the accumulation layers, whereas at 90° it is in the plane of the layers. The disappearance of the oscillations with rotation shows that the SdH effect is coming from the two-dimensional layers rather than the bulk. Particular peaks in the waveform are seen to be at higher fields at 30° than at 0°. The quantization depends on the component of the field in the direction of the layer thickness. Thus, the peak position varies as the cosine of the angle. This can be seen best in figure 2.28 which shows the Fourier transforms of the data at the four angles. The identified peaks are seen to shift to higher frequency with increasing angle as predicted. The rotation is seen to be useful in resolving double peaks. The 1' peak is not clearly resolved in the 0° transform, but the 60° transform shows distinct 1 and 1' components. The rotation also confirms that the subband 0 peak has two components. Figure 2.29 is a plot of the peak positions, normalized to the 0° value, as a function of the rotation angle. The expected $\cos \theta$ dependence is shown, and the agreement is considered reasonable in that the rotation was accomplished by wedges rather than a precision mechanism.

It is instructive to see how well the major peaks in the Fourier transform describe the original SdH data. To do this, an inverse transform of each peak is obtained and the results summed. Some distortion is introduced because the peaks are truncated on each side. Inverse transforms were done for the peaks identified as subbands 0', 0'', 1'', 2'', and harmonic 1'' for element 3I2A in figure 2.21. The waveforms are shown in figure 2.30 along with their sum and the original data. The synthesized spectrum is seen to be a good reproduction of the original. This same reconstruction was done for the more complicated data of element 3I1B from figure 2.24. As shown in figure 2.31, inverse transforms of 12 Fourier peaks were combined and compared with the data. The sum is a reasonable representation of the data, especially at higher values of inverse magnetic field because a greater percentage of the Fourier peak area was identified and transformed at lower frequencies. It is useful to sum the identified components to see if the signal is well represented by them.

(3) Results on TIROS Detectors

Figure 2.32 shows the SdH traces for six different TIROS detectors. These are large, single-element devices, about 170 μm by 170 μm. The TIROS detectors of figure 2.32 varied in resistance by a factor of five and the detector current for the measurements was adjusted accordingly. Although similar type SdH oscillations are observed for all the devices, there are reproducible differences which demonstrates that each SdH trace is a unique signature for an individual detector.

The Fourier transforms of the six detectors in figure 2.32 are shown in figure 2.33. They can be categorized into two groups of three detectors each, based on the position of the 1 and 1' subbands. The groups were received at different times which suggests that they were chosen from lots with somewhat different material characteristics or surface passivation. The subband 0 response for detector T60367 is composed of three or four peaks, which suggests a corresponding number of
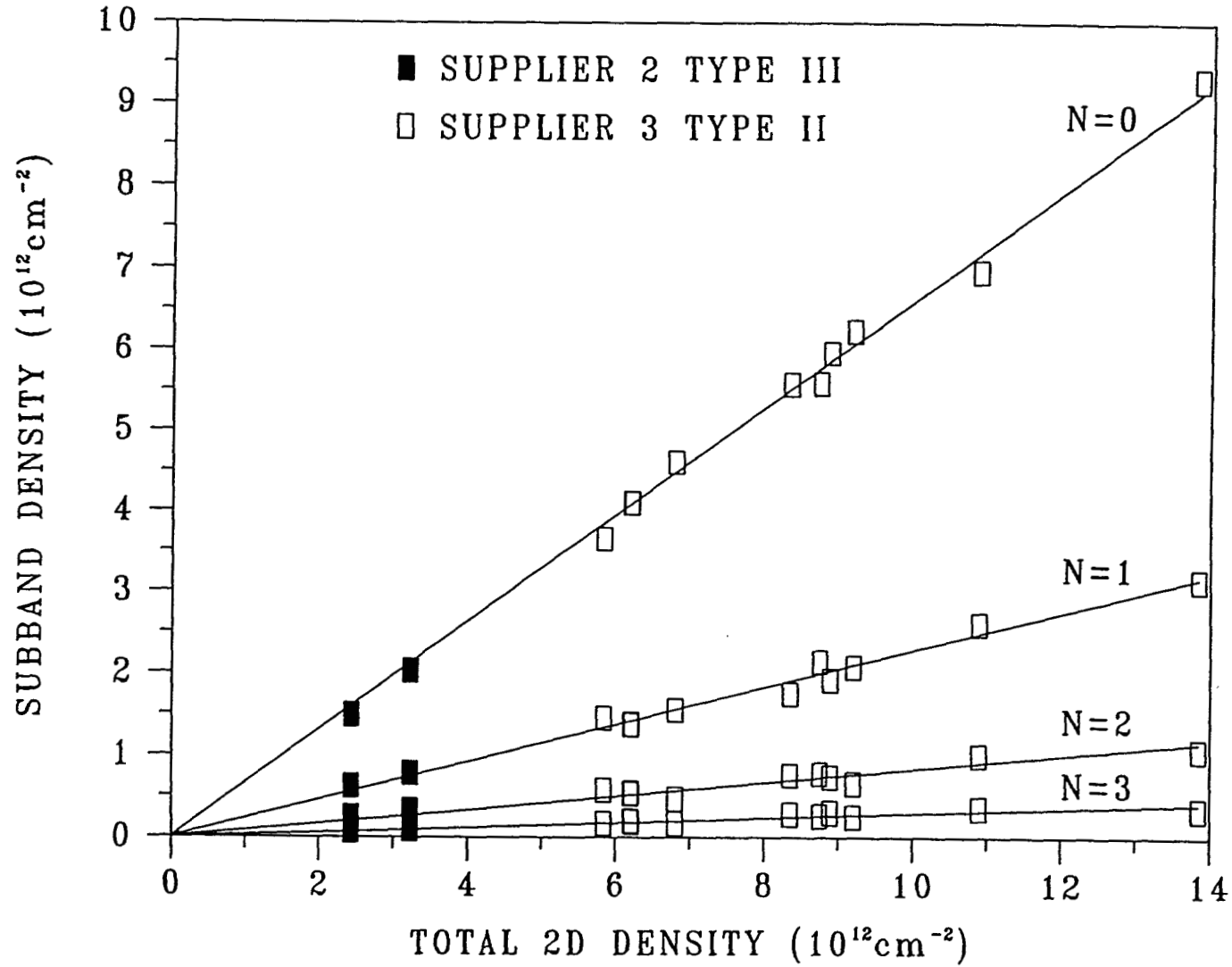
Figure 2.26 Subband carrier density as a function of total density for the Supplier 2 and Supplier 3 type II detector elements listed in tables 2.2 and 2.4, respectively. The type II devices, with alternate passivation, have much higher densities in the accumulation layers than the Supplier 3 type I devices with anodic oxidation. The two surface regions identified for the Supplier 2 device are thought to arise from the second, non-anodic, passivation process. The uncertainties in the data are represented by the size of the symbols shown.

ELEMENT 3I2A   5 K

90°

60°

30°

0°

RELATIVE AC DETECTOR RESPONSE
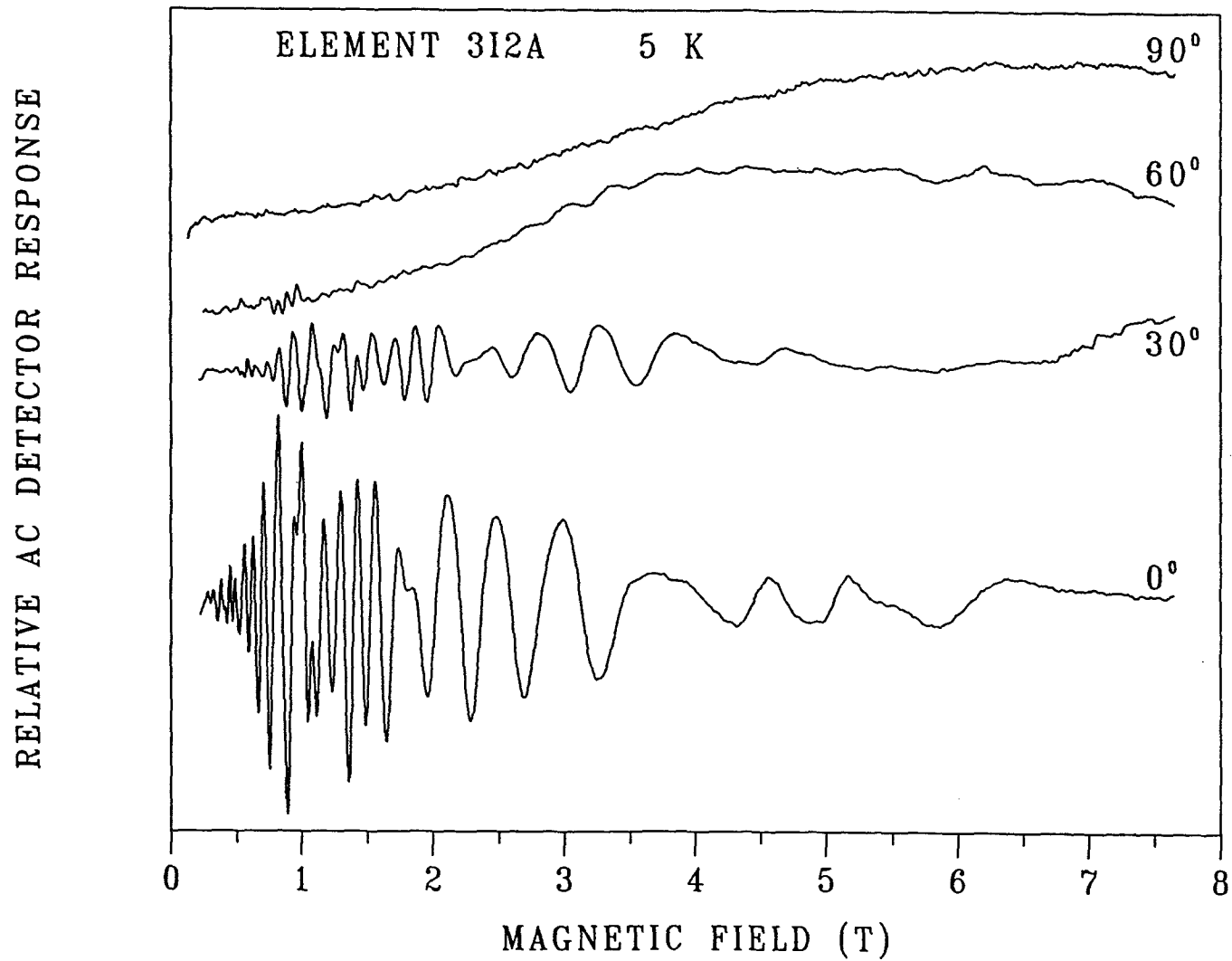
MAGNETIC FIELD (T)

Figure 2.27 Response of element 3I2A when rotated in the magnetic field. At 0° the field is perpendicular to the surface layers whereas at 90° it is in the plane of the layers. The strong damping of the oscillations with angle confirms that the observed SdH effect is associated with the two-dimensional layers rather than the bulk.
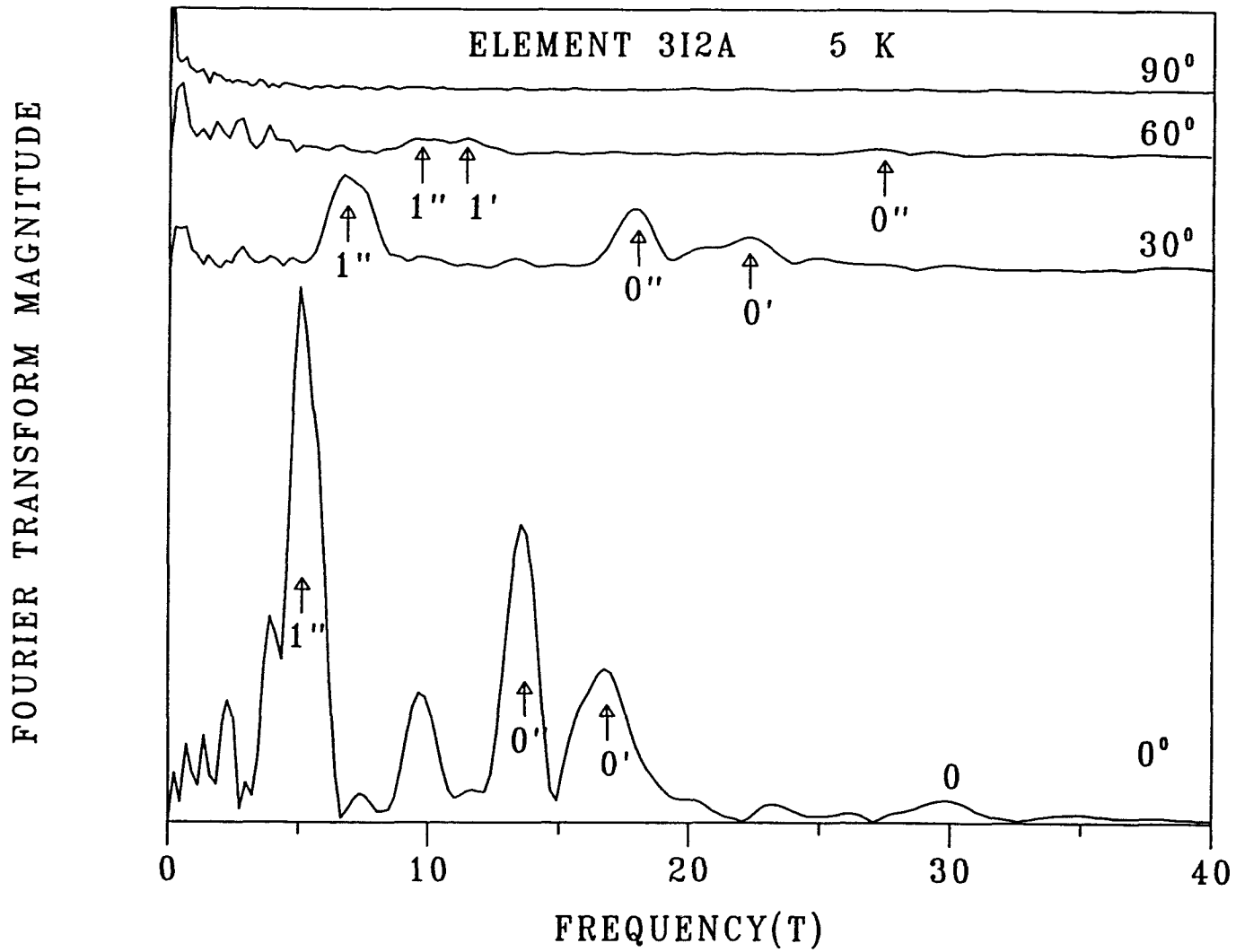
Figure 2.28 Fourier transforms of the rotation traces in the previous figure. The peaks move to higher frequency with increasing angle of rotation as the two-dimensional SdH effect depends on the component of the field in the direction of the layer thickness.
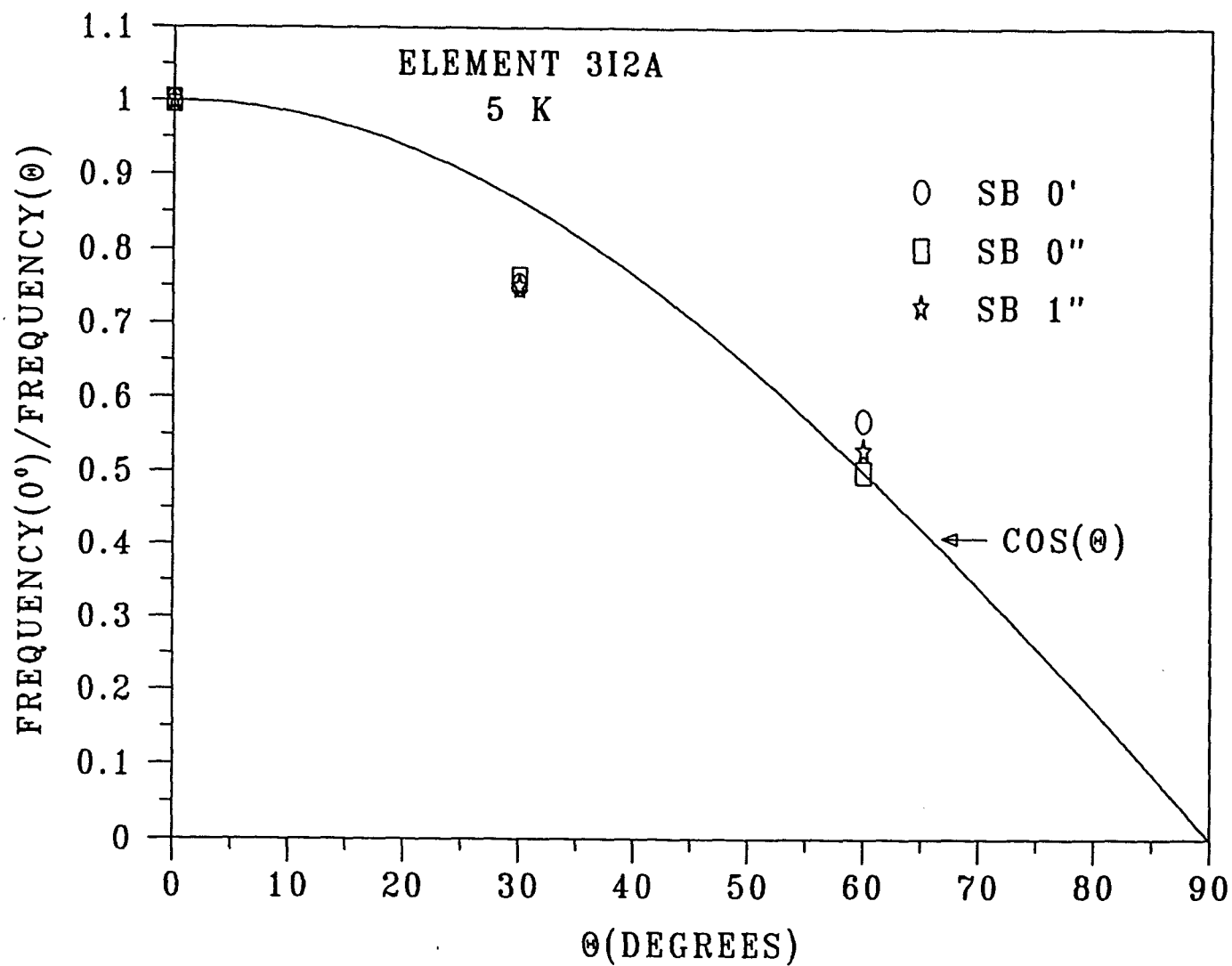
Figure 2.29 Normalized frequency dependence of the Fourier transform peaks for the major subbands of element 3I2A as a function of the angle of rotation in the magnetic field. The results are in reasonable agreement with the expected cos θ variation.
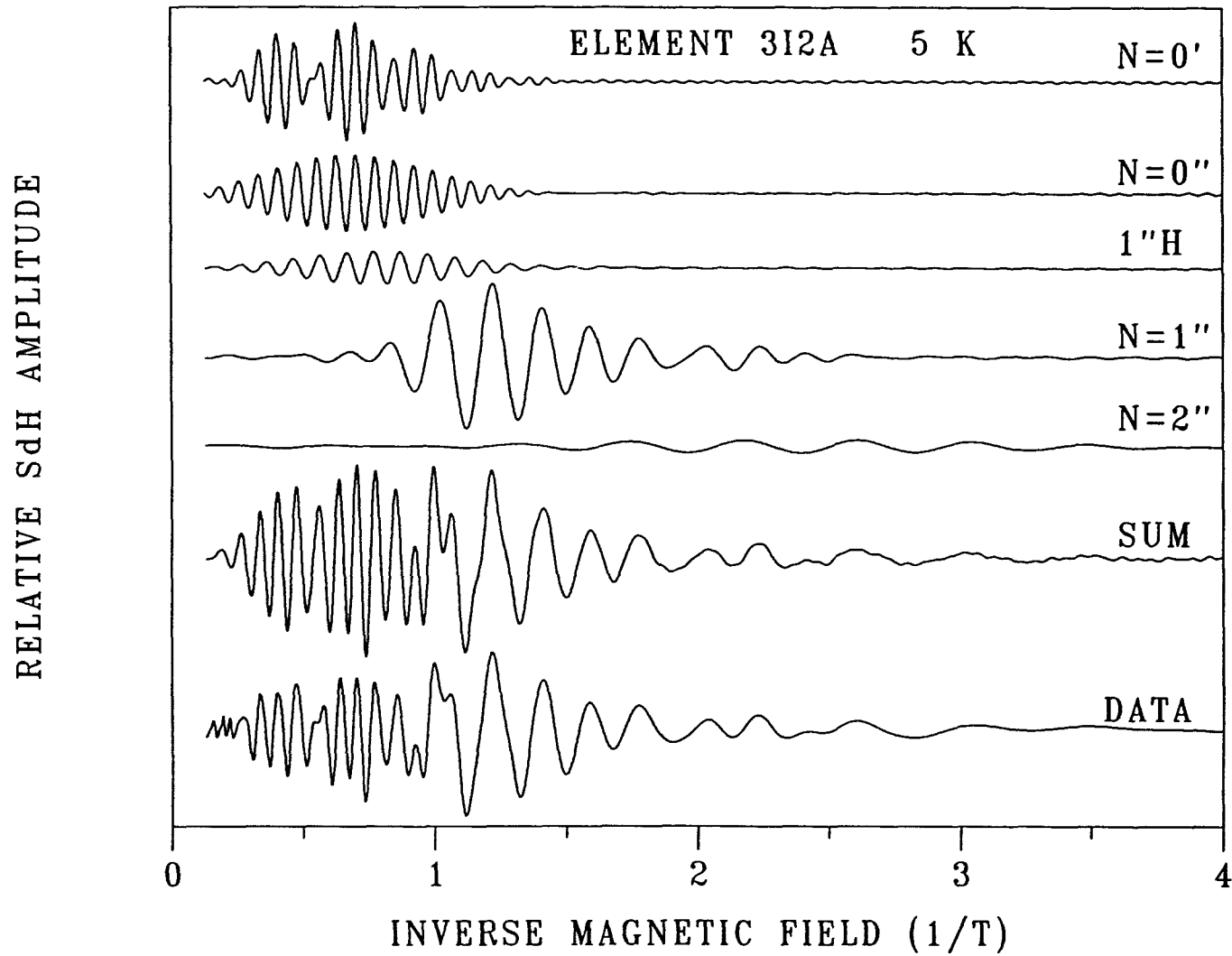
Figure 2.30 Comparison of synthesized and original data for element 3I2A. Inverse transforms were obtained for the major subband and harmonic peaks in the Fourier spectrum. The sum is seen to be a good representation of the data.
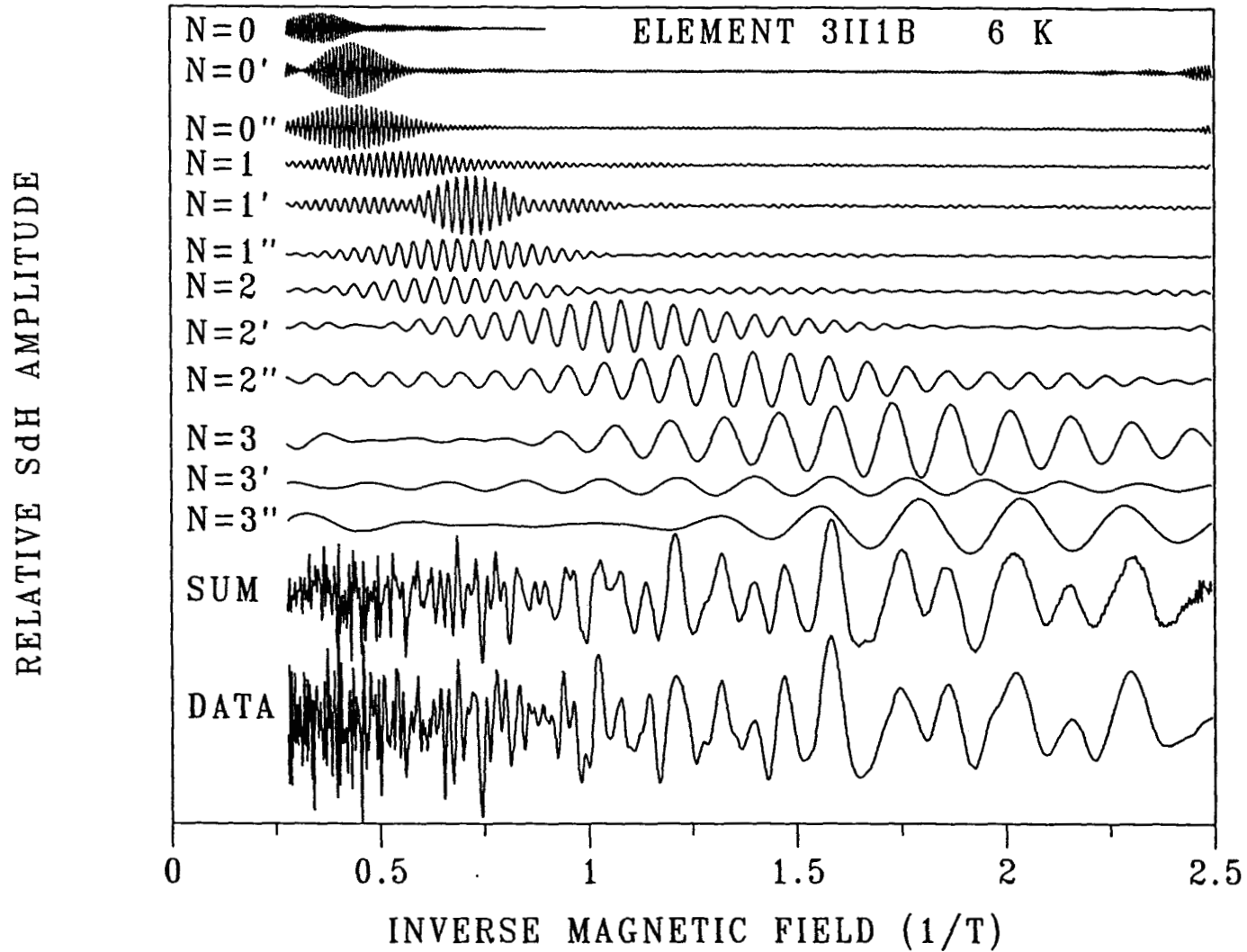
Figure 2.31 Reconstruction of the complicated SdH response for element 3II1B. Shown are inverse transforms for twelve subbands, their sum, and the original data. These subbands are seen to account for most of the oscillations present in the data.
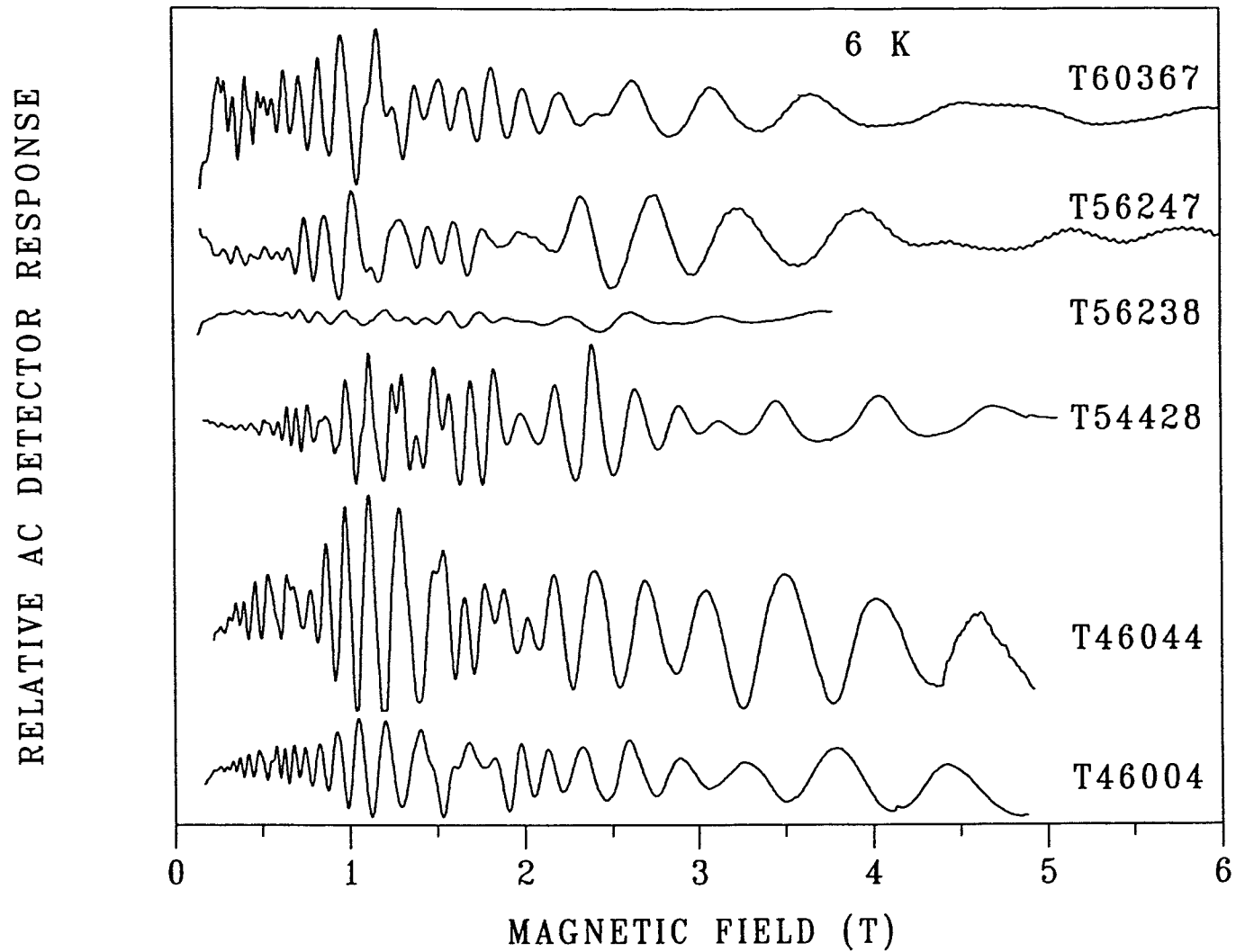
Figure 2.32 SdH response of six TIROS detectors. No adjustments were made for differences in instrument settings or detector current. The signal from T56238 is much lower than that from the others because the ac magnetic-field modulation was lower.
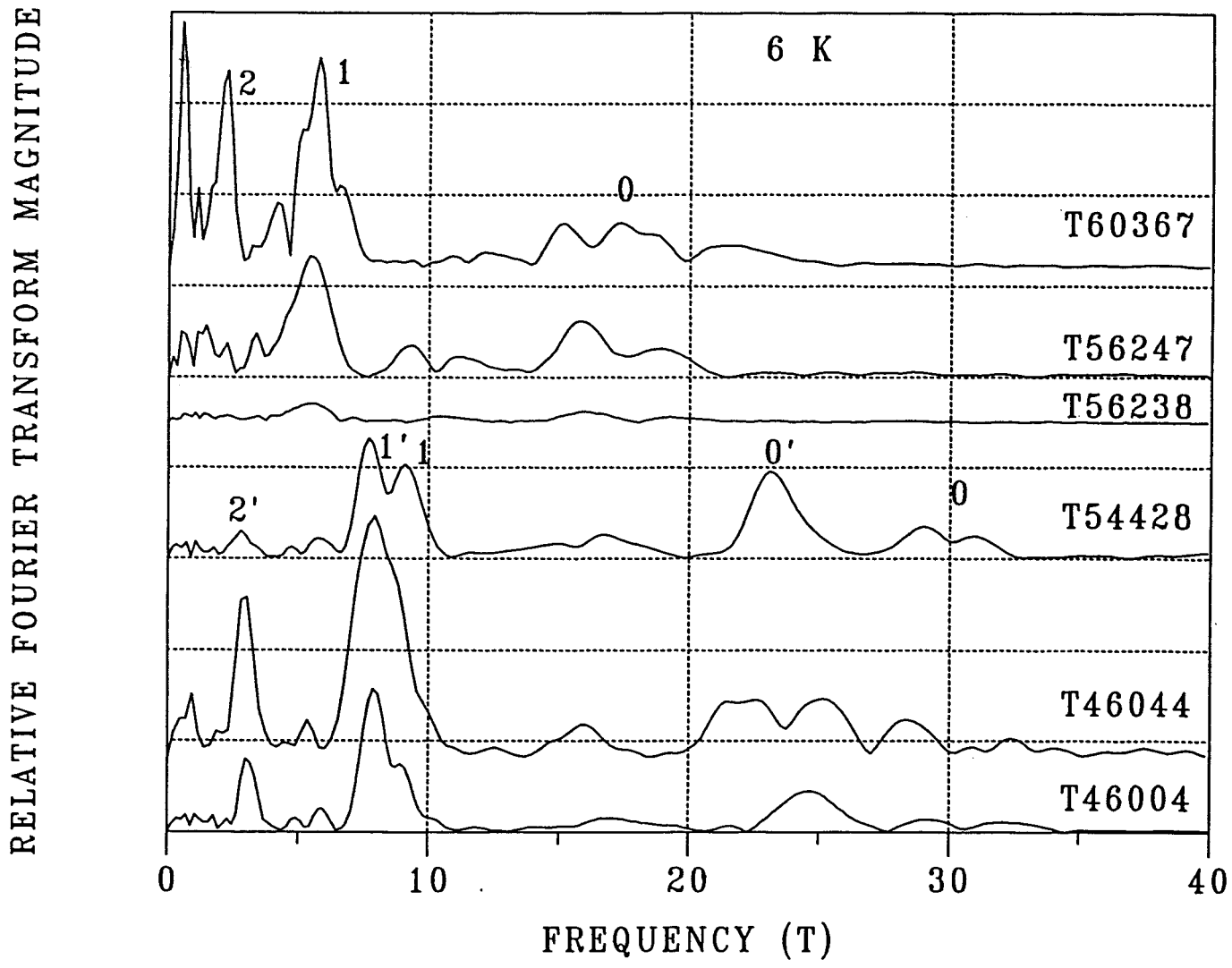
Figure 2.33 Fourier transforms of the six TIROS detectors in the previous figure. They can be divided into two groups of three detectors, each based on the position of the 1 and 1' subbands.

partial surfaces with slightly different electron densities. The composite nature gives rise to shoulders in the subband 1 peak. Detectors T46044 and T46004 were fabricated from the same wafer and have the most similar Fourier transforms, but reproducible differences are still seen. The parameters calculated from the subband peak positions are given in table 2.5.

Figure 2.34 shows the SdH traces for detector T56238 at five temperatures. Evidence of the largest oscillations is seen even at 28 K. The Fourier transforms of these traces are plotted in figure 2.35. The major subband peaks are identified and the frequency positions and calculated parameters are listed in table 2.5. Subband density is plotted versus total density for the TIROS detectors in figure 2.36. Linear fits gave the following relationships good to better than 1%: $N_0 = 0.667\ N_t$, $N_1 = 0.220\ N_t$, and $N_2 = 0.083\ N_t$, in excellent agreement with the theoretically calculated values. All of the subband 3 densities, except one, were calculated using $N_3 = 0.032\ N_t$.

Effective masses for the various subbands were obtained from fits of the inverse transform amplitude as a function of temperature as discussed in an earlier section. Specifically, the logarithms of the amplitudes are fit to the theoretical variation $ln[Tsinh\ (\beta T_o m^*/m_o B)/T_o sinh\ (\beta T m^*/m_o B)]$ by choosing m^* to give the best nonlinear least-squares fit. T_o is the reference temperature, usually the lowest temperature, and $\beta = 2\pi k_B m_o/e\hbar = 14.68$ T/K. The use of the logarithmic dependence produces a more accurate fit because the small signal values at higher temperature contribute more than they would in a linear plot. The fit for the mass of subband 0' for detector T56238 is shown in figure 2.37. The masses obtained for the other subbands of this detector are given in table 2.5.

Dingle temperatures were calculated for the subbands of detector T56238; the values are listed in table 2.5. The procedure is to obtain the inverse transform of the Fourier transform peak for the subband of interest. The inverse signal is divided by all terms except that containing the Dingle temperature. The log of the absolute value of this quantity is plotted as a function of 1/B and the Dingle temperature is calculated from the slope of the line that is tangent to the peaks in the region where the inverse transform is strongest. The plot for subband 0' is shown in figure 2.38.

(4) Intercomparisons

An SdH trace from each group of detectors is shown in figure 2.39. The responses from devices fabricated with alternate passivation, 2I1I1D and 3I11B, have a noisy look, and are much lower in magnitude than the responses from the devices with the standard anodic oxide. When calculating the scale factors, no allowance was made for differences in magnetic field modulation, current, or goes here resistivity. The Fourier transforms of these traces are shown in figure 2.40. Again, the amplitude of the devices with alternate passivation is much less than that of the other devices. Even though the anodic oxide devices all have basically the same set of subband peaks, there are still significant differences. The devices with alternate passivation have a carrier density about 3 to 10 times higher than those with anodic oxidation passivation. The responsivity of the alternate devices reported by the manufacturers is also much higher.

Dingle temperatures could not be reliably extracted for the nonanodically oxidized surfaces. However, the Dingle temperatures are in general agreement from device to device for the anodically oxidized surfaces except that element 3I2A has lower temperatures for the 0 subbands than the rest of the devices. The theory predicts, and NIST results confirm, a systematic decrease in the Dingle temperature in going from subband 0 to subband 3. As discussed in a previous section, this is because the electrons in the lower subbands are closer to the surface, with its lower mobility, than the

Table 2.5. Results of Shubnikov-de Haas Analysis for TIROS Detectors

Detector Element	Electric Subband	Frequency (T)	$\frac{m^*}{m_o} E_F$ (meV)	Carrier Density ($\times 10^{11}$cm^{-2})	m^*/m_o	E_F(meV)	T_D(K)
T56238	0	19.3	2.235	9.32	0.018	122	47
	1	-		3.95$^+$			
	2	-		1.55$^+$			
	3	-		0.49$^+$			
	SUM			15.30			
	0'	15.95	1.847	7.70	0.020	92	43
	1'	5.30	0.614	2.56	0.012	50	30
	2'	2.10	0.243	1.01			
	3'	-		0.37$^+$			
	SUM			11.64			
T60367	0	17.35	2.009	8.38			
	1	5.74	0.665	2.77			
	2	2.23	0.258	1.08			
	3	-		0.40$^+$			
	SUM			12.63			
T56247	0	15.79	1.828	7.63			
	1	5.42	0.628	2.62			
	2	2.23	0.258	1.08			
	3	-		0.37$^+$			
	SUM			11.70			
T54428	0	29.05	3.364	14.03			
	1	9.10	1.054	4.40			
	2	3.32	0.384	1.60			
	3	-		0.66$^+$			
	SUM			20.69			
	0'	23.12	2.677	11.17			
	1'	7.70	0.892	3.72			
	2'	2.80	0.324	1.35			
	3'			0.54$^+$			
	SUM			16.78			

Table 2.5 (Continued)

Detector Element	Electric Subband	Frequency (T)	$\frac{m^*}{m_o} E_F$ (meV)	Carrier Density $(\times 10^{11} cm^{-2})$	m^*/m_o	$E_F(meV)$	$T_D(K)$
T46044	0	22.59	2.616	10.91			
	1	7.92	0.917	3.83			
	2	2.93	0.339	1.42			
	3	0.93	0.108	0.45			
	SUM			16.61			
T46004	0	24.70	2.860	11.93			
	1	7.92	0.917	3.83			
	2	3.03	0.351	1.46			
	3	-		0.57[+]			
	SUM			17.79			

[+] Calculated estimate based on densities of other subbands
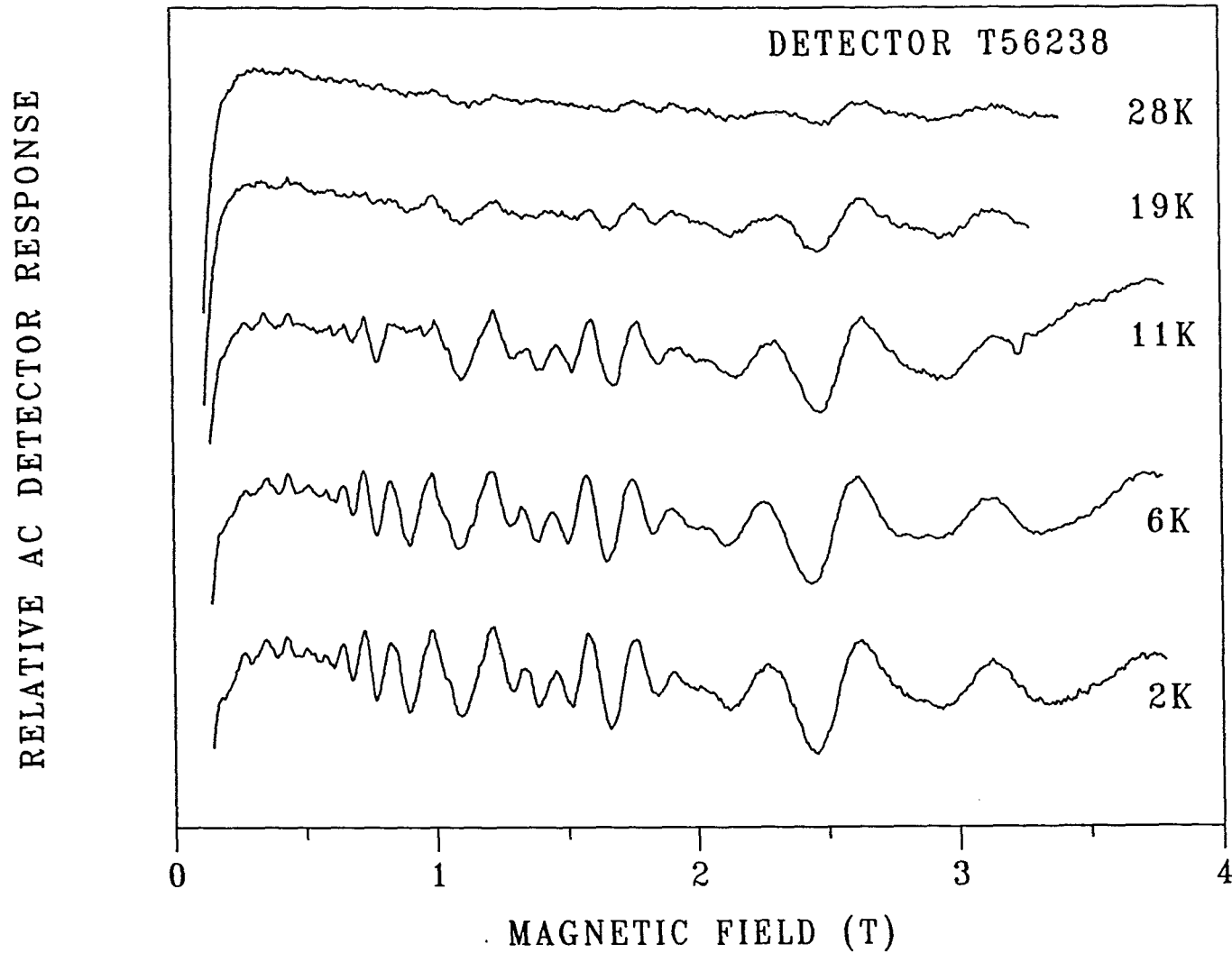
Figure 2.34 SdH traces for detector T56238 at five temperatures. The oscillations at higher field damp more slowly with increasing temperatures than those at lower fields.
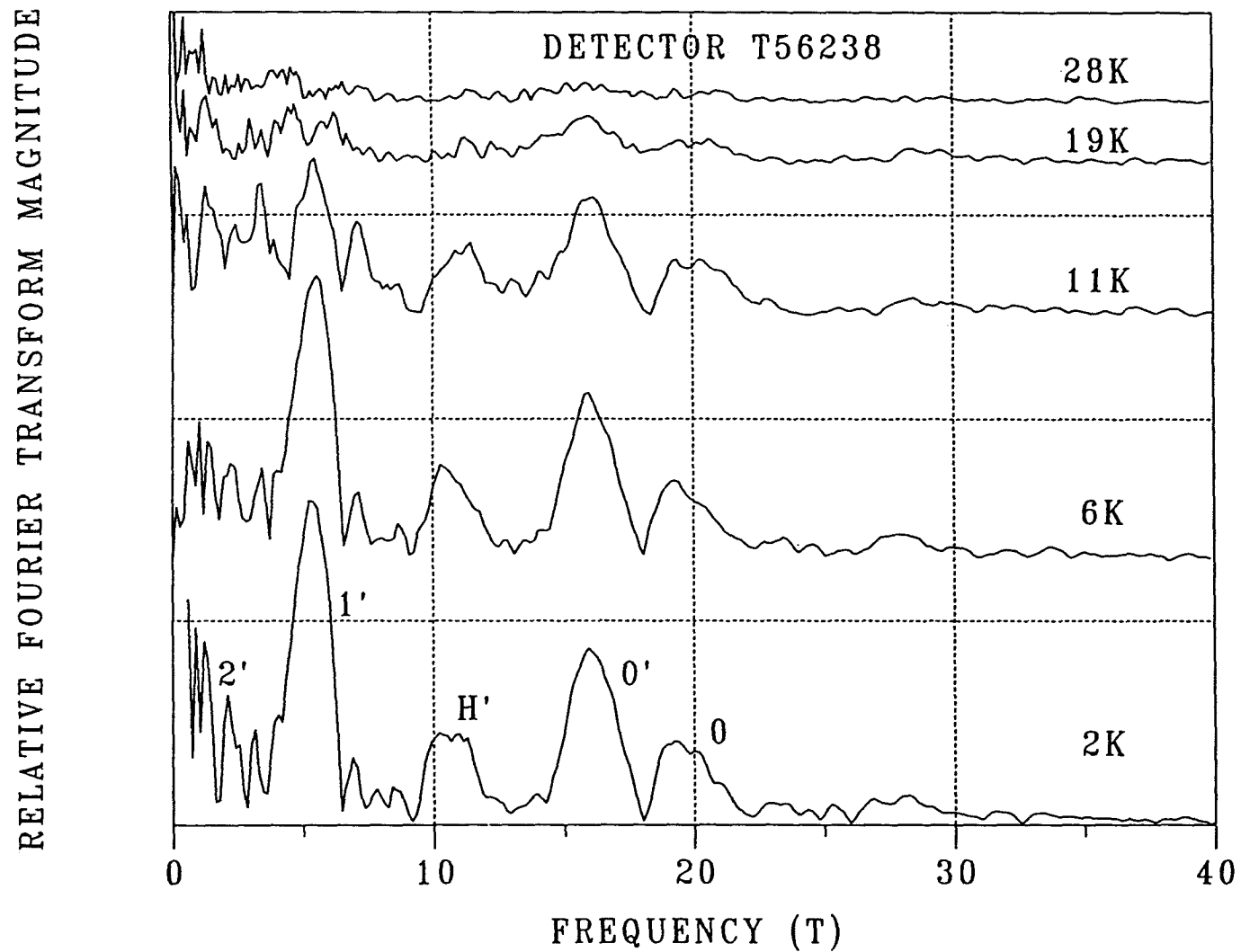
Figure 2.35 Fourier transforms of the SdH traces in the previous figure. The magnitude of the 1′ peak with respect to the 0′ peak decreases with increasing temperature in agreement with the damping seen in the traces themselves.
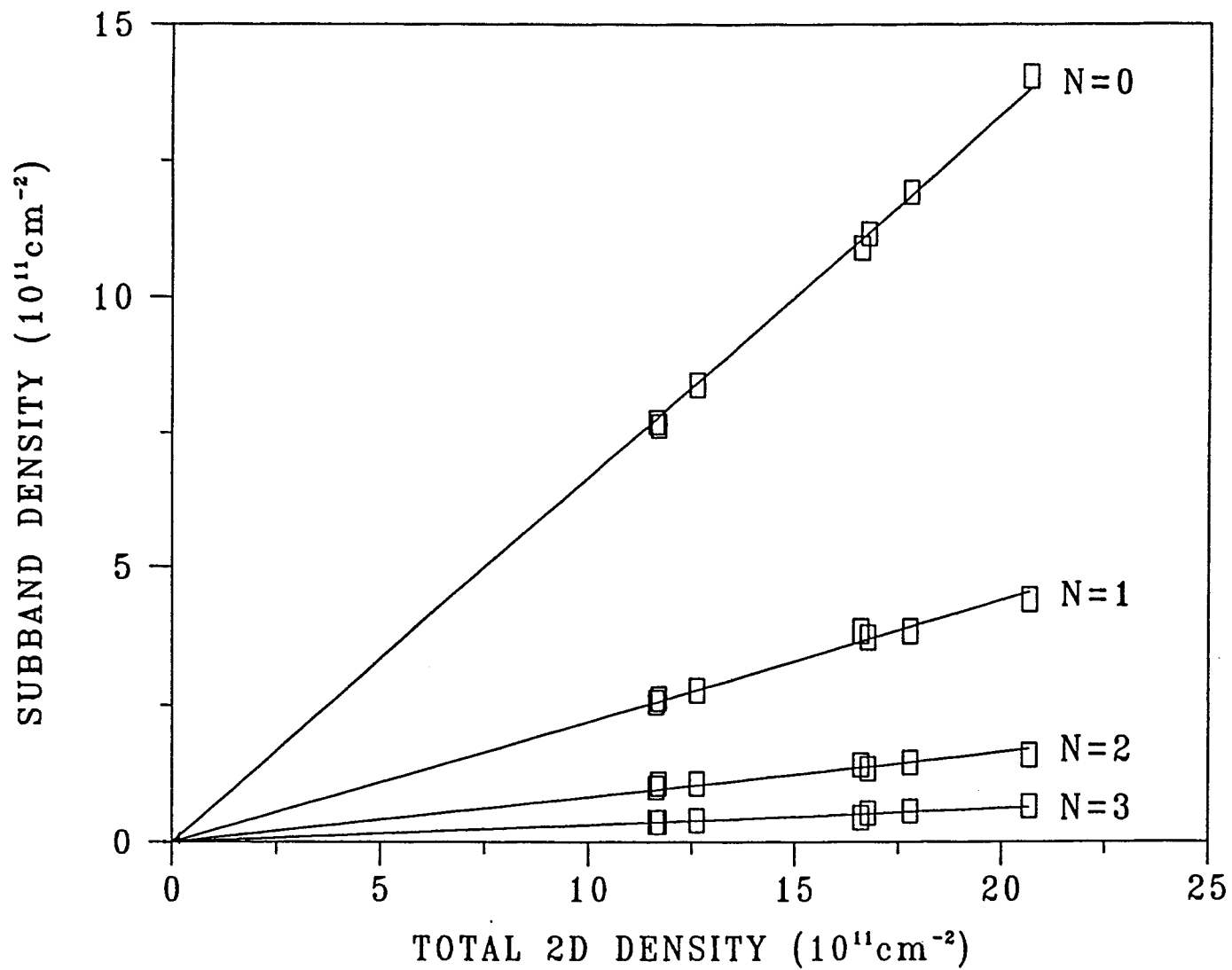
Figure 2.36 Subband density as a function of total density for the six TIROS detectors discussed in this section. The numbers, calculated using the parabolic approximation, are given in table 2.5. The small scatter about the straight line fits confirms that the peaks have been correctly identified. The uncertainties in the data are represented by the size of the symbols shown.
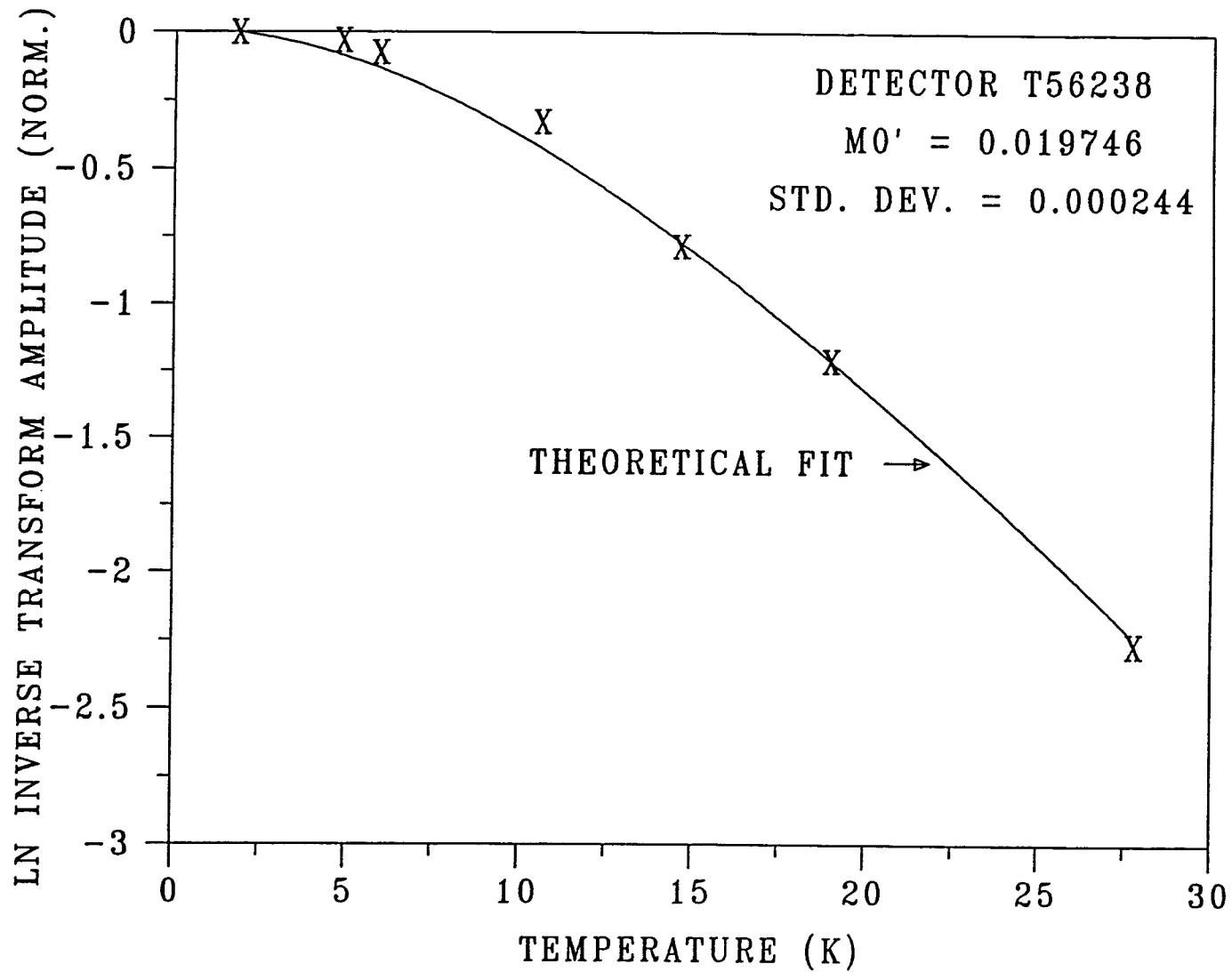
Figure 2.37 Fit to determine the effective mass for subband 0'. The points are the inverse transform amplitude of a given oscillation at each temperature, normalized to the amplitude at the lowest temperature. The line is the least-squares theoretical fit to the data using the expression given in the text.
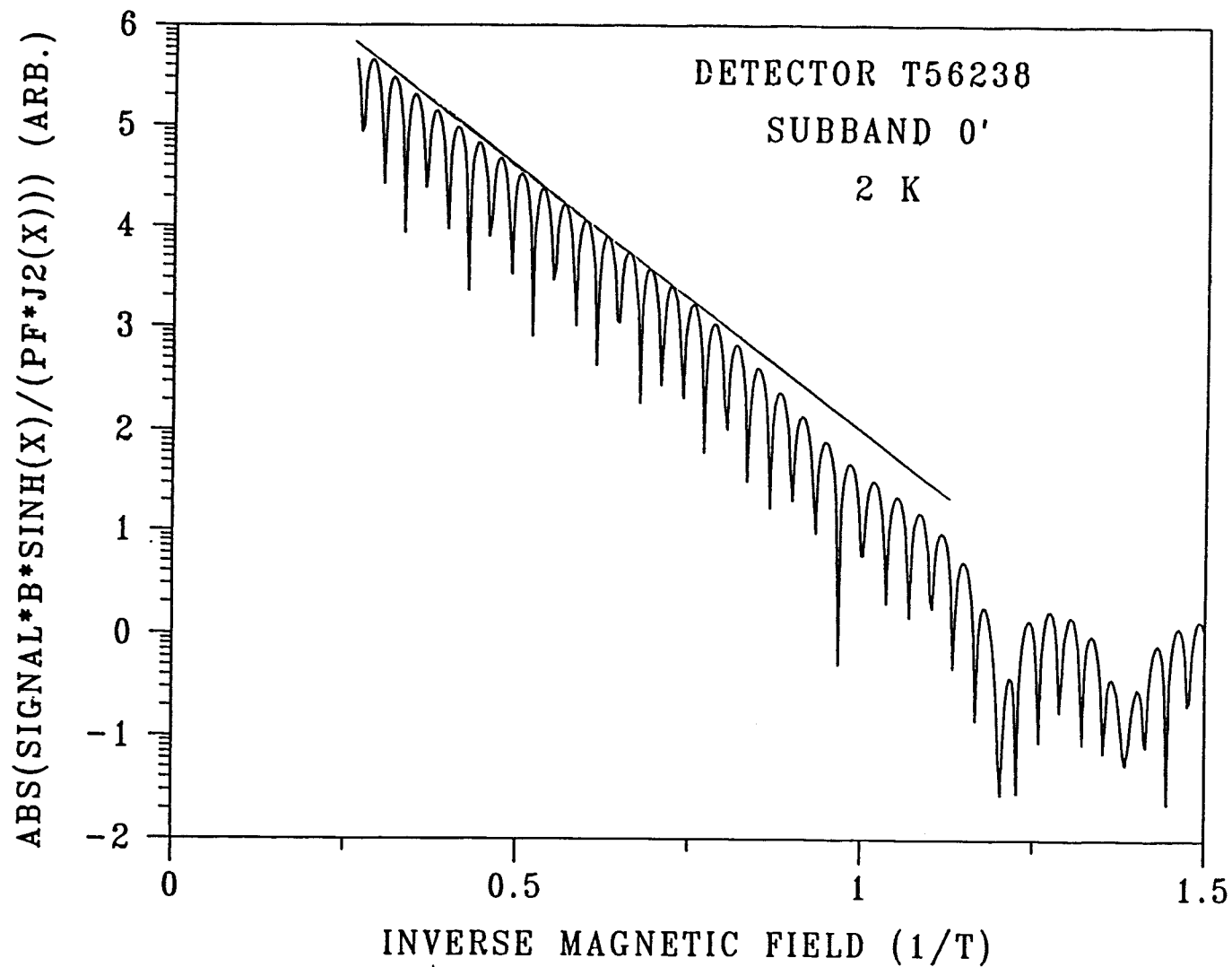
Figure 2.38 Illustration of the determination of the Dingle temperature T_D. The inverse transform signal is divided by all terms not containing T_D and plotted semilogarithmically. The temperature is calculated from a slope drawn tangent to the peaks in the region where the inverse is strongest. From this plot the value obtained for subband 0' was 43 K.
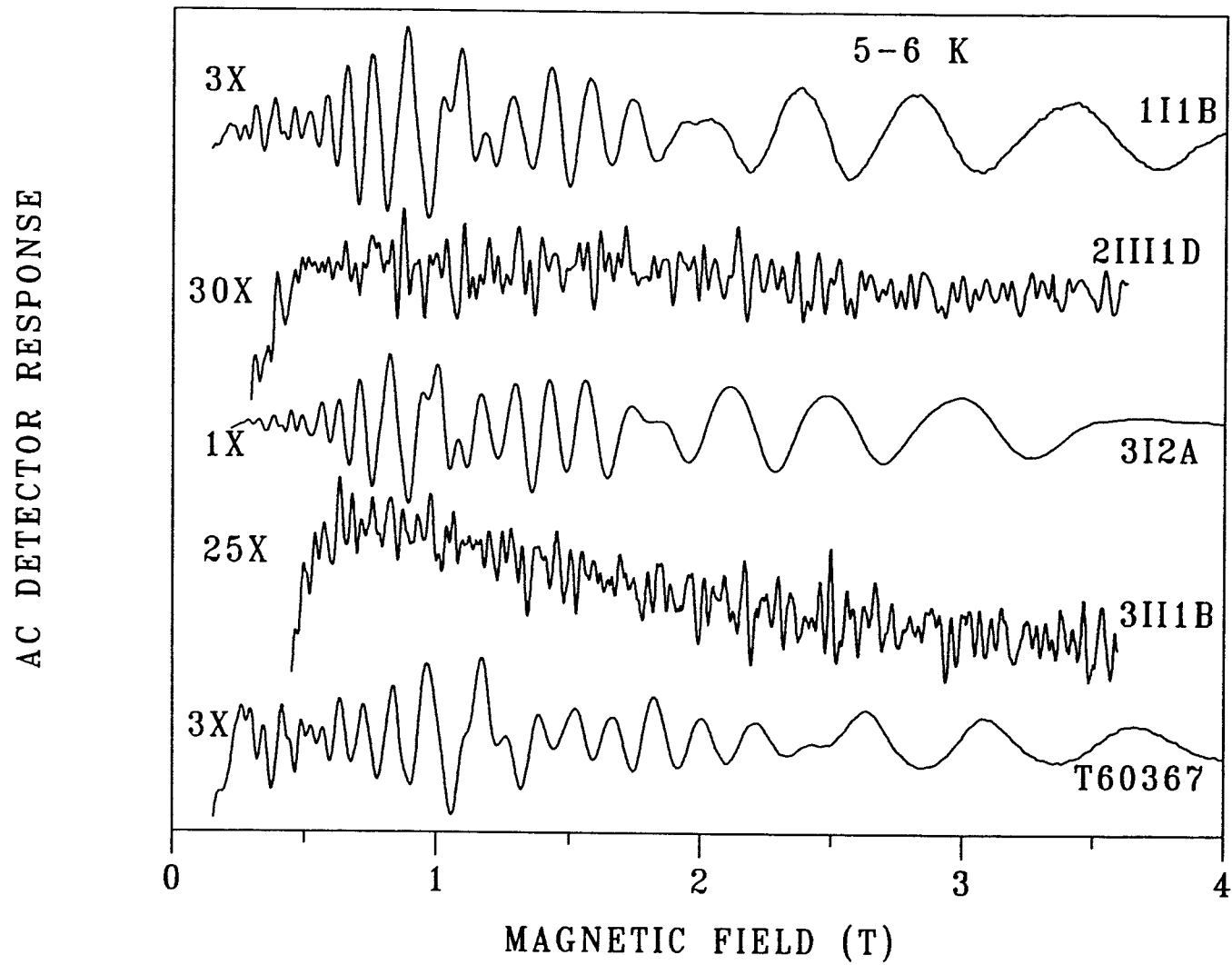
Figure 2.39 Representative SdH traces from each supplier and commercial detector type. The scale factors take into account only instrument settings and not differences in sample resistances, current, or magnetic field modulation.
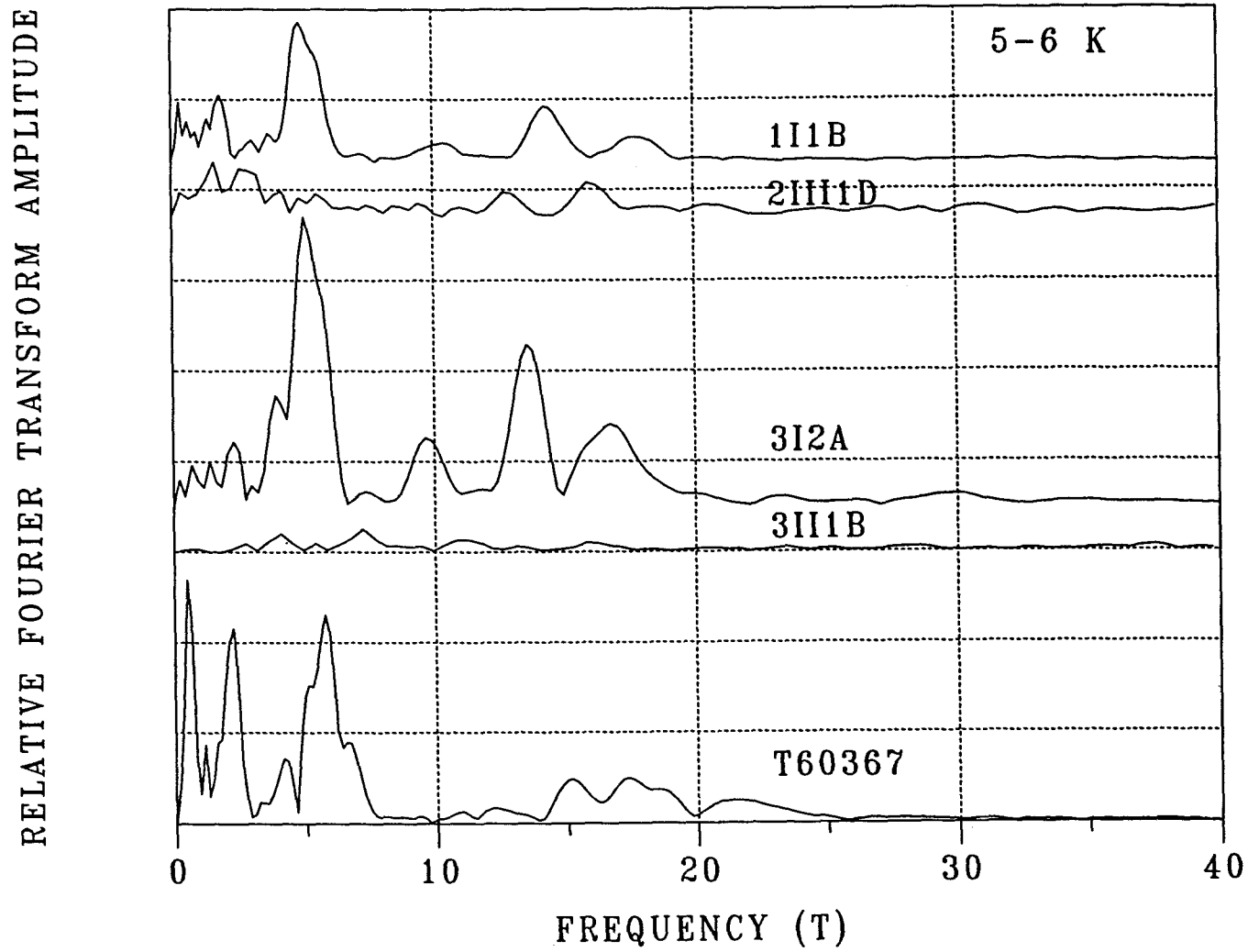
Figure 2.40 Fourier transforms of the SdH traces in figure 2.39. The transform output is normalized to account for differences in the magnetic field range of the raw data. The amplitude of the devices with alternate passivation, 2III1D and 3II1B, is much less than that for the other devices with anodic oxidation passivation.

electrons in the higher subbands.

The values of the Dingle temperature were quite large compared with the values around 3 K which were computed on the basis of the measured mobility. *Theoretical calculations [2.11] have shown that the Dingle temperatures can be much larger than those derived from the conductivity mobility because the relaxation time affecting the Dingle temperature is much more sensitive to forward scattering.* For Coulomb repulsion due to surface-charge scattering, it is expected that the Dingle temperatures should be as large as measured. *Thus, it is concluded that the behavior of the anodic-oxide passivation is well understood.*

D. Summary of Quantum Magnetotransport Characterization Measurements

(1) Comparison between Theory and Experiment for Two Different Detector Types

Shubnikov-de Haas measurements have been made on a number of long-wavelength, commercial, n-type PC detectors with total densities between 5×10^{11} and 1×10^{13} cm^{-2}. The SdH Fourier transforms of two different representative detectors are shown in figures 2.41a and 2.41b. The notations ′ and ″ refer to different surfaces or to different regions on the same surface, since both surfaces of the detector were passivated. The detector in figure 2.41a was passivated with the usual anodic oxidation process [2.12,2.13], while that in figure 2.41b was passivated by a different method. The separations of peaks due to spin-splitting as predicted by theory are about half of that observed, and, thus, it is expected that these multiple peaks are due to different surface densities. The splittings vary somewhat from detector to detector as well. Thus, the effect of spin-splitting is just to broaden each peak. The transform corresponding to the detector with lower total density, element 3I2A in figure 2.41a, has clear, strong peaks, while that for the one with higher density, element 3I1B in figure 2.41b, has peaks that rise less above the background. One reason is that the penetration of the energy gap by the wave functions is much greater for the heavily accumulated case, especially for the lowest subband. *There is a mixture of subband states bound to the conduction band and continuum states that traverse the entire detector.* Thus, the layer of electron accumulation is not well described by a simple 2D electron gas at high densities and small energy gaps. The Fourier transform for a heavily accumulated, narrow-gap detector can have a broad background of contributions from the range of 3D states corresponding to the graded 3D electron density in the accumulation layer. The 2D states, which are bound to the conduction band, appear as well in the Fourier transform and rise above the background because they contribute at only one frequency for each subband. The complexity of the background signature in figure 2.41b may indicate that there is nonuniformity in the surface density as well because of the two surfaces and multiple regions within a surface. Even though the relative amplitude of the oscillations of element 3I1B was almost ten times smaller than that of element 3I2A, the Fourier transform successfully resolved the unique signature of the detector.

The subband electron densities have been computed from the measured cyclotron effective masses and Fermi energies for the first detector. The results from the two surfaces were averaged because the splitting could not be resolved at higher temperatures. For element 3I2A, the measured data and their uncertainties obtained from the fitting are: $m_0{}^* = 0.022 \pm 0.001$, $E_f^0 = 79 \pm 4$ meV, $m_1{}^* = 0.014 \pm 0.001$, and $E_f^1 = 42 \pm 3$ meV. The corresponding theoretical values (and their uncertainties due to calculational imprecisions), based on the calculations shown in section 2.B.4, were obtained by finding the total density for which the m^*E_f values for the subbands best agreed with experiment: $m_0{}^* = 0.023 \pm 0.001$, $E_f^0 = 75 \pm 2$ meV, $m_1{}^* = 0.015 \pm 0.001$, and $E_f^1 = 38 \pm 1$ meV. The predicted total density is found to be 7.9×10^{11} cm^{-2}, which is *considerably less than the value of*
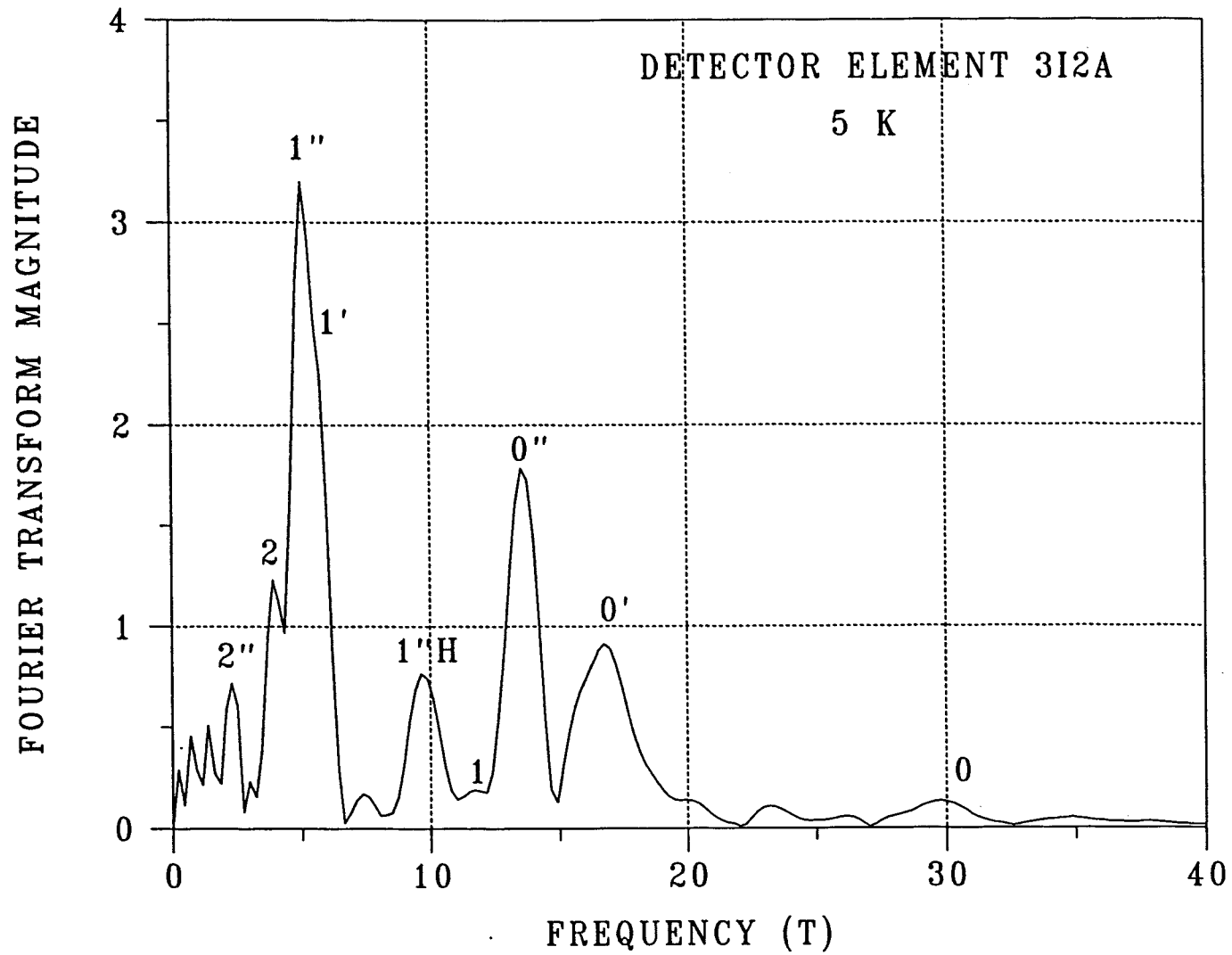
Figure 2.41a Fourier transform of SdH data for detector element 3I2A; the label "H" stands for harmonic; peaks are labeled by subband number.
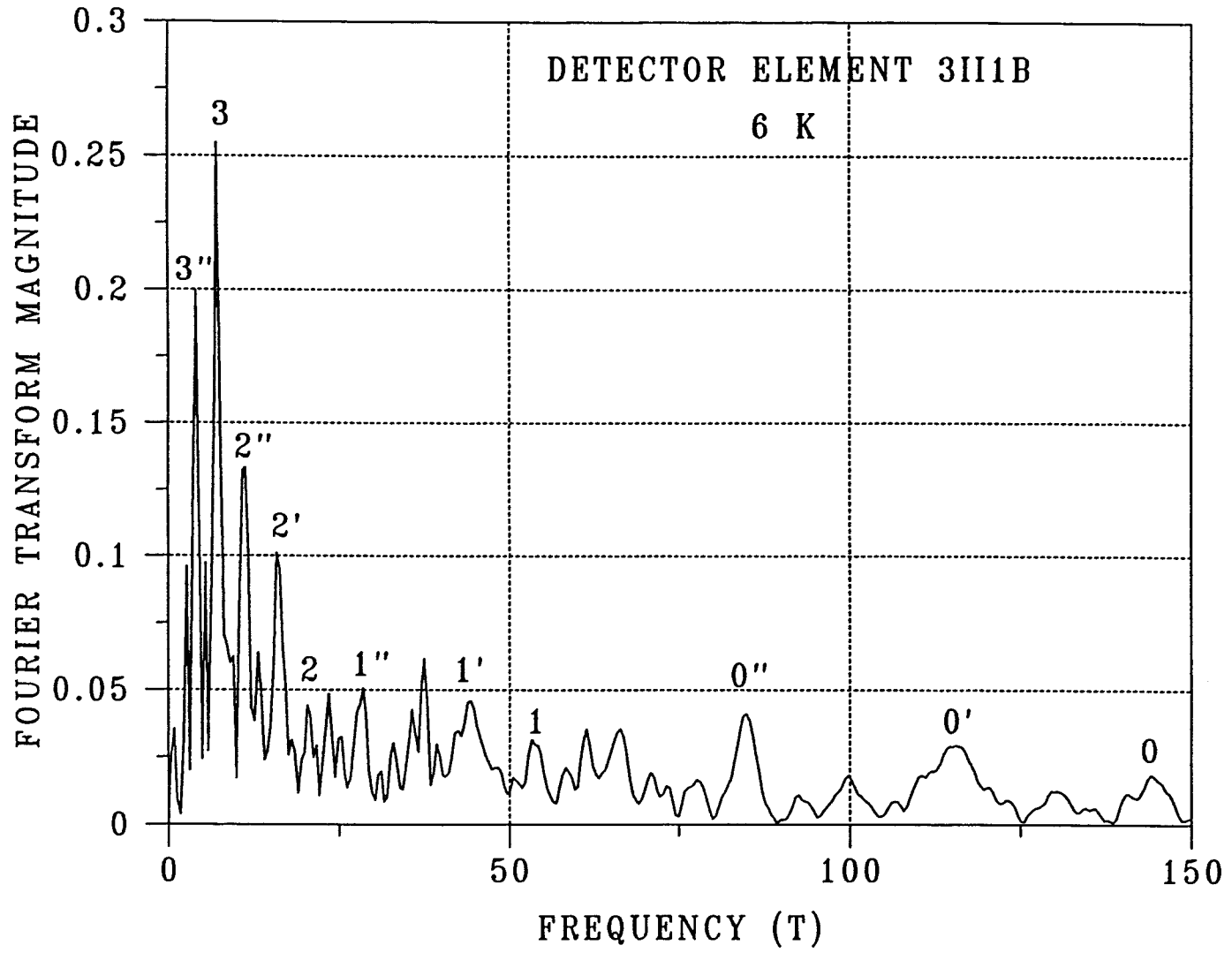
Figure 2.41b Fourier transform of SdH date for detector element 3II1B; the peaks are labeled by subband number.

1.2×10^{12} cm^{-2} that is obtained from the parabolic approximation for the density. The agreement between theory and experiment is within the assigned uncertainty, but the theoretical values for the effective masses are slightly larger than measured. Thus, it is expected that the energy gap may be smaller than the one used. Band-gap narrowing which occurs at high densities because of the many-body interactions between electrons has been included [2.14]. The band-gap reduction is at most 10% at this density. The new theoretical values are: $m_0^* = 0.022 \pm 0.001$, $E_f^0 = 75 \pm 2$ meV, $m_1^* = 0.014 \pm 0.001$, and $E_f^1 = 39 \pm 1$ meV, which are somewhat closer to the experimental values. The remaining differences in Fermi energy may be due either to a slightly smaller value of x or slight differences in the built-in potential between theory and experiment.

No attempt was made to analyze the second detector because its electron density was above the range of the calculations and the peaks were not clean enough to determine the effective masses. Results for the subband densities for the peaks are given in table 2.4, based on the parabolic approximation. These values for densities are probably on the order of 30 to 50% larger than they would be if the effects of nonparabolicity were included.

The agreement of calculations with experiment is good for anodically oxidized detectors and is even improved somewhat by inclusion of the effect of band-gap narrowing. Models such as these provide a basis to characterize the electron states in the accumulation layers of these detectors, which have a large effect on device performance.

(2) Comparison with Detector Performance and Identification of Trends

It is not possible to make detailed comparisons between the responsivities and detectivities of different detectors and the results of the SdH analyses because: 1) the measurement practices differ from supplier to supplier; 2) the substrate wafers are different; and 3) the side-wall delineation, bonding, and packaging are different. However, it should be possible to compare the different elements of a detector because variations due to effects other than passivation should be small. Overall, the element-to-element variations were not very large, both in SdH signature and in responsivity. In section 4, element-to-element variations are shown for multielement detectors by the dc magnetoresistance technique with correlations to detector responsivities.

It is possible, however, to correlate the results of the SdH analyses with expected device performance. The goal of the passivation treatment is to reproducibly create an accumulation layer at the top and bottom surfaces that repels minority carriers so that surface recombination is suppressed. This greatly increases the minority-carrier lifetime in the detectors. However, it is also necessary that the conduction through the accumulation layer be minimized so that the signal is not shunted. Therefore, relatively high electron density and low mobility are desired. The improved responsivities and detectivities of the detectors that use treatments other than anodic oxidation processes are achieved by the higher electron densities and lower mobilities resulting from these processes. Unfortunately, these treatments also lead to a wide variation of detector parameters from device to device. There are two reasons why the corresponding mobilities in these heavily accumulated layers are lower: 1) the conductivity effective mass is larger for the higher electron densities and 2) the surfaces are probably damaged somewhat by the processing. The SdH measurements have shown why these alternative passivation treatments are better and have also indicated the need for further study to understand their chemical and physical properties better. Hall measurements should be performed on similarly processed wafers as well as chemical analyses of the constituents. The stability of these surfaces over

time can be studied by continually measuring the SdH signatures of several detectors. Thus, the SdH method is a very useful tool in determining the nature of the passivation layers of HgCdTe detectors.

3. DC Magnetoresistance Characterization of Detectors

A. Background

The SdH technique just described furnishes detailed information on the electrical properties of the subbands in the accumulation layer. However, it is a somewhat sophisticated technique which requires a high level of analysis. Therefore, a new technique has been considered which is based on the dc magnetoresistance that corresponds to the background signal on which the SdH oscillations are superimposed. This technique is easier to apply and furnishes the total electron density and average mobility of the carriers in the top accumulation layer of the detectors. This new method should be easily adopted by detector manufacturers to improve their quality control.

The magnetic-field dependence of the two-terminal magnetoresistance has been used as a tool to measure both the free-carrier density and the Hall mobility of the top accumulation layers of the detectors situated in a magnetic field, B, which is perpendicular to the plane of the sample. The magnetoresistance normalized to $B=0$, which increases as the length-to-width ratio, α, decreases, has usually been considered an unwanted effect in standard magnetotransport measurements such as the Hall effect, but it was shown to be a valuable characterization technique. It is due to the shorting effect of the Hall voltage by the contacts and is not to be confused with the bulk or "long-bar" transverse magnetoresistance, which is usually much smaller because it only relates to effects due to scattering-lifetime distribution functions and band-structure [3.1]. The cases treated here are very degenerate, and the bulk magnetoresistance is negligible. The two-terminal transverse magnetoresistance effect (or "geometric effect") described here has been used in the past to characterize GaAs Gunn diodes [3.2-3.5] and FET contacts [3.6], but the limiting case of $\alpha \rightarrow 0$ was used because it was considered to be adequate for these cases. This limit is not appropriate for the infrared detectors. Thus, an approximate, general formula for the magnetoresistance as a function of both B and α has been derived here to allow this method to be applied to a wider range of semiconductor structures currently being manufactured.

B. Theoretical Analysis

A conformal-mapping calculation was performed by Lippmann and Kuhrt [3.7,3.8] to obtain the normalized magnetoresistance, $R(B,\alpha)$, of a semiconductor layer as a function of B and α, as shown in figure 3.1. A nonlinear least-squares fitting routine [3.9] was used to derive an approximate analytical equation from these calculated curves:

$$R(B,\alpha) = \frac{\alpha}{ne\mu t} (1 + \mu^2 B^2)^r \tag{3.1}$$

where

$$r = (0.98\alpha + 1.01)^{-1} \tag{3.2}$$

85
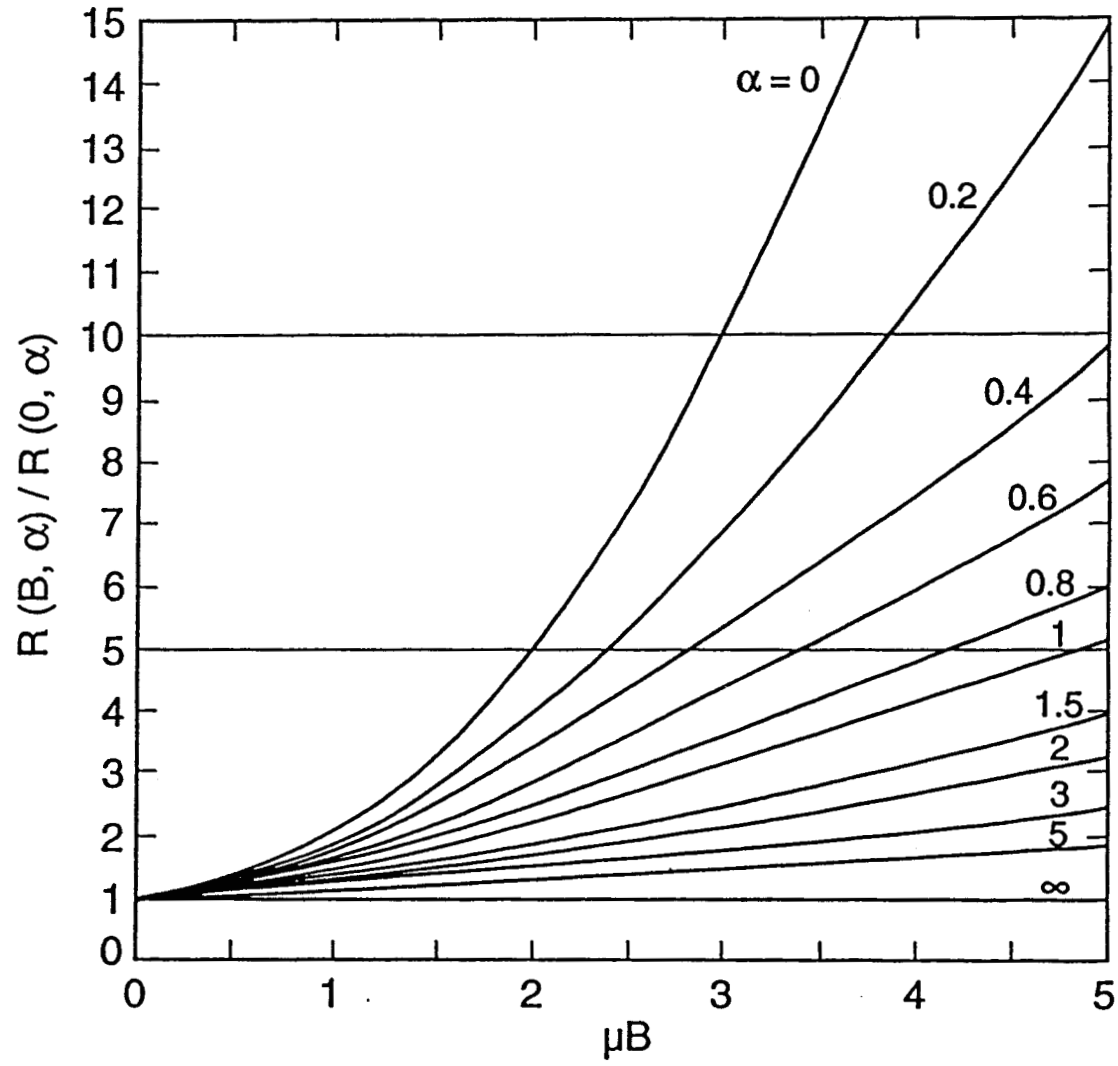
Figure 3.1 Relative resistance as a function of μB for different length-to-width ratios α, from reference 3.8.

and where e is the electronic charge, n is the carrier density, μ is the Hall mobility, and t is the layer thickness. SI units are used throughout. Note that the curves gradually progress from a nearly linear to parabolic dependence on B with decreasing α. The fit is good to about 1% over the fitted range $0.2 < \alpha < 5$ and $\mu B < 5$. Analytic results exist for $\alpha = 0$ and $\alpha = 1$, for which eq (3.1) holds with $r = 1.0$ and 0.5, respectively. These values of r are close to those obtained from the fit, 0.990 and 0.503, respectively. It is expected that the fit should not degrade substantially outside of the fitted range because of the agreement with these two cases for all values of B. Because of the functional form for these two cases, the form of eq (1) was chosen. The case $\alpha = 0$ corresponds to a Corbino disk, for which this method has been applied in the past [3.1]. For a multilayer structure, eq (1) can be used for each layer with its own set of parameters, but only if the layers are electrically isolated so that circulating currents associated with different Hall voltages in each layer can be neglected. It is important that the value of α be known accurately, which should be possible from the mask dimensions used to fabricate the devices. To employ the technique, one requires high enough fields such that μB at least approaches unity. Thus, for layers with $\mu = 10$ m^2/Vs, a field of only about 0.1 T would suffice, whereas for layers with $\mu = 0.1$ m^2/Vs, a superconducting magnet producing fields up to 10 T would be needed.

C. Experimental Work and Results

Four detectors have been characterized, some with multi-elements, to demonstrate the usefulness of this technique and determine the properties of the accumulation layers. An illustration of a typical detector element is shown in figure 3.2. Typical dimensions are a length of 50 to 100 μm, a width of about 50 μm, and a thickness of 6 to 8 μm. The detectors were placed in a cryostat with the temperature varied between 6 and 80 K. In this temperature range intrinsic carriers can be neglected. A superconducting magnet was used to obtain a magnetic field of up to 7 T. The voltage was measured across the detector at a fixed current of 100 μA as a function of B to obtain the resistance. The sample geometries were supplied by the manufacturer and checked with an optical microscope. Data were obtained on a digital oscilloscope and transferred to a computer for analysis.

The contacts are made to the top of the detectors with the current spreading down into the multilayer structure. At $B = 0$, much of the current flows through the bulk, which has a nominal electron density of 3×10^{14} cm^{-3} and a mobility of 25 m^2/Vs at 77 K. Even higher mobilities occur at 6 K. As the magnetic field increases, the current eventually flows primarily through the top accumulation layer because the bulk magnetoresistance rises rapidly with field as a result of its high mobility. This prevents current from flowing in the bulk and bottom accumulation layers. It is not possible to fit the bulk or bottom accumulation layer because of the current spreading and the circulatory currents associated with the different Hall voltages of each layer. Therefore, values have been obtained from the fits only for high enough fields that current is limited primarily to the top accumulation layer. Some leakage current could travel along the passivated sides of the sample, but it is estimated to be small. The equation to be solved for the total resistance of the top accumulation layer at sufficiently high B is $R_T(B,\alpha) = R_c + R(B,\alpha)$ where R_c is the contact resistance. A nonlinear-least-squares fit is used to extract the parameters R_c, N, and μ, where $N = nt$. Contact resistance, an unavoidable aspect of two-terminal measurements, can in principle be found from these fits. However, to reduce the number of unknowns, it may be possible to estimate it from other measurements.

Three different types of passivation were studied with this technique. The first, type I, is a typical anodically oxidized detector, while the second and third, types II and III, respectively, employ
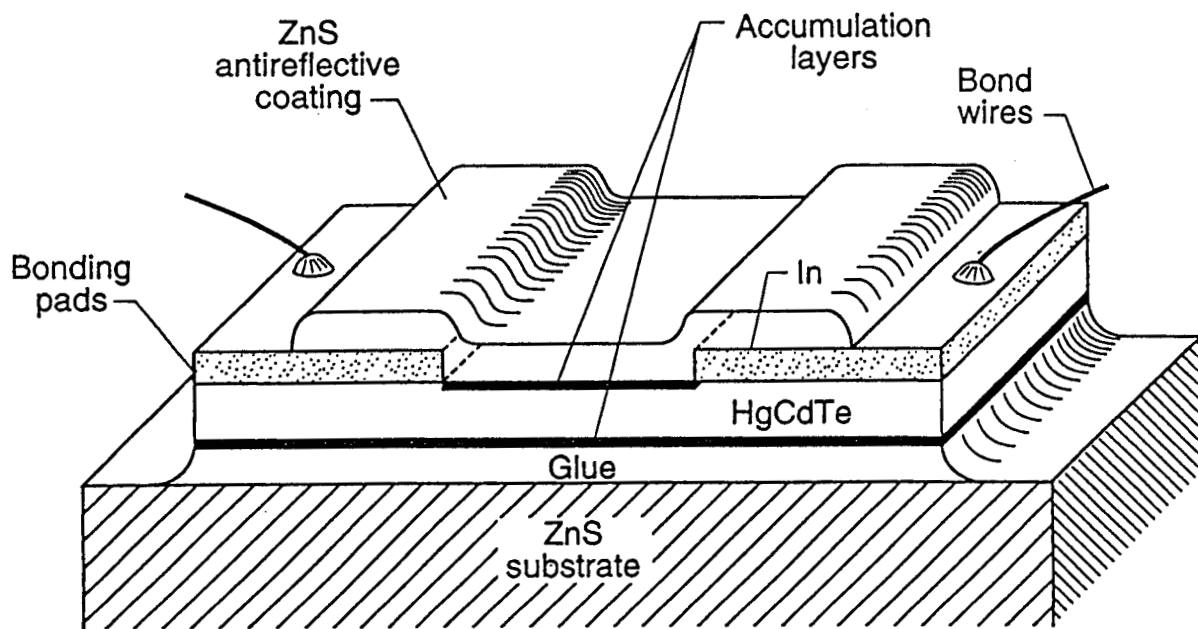
Figure 3.2 Illustration of a typical photoconductive HgCdTe infrared detector.

proprietary passivation techniques that have a smaller surface conductance and are used when high responsivity is required. The dependences of the detector resistance on magnetic field for type I and type II detectors at 6 K are shown in figure 3.3 along with the fits of the high-magnetic-field portions. Note how different the curves are for the two detector types. An expansion of the data at low field is shown at both 6 and 77 K in figure 3.4. It is interesting that the temperature dependence of the mobilities of the two types is opposite in size between 6 and 77 K. For the type I detector, which has $\alpha = 1.21$, the resistance has a nearly linear dependence once the bulk-related contribution to the total conduction is greatly reduced above about 0.1 T. The type II detector, on the other hand, which has $\alpha = 2.04$, shows bulk-related curvature up to nearly 2 T. The bulk remains relatively more conducting to higher fields in this detector because of its larger value of α and the higher zero-field resistance of its accumulation layer. Thus, the resistance-vs.-field data above 0.1 T for type I detectors and above 2 T for type II detectors have been fit because conduction is then mainly through the top accumulation layer.

The magnetoresistance of the third type of detector, type III, is shown in figure 3.5 at 6 K along with the fit. It has $\alpha = 1.2$ and resembles the dependence of the type II detectors. The fit was made above 4 T so that the current flows primarily through the top layer. An expansion of the magnetoresistance at low field is shown in figure 3.6 at 6 and 77 K. The magnetoresistance of a different multi-element type III detector is shown in figure 3.7. It has $\alpha = 1.33$ and is similar to the other type III detectors. The elements are all different, and this shows that variations in accumulation-layer properties can occur across the elements of a detector. Specific numerical comparisons are made below. Reduction in these variations can lead to improved pixel performance and better signal-to-noise ratios.

The results of the nonlinear-least-squares fits to the data at 6 and 77 K are shown in table 3.1. The average deviation of the fits from the fitted data was less than 1%. A constant value of 10 Ω was used for the contact resistance. This value was found by comparing two type II detectors with different lengths at 6 K at $B = 0$ and agrees with the manufacturers' estimates. The value of R_c could not be determined by the fit because it is small compared with the fitted resistance values. Manufacturers' values at 77 K for the product of the carrier density and mobility independently determined by multilayer Hall measurements on fully processed wafers formed by both processes are given in table 3.1 [3.10,3.11]. The μN product was found to be nearly constant over their ranges of measured densities for each type of detector. Better agreement was found for the type II detector than for the type I detector. The reason is that the value of α is near unity for the type I detector, and the layer resistance becomes nearly independent of μ for $\mu B \gg 1$. The value of the carrier density, however, is easily extracted and agrees well at both temperatures. The values of the carrier densities for both detectors were also within the range of the manufacturers' estimates. Thus, it has been shown that this technique can determine N and μ for the top layers of these infrared detectors.

The type III detectors have top accumulation layers with as low mobility as the type II detectors. However, their electron densities are between a third and a half of the type II detectors. Thus, the leakage through the accumulation layers of the type III detectors as evident by the $N\mu$ product is less than for the type II detector, which have in turn less leakage than the type I detectors. The effectiveness of the accumulation layer in repelling minority carriers, as evident by the value of N, is best for the type II detectors, next best for the type III detectors, and worst for the type I detectors. Thus, both proprietary processes provide accumulation layers with improved performance over the anodic oxidation process. This technique is seen as providing the analysis necessary for understanding why these processes are better.
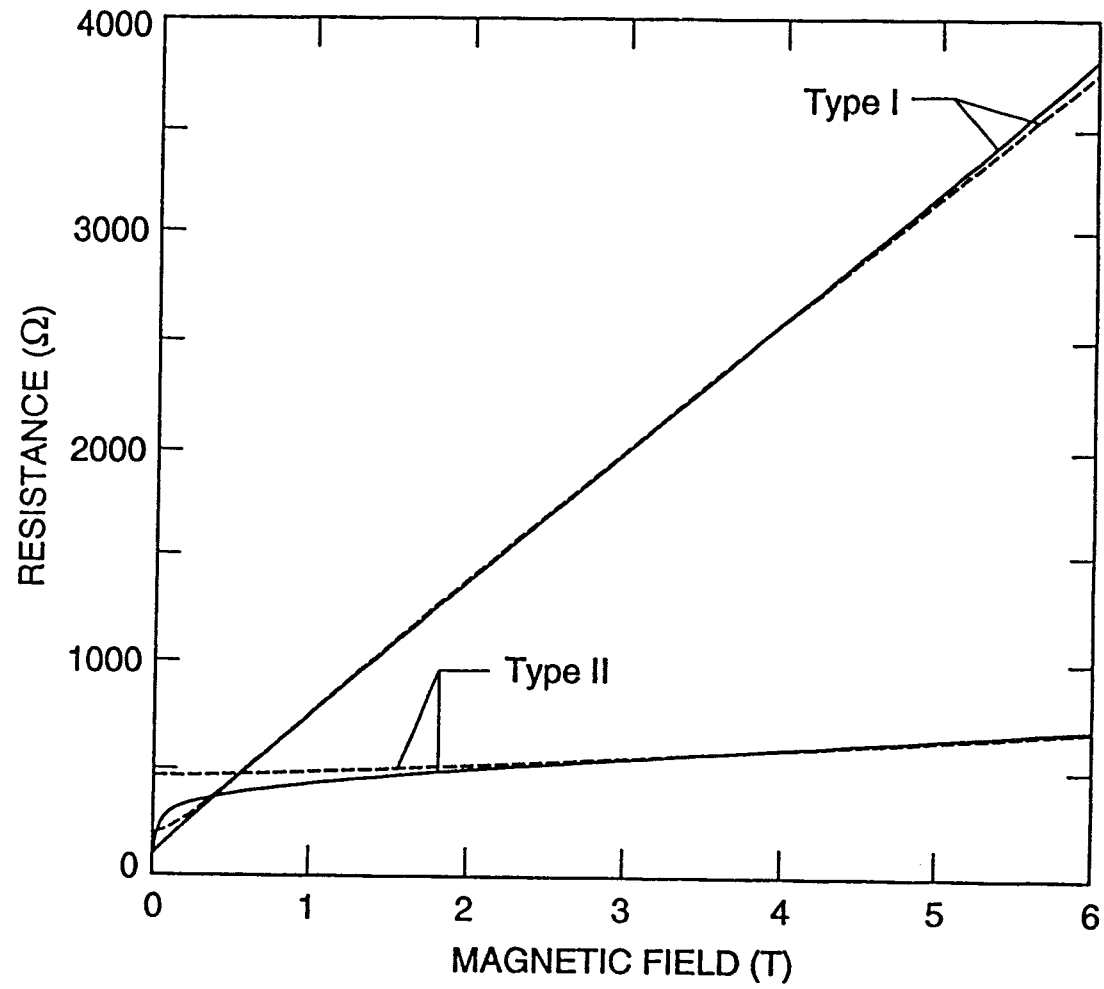
Figure 3.3 Two-terminal transverse magnetoresistance as a function of B for a type I passivated detector and a type II passivated detector at 6 K (solid). Dashed lines show fit to high-field behavior.
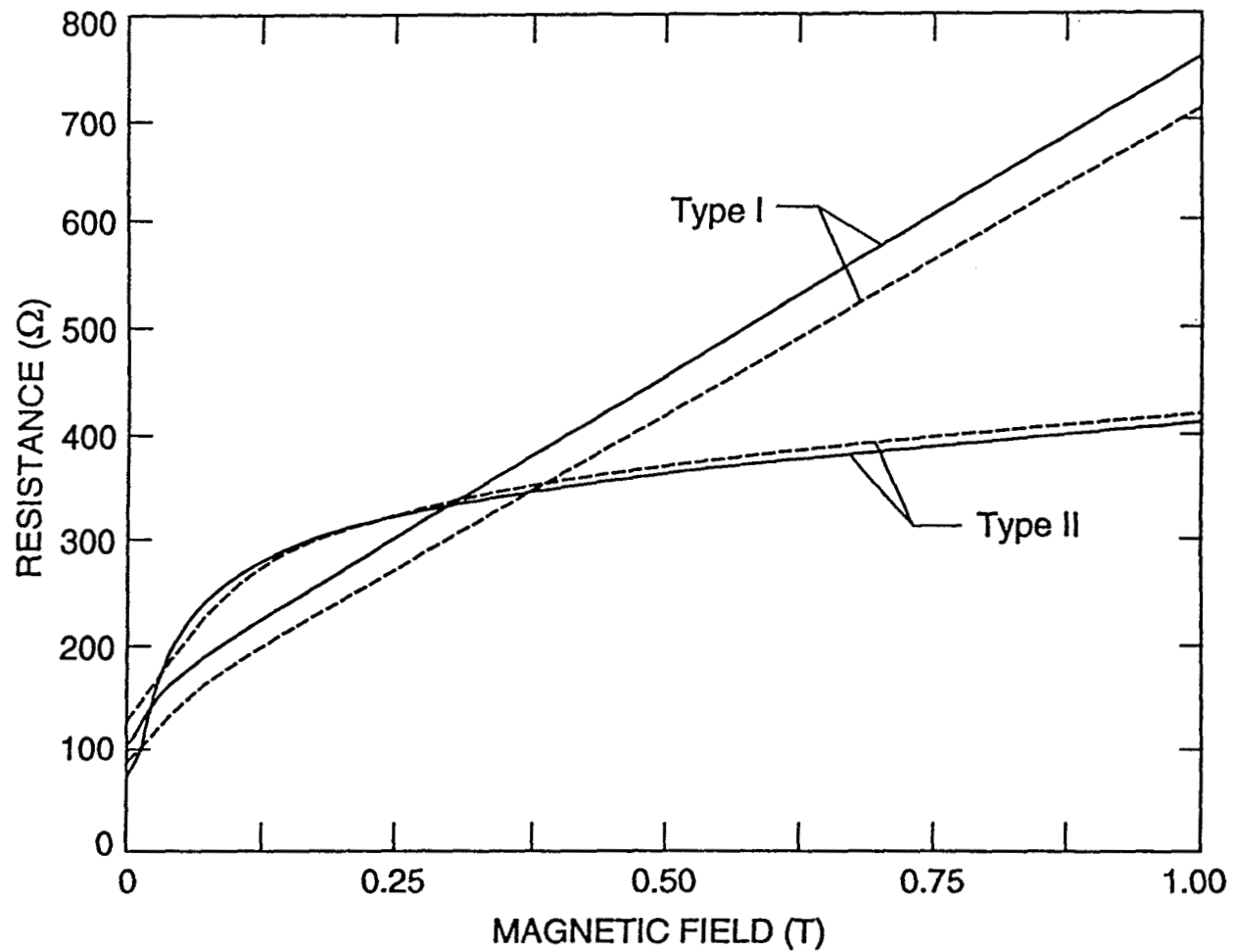
Figure 3.4 Expanded scale of the low-field behavior of the transverse magnetoresistance as function of B for type I and type II detectors at 6 K (solid) and 77 K (dashed).
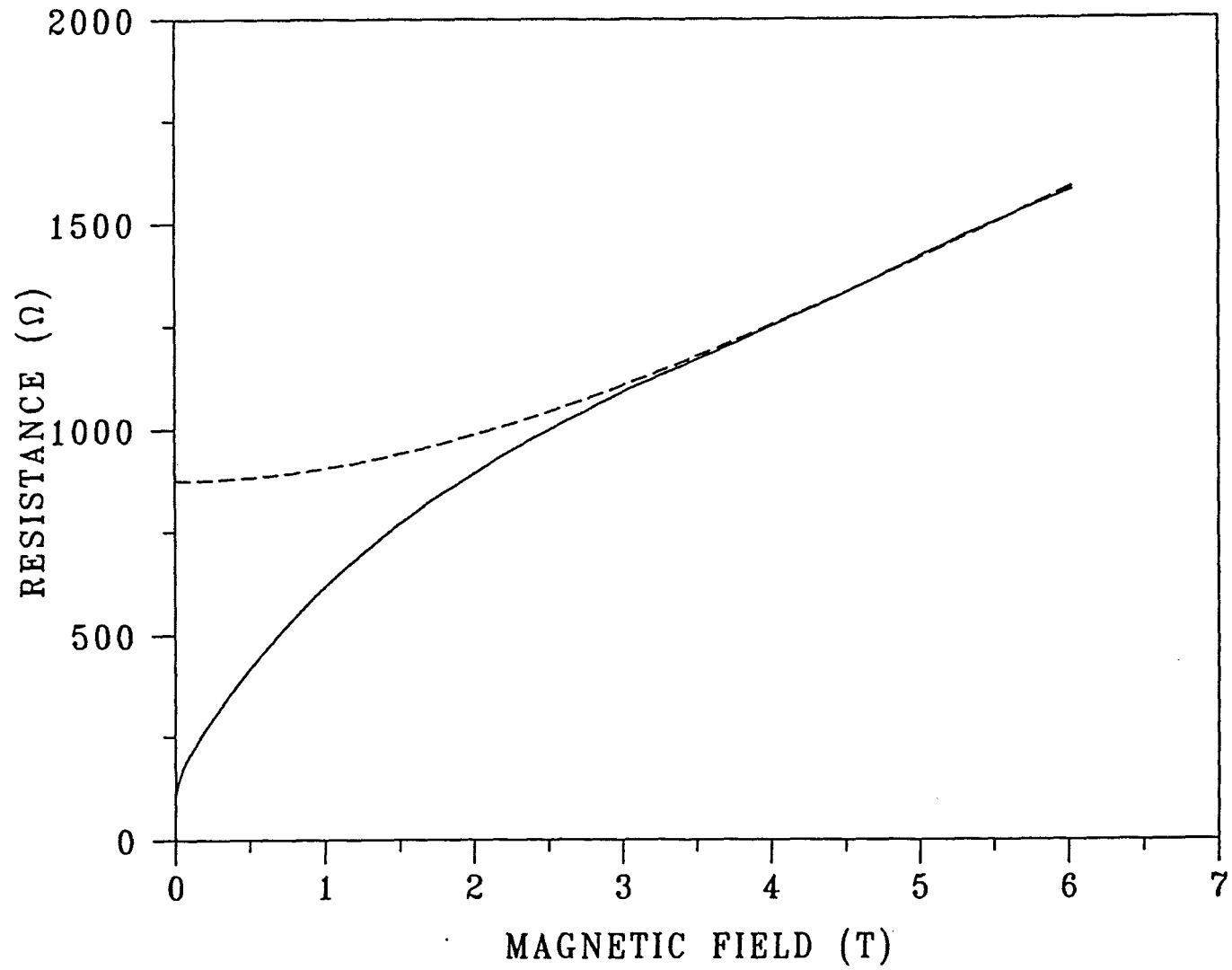
Figure 3.5 Two-terminal transverse magnetoresistance as a function of B for a type III passivated detector at 6 K (solid). Dashed line shows fit.
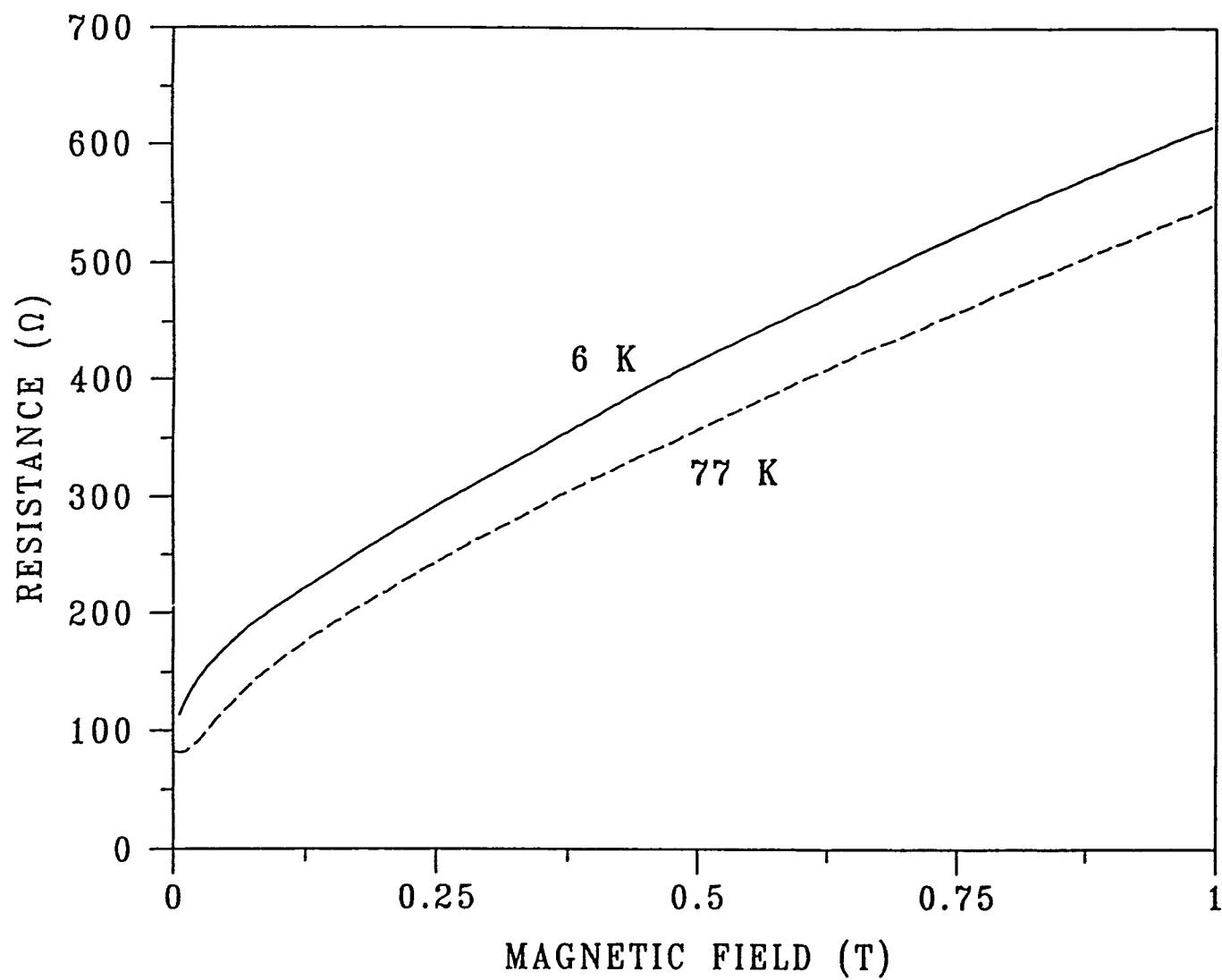
Figure 3.6 Expanded scale of the low-field behavior of the transverse magnetoresistance as a function of B for a type III detector at 6 and 77 K.
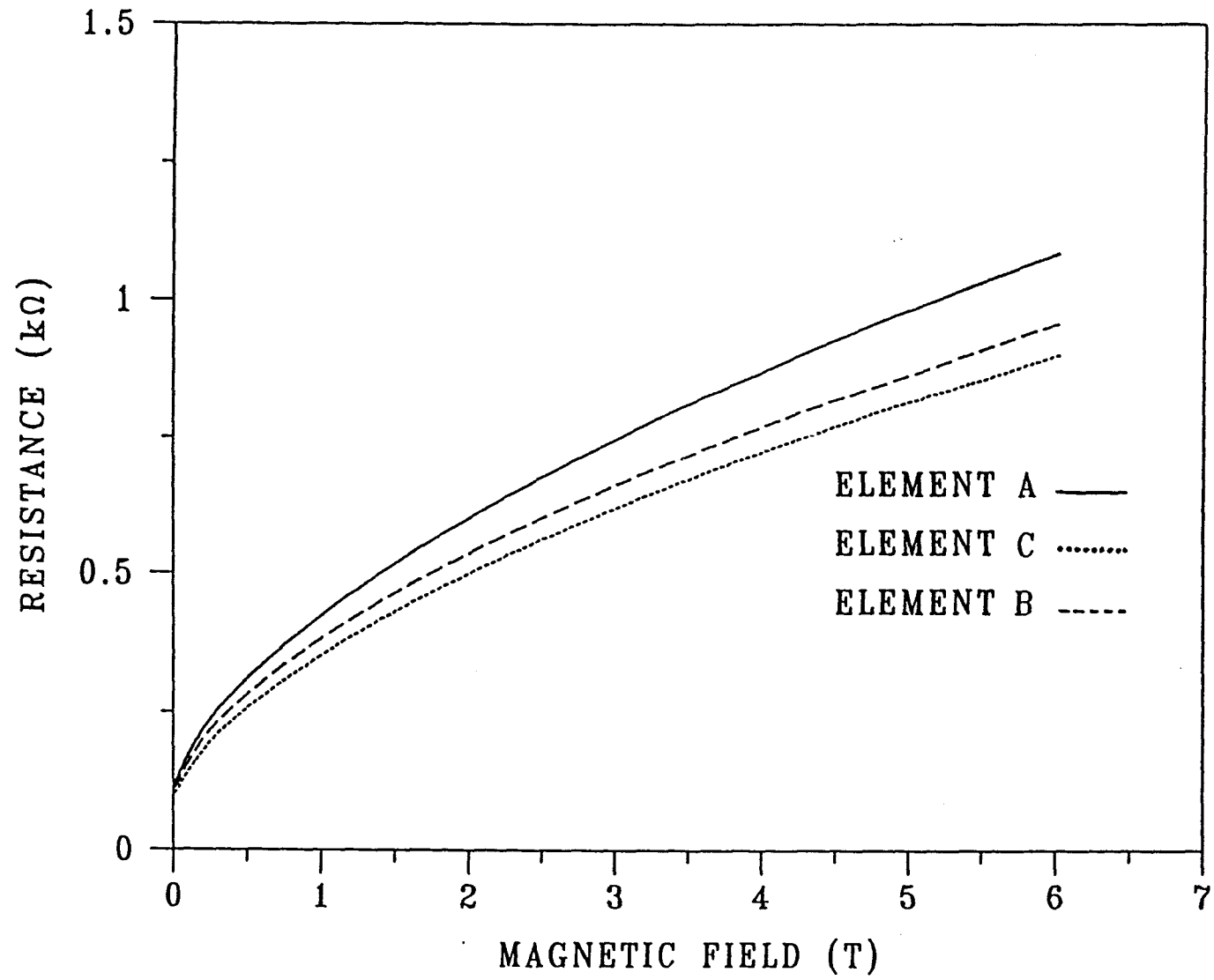
Figure 3.7 Two-terminal transverse magnetoresistance as a function of B for a multi-element type III detector at 6 K.

TABLE 3.1 Parameter Values Extracted by the Transverse Magnetoresistance Method. Values for the top accumulation layer of n-type HgCdTe PC infrared detectors passivated by three different types of processes and manufacturers' estimates are denoted by subscript "m." For multi-element detectors, element identification is denoted by a trailing letter.

Detector Element	Type	T(K)	$N(m^{-2})$	$\mu(m^2/Vs)$	$N\mu(1/Vs)$	$N_m\,\mu_m(1/Vs)$
2I6	I	6	$9.0 \times 10^{15}\ (\pm1\%)$	$4.2\ (\pm10\%)$	$3.8 \times 10^{16}\ (\pm10\%)$	
2I6	I	77	$9.0 \times 10^{15}\ (\pm1\%)$	$4.9\ (\pm10\%)$	$4.4 \times 10^{16}\ (\pm10\%)$	$5.0 \times 10^{16}\ (\pm10\%)$
3II1A	II	77	$1.1 \times 10^{17}\ (\pm2\%)$	$0.25\ (\pm4\%)$	$2.8 \times 10^{16}\ (\pm4\%)$	$3.0 \times 10^{16}\ (\pm10\%)$
3II1B	II	6	$1.1 \times 10^{17}\ (\pm2\%)$	$0.26\ (\pm4\%)$	$2.9 \times 10^{16}\ (\pm4\%)$	
3II1B	II	77	$1.1 \times 10^{17}\ (\pm2\%)$	$0.25\ (\pm4\%)$	$2.8 \times 10^{16}\ (\pm4\%)$	$3.0 \times 10^{16}\ (\pm10\%)$
3II1C	II	6	$9.4 \times 10^{16}\ (\pm2\%)$	$0.30\ (\pm4\%)$	$2.8 \times 10^{16}\ (\pm4\%)$	
3II1C	II	77	$9.8 \times 10^{16}\ (\pm2\%)$	$0.28\ (\pm4\%)$	$2.7 \times 10^{16}\ (\pm4\%)$	$3.0 \times 10^{16}\ (\pm10\%)$
2III7	III	6	$3.4 \times 10^{16}\ (\pm4\%)$	$0.26\ (\pm10\%)$	$8.8 \times 10^{15}\ (\pm10\%)$	
2III7	III	77	$3.2 \times 10^{16}\ (\pm4\%)$	$0.28\ (\pm10\%)$	$8.9 \times 10^{15}\ (\pm10\%)$	
2III2A	III	6	$5.5 \times 10^{16}\ (\pm4\%)$	$0.23\ (\pm10\%)$	$1.3 \times 10^{16}\ (\pm10\%)$	
2III2A	III	77	$5.0 \times 10^{16}\ (\pm4\%)$	$0.26\ (\pm10\%)$	$1.3 \times 10^{16}\ (\pm10\%)$	
2III2C	III	6	$6.7 \times 10^{16}\ (\pm4\%)$	$0.23\ (\pm10\%)$	$1.5 \times 10^{16}\ (\pm10\%)$	
2III2C	III	77	$6.1 \times 10^{16}\ (\pm4\%)$	$0.26\ (\pm10\%)$	$1.6 \times 10^{16}\ (\pm10\%)$	
2III2B	III	6	$6.3 \times 10^{16}\ (\pm4\%)$	$0.23\ (\pm10\%)$	$1.4 \times 10^{16}\ (\pm10\%)$	
2III2B	III	77	$5.8 \times 10^{16}\ (\pm4\%)$	$0.26\ (\pm10\%)$	$1.5 \times 10^{16}\ (\pm10\%)$	

A comparison of elements A, B, and C of detector 2III2, shown in figure 3.7, with the measured responsivities, shows how the accumulation-layer properties correlate with performance. At 77 K the inverse ratios of the densities and μN products of the elements B and C to element A are 0.86 $\pm$ 0.03 and 0.82 $\pm$ 0.03, respectively, while the corresponding ratios of the responsivities are 0.91 $\pm$ 0.01 and 0.82 $\pm$ 0.01, respectively. The uncertainties given here are from the residuals resulting from the DATAPLOT fits. The agreement is good, which shows the controlling effect of the top accumulation layer.

In order to obtain information about the bulk, bottom accumulation layer, and contact resistance, the top layer conductance determined from the fit can be subtracted from the total conductance at $B = 0$. Variations in this conductance difference as well as in the top-layer conductance from detector to detector can be used to determine when the process is not in control. The reasons for the variations can then be diagnosed. For example, the conductances of elements A, B, and C of detector 2III2 at $B = 0$ and at 77 K are 8.33×10^{-4}, 9.01×10^{-4}, and 9.80×10^{-4} S, respectively. Subtracting the respective top-layer conductances leads to the remaining conductances of elements A, B, and C which are 6.77×10^{-3}, 7.21×10^{-3}, and 7.88×10^{-3} S, respectively. If the bulk conductance is the same for all three elements, these variations would be due to the bottom accumulation layer.

D. Conclusions

In conclusion, a practical magnetoresistance method has been demonstrated for measuring the carrier density and Hall mobility of a semiconductor layer by using only a two-terminal configuration, a situation applicable to a number of industrially relevant devices. An equation has been fit to published calculations of this phenomenon so that it can be applied to a wide range of rectangular geometries. Application of this technique to four GOES HgCdTe PC infrared detectors gives results which are in excellent agreement with previous Hall data, showing the validity and usefulness of this method. The variation in the electron density of the top accumulation layer of three elements of a multi-element detector was shown to correlate with the responsivity. The reduced leakage and increased electron density of the type II and type III processes are shown to be the reasons for their improved performance characteristics. This technique can be used in the future by the detector manufacturers to characterize their processes and thereby improve detector performance.

PART II - OTHER CHARACTERIZATION STUDIES

4. BONDING, METALLIZATION, AND PACKAGING FOR GOES AND TIROS INFRARED DETECTORS

A. Overview and Rationale[1]

Evaluation studies of GOES HgCdTe detector packaging were made at NIST during FY 1991 and 1992. Problems that can reduce the yield (increasing the cost) and/or reliability of the devices were found. Several such problems were documented in earlier reports (see NISTIR 4687, September 1991) and in NOAA program reviews. Others are retained in files of NIST's scanning electron microscope (SEM) studies of these devices. Therefore, work was done in FY 1992 in the area of detector packaging to improve the above situation and, hopefully, to prevent surprise problems from arising that can delay launch dates and necessitate retrofits or otherwise increase NOAA satellite costs. The objectives and rationale of the NIST packaging work during FY 1992 are given below.

1) Develop a set of Recommended Practices (guidelines) for packaging of NOAA space sensors (detectors). This will include recommendations for reliable wire bonding (interconnections), package electroplating, device metallization, and molecular cleaning methods.

   Circulate the Recommended Practice to appropriate detector contractors and other interested organizations for their comments. Their comments will be evaluated, negotiated, and incorporated in the final document. This document will be given out to appropriate contractors for implementation on future NOAA infrared sensors.

2) Request the detector manufacturers to submit examples of detectors (electrical or optical rejects) mounted in packages designed for incorporation in NOAA satellites. NIST will then examine (with SEM and/or other appropriate analytical methods) for compliance with the above guidelines in (1), with emphasis on potential reliability and yield enhancement. If problems are found, NIST will then:

   a) Assist sensor (detector) contractors with necessary information, visits, and training, so they can package devices in conformance with these guidelines.

   b) Serve as packaging and materials science consultants for any problems that may arise in NOAA infrared detector manufacturing, and present training seminars on reliable packaging.

3) Many wire bond yield and reliability problems are traceable to the lack of molecularly cleaned bonding surfaces. Studies will be carried out to establish the best cleaning methods that are compatible with the normal HgCdTe detector packaging methods.

---

[1] Large integrated circuit (IC) packaging houses make hundreds of thousands of devices and millions of wire bonds per week. They can therefore employ a number of engineers who are experts on bonding. However, infrared sensor companies make so few bonds that no one engineer can specialize in this area; thus such companies may have more bond yield and/or reliability problems than the IC companies.

4) Cooperate with other NIST HgCdTe detector studies, such as preparing samples for low temperature Shubnikov-de-Haas and other measurements.

B. Accomplishments

A first version of the "RECOMMENDED PRACTICE FOR THE WIRE BONDING AND METALLIZATION USED IN RADIATION DETECTORS PREPARED FOR USE IN GOES, TIROS, AND OTHER SPACECRAFT" was written and circulated to eight organizations and, in some cases, to several individuals within an organization. After receiving responses (several did not respond) when questions remained, those individuals were contacted for resolution. The final document includes references to ASTM as well as to various Military Class "S" (space) specifications and standards. The **"Recommended Practice" document** is in Section C. Because of some late responses there was not time to recirculate the new document for final comments. Readers are urged to make any such comments as soon as possible after receiving this report. If significant changes are suggested and made, then the **"Recommended Practice"** will be revised and republished later as final. The document was also presented to a standards organization, ASTM Subcommittee F-1.07 (the wire bonding committee) at its meeting on January 28, 1993 for additional comments from a different but very knowledgeable audience.

A total of six visits were made to three GOES and TIROS infrared detector manufacturers during FY 1992. The first visit to each site was made to evaluate their production lines and processes. Later visits were made to help them with the packaging of their detectors including, in one case, a 2.5-hour seminar on wire bonding and the reliability of the metallurgical systems used in packaging HgCdTe detectors. Over 30 people attended that seminar. A more informal, hour-long presentation was made at another company where six/seven engineers and management personnel attended. Extra time was spent in their packaging laboratories discussing equipment, etc. A study was made of detectors from one manufacturer and several defects were found (the results were presented at a GOES project review at NASA Goddard on July 10, 1992). This information, with proposed solutions, was also fed back to the manufacturer to help them improve their product.

Many wire-bond yield and reliability problems are traceable to molecular-level contamination of the bonding surfaces resulting from handling, epoxy outgasing residues, etc. The high-reliability microelectronics hybrid industry routinely uses oxygen and argon plasma or ultraviolet-ozone (UV-ozone) cleaning procedures to greatly enhance their wire-bond yield and reliability. The HgCdTe detector industry has been afraid to use such cleaning methods before bonding because of possible damage to the detectors or to their surface coatings. These concerns have never been documented, but there is some possibility that oxygen plasma cleaning could attack the antireflection coatings. Therefore, NIST proposed to study the effects of UV-ozone cleaning on HgCdTe detectors. This work was planned to determine whether the cleaning had any effect on the sensitivity and noise of the detectors, as well as any effect on the various optical absorptive coatings that may be used inside the housing (but not on the device).

Preliminary UV-ozone cleaning experiments were carried out at NIST on available detectors and absorptive coatings. No physical damage was observed. However, there was no equipment available at NIST to evaluate any possible optical or electrical damage to the detectors. Thus, for these additional measurements, it was necessary to visit two cooperating detector manufacturers and perform the experiments there. For this, the UV-ozone cleaning equipment was hand-carried [on airplanes] to the manufacturers' locations. Previously tested detectors were irradiated in the NIST

equipment at their plants, but retesting for electrical and optical properties had to be scheduled for a later time. One organization has reported its first set of measurements made within one week of irradiation. The data indicate that the detector noise measurements show no change due to UV-ozone treatment. However, the infrared sensitivity was found to decrease in all samples by an average of 11%. The organization plans to remeasure the detectors in 3 months to see if this decrease is temporary or permanent. If temporary it should be removed by minimal heat treatment (perhaps an hour at 80 °C). However, if the sensitivity loss is permanent, then another method of cleaning will have to be investigated. Cured black light-absorbing paint was irradiated at NIST, and no damage to its light-absorbing properties was detected.

In addition to the possible detector damage studies, other experiments were performed to show the effects of cleaning on wire bondability at the manufacturers' plants. Problems immediately arose at one manufacturer because the intended bonder was in use and another had to be substituted. This bonder was not in good condition and did not make reproducible bonds (the work-holder was not flat, the bonding tool moved laterally during bonding, etc.) Also, some of experiments that were performed appeared to show that cleaning actually decreased bondability (something that has not been observed before and is presumed to result from the bonder problems). The organization planned to obtain their own UV-ozone cleaner and rerun the experiments later. Other problems relating to peeling metallization were found at another manufacturer. Thus, in order to reach any conclusion, both of these experiments must be continued.

Ten special HgCdTe infrared detectors received from manufacturers were prepared and mounted in low-temperature carriers for Shubnikov-de-Haas and other liquid-helium temperature measurements. New removable adhesives that would tolerate these low temperatures had to be found, and special carriers (packages) were made. Several repairs to soldered or wirebonded interconnections were affected. In addition, various other techniques such as microsoldering had to be developed.

C. Recommended Practice for Wire Bonding and Metallization Used in Radiation Detectors Prepared for Use in GOES, TIROS, and Other Satellites

1) The bonding wire should be made of the same metal as the bond pads on both the detector and the package. This is normally gold. If there is a difference between the metallization on the chipside and the packageside, then the wire material will match that of the chip-side bond pads.
   a) Electroplated (or vapor deposited, etc.) gold [metal] should be pure, soft and uniform in optical appearance and thickness. It should contain <1 ppm of thallium and have <50 ppm total impurity content. The hardness should be <80 Knoop. Any unusual surface appearance should be investigated with appropriate magnification (100x optical microscopy or up to 400x for a scanning electron microscope). If blistered, cracked, or peeling, it should be further investigated (see Mil-Std-883, Method 2010.10, ¶ 3.1.1.4). It is clearly rejectable if a metal-deposition-defect is in the bond pad area and is equal to or greater than one quarter the area of the bond nugget and positioned so that the bond must be placed on top of it. The same condition should be applied to an external soldering area (substituting solder in place of bond nugget). It is also of concern if the metal defect is elsewhere, since this indicates that the metallization process is out of control and may therefore produce defects in critical areas on other packages in the same lot that may not undergo inspection.

2) Bond pads should not be placed on brittle, crater-prone material such as HgCdTe. Special designs involving ($\geq 0.5\mu$m) under-layers of hard metals such as titanium and/or tungsten on

brittle materials may be acceptable if demonstrated to prevent bond cratering. (Such layers have long been used to prevent cratering in silicon and gallium arsenide devices. For HgCdTe devices, a hard underlayer thickness of 0.5 to 1 μm is a good starting point, followed by $\geq 1\mu$m of gold.)

3) The bond pad metal must be clean and uniform to be wire bondable with a high yield.

   a) Cleaning of the open, packaged, detector should be done (with plasma (O_2 or Ar) or UV/Ozone) within 2 hours of bonding, if such cleaning processes do not damage the device. Vapor degreasing has been used, but it is not as effective as one of the molecular cleaning methods above. (The recommended method of cleaning HgCdTe detectors before bonding is currently being investigated by NIST in cooperation with two detector manufacturers.)

   b) Any evidence of scratching the detector or package bond pad metallization, either during handling or to mechanically clean the surface intentionally in order to enhance bondability, should be questioned and will be cause for rejection if more than 25% of the bond pad area is disturbed (see Mil-Std-883, Method 2010.10, ¶ 3.1.1.1.h). Probe marks and **carefully removed** test bonds, are exempt unless their remains are so large as to interfere with final bonding.

   c) Any evidence of rebonding, either lifts or residual pieces of earlier bond attempts (other than necessary test bonds), should also be questioned. Any of these evidences may be cause for rejection or performing a nondestructive wirebond pull test to verify the bond integrity if they interfere with the final chip-to-package bonding. (Note: Use of the nondestructive pull test will raise the loop height, and may result in the wire interfering with a closely placed lens or some other package height constraint.)

4) Bonding requirements and methods for gold-gold interfaces

   a) Although gold-gold bonds can be made reliably at room temperature, the bonding window is narrow and any surface impurities will reduce the bond yield significantly. The highest bond yield and the broadest bond parameter window occurs when the interface is heated. Therefore, when using ultrasonics, it is also desirable to apply work-stage heat or use a heated bonding tool. The latter must be 200 - 300 °C to be helpful. In general, use the highest bond interface temperature possible (up to 300 °C) considering the thermal limitations of the device, epoxies, and other packaging materials. Even a 75 °C heated substrate improves the bondability and reliability of a gold-gold bond.

   b) The wedge bonding of gold wire to gold pads normally requires the use of a special gold bonding tool, which will have a cross-groove and/or a roughened surface.

   c) Wire bonding takes place at a higher bond yield if the surfaces are flat (perpendicular to the axis of the bonding tool). Round or angled surfaces reduce the bond yield and should be avoided. If they cannot be flattened, then special care should be taken, such as tipping the substrate, bonding straight along the highest portion of a cylindrical surface, etc., in order to maximize the bond yield.

5) The bond appearance should be normal.

   a) Ultrasonic wedge bonds should not be over- or under-deformed (the range for reliable gold wedge bonds is between *approx.* 1.5 to 2.5 wire diameters and 1.5 to 2.0 wire diameters for aluminum wire bonds). There should be no evidence of smearing, either on the bond itself or on the adjacent bond pad area. (When gold wire is wedge bonded to gold at low temperature (< 100 °C), the bonding window is narrow and bonds with low deformation (< 1.5 wire diameters) may not be reliable.)

   b) The bond heels should not be cracked, and particularly, if a cross-grooved bonding tool was used for gold bonding, both the front and rear of the bond should be normal. (For example, the front portion, in front of the groove, should be neither separated from the body, over- nor under-deformed, nor be missing.)

6) Wedge bonds should be tested using an appropriate statistical sampling method (e.g., MIL-M-38510J, Appendix B) using the pull test for machine setup and evaluation. Electrical reject samples may be used for setup purposes, and several bonds may be placed on one pad if there is room. Under some conditions, the nondestructive pull test may be used on completed devices, where critical verification is necessary. Use class "S" requirements in the test methods below (if applicable).

   a) Use Mil-Std-883, Method 2011 for the destructive pull test.

   b) Use Mil-Std-883, Method 2023 for the nondestructive pull test.

   c) Use ASTM F 1269-89 (Ball Shear Test) if ball bonds are used.

7) Fine gold wires (≤ 75 μm diameter) must not be soldered, but must be welded by a standard method used in microelectronics (thermosonic, ultrasonic, split-electrode electrical discharge, etc.).

8) This Recommended Practice may also be applied to bonding in non-HgCdTe types of detectors such as bolometers, etc.; in that case the same metal (gold in 1) may be omitted, and either the pad and/or the wire may be aluminum. (If the wire is aluminum, then no bonding advantage is obtained from using special bonding tools.)

   a) On occasion, conductive polymers (e.g., gold- or silver-filled epoxy) are used instead of metallurgical welding to obtain electrical conductivity. This presents many complex material choices and cannot be addressed by this Recommended Practice. (For example, silver-filled epoxy should not be used to electrically connect wires to aluminum surfaces, but under some circumstances may be acceptable for use at cryogenic temperatures.)

D. Glossary

HgCdTe is mercury cadmium telluride, a semiconductor material used for far-infrared detectors. This material is very brittle and has a low fracture toughness. It craters easily. It is typically used at cryogenic temperatures ≤ 100 K.

Cratering, crater-prone. Cratering refers to crystallographic damage in a semiconductor underneath a bond. It can range from microscopic damage to large divots of the semiconductor that are pulled up during bonding or in a pull test. Brittle materials with low fracture toughness crater easily during bonding, and HgCdTe is such a material.

Military Standards: Mil-Std-883. This is the "Test Methods and Procedures for Microelectronics." The specific version referred to in this Recommended Practice is 883D, 15 November 1991. Although it was not specifically designed for spacecraft detectors, its class "S" provisions as well as its bond pull test requirements are used almost universally for other parts of spacecraft electronics. Only those parts applicable to this Recommended Practice are cited. MIL-M-38510. This is "Military Specification, Microcircuits, General Specification For" This is cited for its statistical sampling methods.

Yield is used in this document to mean the fraction of acceptable wire bonds produced in the manufacturing process.

E. Typical Bonding Characteristics and Appearance of Plated Gold Films

(Not a part of the Recommended Practice--for information only)

(1) Gold films that bond well and are reliable:
   a)   Are pure yellow in color.
   b)   Are uniform, matte, and lusterless in appearance.
   c)   Are smooth and free from pits, blisters, or other blemishes.
   d)   Are soft (<80 Knoop), ductile, and dense.
   e)   Have <50 ppm of total impurity content.
   f)   Have <1 ppm thallium and low hydrogen content for Al wire bonding.
   g)   Have a wide bonding parameter window.

(2) Gold films bond poorly and/or are not reliable if they:
   a)   Appear dark, have large nodules, or are very bright.
   b)   Shed minute particles on handling.
   c)   Have a lenticular or columnar structure and/or high porosity.
   d)   Have a high hydrogen or thallium content and/or >50 ppm total impurities.
   e)   Are hard, nonductile, and/or have high internal stress.
   f)   Give poor corrosion protection.
   g)   Have a narrow bonding parameter window.

(3) A pragmatic test to evaluate gold films for aluminum ultrasonic bonding: make aluminum bonds to the film, bake 300 °C for 1 h, and reject if bond lifts in pull test. (This is based on Mil-Std-883, Method 5008, ¶ 3.5.3.3). This is a destructive test and is often used to screen packages or films before acceptance from a vendor. It would not be used on a completed detector.

5. SEMICONDUCTOR ELECTRONIC TEST STRUCTURES: APPLICATIONS TO INFRARED DETECTOR MATERIALS AND PROCESSES

A. Introduction

Test structures are microelectronic devices which are fabricated by the same processes used to manufacture semiconductor electronic products, and that are used to measure selected material, process, or tool parameters by means of electrical tests. Properly designed test structures can be used to evaluate semiconductor materials, to determine and monitor process-centering parameters, to measure critical device and circuit parameters (which can be input to device models), to identify and quantify yield limiting defects, and to measure processing tool performance.

Test structures are essential tools for fabrication process development and process maintenance of silicon integrated circuits (ICs) and gallium arsenide monolithic microwave integrated circuits (MMICs). However, test structures have not been as widely applied in the process development and manufacture of infrared detectors, nor have the ways in which they are used been well documented in the open literature. Considering the substantial impact of test structures on other semiconductor products, the current state-of-the-art applications of test structures to HgCdTe-based IR detectors have been reviewed. The study had several goals:

1) To communicate and encourage application of the substantial experience gained with test structures in Si and GaAs to HgCdTe IR detectors;

2) To document test structures, appropriate to IR detector technology, so that they could be more readily assembled into test chips;

3) To determine new ways in which test structures could be applied to improve HgCdTe uniformity, to increase detector yield, and to enhance performance of detectors;

4) To identify test structures and measurements to complement and correlate with the Shubnikov-de Haas and other magnetotransport measurements.

To meet the goal of communicating to the IR detector community, the results of this study were presented at the Measurement Techniques for Characterization of MCT Materials, Processes, and Detectors Workshop in Boston, Massachusetts, on October 16, 1992. A publication entitled: "Review of Semiconductor Electronic Test Structures with Applications to Infrared Detector Materials and Processes" has appeared in the workshop proceedings published in *Semiconductor Science and Technology* in 1993 [5.1]. This publication is the most complete review of test structures applied to IR detectors and contains suggestions on how to improve IR detector process control, yield, performance, and reliability through the intelligent application of test structures. The complete paper is reproduced in Appendix B.

A major element of this study was a comprehensive review of specific test structures used by the IR detector industry. A thorough review of the literature concerning applications of test structures to IR detectors was conducted. Details of device design and measurement methodologies were also considered. In addition, experts in the electrical characterization of IR detector materials and devices were consulted. A site visit to Loral Infrared and Imaging Systems was conducted; other consultations took place via telephone. A variety of reasons were suggested for the underutilization

of test structures with IR detectors:

1) The relatively small numbers of devices required and the nature of the market have not demanded large yields to satisfy product demand or to assure profitability. However, even if production goals can still be satisfied with a low-yield process, the long-term reliability of devices fabricated with a low-yield process could be compromised.

2) The need to test devices at low temperatures and as a function of irradiation has often been most easily satisfied by packaging devices before any testing. Consequently, development and use of low-temperature automated probe stations to acquire statistically significant amounts of data at the wafer level and before packaging (a major application of Si and GaAs test structures) were not vigorously pursued.

3) The perceived need to package devices before test resulted in a conclusion that completed detectors were their own best test structure. A larger emphasis was placed on the quality of detector performance rather than the direct measurement of specific material and process parameters with test structures. Instead of test structure measurements, the electrical characteristics and figures-of-merit of detector elements have been used to deduce some material parameters, and as a general indicator of device and process quality.

4) Early on, the poor quality of HgCdTe and resultant low yield of fabricated devices has, paradoxically, encouraged a reluctance to devote valuable HgCdTe surface area to test structures. Without test structures to verify process and material parameters, poor detector performance or unexplained failure of elements in an array is often attributed, without evidence, to low-quality starting material.

The experience of both the silicon IC and GaAs MMIC industries has shown that a comprehensive test structure program is essential for effective process development and maintenance. Communication of this previous experience would encourage wider applications of test structures in the manufacture of IR detectors. Thus, a second critical aspect of this study was to review the general principles of applying test structures determined through experience with silicon ICs and GaAs MMICs. Much of this experience is in contrast to the practices described above. For example, it is accepted that for silicon ICs, an intelligently selected and applied set of test structures is more informative than finished product performance in the diagnosis of which specific process steps may be limiting detector performance or yield. Test vehicle (chip) design methodology facilitates judgment as to the appropriate number and kind of test structures, as well as a percentage of substrate area to devote to test structures, even for processes with very low yields.

The third aspect of this study was to extract principles and ideas for test structure applications from the Si and GaAs experience that could be used to further enhance the manufacturability of IR detectors. The central lesson is that yield improvement requires improved process control by means of the intelligent application of test structures. An increased emphasis on applications of test structures is indicated for IR detectors. While the methodologies developed from previous experience can serve as a model for implementing test structures as tools for IR detector process development and control, substantial effort will be required to:

• Determine what information is needed from test structures by correlating detector performance and yield with material and process parameters.

104

- Determine how that information will be obtained by correlating the output from test structure measurements with relevant HgCdTe material and process parameters.

- Develop and document standard, well-characterized test structure designs as cells in a CAD library.

- Develop and document a detailed test plan.

- Develop and document detailed data analysis procedures.

Data acquisition may be simplified and accelerated by development of automated probe stations which are compatible with low-temperature measurements and which use lightly contacting or noncontact (i.e., low-damage) probes.

B. Conclusions

The conclusions of this study can be summarized as follows: Greater application of test structures to IR detector manufacture could lead to real improvements in the yield, reliability, and performance of the detectors. The previous experience with test structures in the Si and GaAs industries provides a useful guide and methodology for expanding the applications of test structures to IR detectors. However, further applied research will be necessary to optimize these applications of test structures.

The experience of researchers at the National Institute of Standards and Technology is a resource for extending the current applications of test structures to IR detectors. Potential areas of impact will be to augment the design and applications of the existing test structures, to develop new test structures aimed at specific process or material problems, and to develop comprehensive test structure implementation plans. Cooperation among the users can further increase the impact of test structures on IR detector manufacturability. NIST and industry should work together to develop common test structures and implementation approaches.

6. SCANNING CAPACITANCE MICROSCOPY: A NONDESTRUCTIVE CHARACTERIZATION TOOL

A. Background

Scanning Capacitance Microscopy (SCM) is being established at NIST as an internally funded initiative. SCM is a type of scanning probe microscope (SPM), like the scanning tunneling or atomic force microscopes (STM or AFM). SPMs produce images by recording the strength of some interaction between a mechanical probe tip in close proximity to a surface as that probe tip is scanned in two-dimensions above the surface. Nanometer resolution is readily achievable.

Scanning Capacitance Microscopy is expected to be sensitive to nanoscale variations in dopant density, composition, defects, mobility, and charge within a semiconductor. Because of these capabilities, SCM will have some very important applications to IR detector material, process, and device characterization. For example, the spatial resolution of the SCM will be such that performance difference between two photoconductive detector elements, which appear to be identical by visual inspection, can be investigated by imaging the electrical properties of the active region between the contacts. SCM has the potential to provide nondestructive prefabrication material screening, so that detector fabrication is undertaken by using only the highest quality material. Examination of cross sections of epitaxial layers or diffused regions will allow the dopant and compositional variations to be determined with unprecedented resolution and accuracy. In addition, topography, such as epitaxial island thickness and uniformity, can be measured with an AFM.

One possible implementation of SCM uses the Metal tip of an STM and the Insulating air gap between the tip and a Semiconductor to form an M-I-S capacitor. Capacitors of this sort have long been a basic test structure to determine the properties of semiconductors. The SCM provides an MIS capacitor that is nondestructive, highly localized, and mobile. Thus, many of the measurements made with capacitive test structures on semiconductors could now be implemented as a microscopy; i.e., the spatial variations of the measured parameter could be mapped into an image. The concept of a scanning capacitance microscope was demonstrated by Matey in 1985 [6.1], and a capacitance probe was first integrated with an STM by Williams in 1989 [6.2]. SCM has also been demonstrated by using an AFM by Barrett in 1991 [6.3].

B. Applications of SCM to GOES and Related Infrared Detectors

Scanning Probe Microscopes are expected to have an enormous impact on the semiconductor electronics industry, perhaps surpassing that of electron microscopy. Significant applications are envisioned not only in the silicon integrated circuit industry, but throughout the wide range of industries based on semiconductors, including infrared detectors based on HgCdTe and other materials. SPMs will be important because of these unique capabilities:

1) High Resolution — Atomic resolution is "easily" achievable with STM and other SPMs. As device dimensions are reduced below a micrometer, SPMs allow features to be seen that are beyond the resolution of optical or electron microscopes.

2) Nondestructive — In general, SPMs are noncontact and nonintrusive. Microscope vendors have begun building stages compatible with in-line examination of 200-mm-diameter wafers. Thus, most nominally flat surfaces are accessible, as well as some types of packaged devices.

106

3) Sensitivity to material properties — SPMs exist that are sensitive to various physical parameters of importance to semiconductor electronics. These include the AFM which is sensitive to surface topography, SCM which is sensitive to the parameters that determine capacitance (such as dopant density), as well as other microscopes such as a Kelvin probe microscope which is sensitive to work function differences.

The possible applications of SCM to metrology problems of importance to GOES and related infrared detectors include:

Materials Characterization
    Nanoscale microscopy of bulk electrical properties
        Dopant density
        Composition
        Defects
        Interface properties
        Mobility
    Pre-fabrication wafer screening
    Characterization of nanostructured materials, such as structures grown by molecular beam epitaxy

Process/Device Characterization
    Junction profiling
    Insulator/passivation charge mapping and manipulation
    Topography and surface roughness
    Fine-scale C-V measurements (and associated analysis)
    Insulating layer integrity/defects/damage/uniformity
    Metallization integrity/grain structure

Failure Analysis
    Process-induced damage
    Electrostatic discharge damage
    Process fault and material diagnosis

C. Establishment of Facility

The significant challenges in bringing SCM from the lab to a practical (potentially in-line) analytical technique are to 1) develop measurement procedures, 2) improve signal-to-noise and sensitivity, and 3) develop the theoretical interpretation and models to relate measured signals to relevant material parameters.

A Digital Instruments Inc. Nanoscope III[2] with a large sample stage was procured as the basis for the NIST SCM. A schematic of the interface of the SCM with the AFM is shown as figure 6.1. The system can perform both STM and AFM and has a fully automated stage with 200-mm wafer

---

[2] Certain commercial equipment, instruments, or materials are identified in this paper in order to adequately specify the experimental procedure. Such identification does not imply recommendation or endorsement by NIST, nor does it imply that the materials or equipment used are necessarily the best available for the purpose.
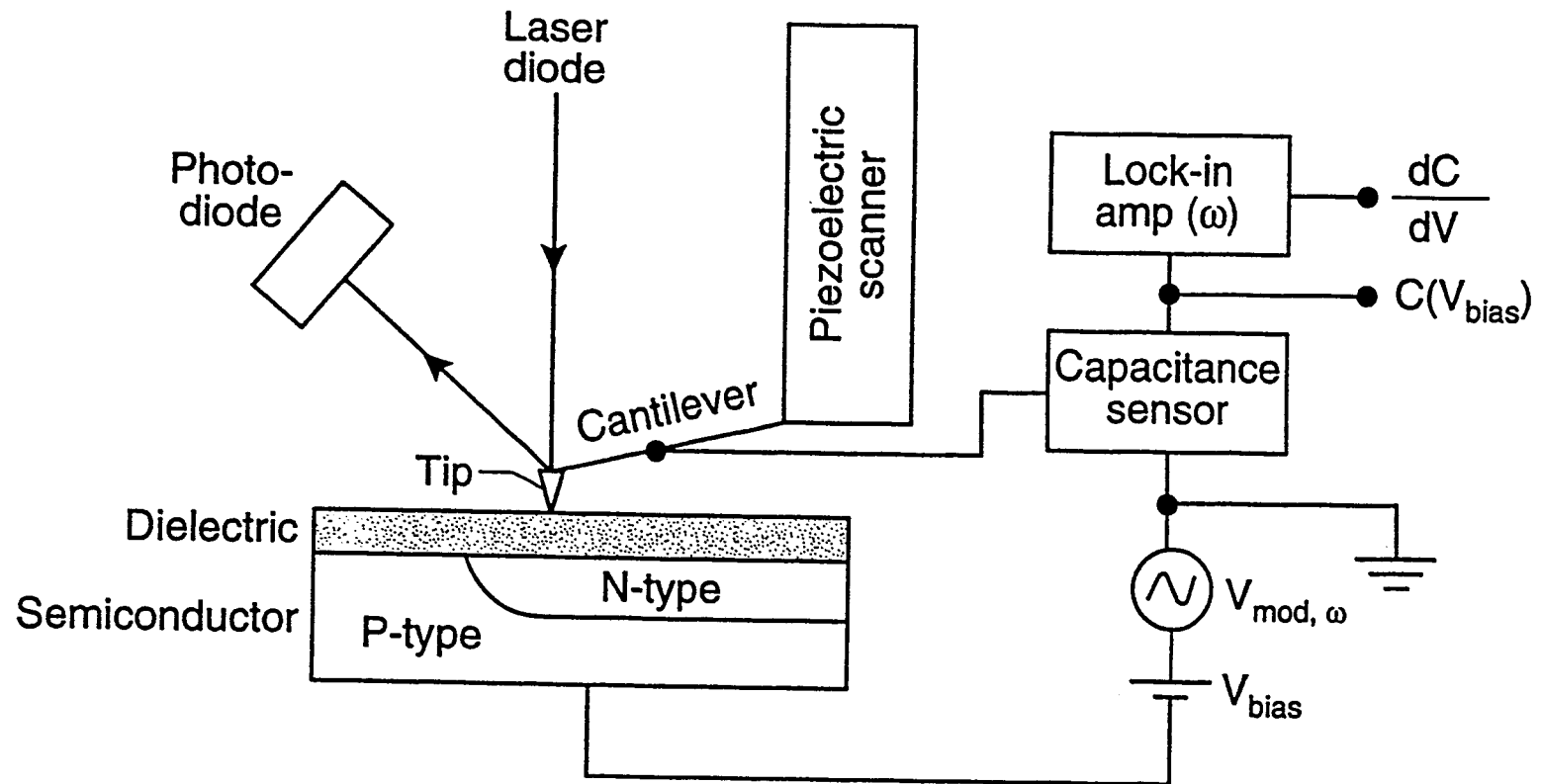
Figure 6.1 Digital Instruments Inc. Nanoscope III atomic force microscope with a large sample stage similar to the system operational at NIST. With the addition of capacitance-sensitive circuitry, this system can be made to operate as a scanning capacitance microscope.

capability. Scanning capacitance microscopy will be initially implemented in the atomic-force-microscopy mode. SCM in the scanning-tunneling-microscopy mode will also be investigated in the coming year. The SCM will be an important addition to existing efforts to characterize and screen infrared detector materials and devices.

Capacitance-sensitive circuit

After Matey [6.1] and Williams [6.2], the capacitance-sensitive circuit from an RCA video disc player will initially be used. This provides an inexpensive, high-sensitivity, and miniaturized capacitance sensor. Other means of capacitance measurement will be investigated with the goals of increased sensitivity and dynamic range of the capacitance measurement.

Modeling effort

An effort to model the measurement of capacitance with the SCM probe is ongoing. The SCM capacitor is in a hemispherical geometry rather than the more usual and more highly studied parallel plates. The initial thrust will be to numerically simulate the electromagnetic field between the probe tip and semiconductor by using currently available software. While several groups have demonstrated the concept of SCM, the measured signal has not yet been quantitatively related to the semiconductor dopant variations.

It is worth noting that applications of the interactions of a scanning probe tip and a semiconductor, especially when subjected to transient electrical and optical signals, are still a new area of investigation. It is likely that many semiconductor parameters will ultimately be accessible with some type of SPM.

D. **Preliminary Results**

At the writing of this report, the AFM/STM which will form the basis of the SCM facility has been operational only a short time. AFM images were made of some photoconductive detector elements to illustrate the potential resolution and image quality of an SCM based on the AFM system. Images were made at room temperature and in air on a packaged device. No sample preparation other than mounting the package to the microscope stage was needed.

Figure 6.2 is a low-magnification AFM image showing parts of three photoconductive detectors. AFM provides a precise means of determining layer heights and device topography. In the initial implementation of SCM, AFM will be used to measure material topography simultaneously with SCM measurements. An independent measurement of topography greatly simplifies the interpretation of the scanning capacitance image.

Since an SPM acquires images as arrays of digital data, rapid image manipulation and analysis is possible. Figure 6.3 shows a cross-sectional analysis of an AFM image of the boundary between the passivated active layer and the metal pad of a detector element from figure 6.2. The AFM image reveals a 150-nm dip in the passivation layer at the probe-pad boundary and a step in the probe-pad wall which could not have been as easily imaged with an optical microscope or SEM. Statistical analysis of topography or surface roughness is also readily available.
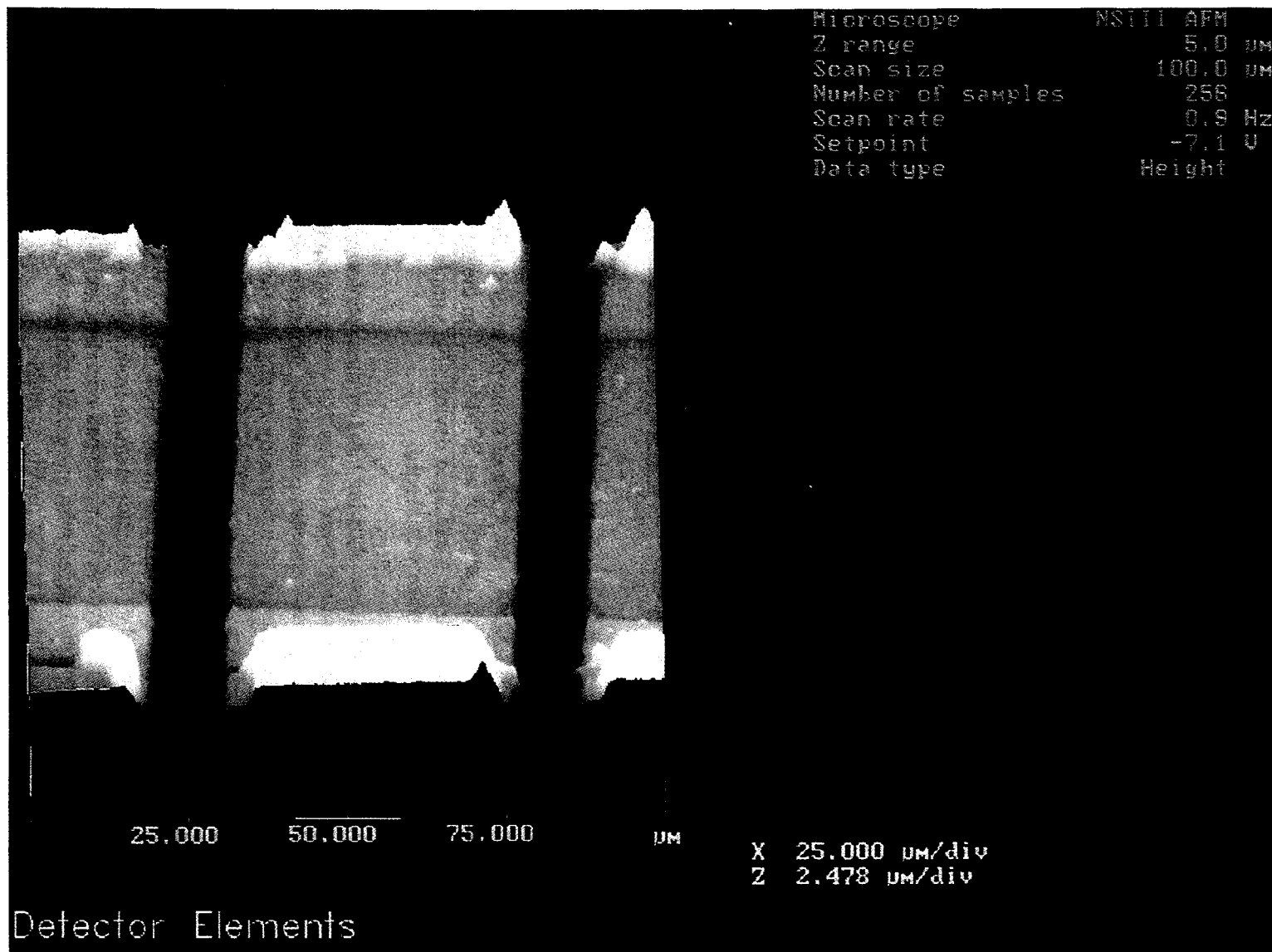
Figure 6.2 Low-magnification AFM image showing parts of three photoconductive detectors. AFM will be used to measure material topography simultaneously with SCM measurements.

Section Analysis
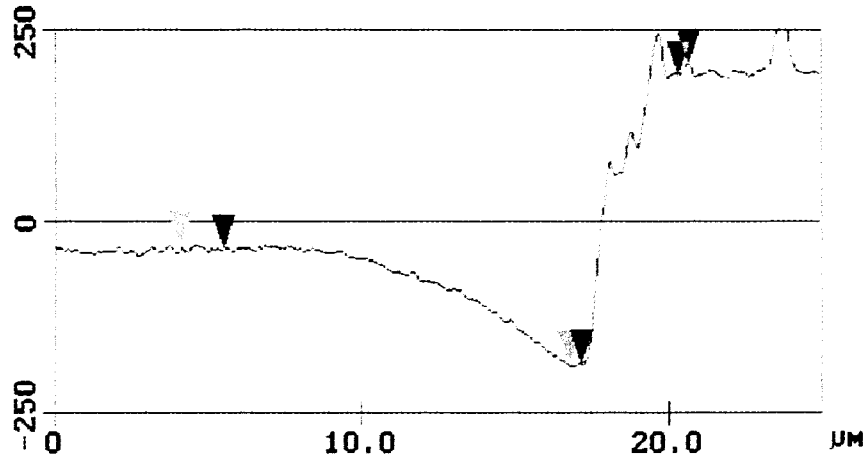
L	3.516 µm
RMS	121.30 nm
lc	25.000 µm
Ra(lc)	17.831 nm
Rmax	186.20 nm
Rz	167.94 nm
Rz Cnt	4
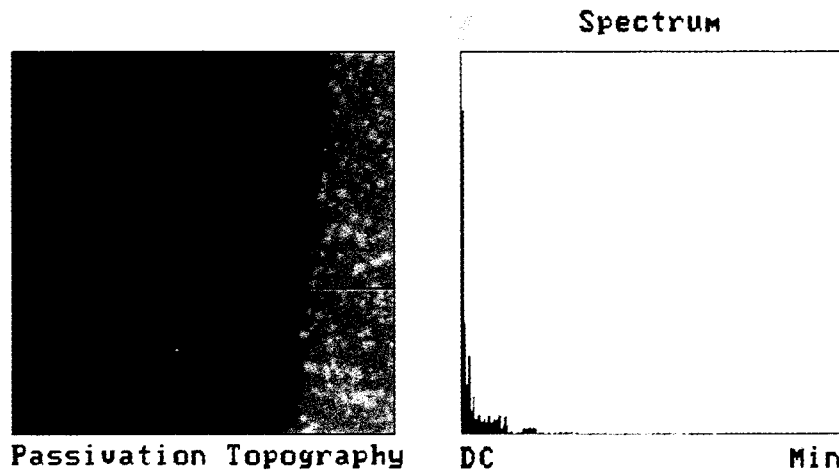
Spectrum

Horiz distance	14.844 µm
Vert distance	228.01 nm
Angle	0.880 deg
Horiz distance	3.516 µm
Vert distance	390.89 nm
Angle	6.345 deg
Spectral amp	86.921 nm

Passivation Topography   DC   Min

Figure 6.3 Cross-sectional analysis of an AFM image of the boundary between the passivated active layer and the metal pad of a detector element. The AFM image reveals a 150-nm dip in the passivation layer at the probe pad boundary and a step in the probe pad wall which could not have been as easily imaged with an optical microscope or SEM.
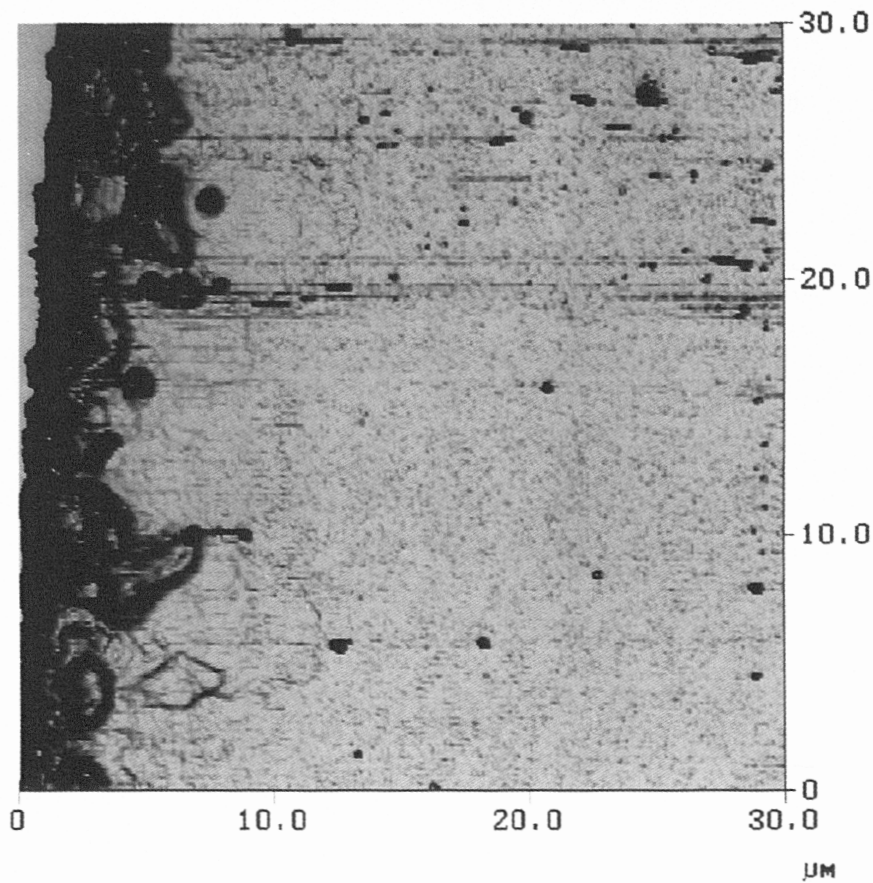
Detail of Detector Edge

Height

Figure 6.4 AFM image of the edge of a photoconductive detector revealing fine structure in the topography clustered at the edge of the active area. SCM will be able to resolve variations in <u>electrical properties</u> with similar or better resolution.

Figure 6.4 shows a higher magnification AFM image of the edge of the active area of a detector element. Considerable structure to the topography is seen clustered along the edge of the active area with resolution of less than 1 μm. Resolution of AFM is less than 10 nm and would permit the surface roughness of materials and device layers to be quantified. SCM will certainly be capable of similar resolution which would be sufficient for planar materials characterization. Resolution of 100 nm has been demonstrated with SCMs similar to the one being constructed at NIST, enabling the dopant variations across p-n junctions or heterostructures to be quantified.

It is difficult to identify the origin of the fine structure seen in the topography at the detector edge without more extensive measurements. It may be due to particulate contamination concentrated by a wet process step before or after passivation deposition. Indeed, development of SCM will permit the electrical effects of such topography disturbances to be probed and their likely effects on detector performance to be evaluated.

E. **Summary**

Scanning capacitance microscopy is a new, nondestructive metrology tool expected to have significant applications to infrared detector materials, processes, and devices. SCM will produce images that can be related to material electrical properties with spatial resolution comparable to the dimensions of detector elements. SCM applications expected to have a large impact on the quality, yield, and manufacturabilty of detectors include: nondestructive diagnosis of material variations within the active regions of detectors, nondestructive prefabrication materials evaluation, and dopant depth profiling of nanostructured materials.

7. NIST REVIEW OF THE GOES CALIBRATION PROGRAM

Contributed by
B. Saunders, C. Johnson, and C. Chromer
Radiometric Physics Division, NIST

A. Purpose

The goals of this task were to investigate the radiometric calibration procedures of the GOES program and to report NIST evaluation of the calibration capabilities of the prime vendors. Out of this evaluation NIST was to suggest recommendations for an improved calibration program for the infrared sensor system on the GOES platform. NIST staff would visit the three main contractors associated with developing the instruments for the infrared radiometric measurements. Although LORAL is the main contractor for the GOES program, they were not directly involved in the radiometric calibrations, and as a consequence, NIST staff did not visit or discuss radiometric calibrations with LORAL staff.

NIST staff first visited and examined the radiometric calibration programs of the detector vendors and followed with a trip to the system integration contractor (ITT Fort Wayne) where the final radiometric calibrations of the GOES satellite are performed.

B. Summary of Visits to Facilities

1) Supplier 2

Supplier 2 supplied the indium antimonide detectors and the associated collecting lens system used for the short wave infrared channels of the GOES sensor system. The only radiometric calibration specification that the detector was contractually required to meet was a specified blackbody D* for bare detectors. These test were performed using a 500-K blackbody as a standard for the blackbody D* determination. This is a straightforward measurement and is routinely made at a precision of few percent. NIST observation at Supplier 2 confirmed the measurements were being done according to accepted practice. Because of the detector sensitivity requirements of the GOES sensors, only one detector in a hundred met the requirements and could be selected for further processing. At this point, the calibration program at the detector manufacturer ceases, and the detectors are not further characterized until they arrive at ITT for integration. The next step at the detector manufacturer is the fitting of the detector optics onto the detector. The only requirement for the detector manufacturer is that the optics meets certain fabrication specifications and that the optical elements be tested for transmittance. The detector manufacturer is not informed about the criteria for the final selection process for the integrated detector package. The detector manufacturer is not responsible for the technical operation of the assembled detector after the lens is integrated on the detector. No check or test of responsivity or noise of the lens-detector systems is performed by the primary manufacturer.

2) Supplier 3

Supplier 3 is the manufacturer of HgCdTe detectors for the long wave channels. During the visit, NIST staff was shown the manufacturing process for the detector but was not able to review any calibration program of the detector package. This apparently was due to the fact that the calibration

program for the detectors was not operational at the time of the visit. Supplier 3 performs some general radiometric characterizations but does not provide detailed radiometric characterizations. Limited performance checking is the basis for selection of detectors to be used for the GOES satellite.

C. Recommendations

a. The calibration process must be studied from the fundamental optical physics viewpoint, the sources of error identified, and their effects on the final measurement determined. A comprehensive approach to this problem involves writing a measurement equation that incorporates all the relevant parameters and their relationships.

b. Determine the critical parameters that are needed to characterize and develop a calibration plan before manufacturing the components. This calibration plan can be done in several steps. In GOES, there should be a calibration and characterization program for each step of the manufacturing process. The different components, such as the detectors should be characterized before proceeding to the next step of reassembly. These detector packages are the heart of the GOES sensor system and are required to meet specifications that are at the theoretical limits of the detectors. Presently, the bare detectors are only being tested for blackbody D*. Although this is a critical parameter, the detectors should be tested for parameters other than blackbody D*. Parameters that affect detector performance are internal shunt resistance, spatial radiometric uniformity, stability, spectral responsivity, spectral D*, and linearity; if any of these parameters is unacceptable, then it is pointless to proceed to the integration of the lens onto the detector. The parameters such as spatial radiometric uniformity and geometric radiometric response function (response as a function of angle) should be determined after the lens is mounted on the detector.

c. Detailed records showing the history of the contributing test and changes should be maintained. These records should follow the component though its incorporation into the satellite. These records could be used to determine the stability and performance of the detectors [aspect of the sensor system.]

d. There should be a coordinated effort to maintain calibration assurance between the different manufacturers and the assemblers. This will help each manufacture plan a suitable and appropriate calibration program. In NIST's investigation, it was found that the different manufacturers of the detectors involved did not know how the detectors were going to be tested in the next stage. Not only is this costly but a lot of valuable expertise is not passed down the manufacturing chain. Also, the manufacturer is not held responsible for the performance and ability of his product to integrate it to successive stages of the assembly. Each manufacturer should be held responsible for meeting the specification of the next stage.

e. To achieve a reliable sphere source, considerably more attention to the calibration and care of the sphere will be necessary. The sphere should be calibrated more frequently and a history of the calibration maintained. Departures or significant change from the baseline need immediate attention. The calibration schedule of the sphere should closely bracket the calibration of the GOES sensors.

f. Since the final product is a radiometric calibration problem, staff trained in radiometric measurements are essential in the GOES program. Although the GOES program includes

many talented people whose expertise is needed, NIST did not find evidence of radiometric training or expertise on the calibration staff.

g. The GOES should be calibrated as close to the time of its use as possible. This will help ensure that the GOES has the optimal calibration at the time of launch. However, this procedure will not ensure that the GOES can make measurements of the same accuracy later due to changing environmental circumstance that can effect the optics and detection in space and during launch.

h. It is recommended that the GOES be calibrated several times before launch. This will establish a calibration history and base line. It will also set a limit as to the accuracy that can be achieved in the use of the instrument once launched. While it is a recognized departure from present strategy and perhaps contains difficulties, it is recommended that NOAA/NASA consider developing a strategy for calibration checks or calibration while the instruments are in space orbit. This could include onboard calibration devices or the use of celestial sources that could be viewed for calibration and stability checks. If a scenario for the present GOES cannot be developed that addresses this problem, the insights gained in such a study can be used for future design considerations in future observational satellites.

8. SUMMARY AND CONCLUSIONS

A. Magnetotransport Measurements

Shubnikov-de Haas (SdH) oscillations in the transverse magnetoresistance have been used to characterize the accumulation layers of the infrared detectors used in the GOES and TIROS weather satellites. The electron densities, cyclotron effective masses, and Dingle temperatures can be obtained from the data for each subband in the 2D electron gas formed by the accumulation layer. A first-principles calculation of the subband energy dispersion relations has been performed in order to compare theory and experiment. The model is needed in order to extract the density from the data, because the energy bands are very nonparabolic in narrow-gap HgCdTe. The agreement between predicted and measured masses and Fermi energies was excellent for anodically oxidized layers. The masses could not be obtained for the other processes because the signals were weak and complex.

A large number of detectors from each of three suppliers were measured by the SdH effect and analyzed to obtain the densities, effective masses, and Dingle temperatures of their accumulation layers. Results were obtained for devices (five elements from two detectors) from Supplier 1 with type I (anodic oxidation) passivation. The Fourier transforms have large, well-defined peaks from which the carrier density of the accumulation layer was obtained. Two detectors with four elements each from Supplier 2 were measured. The front and back surfaces have different passivations (combination designated type III), which make it difficult to interpret the results. Consequently, three experimental detectors were fabricated and measured to help understand the individual surfaces. Two classes of detectors were received from Supplier 3. The eight elements with type I passivation were similar to the type I units from Supplier 1. The four elements with a different passivation, type II, had weak SdH response which resembled that of the type III devices from Supplier 2. The carrier densities of the accumulation layers of type II and III detectors were much greater than those for the type I detectors. Six TIROS detectors were also measured. These are larger devices with type I passivation. The carrier densities were similar to those on the other type I detectors. Angular rotation studies were performed on devices from Suppliers 2 and 3 to verify that the SdH signal was coming from the two-dimensional accumulation layer. Effective masses and Dingle temperatures were calculated for one or more elements with type I passivation from each supplier. The values were in good agreement with the theoretical calculations. More work is needed to obtain meaningful values of effective mass and Dingle temperature on other types of accumulation layers.

A new and simpler method that is based on the dc magnetoresistance upon which the SdH oscillations occur has been investigated. The electron density and mobility of the top accumulation layer can be determined from the magnetic-field dependence of the magnetoresistance at high magnetic field. Agreement between the densities and mobilities of the accumulation layers of type I and type II detectors with Hall measurements by the manufacturers showed that the method was accurate. Measurements were made on a large number of detectors from Suppliers 2 and 3. The results showed variability of the accumulation-layer density by 20% among three elements of a multi-element detector. The generally lower mobilities and higher densities of accumulation layers on type II and type III detectors led to their improved performance because of reduced leakage and decreased surface recombination.

117

B. Other Characterization Studies

Bonding, Metallization, and Packaging

A total of six visits was made to three GOES and TIROS infrared detector manufacturers during FY 1992. The first visit to each site was made to evaluate their production lines and processes. Later visits were made to help them with the packaging of their detectors. This included one 2.5-hour seminar on wire bonding and the reliability of the metallurgical systems used in packaging HgCdTe detectors. Over 30 people attended that seminar. For another company, a more informal hour-long presentation was made to six/seven engineers and management personnel. Extra time was later spent in their packaging laboratories. An SEM study was made of detectors from one manufacturer and several defects were found (the results were presented at a GOES project review at NASA Goddard July 10, 1992). This information, with proposed solutions, was also fed back to the manufacturer to help them improve their product. Studies were carried out at NIST and at two detector manufacturing sites to establish the best molecular-cleaning methods that are compatible with the normal HgCdTe detector packaging methods. For this work, ultraviolet cleaning equipment was hand carried to detector manufacturers so that tests could be performed there. A set of recommended practices was developed and provided to the manufacturers to help them improve their yields.

Test Structures

Because of the substantial impact of test structures on other semiconductor circuits, the current state-of-the-art applications of test structures to HgCdTe-based IR detectors were comprehensively reviewed. To place these applications in context, the general principles of applying test structures, determined through experience with silicon ICs and GaAs MMICs, were also reviewed. From these two reviews, principles and ideas were extracted for test structure applications that could be used to further enhance the manufacturability, yield, and performance of IR detectors. To communicate and encourage application of test structures, the results of the study were presented at the Measurement Techniques for Characterization of MCT Materials, Processes, and Detectors Workshop held in Boston, MA during October 1992 and published in Semiconductor Science and Technology. A reprint of this paper is attached in Appendix B.

Scanning Capacitance Microscopy

Scanning capacitance microscopy is a new, nondestructive metrology tool that merges a high-sensitivity capacitance sensor with an atomic force microscope (AFM). SCM applications that could be expected to have a large impact on the quality, yield, and manufacturability of detectors include: nondestructive diagnosis of material variations within the active regions of detectors, nondestructive prefabrication materials evaluation, and dopant depth profiling of nanostructures. AFM images were made of some photoconductive detector elements to illustrate the feasibility, potential resolution, and image quality of SCM applied to IR detectors.

GOES Calibration Program

NIST staff visited and examined the radiometric calibration programs of the detector suppliers as well as the system integration contractor where the final radiometric calibrations are performed. NIST recommends that a fundamental calibration program be established that is coordinated between the

different manufacturers and assemblers. NIST also recommends that the GOES detectors be calibrated several times before launch to establish a calibration history and base line.

Industrial Survey of Characterization Measurements for HgCdTe Materials, Processes, and Devices

Appendix C contains a reprint of this work. An extensive industrial survey of the importance and use of characterization measurements for HgCdTe materials, processes and devices has been completed. Seventy-two characterization/measurement techniques were considered, and thirty-five responses were received. This information was sought for a study on materials characterization and measurement techniques of parameters and properties necessary to improve the manufacturing capabilities of HgCdTe infrared detectors. The nature of materials characterization is defined, and an overview is given of how it is related to improving IR detector manufacturing. Finally, we present a description of the characterization survey and a summary of the survey results. Major aspects of the results include: (1) ranking the 72 techniques by their importance and frequency of use, (2) listing the parameters or properties determined by each technique, (3) enumerating the most important properties that need to be measured, (4) indicating the key measurement techniques that most need to be developed, enhanced or improved, and (5) giving key overall comments.

9. REFERENCES

[1.1]   D. G. Seiler, G. G. Harman, J. R. Lowney, S. Mayo, and W. S. Liggett, Jr., HgCdTe Detector Reliability Study for the GOES Program, National Institute of Standards and Technology, NISTIR 4687 (September 1991).

[1.2]   HgCdTe Detector Degradation Task Force Meeting Booklet, May 2, 1991, p. 76.

[1.3]   J. R. Lowney, D. G. Seiler, W. R. Thurber, Z. Yu, X. N. Song, and C. L. Littler, Heavily Accumulated Surfaces of Mercury Cadmium Telluride: Theory and Experiment, J. Electronic Materials 22, 985 (1993).

[2.1]   R. J. Nicholas, F. Nasir, and J. Singleton, High Magnetic Field Characterization of (Hg,Cd)Te Surface Layers, J. Crystal Growth 86, 656 (1988).

[2.2]   D. G. Seiler, G. B. Ward, R. J. Justice, R. J. Koestner, M. W. Goodwin, M. A. Kinch, and J. R. Meyer, Shubnikov-de Haas Measurements on n- and p-type HgTe-CdTe Superlattices, J. Appl. Phys. 66, 303 (1989).

[2.3]   S. Yamada, H. Asai, and Y. Kawamura, Subband Effective Mass and Mobility of Two-Dimensional Electrons in Uniformly Si-Doped GaInAs/AlInAs Multiple Quantum Wells, J. Appl. Phys. 72, 569 (1992).

[2.4]   T. Ando, Theory of Quantum Transport in a Two-Dimensional Electron System under Magnetic Fields. IV. Oscillatory Conductivity, J. Phys. Soc. Japan 37, 1233 (1974).

[2.5]   I. Nachev, Bound States in Inversion layers on p-$Hg_{1-x}Cd_xTe$: Self-Consistent Results, Semicond. Sci. Technol. 3, 29 (1988).

[2.6]   See Ref. 1.3.

[2.7]   E. Kane, Band Structure of Indium Antimonide, J. Phys. Chem. Solids 1, 249 (1957).

[2.8]   J. Sune, P. Olivo, and B. Ricco, Self-Consistent Solution of the Poisson and Schrödinger Equations in Accumulated Semiconductor-Insulator Interfaces, J. Appl. Phys. 70, 337 (1991).

[2.9]   D. G. Seiler, J. R. Lowney, C. L. Littler, and M. R. Loloee, Temperature and Composition Dependence of the Energy Gap of $Hg_{1-x}Cd_xTe$ by Two-Photon Magnetoabsorption Techniques, J. Vac. Sci. Technol. A8, 1237 (1990).

[2.10] J. P. Harrang, R. J. Higgins, R. K. Goodall, P. R. Jay, M. Laviron, and P. Delescluse, Quantum and Classical Mobility Determination of the Dominant Scattering Mechanism in the Two-Dimensional Electron Gas of an AlGaAs/GaAs Heterojunction, Phys. Rev. B 32, 8126 (1985).

[2.11] S. Das Sarma and F. Stern, Single-Particle Relaxation Time Versus Scattering Time in an Impure Electron Gas, Phys. Rev. B 12, 8442 (1985).

[2.12]   Y. Nemirovsky and G. Bahir, Passivation of Mercury Cadmium Telluride Surfaces, J. Vac. Sci. Technol. A7, 450 (1989).

[2.13]   Y. Nemirovsky and I. Kidron, The Interface between $Hg_{1-x}Cd_xTe$ and Its Native Oxide, Solid-State Electronics 22, 831 (1979).

[2.14]   A. J. Rimberg and R. M. Westervelt, Electron Energy Levels for a Dense Electron Gas in Parabolic GaAs/AlGaAs Quantum Wells, Phys. Rev. B 40, 3970 (1989).

[3.1]   K. Seeger, *Semiconductor Physics*, Springer-Verlag, New York, 1985, p. 63.

[3.2]   R. D. Larrabee, W. A. Hicinbothem, and M. C. Steele, A Rapid Evaluation Technique for Functional Gunn Diodes, IEEE Trans. Electron Devices ED-17, 271 (1970).

[3.3]   T. R. Jervis and E. F. Johnson, Geometrical Magnetoresistance and Hall Mobility in Gunn Effect Devices, Solid-State Electronics 13, 181 (1970).

[3.4]   W. S. C. Gurney and J. W. Orton, New Techniques for the Study of Gunn Diode Contacts, Solid-State Electronics 17, 743 (1974).

[3.5]   M. J. Howes, D. V. Morgan, and W. J. Devlin, Applications of Magnetoresistance Measurements in the Evaluation of Transferred Electron Device Performance, Phys. Stat. Sol. (a) 41, 117 (1977).

[3.6]   D. C. Look, A Two-Layer Magneto-TLM Contact Resistance Model: Application to Modulation-Doped FET Structures, IEEE Trans. Electron Devices ED-35, 133 (1988).

[3.7]   H. J. Lippmann and F. Kuhrt, Geometry Influence on the Transverse Magnetic Resistance Effect in Rectangular Semiconductor Plates [Der Geometrieeinflusz auf den transversalen magnetischen Widerstandseffekt bei rechteckformigen Halbleiterplatten], Z. Naturforsch. 13a, 462 (1958) (in German).

[3.8]   H. Weiss, Magnetoresistance, in *Semiconductors and Semimetals*, Vol. 1, ed. by R. K. Willardson and A. C. Beer, Academic Press, New York, 1966, p. 315.

[3.9]   DATAPLOT is a software package developed at NIST for analyzing and displaying data; see *DATAPLOT- Introduction and Overview*, NBS Special Publication 667 (U.S. GPO, Washington, DC, 1984).

[3.10]   M. B. Reine, K. R. Maschhoff, S. P. Tobin, P. W. Norton, J. A. Mroczkowski, and E. E. Krueger, The Impact of Characterization Techniques on HgCdTe Infrared Detector Technology, Semicond. Sci. and Technol. 8, 788 (1993).

[3.11]   M. B. Reine, private communication.

[5.1]   J. J. Kopanski and C. E. Schuster, Review of Semiconductor Microelectronic Test Structures with Applications to Infrared Detector Materials and Processes, Semicond. Sci. Technol. 8, 888-910 (1993).

[6.1]   J. R. Matey and J. Blanc, Scanning Capacitance Microscopy, J. Appl. Phys. 57, 1437 (1985).

[6.2]   C. C. Williams, W. P. Hough, and S. A. Rishton, Scanning Capacitance Microscopy on a 25 nm Scale, Appl. Phys. Lett. 55, 203, (1989).

[6.3]   R. C. Barrett and C. F. Quate, Charge Storage in a Nitride-Oxide-Silicon Medium by Scanning Capacitance Microscopy, J. Appl. Phys. 70, 2725 (1991).

Heavily Accumulated Surfaces of Mercury Cadmium Telluride Detectors: Theory and Experiment

J.R. LOWNEY, D.G. SEILER, and W.R. THURBER

Semiconductor Electronics Division, National Institute of Standards and Technology, Gaithersburg, MD 20899

Z. YU, X.N. SONG, and C.L. LITTLER

Department of Physics, University of North Texas, Denton, TX 76203

Some processes used to passivate n-type mercury cadmium telluride photoconductive infrared detectors produce electron accumulation layers at the surfaces, which result in 2D electron gases. The dispersion relations for the electric subbands that occur in these layers have been calculated from first principles. Poisson's equation for the built-in potential and Schroedinger's equation for the eigenstates have been solved self-consistently. The cyclotron effective masses and Fermi energies have been computed for each subband density for 12 total densities between 0.1 to 5.0×10^{12} cm^{-2}. The agreement with Shubnikov-de Haas measurements is very good at lower densities with possible improvement if band-gap narrowing effects were to be included. At higher densities, larger differences occur. The simple 2D description is shown to break down as the density increases because the wave functions of the conduction and valence bands cannot be well separated by the narrow band gap of long-wavelength detectors. These results provide a basis for characterizing the passivation processes, which greatly affect device performance.

Key words: HgCdTe photoconductive detectors, Shubnikov-de Haas oscillations, surface passivation, 2D electron gas

INTRODUCTION

The II-VI compound semiconductor $Hg_{1-x}Cd_xTe$ is today's most widely used infrared detector material. It provides, for example, high-performance photoconductive (PC) detectors in the 4 to 6 and 8 to 12 μm spectral ranges. The properties of these detectors are very sensitive to their surface passivation, which is often a dominant factor in limiting device performance. The complexity of the surface passivation process arises from the different chemical properties of the constituents and the formation of electrically active defects in the interface region.[1] Often HgCdTe detectors are passivated by processes (e.g. anodic oxidation) that produce accumulated surfaces, which result in 2D electron gases with areal electron densities on the order of 10^{11} to 10^{12} cm^{-2}. The resulting surface potential can be greater than the band-gap

energy in long-wavelength detectors, and the surfaces can thus greatly influence the characteristics of the detector. Consequently, the development of theories and models that predict the conduction properties of the electrons in these accumulation layers is very important.

In this paper, first-principles calculations have been used to determine the accumulation-layer potentials, electron densities, cyclotron effective masses, and Fermi energies of the resulting 2D electron gases. Shubnikov-de Haas (SdH) measurements were also carried out on a wide variety of n-type PC detectors to compare them with the calculated results. The electron densities and mobilities of such layers were obtained in the past by Nemirovsky and Kidron[2] by using Hall-effect and capacitance-voltage measurements for a wide range of densities. Nicholas et al.[3] have used SdH measurements to characterize these surface layers, and they have found that the layers can be described by a 2D electron gas with a number

of 2D subbands. SdH oscillations occur in the magnetoresistance at high magnetic field and result from the redistribution of carriers caused by the crossing of the Fermi energy by a Landau level. This technique has the advantage that measurements can be made directly on commercial photoconductive detectors, which have only two terminals. The oscillations are periodic when plotted as a function of the inverse of the magnetic field, B, and a Fourier transform of the signal as a function of 1/B shows peaks at fundamental frequencies corresponding to the densities of each subband. For parabolic subbands, the electron densities can be obtained directly from these frequencies. However, HgCdTe is very nonparabolic because of its small energy gap, and therefore a model is needed to deduce the densities. The subband Fermi energies can be obtained from the fundamental frequencies once the cyclotron effective masses are determined from the measured temperature dependence of the amplitude of the oscillations. The model then relates these measured quantities to the electron densities.

We have calculated the dispersion relations of the subbands self-consistently from the accumulation-layer potentials to obtain the model needed to relate the electron densities to the measured parameters. There have been various approaches to the solution of the subband dispersion relations, most of which have used a WKB approximation.[4-6] We have followed the work of Nachev,[7] who solved the matrix Hamiltonian for the conduction band and heavy-hole, light-hole, and split-off valence bands. The built-in potential in the electron accumulation layer is included directly in the matrix equation, and a second order differential equation is obtained for a wave function that contains terms that depend both on the potential and the electric field in the accumulation layer. The field terms cause a spin-splitting of the eigenvalues. The actual subband wave functions can then be determined from the solutions of this differential equation.

First we solved Poisson's equation for a continuum model of the electron density to obtain an initial built-in potential. Then we solved Schroedinger's equation for the eigenfunctions and eigenvalues for the electric subbands that are allowed in the 2D electron gas that describes the accumulation layer. From the wave functions obtained, we recomputed the potential and iterated the potential until self-consistency was obtained. We then computed the Fermi energies and cyclotron masses from the calculated subband dispersion relations for twelve electron densities between 0.1 to 5.0×10^{12} cm^{-2}. Agreement of our theoretical results with our measurements for a detector with an electron density of 7.9×10^{11} cm^{-2} is very good. In contrast, the theory predicts values for cyclotron effective masses that are much smaller and Fermi energies that are much larger than the measured values for a detector with 3.4×10^{12} cm^{-2}. We expect that if we were to include the effect of band-gap narrowing,[8] which occurs at these fairly large carrier densities, we would obtain better agreement. There is also the possibility that the surface could be under

some strain, which could affect the energy gap.

There is a gradual breakdown in the 2D electron gas model for the accumulation layers as the density increases because the energy gaps are so small in long-wavelength detectors. It becomes difficult for the electrons to remain confined solely to the conduction band because their wave functions can cross the energy gap into the valence band when the potentials become large. For the 2D model to be completely valid, the conduction-band wave functions must decay sufficiently in the energy gap that they can be considered isolated. For the low-order subbands in very heavily accumulated surface layers, this isolation weakens, and a large number of states are then allowed that traverse the entire thickness of the detector. Thus, the model approaches the limiting case of a graded 3D layer with a SdH Fourier transform that has a broad featureless background for the range of 3D electron densities in the accumulation layer.

THEORY

We have extended the work of Nachev,[7] who has performed the most rigorous analysis of the subband dispersion relations, to the entire set of allowed subbands for a wide range of electron densities. He has derived the 8×8 matrix Hamiltonian for the conduction band and the heavy-hole, light-hole, and split-off valence bands for both spin directions ($\pm$). He then reduced the Hamiltonian to a second-order differential equation for the wave function $\phi_\pm$ in the direction z perpendicular to the accumulated surface:

$$\frac{d^2\phi_\pm}{dz^2} = a\frac{d\phi_\pm}{dz} + (k^2 - b)\phi_\pm \pm \frac{1}{3}ck\phi_\pm \qquad (1)$$

where

$$a = \frac{2\alpha^2 + \beta^2}{2\alpha + \beta}\frac{dV(z)}{dz} \qquad (2)$$

$$b = \frac{3\gamma}{P_0^2(2\alpha + \beta)} \qquad (3)$$

$$c = \frac{3(\alpha^2 - \beta^2)}{2\alpha + \beta}\frac{dV(z)}{dz} \qquad (4)$$

and

$$\alpha = \frac{1}{E_v(z) - E^\pm} \qquad (5)$$

$$\beta = \frac{1}{E_v(z) - \Delta - E^\pm} \qquad (6)$$

$$\gamma = E_c(z) - E^\pm \qquad (7)$$

In the above equations, k is the wave number in the plane of the surface and refers to the 2D free electron

gas, $V(z)$ is the built-in potential in the accumulation layer due to the oxide charge, $E_c(z)$ and $E_v(z)$ are the conduction and valence band energies, respectively, including the effect of the potential, Δ is the split-off band separation from the valence band edge, P_0 is a number proportional to the momentum matrix element as given in Kane's band model for HgCdTe,[9] and $E^{\pm}$ are the eigenvalues for the two spin directions.

The wave functions $\phi_{\pm}(k,z)$ are real and the actual subband wave functions, Ψ, can be computed from them by solving for the eight envelope functions f_n because

$$\Psi(r) = \sum_{n=1}^{8} f_n(z) u_n(r) \qquad (8)$$

where $u_n(r)$ denotes the periodic part of the Bloch function at $k = 0$. The envelope wave functions of the conduction band, $f_1(z)$ and $f_5(z)$, are found directly in terms of $\phi_{\pm}(k,z)$:

$$\phi_{\pm}(k,z) = i\,(k_+/k)f_1(z) \pm f_5(z), \quad k_+ = k_x + ik_y. \quad (9)$$

The other envelope functions are found from the matrix Hamiltonian in terms of these two envelope functions by direct substitution. The equations for them, which are somewhat lengthy, involve the derivatives of $f_1(z)$ and $f_5(z)$ as well because of the momentum operator in the Hamiltonian. The volumetric electron density can then be computed directly from Ψ and the areal density of the 2D electron gas.

The initial potential is found by solving Poisson's equation for a non-quantized 3D free electron gas. The standard Kane k-p band model,[9] which treats the coupling of the light-hole and split-off valence bands with the conduction band, is used. Poisson's equation is solved by a nonlinear two-point boundary value method based on finite differences with deferred correction and Newton iteration. Equation 1 is then solved by integrating the equation from an initial value and slope at the boundary opposite to the accumulation layer, and eigenvalues are found by selecting those solutions that vanish at the surface.

As in Ref. 7, the interior boundary, where the conduction-band wave functions go to zero, has been chosen to be at the middle of the energy gap for a given eigenvalue or at a maximum distance of 0.5 μm if the eigenvalue always lies above midgap. Thus, we accept only those states that are effectively bound by the conduction band and constitute a 2D electron gas. This approximation is based on the assumption that the wave functions decay sufficiently in the energy gap that those associated with the conduction band can be separated from those associated with the valence band. As the gap becomes very small, this approximation breaks down and a continuum background of states that traverse the entire thickness of the detector becomes allowed. This effect is discussed further below.

Equation 1 is solved for at most 50 k values to construct the dispersion relations for the allowed subbands. A new potential is computed from the calculated wave functions between the surface and 0.1 μm; beyond this point, the original bulk potential is used. Were we to use the calculated wave functions beyond 0.1 μm, there would be a difficulty because of the artificial boundary condition at 0.5 μm where the wave functions are forced to be zero. The process is iterated until the input and output potentials agree to within 1%. In order to prevent the potentials from gradually diverging from their original values, they are scaled each time by the ratio of the initially computed areal electron density to that just computed.[10] When this factor is between 0.99 and 1.01, convergence is obtained. It was discovered that convergence could be obtained more rapidly, and often only, if the initial potential were modified slightly between the surface and 0.025 μm to take into account the strong differences between the electron density computed initially and quantum-mechanically near the surface in the accumulation layer. The initial potential was thus subsequently scaled by a quadratic function to make it agree better with the shape of the first calculated potential over this range.

Once the self-consistent subband dispersion relations were found, we computed the subband densities, Fermi energies, and cyclotron effective masses at the Fermi energy by performing either a parabolic spline interpolation or linear extrapolation of our computed eigenvalues to the Fermi energy. The spin-averaged cyclotron effective mass, m^*, is obtained from the expression

$$(m^*)^{-1} \approx \frac{\hbar^{-2}}{2} \sum_{\pm} \left(\frac{1}{k} \frac{dE^{\pm}}{dk} \right) \qquad (10)$$

evaluated at the Fermi energy, E_f. These quantities now allow one to compute the value of the subband densities from the peaks in the Fourier transform of the SdH data. The frequencies corresponding to the peaks equal $m^*E_f/\hbar e$ for each subband.[11] The value of m^* is determined from the measured temperature dependence of the amplitude of the SdH oscillations.[12] Thus, one can find the subband density for which the theoretically computed product of m^*E_f has the measured value for each subband. For the case of parabolic subbands, $m^*E_f = \hbar^2 \pi N$, where N is the electron density, and the peak frequencies provide N directly. We refer to this relation as the parabolic approximation.

EXPERIMENT

Shubnikov-de Haas measurements have been made on a series of long-wavelength n-type HgCdTe PC infrared detectors with accumulation-layer electron densities between mid 10^{11} and mid 10^{12} cm^{-2}. They were square with active areas between 2 and 4×10^{-5} cm^2. Their top and bottom surfaces were passivated by various methods that produced electron accumulation layers. Indium contacts, sometimes extended, were used to achieve excellent ohmic behavior.

Some of these detectors were measured as a function of temperature between 1.5 and 30K to obtain effective mass data. Here we report on two detectors

ENERGY BAND DIAGRAM

a

SUBBAND DISPERSION RELATIONS
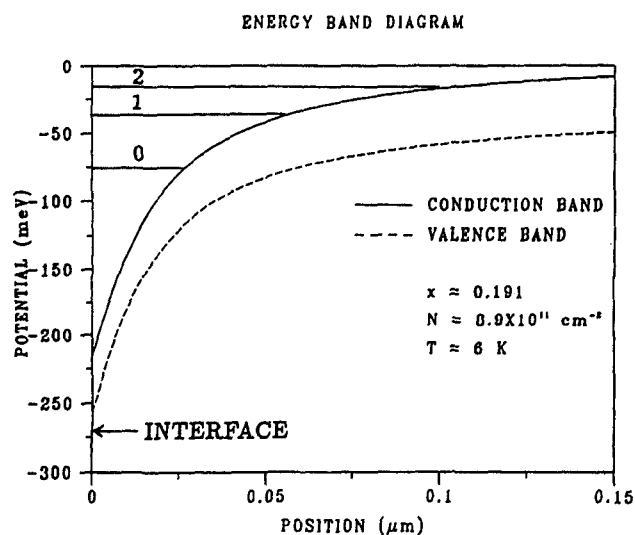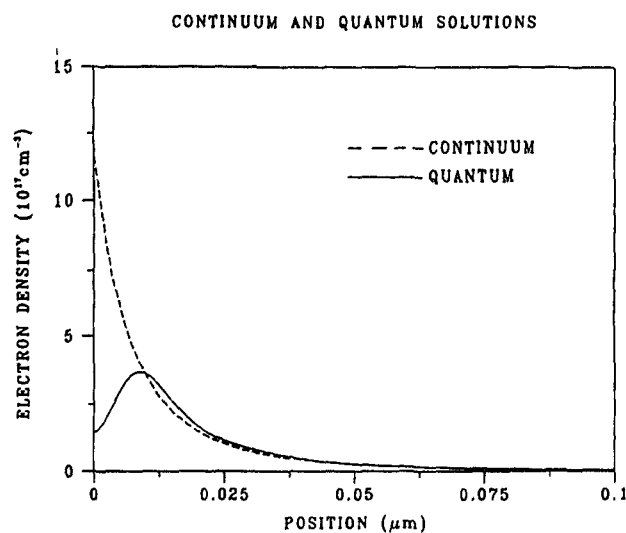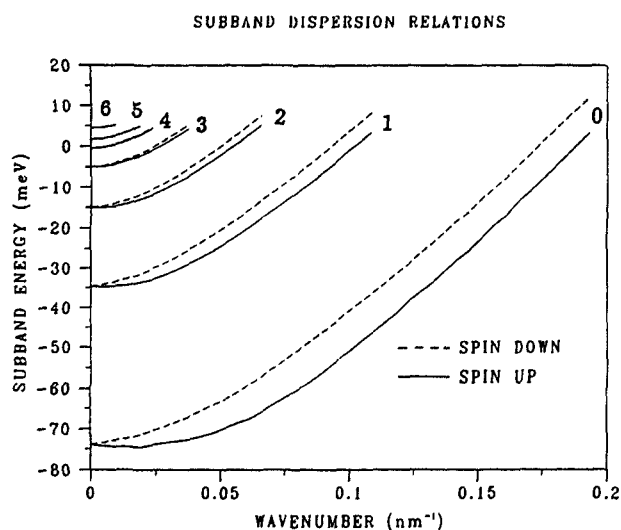
b

Fig. 1.(a) Built-in potential for accumulation layer with total electron density of 8.9×10^{11} cm^{-2} and alloy fraction x = 0.191. The horizontal lines are the subband-edge energies for the first three subbands (n = 0,1,2). (b) Dispersion relations for the subbands for this potential, showing spin-splitting. The curves are labeled by subband number from 0 to 6.

CONTINUUM AND QUANTUM SOLUTIONS

a

SUBBAND POPULATIONS

b

Fig. 2. (a) Electron density computed by solving Poisson's equation for a charge continuum (dashed) and from full quantum-mechanical calculation (solid) for case of Fig. 1. (b) Suband densities as a function of total density. Lines are linear least-squares fit. The curves are labeled by subband number from 0 to 3, and x = 0.191.

that have had extensive measurements made on them. Ac magnetic-field modulation and lock-in amplifier techniques that use the second harmonic detection were used to obtain the signal for magnetic fields up to 12 T.[12] The SdH oscillations are a small percentage of the total magnetoresistance, and ac techniques significantly enhance the measured SdH oscillations in these detectors.

Excellent signal-to-noise ratios were obtained in most detectors even at temperatures as high as 30K. Measurements made at 30, 60, and 90 degree rotations of the sample about the perpendicular to the surface showed that the peak frequencies varied as 1/cos(θ), where θ is the rotation angle, as expected for a 2D electron gas.

RESULTS AND DISCUSSION

Calculations of the subband dispersion relations and related quantities have been made for the range of areal electron densities between 0.1 and 5.0×10^{12} cm^{-2}. The x-value of the detector was taken to be 0.191, with a corresponding energy gap of 41.1 meV,[13] which is representative of long-wavelength detectors and equal to that of the detectors we report on below. The background electron doping density was assumed to be 3.9×10^{14} cm^{-3}, which was reported for these detectors, along with a bulk mobility of 2.5×10^5 cm^2/Vs at 77K. Bulk SdH oscillations were not observed because of their low frequency, which implies that they would have been observed only at low magnetic

fields where broadening effects greatly reduce their signal strength. The temperature is taken to be 6K, at which the material is degenerate. As an example, the built-in field and subband dispersion relations for an areal density of 8.9×10^{11} cm^{-2} are shown in Figs. 1a and 1b, respectively. The surface potential in Fig. 1a is about three times greater than the energy of the lowest subband edge and over five times the energy gap. The spin splitting is evident in Fig. 1b, and is greatest for the lowest subband. The density of electrons in the spin-up subband is about 15% greater than in the spin-down subband for the lowest four subbands. At the lower densities, this percentage decreases somewhat, especially for the higher subbands, while at higher densities it remains nearly the same for all subbands. Note also that the deviation from a parabolic to a nearly linear dependence of E on k is clear for energies only about 10 meV above the subband edges. The small oscillations in these curves are due to 1% numerical uncertainty in the solutions.

The corresponding electron density in the accumulation layer is shown in Fig. 2a for both the semiclassical result from the initial solution of Poisson's equation and the final quantum-mechanical result from the subbands. The width of the accumulation layer is seen to be about 0.1 μm. The latter density is greatly reduced at the surface because of the boundary condition on the wave functions. It goes to zero discontinuously across the boundary because of the dependence of the wave function on the derivatives of f_1 and f_5, which undergo a discontinuous change from a finite to zero value at the boundary. Therefore the shape of the potential near the interface is different in the two cases, and the value of electron density obtained quantum-mechanically is less than that of the initial semiclassical solution. The electron densities of the first four subbands are plotted as a function of total density in Fig. 2b. We compute the total density from a sum over only the first four subbands, for which we can perform accurate computations. We estimate the error incurred by this approximation to be less than 1%. The relations are nearly linear with average slopes of 0.673, 0.223, 0.077, and 0.027 for the first (n = 0) through fourth (n = 3) subband, respectively. The deviations from linearity are less than 1%. These values differ somewhat from our corresponding experimental values of 0.609, 0.258, 0.101, and 0.032, which have deviations from linearity of only a few percent, although the experimental values may not be completely accurate because they are based on the parabolic approximation for the density in the SdH analysis. This near linearity shows that the shape of the potential distribution is relatively insensititve to the magnitude of the surface potential. The difference between theoretical and experimental slopes may indicate that the potential distribution is somewhat distorted, which can be caused by strain or band gap narrowing.

The subband Fermi energies and cyclotron effective masses are shown in Figs. 3a and 3b, respectively, as a function of total density. The Fermi energy in the

bulk is computed to be 5.44 meV for an assumed bulk density of 3.9×10^{14} cm^{-3}. The scatter in the mass values is due to the derivative in Eq. 10. Although the calculated eigenvalues appear relatively smooth in Fig. 1b they are only accurate to about 1%, and this uncertainty as well as that due to the discreteness of the k-values causes the theoretical masses to have errors of about 5% occasionally. A more refined calculation would lead to better accuracy. The strong variations of the masses with density attest to the nonparabolicity of the dispersion relations, which have an effect on the optimization of device performance. The serpentine shape of the curves is due to the strong curvature of the built-in potential.

We have made SdH measurements on a number of
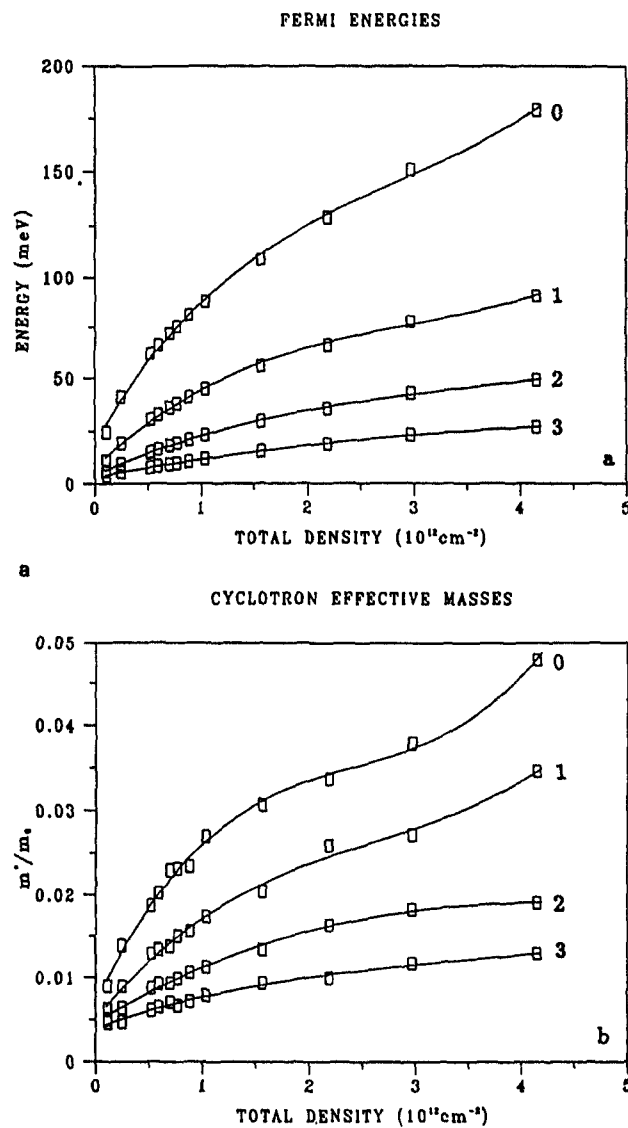
Fig. 3. (a) Subband Fermi energies as a function of total density, measured from the bottom of each subband. (b) Ratio of subband cyclotron effective masses to the electron mass at the Fermi energy as a function of total density. Lines are cubic least-squares fit. The curves are labeled by subband number from 0 to 3, and x = 0.191.

FOURIER TRANSFORM OF SHUBNIKOV-DE HAAS DATA

a

FOURIER TRANSFORM OF SHUBNIKOV-DE HAAS DATA

b
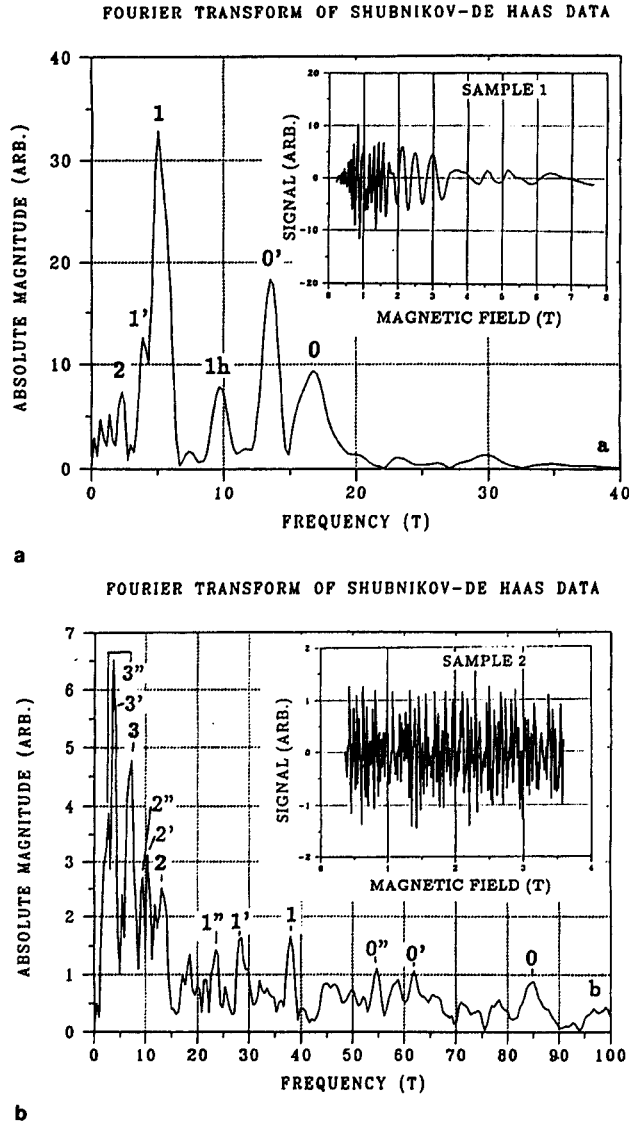
Fig. 4. (a) Fourier transform of SdH data at 5K for Sample 1; the label "h" stands for harmonic; peaks are labeled by subband number. (b) Same for Sample 2, except at 2K. Actual SdH data for the signals as a function of magnetic field are given in insets and x = 0.191.

long-wavelength, commercial, n-type PC detectors with total densities between 5×10^{11} and 5×10^{12} cm^{-2}. The SdH Fourier transforms of two different representative detectors are shown in Figs. 4a and 4b along with the actual SdH data, which show the oscillations vs magnetic field. The notations ' and " refer to different surfaces or to different regions on the same surface since both surfaces of the detector were passivated. The detector in Fig. 4a was passivated with the usual anodic oxidation process,[1] while that in Fig. 4b was passivated by a different method. The separations of peaks due to spin-splitting are predicted by our theory to be about half of that we observed, and thus we expect that these multiple peaks are due to different surface densities. The splittings vary somewhat from detector to detector as well. Thus, the effect of spin splitting is just to broaden each peak. The

transform corresponding to the detector with lower total density, Sample 1, in Fig. 4a, has clear, strong peaks, while that for the one with higher density, Sample 2, in Fig. 4b, has peaks that rise less above the background. One reason is that the penetration of the energy gap by the wave functions is much greater for the heavily accumulated case, especially for the lowest subband. There is a mixture of subband states bound to the conduction band and continuum states that traverse the entire detector. Thus, the layer of electron accumulation is not well described by a simple 2D electron gas at high densities and small energy gaps. The Fourier transform for a heavily accumulated, narrow gap detector can have a broad background of contributions from the range of 3D states corresponding to the graded 3D electron density in the accumulation layer. The 2D states, which are bound to the conduction band, appear as well in the Fourier transform and rise above the background because they contribute at only one frequency for each subband. The complexity of the background signature in Fig. 4b may indicate that there is nonuniformity in the surface density as well because of the two surfaces and multiple regions within a surface. Even though the relative amplitude of the oscillations of Sample 2 was almost ten times smaller than that of Sample 1, the Fourier transform successfully resolved the signature of the detector.

We have computed the subband electron densities from the measured cyclotron effective masses and Fermi energies for these two detectors. The results from the two surfaces were averaged because we could not resolve the splitting at higher temperatures. For sample 1, the measured data are: $m_0^* = 0.022 \pm 0.001$, $E_f^0 = 79 \pm 4$ meV, $m_1^* = 0.014 \pm 0.001$, and $E_f^1 = 42 \pm 3$ meV. The corresponding theoretical values were obtained by finding the total density for which the m^*E_f values for the subbands best agreed with experiment: $m_0^* = 0.023 \pm 0.001$, $E_f^0 = 75 \pm 2$ meV, $m_1^* = 0.015 \pm 0.001$, and $E_f^1 = 38 \pm$ meV. The predicted total density is found to be 7.9×10^{11} cm^{-2}, which is considerably less than the value of 1.2×10^{12} cm^{-2} that is obtained from the parabolic approximation for the density. The agreement between theory and experiment is within the assigned uncertainty with the theoretical values for the effective masses slightly larger than measured. Thus, we expect that the energy gap may be smaller than the one we are using. This may occur because of band-gap narrowing, which occurs at high densities because of the many-body interactions between electrons. We estimate the band-gap reduction to be at most 10% at this density.[8] For Sample 2, we report the results for the peaks labeled with " because the unprimed peaks were above our calculated densities, and some of the single-primed peaks were not as well separated from the background. We do not report the n = 2 and n = 3 peaks because they are also not very well separated. The measured data for the peaks labeled with " are: $m_0^* = 0.020$, $E_f^0 = 312$ meV, $m_1^* = 0.010$, and $E_f^1 = 277$ meV. The uncertainties for these numbers are about 20%.

We obtain from the total density that gives best agreement between our theory and the measured subband m^*E_f values: $m_0^* = 0.039 \pm 0.002$, $E_f^0 = 160 \pm 3$ meV, $m_1^* = 0.029 \pm 0.001$, and $E_f^1 = 80 \pm 2$ meV. The predicted total density is then found to be 3.4×10^{12} cm^{-2}, which is also considerably less than the value of 4.3×10^{12} cm^{-2} from the parabolic approximation. However, Sample 2, which was made by a different process from the traditional anodic oxidation method[2] that was used for Sample 1, disagrees with the predictions, because the measured masses are so much smaller and the Fermi energies so much larger than the predicted values. Band-gap narrowing would be larger for these samples, probably in excess of 10% of the energy gap, and the gap could become very small. However, much more work is needed to understand the cause of this disagreement, which may involve strain as well. The relatively large Fermi energies and small masses could imply that the built-in potential is more like a square well in these detectors with heavy accumulation.

CONCLUSIONS

The dispersion relations for all the 2D subbands in the accumulation layers of HgCdTe detectors have been computed by solving the 8×8 matrix Hamiltonian for a large range of electron densities (0.1 to 5×10^{12} cm^{-2}). The subband densities, Fermi energies, and cyclotron effective masses have been computed as a function of the total electron density. The results show strong nonparabolicity and a breakdown in the simple 2D model of the electron gas at high densities and small energy gaps. The near linear dependence of the subband densities on total density, which has been observed experimentally, has been confirmed theoretically. The agreement of our calculations with experiment is good at the lower densities and may possibly be improved by inclusion of the effect of band-gap narrowing. At the higher densities differences are large, and further work including the effects of band-gap narrowing and strain is needed to understand the measurements. Models such as these provide a basis to characterize the electron states in the accumulation layers of these detectors, which have a large effect on device performance.

The direct application of these results to the characterization of detectors is not simple, however. The properties of the accumulation layers constitute only one of the controlling factors in detector performance. Others include the bulk electrical and optical properties, the type and quality of the contacts and packaging, and the effects from the method of delineating the detectors, such as ion milling. The contribution of this work has been to present a direct, two-terminal measurement that can be used to determine the electron density of the accumulation layers of a detector. Failure to have sufficient accumulation can lead to increased surface recombination and degradation of detectivity. Excessive accumulation, on the other hand, can lead to a large shunt conductance, which also can degrade detectivity. Thus, one can use this method to study the dependence of detectivity on the method of passivation and the resulting level of accumulation. The optimum process can be determined, and subsequently this method can be used to monitor the accumulation layers during manufacturing and to monitor their stability as a function of time.

REFERENCES

1. Y. Nemirovsky and G. Bahir, *J. Vac. Sci. Technol.* A7, 450 (1989).
2. Y. Nemirovsky and I. Kidron, *Solid-State Electron.* 22, 831 (1979).
3. R.J. Nicholas, F. Nasir and J. Singleton, *J. Cryst. Growth* 86, 656 (1988).
4. W. Zawadzki, *J. Phys. C* 16, 229 (1983).
5. Y. Takada, *J. Phys. Soc. Jpn.* 50, 1998 (1981).
6. G. Nachtwei, P. Schulze, G. Gobsch, G. Paasch, W. Kraak, H. Kruger, and R. Herrmann, *Phys. Status Solidi* b 148, 349 (1988).
7. I. Nachev, *Semicond. Sci. Technol.* 3, 29 (1988).
8. G. Trankle, E. Lach, A. Forchel, C. Ell, H. Haug, G. Weimann, G. Griffiths, H. Kroemer, and S. Subbanna, *J. de Phys. Coll.* C5, 48, 385 (1987).
9. E. Kane, *J. Phys. Chem. Solids* 1, 249 (1957).
10. J. Sune, P. Olivo and B. Ricco, *J. Appl. Phys.* 70, 337 (1991).
11. S. Yamada, H. Asai and Y. Kawarnura, *J. Appl. Phys.* 72, 569 (1992).
12. D.G. Seiler, G.B. Ward, R.J. Justice, R. J. Koestner, M. W. Goodwin, M. A. Kinch and J. R. Meyer, *J. Appl. Phys.* 66, 303 (1989).
13. D.G. Seiler, J.R. Lowney, C.L. Littler and M. R. Loloee, *J. Vac. Sci. Technol.* A8, 1237 (1990).

INVITED PAPER

Review of semiconductor microelectronic test structures with applications to infrared detector materials and processes*

J J Kopanski and C E Schuster

Semiconductor Electronics Division, National Institute of Standards and
Technology, Gaithersburg, MD 20899, USA

Abstract. The impact of microelectronic test structures, as they have been applied
to silicon integrated circuits (ICS) and gallium arsenide monolithic microwave
integrated circuits (MMICS), is reviewed. General principles for the use of test
structures with possible applications to infrared (IR) detector technology based on
HgCdTe and other materials are emphasized. The uses of test structures for Si
and GaAs, test chip design methodology and some examples of how test
structures have been applied for process control and to increase yield are
discussed. Specific test structures and techniques that have been applied to IR
detectors are also reviewed. The basic design considerations and measurements
possible with each class of test structure are discussed. The important experience
of the Si and GaAs industries, applicable to IR detectors, is that significant yield
improvement is possible with improved process control using test structures.
Increased research efforts to expand the applications of test structures to IR
detector manufacture are indicated.

1. Introduction

Since the mid-1970s, the National Institute of Standards and Technology has engaged in a programme to develop well characterized test structures, test methods and data analysis techniques for use by the semiconductor manufacturing industry. Test structures are micro-electronic devices that are fabricated by the same processes used to manufacture semiconductor integrated circuit products, and that are used to measure selected material, process or tool parameters by means of electrical tests. Properly designed test structures can be used to evaluate semiconductor materials, to determine and monitor process centring parameters, to measure critical device and circuit parameters (which can be input to device models), to identify and quantify yield-limiting defects and to assess processing tool performance.

As they are used today, test structures are indispensable to the successful process development and manufacture of Si and GaAs devices and circuits. The use of test chips speeds up process development, product fabrication and test, and enhances the reliability of the product—all at decreased cost. The use of test structures as part of a comprehensive test programme can ensure that performance and reliability have been built into circuits. The prominence of test structures is the result

of many years of experience with their use in the manufacture of silicon ICS and, more recently, GaAs MMICS.

The next section contains a tutorial describing how test structures have been applied to silicon ICS and GaAs MMICS. It is the intention of this tutorial to encourage greater acceptance and use of test structures in IR detector manufacture by developing an understanding of the ways test structures have had an impact on the larger silicon and GaAs industries. Elements of a hierarchical test chip design methodology, which maximizes the impact of using test structures, are described. This bottom-up approach to test chip design provides a blueprint for applying test structures to any semiconductor device fabrication process. On the basis of experience with silicon and GaAs test structures, a guide to selecting the appropriate kind and number of test structures, as well as principles for effective application of these devices, is provided. Three examples of how test structures have been applied for process control and to increase yield are included. The first two examples are from Si technology and illustrate process/tool control using the analysis of results of measurements on test structures. The third example describes how test structures suggested an improvement of an etch process for GaAs MMIC fabrication and illustrates the importance of using a high area density of test structures early in process development.

In the third section, the current use of test structures and specialized measurements most commonly applied

to IR detector devices, processes and materials are discussed. The characterization concerns of IR detectors are compared and contrasted with Si and GaAs circuits. Design considerations and the uses of each test structure are discussed. The section is meant to be a comprehensive listing of devices that are well described in the literature and that are thus candidates for inclusion in IR detector test chips.

The final section contains a discussion of specific test structures and principles for the expanded application of test structures which have the potential for enhancing IR detector technology. Areas where further study is needed are outlined. Relevant principles from the current body of test structure experience are used to suggest changes in practices that could ultimately affect the manufacturability of IR detectors.

2. Using test structures effectively

This section summarizes test structure utilization from a Si and GaAs perspective, but with the goal of featuring ideas which should also be applicable to the IR detector industry. First, some selected applications and implementations of test structures are presented to illustrate why and how test structures can be used. Then, a discussion of test structure methodology explains how to develop successful test structure implementations. Finally, case studies from the Si and GaAs industries are used to show how three types of problem, potentially applicable to IR detector manufacturing, were discovered and solved using test structures.

2.1. Why test structures are used

Test structures provide a means for obtaining parameters that can be used to diagnose, monitor and predict the performance of the fabrication process, the products manufactured and the manufacturing equipment. Test structure data can be used to establish, improve or ensure process control and product yield. The results of test structure data analysis may be used as feedback to the manufacturing process or as the basis for future development work.

Test structure data can be collected rapidly using a computer-controlled probe station. This enables many samples of many types of parameters to be collected during processing without a significant impact on manufacturing time. Test structure measurements also enable users to derive parameters that cannot be obtained at all, or as economically, from other forms of testing. If the collected data are efficiently reduced and evaluated, processing and yield-limiting problems can be detected and solved promptly, improving the economics of the manufacturing process.

Test structures can be applied to processes, products and process tools throughout the manufacturing lifecycle—in development, production, technology transfer and buying and selling. The following discussion describes some typical uses of test structures during these times.

During developmental phases, process control and adequate yields must be established for successful production of products. Collected test structure data are evaluated to identify critical factors in the various process steps that must be controlled and to detect problems that limit product yield. When diagnosing control and yield-limiting problems, the user may also correlate collected data with historical or simulated data. Collected data can also be used as input to modelling studies used in extended developmental evaluations, such as new process development, device and circuit modelling and logic and fault simulation.

During development and production, after process control and adequate yields have been achieved, test structures can be used to monitor the critical parameters. Collected test structure data are compared with data from previously verified lots to ensure that process control is maintained. For a well controlled and well characterized process, test structure data can also be evaluated to determine if existing correlations can be used to reduce the set of test structures needed to monitor the process.

In efforts involving technology transfer, comparison of test structure data between participants is useful for verifying that the desired performance criteria are successfully met on all manufacturing lines. This is important in developing multiple sources for materials, processes and products and in demonstrating the applicability of new processing tools.

When buying and selling, performance criteria derived from test structures can be used as manufacturing specifications. Such specifications help the seller to market products and services and enable buyers to make comparisons when selecting materials, processes, devices, circuits and processing tools.

Test structures to support these applications can be categorized into several classes according to their general purpose: to extract material, process, device or circuit parameters; to detect or quantify random faults and processing defects; to establish product reliability and yield; to formulate layout design rules; and to assess processing tool performance. The remainder of section 2.1 discusses typical user goals that can be achieved, and the test structures, parameters and types of analysis required. It also provides references for further reading. The reader should note that, in many cases, the references (and their references) reveal assumptions, limitations or requirements which are beyond the scope of this discussion.

2.1.1. Test structures to extract material, process, device and circuit parameters. Material, process, device and circuit parameters are either directly measured or indirectly extracted from test structures. These characterization parameters are then compared and correlated to diagnose and monitor processes or products. Characterization parameters can also be used to build models for software simulation of processes, devices or circuits

[1, 2]. Such simulations provide results which can be used in evaluations to diagnose existing process problems, develop process enhancements or future processes, determine target and tolerance values or layout rules, or design devices and circuits. The discussion below identifies the major characterization parameters and test structures used to characterize materials, processes, devices and circuits.

Materials. Test structures can be used to determine properties of starting materials, surface and interfacial regions, ion-implanted layers and deposited films. Here, test structures provide an efficient and economical means of measuring parameters that are otherwise impossible or difficult to obtain, such as those requiring advanced physical analysis techniques. Evaluation and diagnosis of materials parameters are used to ensure the uniformities needed to support manufacture of functioning devices, as they may correlate with performance factors [3] or device quality [4, 5]. Since materials parameters are obtained early in the processing, correlations with other test structure parameters are timely indicators for monitoring and predicting product performance.

To determine starting material parameters associated with deep-level defects, an integrated gated-diode electrometer is used [6, 7]. This test structure consists of a gated-diode with a preamplifier and is used to measure leakage current, from which both carrier lifetime and surface recombination velocity can be extracted by using an equivalent circuit model. Information related to impurity concentration in the material is determined using a Hall structure for the Hall mobility and a long gate-length transistor for the drift mobility [8].

For ion-implanted layers, test structures are used to determine the doping profile and information about residual substrate impurities [4]. The dopant density and depletion width can be determined using transistors, capacitors or diodes [9]. These structures also allow C–V profiling to be done, which indicates further information about drift mobility, the presence of traps, activation energy, carrier concentration, ideality factor and barrier height [5, 10].

Parameters such as conductivity and contact resistance are sometimes considered as measures of material quality [8, 11], but are more accurately measures of process quality [12]. Regardless of this, these parameters are critical to making good Hall measurements [11] and must be evaluated when making Hall measurements. Test structures and references for conductivity and contact resistance measurements are found in the following section.

Processes. Process parameter test structures provide information about layer uniformity, layer interface conditions and feature definition resulting from the various process steps. These parameters are important for making correlations related to monitoring, diagnosing and predicting process and process tool performance. The test structures most frequently used to provide process parameters include van der Pauw sheet resistors,

cross-bridge sheet resistors, interfacial contact resistors, potentiometric alignment structures, transistors, capacitors and diodes.

The van der Pauw sheet resistor, cross-bridge sheet resistor, interfacial contact resistor and potentiometric alignment structure are implemented in each of the process layers where uniformity or particular target values are critical. The van der Pauw sheet resistor measures conductivity [4, 13–15]. The interfacial contact resistor provides the interfacial contact resistance, which is used to evaluate the quality of the contact formation process [16–18]. A cross-bridge sheet resistor [14, 15, 19–21], which provides sheet resistance and allows extraction of linewidth, is used to evaluate the quality of film deposition processes. The potentiometric alignment structure [22, 23] provides a measure of the misregistration of photomask features between two conducting layers. Alignment structures are also used to indicate process tool performance (see section 2.1.5) and to formulate or evaluate geometric layout rules (see section 2.1.4).

Transistor, capacitor and diode structures provide information about processing, as well as materials. For example, threshold voltage data from transistor-based test structures have been correlated with sheet resistance data to diagnose contamination problems [24]. Threshold voltage data have also been used to infer parameters, such as dopant concentration, for which no direct measurement method exists, as described in section 2.4.1. Other process parameters commonly measured are oxide thickness using capacitors, and leakage currents using diodes.

Devices. Test structures for characterizing device parameters are useful in process control and simulation. Like process parameters, device parameters can be indicators of process quality or product yield, as demonstrated in section 2.4.2. Device parameters also frequently correlate with other test structure data. Test structures for characterizing devices include transistors, diodes, resistors and capacitors that have the same layouts, operating conditions and measurement conditions as the devices used to construct the IC product. This allows meaningful comparison and correlation for monitoring, diagnosing or predicting product performance. Such test structures can also be used to develop specifications for designers, buyers and sellers.

Parameters typically measured from field effect transistors include threshold or pinch-off voltage, saturation voltage, breakdown voltage, leakage current, transconductance, parasitics associated with device terminals and any other parameters needed for equivalent circuit models [12, 25]. Many of these parameters can be extracted from diodes as well. Information needed by a circuit designer to interconnect devices and assess loading conditions can be determined using resistance, capacitance, delay and gain values measured from resistors, capacitors and transistors.

Circuit elements. Circuit characterization test structures

are used to determine circuit performance and to verify or predict that functional circuits can be fabricated by a given process [26]. They provide data that can often be correlated with fundamental processing parameters, as in the example of ring oscillator frequency and linewidth [27]. They also provide parameters that can be used as product specifications. Basic circuits often used include inverters, counters, amplifiers and oscillators. Typical circuit parameters that are measured or extracted include frequency response, delays [28], gains, noise, drive capability and power dissipation.

2.1.2. Test structures to detect or quantify random faults (yield).

Random fault test structures help users monitor materials-based process faults, their failure rates and their effects on product yield [24]. They provide information about critical process steps such as etching, metallization and contact formation. Random fault test structures are useful in that process problems unknown to a manufacturer, which also reduce yield, can be identified and corrected, the performance of multiple manufacturers can be compared and product acceptance criteria can be specified. These structures are also used to determine layout design rule constraints such as minimum spacings for successful isolation or contacts (see section 2.1.4).

The random faults to be detected are due to either a physical fault that causes a circuit failure or a parametric fault that may or may not cause a circuit failure. Examples of random physical faults are a pinhole in oxide, a break in a metal line, or a gate-to-source short in a transistor.

Random fault test stuctures are generally implemented as arrays of identical transistors, capacitors or resistors. The test structure arrays are sized to permit fault detection and to provide statistically significant data for obtaining failure rates for the process. Based on the results of continuity tests, these arrays indicate what percentage of the total elements are successfully fabricated. Examples of random fault test structures include a capacitor array for detecting oxide pinholes, a serpentine array of resistors for detecting breaks in metal step coverage [29], a transistor array for dielectric integrity or transistor defect type and rate, and a comb configuration of resistors for isolation integrity.

The arrays can be addressable, to allow location of the sites of failures. As the array sizes needed for statistics are large, using addressable arrays to locate the faults makes visible inspection following fault location tractable. Addressable arrays also enable possible clustering of faults to be observed. For example, in a MOSFET array [24], clustering of excessive leakage current and low breakdown voltage were found.

Random fault data have further utility related to test vector generation and logic simulation [1]. Logic simulation performed with fault models constructed from test structure data can indicate design flaws which could be actuated by random faults. This permits faults to be found before completing product fabrication. Random fault data also provide the basis for models used in fault

simulations that describe more than the classical stuck-at-one, stuck-at-zero or open-circuit faults.

2.1.3. Test structures to establish product reliability.

Reliability test structures [26] are used to identify faults due to environmental stresses such as temperature, voltage, humidity and radiation. These stress-related faults are most frequently manifested as problems in oxide or metal that prevent the final product from functioning, or lead to its early failure. Like random fault test structures, reliability test structures are often implemented as arrays and provide failure-rate data. Capacitor and transistor arrays can detect oxide problems by determining dielectric breakdown, leakage current and oxide charge density. Resistor-based structures, implemented as serpentines and combs, can detect opens and shorts in metallization due to electromigration [30] and corrosion.

2.1.4. Test structures to formulate layout design rules.

These test structures are used to formulate the design rules for a process. Test structure data relevant to width and spacing of process features are evaluated to produce the geometric layout rule set. Optimum widths and spacings of the process features can be determined on the basis of yield for each of the test structure types, which are implemented in various widths and spacings [31]. The test structures used include cross-bridge resistors for feature linewidth, alignment resistors for feature-to-feature alignment, isolation resistors for feature isolation [26] and contact arrays for contact window opening sizes and spacing [7].

2.1.5. Test structures to assess processing tool performance.

This class of test structures is used mainly to evaluate lithographic systems for performance or acceptance of equipment, for operator performance, and for separation of equipment-related problems from other processing or materials effects. One strength of the test structures in this class is that they provide accurate and rapid measurements needed for successful feedback related to tool performance.

The cross-bridge can be applied in a variety of ways related to its capability to rapidly provide accurate linewidths. It has been used to evaluate the linewidth uniformity of a wafer stepper system [32], a step-and-repeat camera [33], a mask aligner [34], and to evaluate the performance of a plasma descumming step intended to improve linewidth uniformity achievable by an electron-beam system [35]. An extension of the cross-bridge can be used to estimate proximity exposure effects in an electron-beam system [35]. A cross-bridge used in conjunction with serpentine and comb interconnect resistors can be used to evaluate and improve the software and procedures for exposing electron-beam resist in the submicrometre regime [36].

Electrical alignment test structure measurements can help to determine origins of alignment errors. Whether errors are caused by operator rotation or translation, wafer warpage, photomask problems or the actual

alignment characteristic of the alignment equipment itself can be resolved through analytical methods and vector maps of measurements across a wafer [34].

2.2. How test structures are implemented

Test structures are commonly implemented on a semiconductor wafer in one of four arrangements. First, discrete structures are placed adjacent to particular devices or products at selected locations on the wafer. Second, a collection of structures small enough to be located on-chip or in the kerf (between products) area is used. These test strip-type implementations have various names, including test strip, test coupon, plug-bar and pellet. Third, a test chip is formed from a collection of structures and used in place of an entire product chip at selected chip sites on the wafer. These are usually referred to as drop-ins. Fourth, a high density of the chips on the wafer are test chips. Particular applications and details for each of these implementations are described below.

Discrete test structures monitor specific parameters of high interest in production environments. Known correlations between the test structure and device or product must be well established for this implementation to be useful. Uniformity of the correlated parameters must exist if discrete structures are used at only a few locations on the wafer.

Test strip-type and drop-in implementations are used in production environments to assure process control. They are sometimes called a process control monitor (PCM) or process validation monitor (PVM). Since they consist of various types of test structures, they provide more information than a discrete structure and can be used to evaluate wafer-to-wafer and lot-to-lot performance. Their advantage is that they collect a variety of parameters without using a lot of wafer area, so their use has a minimal effect on production economics. Because these implementations monitor only specific wafer areas, process uniformity is a prerequisite for their use, as shown in section 2.4.2.

Test strip-type structures may be placed either at multiple locations on the wafer, near particular circuits that they are designed to monitor or in one location on the wafer. A popular use of test strips is in Si foundries to verify that the products have been correctly fabricated. Some GaAs manufacturers who need an on-wafer plating bar accompany it at the wafer flat with a plug-bar implementation of test structures to ensure process control. Drop-ins are usually geometrically placed on the wafer. Some frequent placements include one chip per quadrant and one in the centre, or all the chips along the diagonals in a cross pattern.

High-density implementations are needed if evaluating intrawafer uniformity is critical. They are used in both production and development environments. Since high-density implementations replace significant amounts of product area with test chips, they are suitable for production environments only if they are applied as a process validation wafer (PVW). In a PVW, test chips cover an entire wafer, but only one or two wafers per lot are PVWs. Applied in this manner, PVWs can be used for vendor qualification and circuit acceptance, where lot-to-lot process and device uniformities are critical [37, 38]. In development environments, full-wafer or other high-density implementations are used to evaluate uniformities. Other high-density implementations arrange test chips and product chips in checkerboard-like patterns. This allows spatially sensitive correlation of process and product characteristics. Also, the process and products can be diagnosed using the same mask and possibly the same wafers. Several lots of several wafers each may be needed to obtain significant statistics when establishing process control, building software models or applying built-in reliability concepts [39].

2.3. Developing successful test structure implementations

The test vehicles described in the previous section are most successfully implemented when the user makes a concerted effort to develop and document a test structure methodology. Development of a test structure methodology is a hierarchical process. The user needs to address the elements of the methodology in this order:

(i) user specific application;
(ii) test structure designs;
(iii) measurement methods;
(iv) data analysis techniques; and
(v) test vehicle implantation.

When developing a methodology, users must consider many factors in their own environment in addition to the principles of the methodology discussed below.

Trade-offs should not be made that are counter to the most basic goals of test structure use. Test structures are intended to provide accurate and rapid diagnostic information about manufacturing processes. Sufficient data need to be collected and reduced in forms that meet user goals. Test structures must be compatible with the user environment, use a minimum of space, be easily fabricated and, most importantly, must address user goals. These concepts have been effective for nearly 20 years and are expressed in more detail in one of the first documents on test structure methodology [40] and in a more recent one [12].

The test structure methodology has been developed in the context of test structure data collection using a computer-controlled parametric test system with wafer probes that make electrical contact with the probe pads of the test structure. Parameters are obtained by direct measurement from the test structure or by extraction from test structure measurements. The collected measurements are reduced to the desired parameters using physics-based computations, statistical analysis, graphical techniques and modelling efforts. Further analysis is performed using computer-based techniques to achieve the user-specific application goals. For HgCdTe detectors, the same series of steps needs to be addressed while taking into account the so-far limited applications of automated probe stations with this technology.

2.3.1. User-specific application. Until it can be clearly stated why test structures are needed, the data that must be collected to meet goals cannot be specified, and test structure and test vehicle designs cannot be selected. The initial consideration involves whether test structures are to monitor well controlled production environments or to support development environments. This influences the test vehicle implementation. Knowledge of the materials, process, devices and circuits helps to define the parameters that need to be evaluated and the precision and accuracy required. This influences the test structure designs to be implemented on the test vehicle.

2.3.2. Test structure designs. Test structure designs should be modular and contained in a computer-aided design (CAD) test structure library. This allows efficient placement of the same designs anywhere on the test vehicle and ensures that designs on future test vehicles provide data consistent with established process history. The designs should be integrated with modular probe pads [41] to ensure rapid collection of data and ease of test code development. Kelvin probe pads should be used to eliminate probe-to-probe pad parasitic resistance, thereby improving measurement accuracy.

Test structures should be designed to minimize the effects of process faults or fabrication limitations; otherwise, the test structure may not be functional. Only well characterized test structures producing accurate, validated and consistent results should be implemented unless the purpose is to assess new test structure designs. Designs should generally use the same lay-out rules as the process, be tolerant of misalignments and use conservatively sized features unless smaller sizes are needed to induce the random faults the user wants to quantify. Users should consider designing structures with several sizes of linewidths, contacts and spacings, including those smaller than current design rules, to assess design rule limits and to enable the same mask to be used on future processes having smaller feature sizes. The designs and design constraints must be documented so that the CAD for the masks can be generated using the document, rather than relying on a collection of experts.

2.3.3. Measurement methods. Test equipment must be available to provide the precision required for the test structures selected to meet user goals. For example, a test structure such as the potentiometric alignment structure requires that enough current be forced to measure only a small difference in voltage; this measurement requires microvolt resolution. If an instrument with this precision is not available, making this type of measurement is likely to be useless.

The hardware and software of the tester system need to be validated to ensure quality measurements. Instruments should be regularly calibrated. The switching matrix and probe card responsible for connections used in probing should be verified using tester system diagnostics. Benchmarks and known artifacts should be used to check that, under software control, the correct currents and voltages are forced or measured at the right times and that sufficient settling times are allowed.

Once measurements are made, their reproducibility should be ensured. This is done after the desired set of measurements is made, by retesting selected sites on the wafer. For a PVW (process validation wafer) implementation, this usually means making complete test chip measurements at one chip site in each quadrant and one in the centre.

Similarly to the documentation for test structure designs, measurement method documentation should enable test code to be written and the measurements made.

2.3.4. Data analysis techniques. Data management was cited as a key problem when the first test structures were being measured [40] and remains so today. Large numbers of data can be easily collected, but presenting them for analysis is not trivial. Before analysis related to the user goals is begun, two evaluations should be made. First, retest data should be examined to ensure that the measurements are reproducible. If they are not, a determination of the cause and remeasurement are needed. A second pre-analysis evaluation is then made to exclude outliers [42] that will skew further statistical analysis.

In performing further analysis, experts in materials, processing and statistical engineering are needed. A variety of graphical representations of data [40] is useful for analysis. Some of these, such as box plots and wafer maps to show lot-to-lot and intrawafer variations and correlations, are illustrated in the case studies. These analytical techniques are successfully used to address user goals, but they are time-consuming and the results are somewhat analyst-dependent.

Advanced data analysis techniques based on machine learning [43], neural nets [44] and expert systems [45] are being investigated. They can address user goals in a more direct and consistent manner with varying degrees of success. These methods are not intended to replace an analyst but to aid in improving the scope and consistency of analysis.

2.3.5. Test vehicle implementation. The test vehicle implementation depends on the user goals identified in the application description. For process diagnosis and modelling tasks, a full-wafer or high-density implementation is needed. For comparing or monitoring a well controlled and well characterized process, reduced implementations are adequate. If valid comparisons must be ensured between manufacturers, a standard test vehicle is needed.

To lay out the selected test vehicle, the user must decide what test structures should be placed near each other to allow correlation and wafer mapping of the material, process, device and circuit parameters of interest. Designers should also prioritize the selected set of test structures so that if space limitations are encountered, the most important structures are not omitted. If space and the nature of a structure permit,

validation test structures should be included to corroborate test structure performance. For example, a validation alignment structure with a built-in offset, placed adjacent to the actual measurement structure, provides verification of the actual structure and is more efficient than optical verification.

Once a conceptual layout is specified, the use of a CAD cell library expedites layouts for the mask layers. During layout, the documented layout constraints should be observed if library designs are modified, because failure to do so can defeat the intended purpose of the test structure.

2.4. How test chips are applied to solve problems

This section presents three case studies examining how test structure data analysis techniques have been used to solve different types of process control problems. The first and second examples relate to a Si-based process and the third to a GaAs process. In the first example, a test structure serves as a direct process monitor for layer uniformity. The second example shows how a test structure can be used as an indicator to monitor a process parameter for which no measurement method is known. The third example illustrates using a test structure as a yield monitor. These examples show the use of box plots, wafer maps and basic physics. They also demonstrate the significance of intrawafer variations, lot-to-lot variations, and the correlation and lack of correlation between parameters. All the examples support the need for a process expert to be involved in the data analysis.

2.4.1. Solving process control problems in a Si-gate process. Both of the examples in this case study are based on data from the same test vehicle [24]. For every lot of wafers manufactured in a radiation-hardened Si-gate CMOS/SOS process, one process validation wafer (PVW) was included. The purpose of the PVW was to identify critical parameters that could be used for process monitoring and control. The PVW contained process-related parametric test structures and random fault test structures. Data sets collected over about two years were evaluated using statistical parameters, box plots and correlation of wafer map patterns.

The first example application shows how a non-uniformity problem in a phosphorus implant layer that was unknown to the manufacturer was discovered and found to be yield-limiting. The next example shows how a critical process parameter, the n-island doping concentration, for which no measurement method existed, was found to have a control and variability indicator in the p-channel threshold voltage.

Identifying a non-uniform layer problem. This example illustrates the use of test structures as process monitors for layer uniformity [24]. Contact resistance data for nearly 100 metal-to-n^+ contacts per lot showed wide lot-to-lot variation, as shown in the upper part of figure 1. As the data for the metal-to-p^+ contacts, as shown in
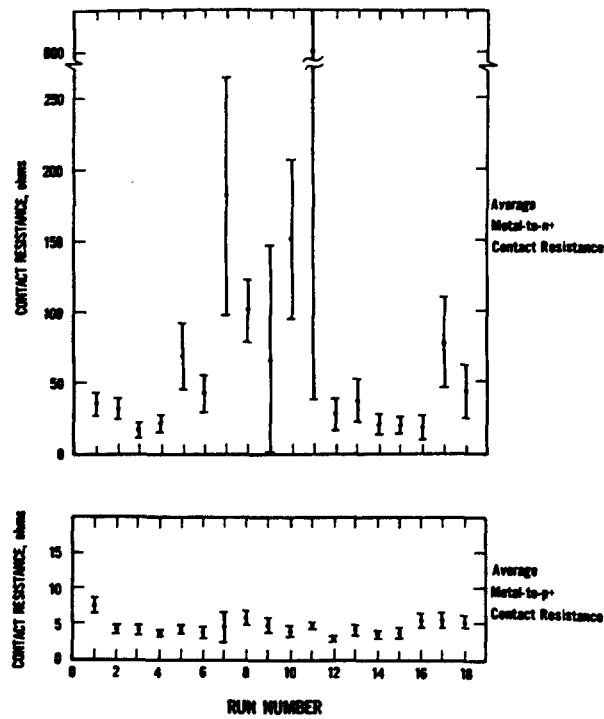
Figure 1. Variations in two closely related process parameters indicate a process control problem. Parameters were measured by lot (run number) over two years, utilizing NBS-16 process validation wafers fabricated with a radiation-hardened Si-gate CMOS process. The average metal-to-n^+ contact resistance (top) shows large lot-to-lot variations; however, the average metal-to-p^+ contact resistance (bottom) remains under control over the same time period.

the lower part of figure 1, showed little lot-to-lot variation and both types of contact were defined with the same process steps, lithography problems were not a likely cause of the variations. Further analysis involved looking for a correlation of the metal-to-n^+ contact resistance with some other process parameter. Once a correlation was found with the n^+ sheet resistance, as shown in figure 2, it appeared that a process step related to sheet resistance was a cause. The rest of the diagnosis was to determine which process steps and measured parameters were related to sheet resistance.

The sheet resistance was controlled by phosphorus implants through a gate oxide. When wafer maps of gate oxide thickness from a capacitor test structure were examined, a correlation with the sheet resistance was found. This led to the conclusion that non-uniform gate oxide caused variations in the concentration of the phosphorus implant, which caused the variations in the sheet resistance.

Identifying an indicator for a non-measurable parameter. This example traces the development of a means to control a process parameter for which no measurement method was available [24]. Data collected from nearly 100 MOSFETs per PVW showed a distinct intrawafer
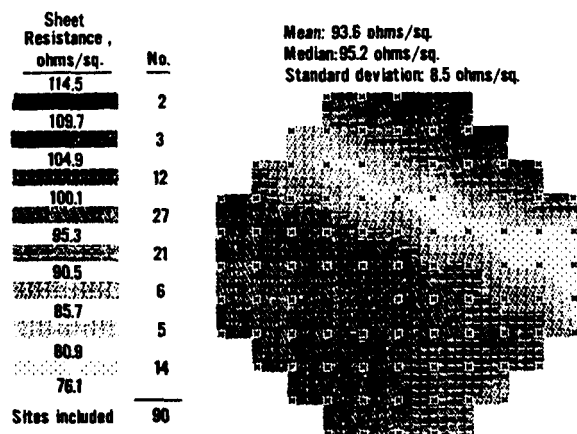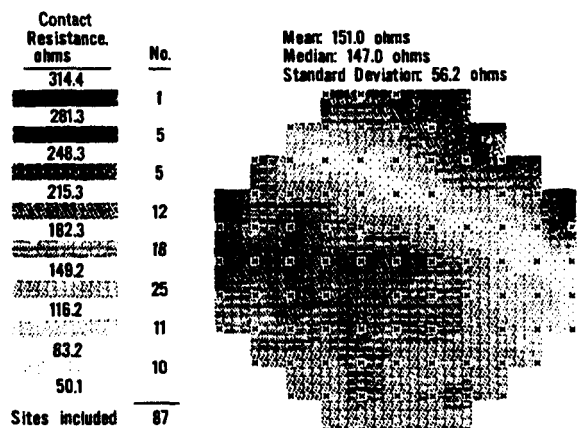
Figure 2. Similar wafer map patterns indicate a correlation between two process parameters from the NBS-16 process validation wafer in lot A10 of a radiation-hardened Si-gate CMOS process. Test results from sites with an 'X' symbol were used to calculate mean, median and standard deviation and to produce the wafer maps of the metal-to-n$^+$ contact resistance (top) and the n$^+$ sheet resistance (bottom).
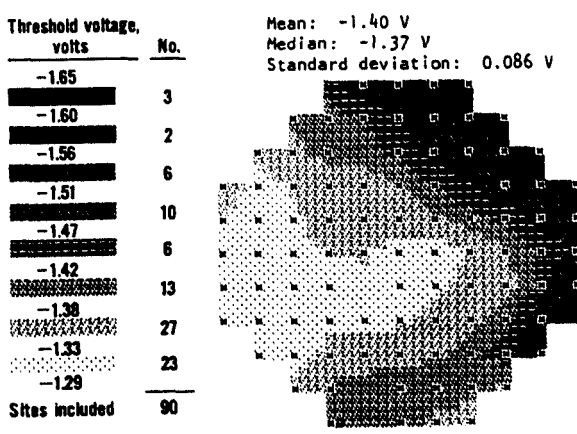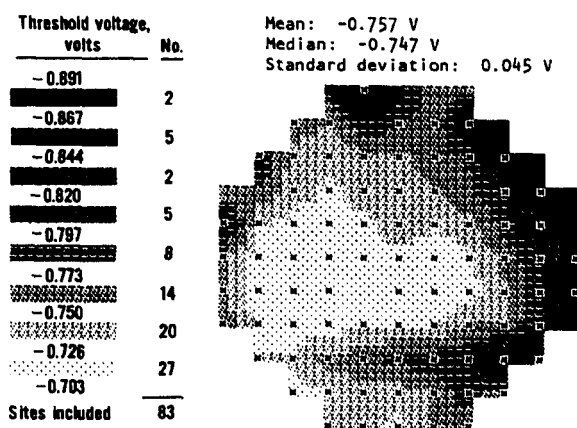
Figure 3. The similar patterns in wafer maps from NBS-16 process validation wafers in lot A16 (top) and lot A11 (bottom) indicate minimal lot-to-lot variations in a process parameter (p-channel threshold voltage). Distinct patterns in wafer maps indicate consistent intrawafer variation, indicating a process control problem related to wafer orientation.

variation and minimal lot-to-lot variations in the p-channel threshold voltage, as depicted in figure 3. As the intrawafer variation is notable with respect to the wafer flat, the cause is deduced to be related to some processing step where the wafer orientation remains fixed. For this process, the lithography and epitaxial growth steps must be examined further.

If lithography problems are the cause, the threshold voltage should correlate to linewidth data for polysilicon, epitaxial and metal. Since none of these linewidth wafer maps correlated with the threshold voltage wafer map, the conclusion was that lithography problems were not the cause.

Evidence concerning the epitaxial growth process was then investigated. From basic physics, dependence of the p-channel threshold on other parameters serves as a clue. The threshold voltage depends partly on the n-island dopant concentration, which is dependent only on the epitaxial growth process. The threshold voltage also depends

partly on the gate oxide capacitance, and the surface state charge, both of which are obtainable from test structure data. As no correlation existed between threshold voltage and either gate oxide capacitance or surface state charge, the answer appears to be in the process controlling the n-island doping. Here, a logical explanation is found for the threshold voltage variation: the wafer is always placed in the epitaxial reactor with the same orientation of the flat, and the wafer map pattern observed is consistent with the expected variation due to depletion of the dopant across the wafer during epitaxial processing.

Once the critical processing steps which affect the variability of the threshold voltage have been identified, control of the threshold voltage is then possible. Although the n-island concentration could not be directly measured, the p-channel threshold voltage provides an accurate indicator for its control. In a similar manner, predictive indicators can be developed for important parameters in any process.

2.4.2. Solving a yield and yield-monitoring problem in a GaAs process. The utility of a test structure methodology using high-density test structures and a comprehensive, standard test chip was demonstrated during the DARPA/ Tri-Service Microwave/Millimeter Wave Monolithic Integrated Circuit (MIMIC) Program [46]. As in the Si example, yield-limiting problems that were unknown to a manufacturer were found because of the high-density implementation of a comprehensive test chip. Because a standard test chip was used, lessons learned by one vendor could be more easily learned by another. Although a cooperative effort such as this may at first seem to be compromising competitive advantages, the end result was that vendors had more to gain than lose and freely participated without proprietary worries. One example that demonstrates these benefits follows.

During the three-year Phase 1 effort, four contractor teams produced sets of test wafers in addition to product development wafers. The vendors' processes were similar but not the same and all were in the later stages of development. With minor exceptions for processing differences, all the vendors used a standard, comprehensive test chip in a full-wafer implementation with about 200 test chips per wafer. Each test chip included FETs, parametric test structures and manufacturer-specific MMICs. Each wafer also included manufacturer-specific PCMs at five drop-in sites, at the middle and in each quadrant of the wafer. This implementation allowed significant statistical analysis, correlation and comparison of material, process and device performance among lots and between vendors. Including the vendor-specific PCM enabled correlation to be made between the Phase 1 data and historical data obtained from test structures that were designed differently but which measured the same parameters as the Phase 1 test structures.

In the following example, the drain-to-source current, I_{ds}, for a 200 μm FET was examined. The data distribution from the full-wafer data was compared with that from the drop-in areas. Only 48.3% of the full-wafer values for I_{ds} were within the parameter target range, as indicated by the black areas of the wafer map in figure 4. Also, the percent standard deviation ($\%\sigma$) is an unacceptable 28.1%. Note that all five drop-ins are within the black areas, indicating acceptable I_{ds} values. These data also have a much lower $\%\sigma$ of 10.7%. Had only the limited drop-in area data been considered, yield could have been considered adequate, rather than poor. The variability in the two data sets is further contrasted by the figure 4 box plots. The range of the two quartiles of data (the bounds of the box) around the median (line inside the box) is much larger for the full-wafer data than the limited data.

These high-density data raised a process control concern not evident with limited data. Investigation revealed that during the manual dip process for etching the channel, I_{ds} data from the drop-ins were used as a process control monitor. If the drop-in data did not meet the target values, additional partial dipping was done to 'correct' the etch depth. The process of manually correcting five areas of the wafer introduced the

Ids Yield

Yield: 504 (1044) = 48.3%
48.3% 250 < Ids < 350
Percent std = 28.1%
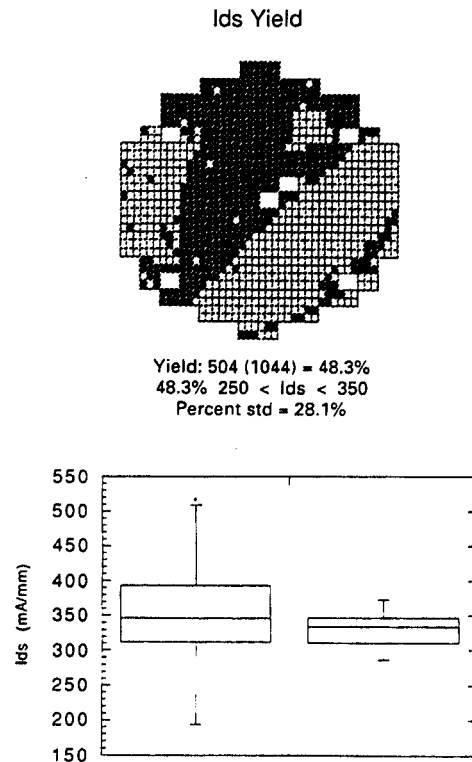
Figure 4. Drain–source current, I_{ds}, data from a transistor test structure used in a GaAs MIMIC process. The map of full wafer data (top) reveals poor yield, and the variability in the full wafer data (box plot, bottom left) reveals poor uniformity. The low variability in I_{ds} from the limited area drop-in site data (box plot, bottom right) illustrates how insufficient test structure sites can be misleading.

variability and non-uniformity observable in the box plots and wafer maps. This analysis prompted the manufacturer to replace the manual dip etch process with an automated spray etch process. This resulted in the improvements shown in figure 5. The full-wafer data yield increased to 83.1%, its $\%\sigma$ decreased to 8.0%, and the distribution and variability of the full-wafer and limited data sets became similar. This indicates good process control for I_{ds}. Now, data from the drop-in areas alone could be used to successfully predict yield. When this example was presented to the other manufacturers, some pursued their own analysis in this area and also adopted the automated spray etch process to improve yield.

Thus, for processes where control has not been demonstrated, high-density data can help manufacturers to detect and solve yield-limiting problems. In developmental or uncontrolled processes, relying on limited drop-in data could cause manufacturers to continue to expend resources on non-productive processing.

3. Current uses of test structures for IR detectors

This section describes the current use of test structures and specialized measurements most commonly applied

Ids Yield

Yield: 893 (1074) = 83.1%
83.1% 250 < Ids < 350
Percent std = 8.0%
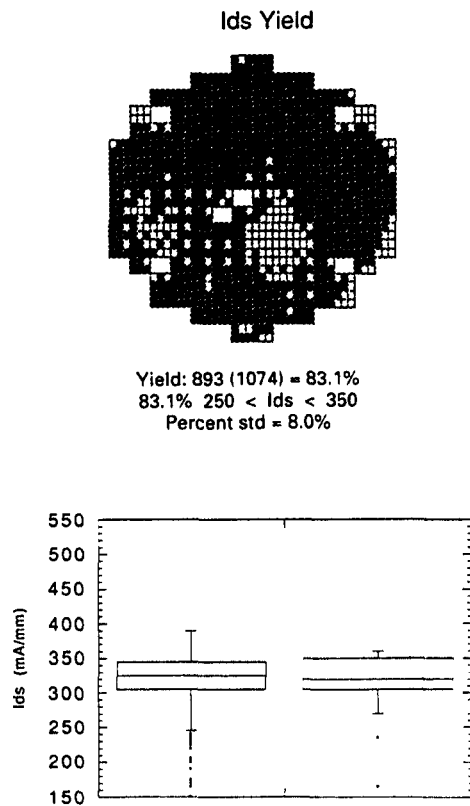
Figure 5. Following process modifications indicated from test structure results, wafer maps of I_{ds} show improved and controlled yield (top). Once the yield-limiting problems were controlled, the variabilities of the data from the full wafer (bottom left) and the limited area drop-in sites (bottom right) became comparable.

to IR detector devices, processes and materials. Section 3.5 presents a comprehensive listing of devices that are well described in the literature and that are thus candidates for inclusion in IR detector test chips.

IR detectors are fabricated as a wide range of devices based on a variety of materials, with a number of basic device structures, and encompassing everything from discrete detectors to large infrared focal plane arrays (IRFPAS). Most of the following discussion focuses on photovoltaic (p–n junction) diodes fabricated in HgCdTe, the technology with currently the most pressing and challenging applications for test structures. However, other significant devices, such as photoconductive and MIS detectors, and materials such as CdTe and silicon, are included as appropriate.

3.1. Similarities and differences with Si and GaAs ICs

IR detectors share some concepts in common with silicon ICs and GaAs MMICs: they are produced with much the same equipment and processes, and they have similar types of device structures. Some IRFPAS are nearing the same complexity and dimensions as large-scale integration (LSI) Si memory chips. Like memories, detector arrays contain many similar, regularly spaced devices.

However, there are pronounced differences between IR detectors and ICs. Infrared detectors are photosensitive devices which interact with electromagnetic radiation, similarly to Si photovoltaic solar cells. Many IR detectors require a narrow-bandgap semiconductor, such as HgCdTe, and must be operated at low temperatures. The need to characterize the material and devices as a function of incoming light and at low temperature has often necessitated that test structures be packaged and cooled in a Dewar before measurement.

$Hg_{1-x}Cd_xTe$ (HgCdTe) is a compound semiconductor whose electrical and optical properties are a function of composition. Detector performance is thus dependent upon composition, and arrays of detectors with uniform responses require material highly uniform in composition. Many detector applications also require thin layers of active material, requiring a precisely controlled thinning process. HgCdTe materials are grown by a variety of methods, including bulk growth, liquid-phase epitaxy (LPE), metal-organic chemical vapour deposition (MOCVD) and molecular beam epitaxy (MBE). The evolving crystal growth technology demands test structures and characterization procedures to evaluate material quality, uniformity and process effects rapidly and precisely.

Compared with Si, HgCdTe is easily damaged by temperature and radiation. Many fabrication processes can change the properties of the material by distributing composition or introducing electrically active defects. Test structures can be used to monitor such changes, as in the use of MIS capacitors to quantify ion milling damage [47]. Damage caused by contact with mechanical probes, especially in the active region of a device, can change the electrical properties of the material.

Compared with many semiconductor products, IR detectors are currently produced in low volume and with yields that are often very low. The starting substrates have small surface areas and, for some applications, the highest quality material is not plentiful. As a consequence, manufacturers have been reluctant to devote large areas on each substrate or in each fabrication lot, to test structures. In fact, the completed IR detectors themselves often serve as the primary test structures.

3.2. Characterization needs and concerns

IR detector material and producibility issues were reviewed in the keynote addresses at the 1991 HgCdTe Workshop [48, 49]. Here are a few of the key areas that are of general concern for HgCdTe photovoltaic materials, processes, devices and packages:

Materials. The uniformity of electrical and optical properties that depend upon composition, defects and dopant variations is a pressing concern for $Hg_{1-x}Cd_xTe$. To achieve a uniform device response over large areas, a low density of bulk defects and rigorous control of surface effects are required. With any photosensitive device, the critical parameters which determine device response are those which describe the recovery of the

semiconductor to equilibrium: minority carrier lifetime τ, diffusion length L and surface recombination velocity S_0.

Processes. Surface effects often dominate IR detector performance. Characterization of the process by which the passivation layer is formed and the quality of that passivation layer are therefore critical. The choice of passivation is more complex for HgCdTe than for Si, with no obvious optimum process for all applications from the wide variety of potentially useful native and deposited insulating layers examined to date.

Increasingly with future generations of detectors, performance will depend on the carefully tailored variations in material properties with depth. A variety of techniques is available to determine dopant profiles with depth (such as secondary-ion mass spectrometry (SIMS), neutron depth profiling and junction capacitance–voltage dopant–depth profiling), but existing non-destructive techniques are limited in their ability to resolve variations between multiple nanoscale layers.

Devices. Characterization of the individual detector performance and variations among detectors is of obvious concern, and is often addressed with test structures, i.e. detector elements fabricated especially for this purpose.

Infrared detectors are produced in four major classes of photon detectors (photoconductive, photovoltaic (p–n junctions), metal–insulator–semiconductor (MIS) and Schottky barrier), each with different device characterization concerns. *Photoconductive* detectors (see the review by Broudy and Mazarczyck [50]) contain no rectifying junctions, limiting the complexity of test structures. For *photovoltaic* detectors (reviewed by Reine et al [51]), the electrical characteristics of the p–n junction photodiodes must be determined, typified by the product of the photodiode dynamic resistance at zero-bias voltage and junction area, R_0A. Much effort has been devoted to understanding the origins of and controlling the dark current and noise. *Metal–insulator–semiconductor* photocapacitors (reviewed by Kinch [52]) are characterized by their capacitance and conductance versus voltage behaviour. An R_0A value is also an important figure of merit for MIS detectors, as well as other MIS properties including: the interface charges, tunnelling currents and the storage time of the MIS device. *Schottky diodes* are characterized by the Schottky barrier height.

Package. Practical detectors depend on sophisticated interconnect and packaging techniques for interfaces with additional signal processing electronics, for interfaces with the incident signal and for permanent installation in Dewars. The reliability of the device, interconnect and package is often characterized by elevated temperature bake-out and thermal cycling.

3.3. Current approaches to test structure use

For IR detectors, a larger emphasis has been placed on the quality of the detector performance, rather than the direct measurement of specific material and process parameters with test structures. Electrical characteristics and figures of merit of detector elements, such as R_0A, have been used as diagnostic tools. Measurements of material parameters have been developed using detector array elements as the test structure, i.e. using the R_0A of a photovoltaic detector as a measure of the lifetime of the material [53, 54], and estimating diffusion length by injecting current at one diode and determining the change in leakage at an adjacent diode.

Considerable pre-detector-fabrication characterization also takes place. For example, it is common practice to make use of a 'fast diode' process. This is a minimum-step, fast turn-around, diode process which can be fabricated on a corner of a substrate and be used to evaluate the quality of the material from the qualities of the 'fast diodes'. Prefabrication characterization also commonly includes Hall effect measurements and many of the non-test-structure characterization techniques discussed in the next section.

As far as test structures are concerned, a common strategy has been to make use of a series of devices which differ in one physical aspect and to see how that variation affects the measured electrical properties. Devices of this type include: (1) variable area diodes, (2) constant area, variable perimeter diodes [55], (3) diodes with varying contact metal areas [56] and (4) diodes with contact pads, both on the diode and off the active area.

As mentioned above, measurements are often not conducted until the devices have been packaged. Measurements on bonded devices from an IR detector process are often more repeatable and reliable than measurements using a probe station. The background photon flux can be difficult to control and quantify in measurements with probe stations. Also, determination of crosstalk and $1/f$ noise is much easier with packaged devices. However, the increased time and cost of packaging devices has no doubt hindered test structure applications in HgCdTe. Recent advances in probe station technology incorporate both low temperature and the use of a non-contact probe adapted from a scanning tunnelling microscope [57], and may facilitate greater pre-packaging test.

Despite the emphasis on other characterization procedures, test structures and test chips more along the lines of those applied in the silicon IC industry have been developed. Test chips consisting of both drop-ins for inclusion with product wafers and complete wafers of test chips for statistical parameter characterization are available for use in the IR detector industry. A layout of a test chip with a comprehensive set of test structures, courtesy of Rockwell International Inc.†, is shown in figure 6. This test chip, for an epitaxial, photovoltaic detector process, contains a mini-array of detectors, variable area diodes, MIS capacitors, lithographic Hall

† Certain commercial equipment, instruments or materials are identified in this paper in order to adequately specify the experimental procedure. Such identification does not imply recommendation or endorsement by NIST, nor does it imply that the materials or equipment used are necessarily the best available for the purpose.
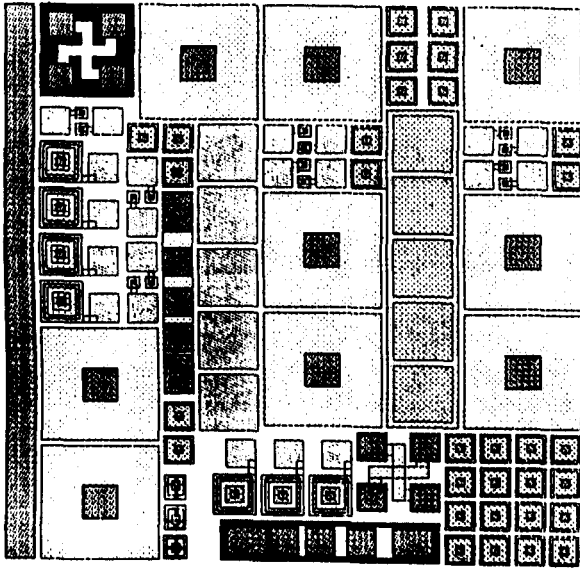
Figure 6. The comprehensive test chip for an epitaxial layer, HgCdTe photodiode process designed by McLevige at Rockwell International Corp., Science Center. (Courtesy Rockwell International Inc., with special thanks to M V McLevige and J Bajaj.)

effect structures and transmission line test structures. Uses of each of these classes of test structures are included in the discussion that follows.

3.4. Non-test-structure characterization

Due in part to the delicate nature of HgCdTe, various optical and non-contact electrical methods have been highly developed and applied to HgCdTe. In practice, these non-contact techniques play at least as large a part as test structures in the characterization of the material and processes. A complete review of such techniques is not possible here. However, any discussion of test structures must take into account the functions of several prevalent non-test-structure characterization techniques.

In particular, optical infrared transmission measurements are universally available to determine wafer composition (bandgap energy) and epitaxial layer thickness [58]. Instruments are available that can rapidly produce compositional maps of bandgap energy at nine or more points evenly spaced across the HgCdTe surface. Photoreflectance [59] provides a non-contact and low-temperature method with which to determine E_1 optical transition lineshapes and information on composition and defects. Other commonly applied optical techniques include: visible and far-infrared reflectivity, ellipsometry, electrolyte electroreflectance and laser-beam-induced current (LBIC) images of electrically active defects [60]. Also prevalent are non-contact methods to measure lifetime [61], such as optically modulated absorption, microwave transmission or reflection techniques, and the frequency response of photoluminescence.

Destructive characterization techniques are also used.

Dopant density as a function of depth has been determined by ion sputtering in conjunction with SIMS, Auger and x-ray photoelectron spectroscopy [62]. A simple measure of dislocation density and uniformity is the etch pit density (EPD) following exposure to an etchant [63]. Electron-beam-induced current (EBIC), usually measured in a scanning electron microscope (SEM), is used to determine minority carrier diffusion length [53, 64].

3.5. Specific test structures

Of the wide variety of test structures that have been developed for Si and GaAs, a smaller subset has been adapted for use with IR detector technology. This section contains a comprehensive listing of the test structures and some of the test methods used to characterize IR detector devices, processes and materials. Design considerations and the uses of each test structure are discussed. Most test structures were originally developed on the basis of Si technology. References in this section are made to applications to HgCdTe, along with a few key references to the original applications in Si.

3.5.1. Detector array elements as test structures. Detector array elements themselves, and mini-arrays (of around five-by-five elements), are important test structures. Separate elements for test allow the detector response to be characterized without compromising a functional array. Since the adjacent elements can limit the optical area and otherwise alter the response of a detector element, mini-arrays are useful to determine device performance while surrounded by other functioning detectors. For ease of interpretation, it is desirable for characterization to be made on detectors identical to working array elements. Variable-area diodes, discussed in the next section, can also be used for this sort of measurement and offer the advantage of quantifying the perimeter and area dependence of any measurement. Array elements have been used to characterize the detectors themselves, the noise and crosstalk, and to estimate minority carrier lifetime.

Detector characterization. Detector elements are quantified and compared by means of several well known figures of merit, which are discussed in detail in previous reviews [51, 52, 65]. The response of an infrared detector to an incident signal is characterized by the responsivity, R, in VW^{-1}, the quantum efficiency, η, the relative spectral response at the cut-off and peak wavelength, λ_{co} and λ_{peak}, in μm, and the time constant of the frequency response, τ in s. The signal-to-noise ratio of the elements is characterized by the noise equivalent power, NEP, in W $Hz^{-1/2}$, and the normalized detectivity, D^*, in cm $Hz^{1/2}$ W^{-1}. Capacitance–voltage dopant–depth profiling of the p–n junction photodiode has also been commonly implemented [64, 66].

Noise characterization. The sources of current noise in photodiodes include: Johnson–Nyquist noise of the

zero-bias impedance, $2kT/R_0$, shot noise, thermal noise due to thermally generated dark currents, and $1/f$ noise, which is characterized by a spectrum that varies as $1/f^\alpha$, with α close to 1 [51, 67].

Much effort has been devoted to the characterization and reduction of excess $1/f$ noise, a limiting factor in the performance of photodetectors and focal plane arrays [68–71]. Understanding the origins of $1/f$ noise is critical to guide actions to reduce it. Measurement of the noise versus frequency spectrum is straightforward (see, for example, the experimental set-up in [70]). Noise current density is usually measured over frequencies in the range of 1 Hz to 10 kHz, and also as a function of diode reverse bias and temperature. The $1/f$ noise has been correlated with detector bias, temperature, diode area and surface leakage currents [69, 71]. More detailed noise studies require a set of variable-area diodes, as discussed below, so that the surface or bulk origin of the noise, the mechanism that generates noise, and the relationship between noise and dark current can be determined [17].

Crosstalk determination. The influence of adjacent elements potentially affects the spatial and frequency resolution of detector array elements. The most straightforward method to quantify crosstalk is to measure the response of an element which is blocked to irradiation while operating adjacent (non-blocked) elements. Alternatively, a focused monochrome beam can be used to actuate individual elements while monitoring the response of adjacent elements.

Minority carrier lifetime from zero bias resistance product. For n^+ on p junction photodiodes, an estimate of minority carrier lifetime can be obtained from the measured R_0A versus temperature, T, via [53, 54]

$$R_0A = (N_A/qn_i^2)(kT/q)^{1/2}(\tau_n/\mu_n)^{1/2} \qquad (1)$$

where N_A is the base acceptor concentration, q is the electron charge, k is Boltzmann's constant, τ_n is the minority electron lifetime and μ_n is the electron mobility. The intrinsic carrier concentration, n_i, is calculated from expressions relating it to x, T and the bandgap, E_g [54, 72]; mobility is obtained from published data, and estimates of N_A from Hall measurements before device fabrication.

3.5.2. Variable-area diodes.

The perimeter-to-area ratio, P/A_j, of a square or circular diode will increase as the length of its side or radius is made smaller. Thus, a smaller-area diode will be more dependent on perimeter or surface effects and less dependent on area or bulk effects than a diode with the same shape but a larger area. This natural separation of surface and bulk effects makes a series of diodes with varying areas a powerful test structure for the evaluation of the potential performance of infrared photovoltaic devices, as well as the quality of the material, process and surface passivation.

Variable-area diodes refer to a series of three or more

p–n junction diodes, identical except for their area. Usually, the diodes are square or circular with junction areas varying by about three orders of magnitude, for example a set of five diodes with areas from 9.0×10^{-6} to $2.5 \times 10^{-3} \, cm^2$ [70]. Some variable-area-diode test structures have been designed with contacts off the active area (to eliminate damage induced by wire bonding) [70] and with a biasable guard ring (to better define the effective optical area of the diode) [73]. Variable-area diodes have been used to evaluate differences in diodes formed in the mesa or planar structures, as well as the qualities of different passivation procedures. A variation of this test structure would be a series of diodes with constant area, but variable perimeter (i.e. with different shapes) [55].

Parameters measured with variable-area-diode test structures include R_0A, dark current density and/or noise current density, often as a function of temperature. Calibration of the actual fabricated diode areas versus designed diode areas would also be desirable. Variable-area diodes have been used to determine the P/A_j dependence of $(R_0A)^{-1}$, the area dependence of the noise current, and the $1/T$ dependence of R_0A.

$(R_0A)^{-1}$ *versus P/A_j.* R_0A_j has been modelled as a sum of bulk-dependent and P/A_j proportional terms [74]:

$$(R_0A)^{-1} = (R_0A)_{bulk}^{-1} + (qn_iS_0W_0/V_{bi})(P/A_j) \qquad (2)$$

where S_0 is the surface recombination velocity in the depletion region where it intersects the HgCdTe surface, W_0 is the depletion width at zero bias and V_{bi} the built-in potential of the junction. The slope of the plot of $(R_0A)^{-1}$ versus P/A_j is proportional to S_0, while the projected intercept with $P/A_j = 0$ (corresponding to an infinite diode) gives $(R_0A)_{bulk}$. $(R_0A)_{bulk}$ is characteristic of the film and should not be dependent on diode geometry or process variations [75]. The degree that $(R_0A)^{-1}$ depends on P/A_j is a relative measure of the influence of surface originating currents on device behaviour. The ideal case is for the lowest possible contribution from surface currents, a low surface recombination velocity (S_0 approaching 0), and no P/A_j dependence.

A linear trend is only observed when hole diffusion lengths, L_h, are short compared with diode radii [75]. When L_h is long compared with diode radii, a significant component of the dark current will be due to lateral diffusion. In this case, smaller diodes will have a larger proportion of diffusion current than larger diodes, and $(R_0A)^{-1}$ versus P/A_j will have a parabolic dependence [75, 76].

If dark current is proportional to $(R_0A)^{-1}$, it would be expected to show the same type of P/A_j dependence.

Noise current density versus A_j. In an analogous manner, variable-area diodes have been used to determine whether noise currents in midwavelength infrared (MWIR) diodes originate at the surface or in the bulk [70, 77]. The analysis is based on Hooge's empirical equation for the noise power spectral density, S_I, in p–n junctions [70, 78]:

$$S_I = \alpha_H I^2/fN. \qquad (3)$$

Here, α_H is a fitted parameter referred to as the Hooge parameter, I is the current flowing in the system and N the number of carriers. Noise current is the square root of S_I. If the noise is due to an area (bulk) source, then both I and N should vary as the diode area, and noise current density should depend on $A^{1/2}$. If the noise is due to a perimeter (surface) source, then both I and N should vary as the square root of diode area, and noise current density should depend on $A^{1/4}$.

$R_0 A$ and/or dark current density versus $1/T$. The temperature dependence of $R_0 A$ and dark current density can be used to separate the contribution of diffusion currents and generation–recombination (G–R) currents to the total current [56, 70, 79]. Insight into the origin of the dominant current components in infrared detectors has been useful in optimizing device performance.

Common practice is to measure R_0 in a temperature range where the dominant carrier mechanism is changing. A plot of R_0 versus $1/T$ is then compared with lines approximating diffusion current ($1/n_i^2$ temperature-dependence dominated)

$$R_0 A_{\text{DIFF}} = (kT/q^2)(N_A/n_i^2)(\tau_n/D_n)^{1/2} \qquad (4)$$

and generation–recombination current ($1/n_i$ temperature-dependence dominated) [79, 80],

$$R_0 A_{\text{G–R}} = [(N_A kT/2\varepsilon) \ln(N_A N_D/n_i^2)]^{1/2}(\tau_0/qn_i) \quad (5)$$

where the subscripts DIFF and G–R refer to the contributions of diffusion and generation–recombination currents, respectively.

From the known behaviour of current-generating processes, diffusion currents are expected to dominate at temperatures higher than around 50 K, while G–R current dominance is expected at lower temperatures. Deviations from the G–R line at lower temperatures are often assumed to be from unknown sources of (most likely) surface leakage [56, 79]. However, tunnelling is often the dominant current mechanism in HgCdTe. Measurements on diodes consisting of n$^+$ on bulk p-type Hg$_{1-x}$Cd$_x$Te ($x \approx 0.22$) have shown that R_0 is diffusion-current dominated at high temperatures, while at lower temperatures, trap-assisted and band-to-band tunnelling currents dominate depending on reverse bias and temperature [56, 66].

An activation energy can be extracted from the inverse temperature dependence of dark current density and noise current densities using an Arrhenius-type equation [70]. The activation energy of the dark current should relate to the energy bandgap, while the activation energy of the $1/f$ noise current has been related to the location of G–R centres at about $0.75E_g$ within the bandgap.

3.5.3. Mini or lithographic Hall effect test structures.
Hall effect measurements are of central importance to the characterization of detector materials as they provide reliable values for carrier concentration and mobility. Hall measurements can be made on small, lithographically fabricated structures, as well as on the bulk samples.

Most interpretation has been developed under the assumption of sample homogeneity perpendicular to the magnetic field. Lithographic Hall bars provide data from a more localized area. When fabricated as part of a detector process, lithographic Hall bars can be made from both the substrate and any epitaxial layer(s). A variety of lithographic Hall bar and van der Pauw geometries have been used [81, 82]. For a discussion of design considerations for lithographic Hall test structures, see [11, 83].

To make the measurement most useful, the key concern is interpretation of the Hall effect measurements and relating the measured electrical quantities to the semiconductor electrical properties. This is particularly important for the case of two-layer structures [84], such as epitaxial layers, which are common in detector technology.

More detailed magnetotransport measurements, as a function of magnetic field and temperature, are of great interest for infrared detector materials because of the coexistence of multiple-carrier species [85]. For example, for p-type HgCdTe, variable magnetic field Hall effect measurements have yielded the Hg vacancy ionization energies, as well as carrier concentrations and mobilities for the majority carriers (heavy holes), minority carriers (electrons) and light holes [86].

The lithographic Hall effect structure can also be used in a variety of other measurements. Conductivity/resistivity measurements are commonly made in conjunction with Hall effect. With the addition of a source of illumination, Hall effect can be extended to the photo-Hall effect [87, 88] or the light-modulated Hall effect [89], which provides a measure of electron mobility in p-type material. Hall effect structures are also used for the photoelectromagnetic (PEM) effect (which can provide a measure of surface recombination velocity) [90–92], Shubnikov–de Haas effect (oscillatory magnetoresistance) [93], and photoconductivity (lifetime) measurements.

The Hall effect measurement has been used as a monitor of processing effects on materials, for example, ion beam milling effects on the surface of HgCdTe [47].

3.5.4. Methods to determine lifetime.
Carrier lifetime is an essential physical parameter for a complete description of the response of any IR detector material. A variety of contact methods, or methods using simple test structures, have been employed in the measurement of carrier lifetime in IR detector materials.

For a recent review of the issues and techniques for the measurement of lifetimes in HgCdTe, see the paper by Lopes et al in this issue [61]. An important issue in the measurement of lifetime is the distinction between lifetime measured by transient methods versus steady-state methods [94]. Significant differences between transient and steady-state lifetime have been detected and are a function of minority carrier trapping [94]. The steady-state lifetime appears to be more significant for device performance and a more appropriate measure of material quality [94].

Lifetime measurements are often conducted as a function of temperature, carrier concentration and composition. The dependence of the lifetime on these variables has been used to identify the dominant generation–recombination process within the test structure [64]. Minority carrier lifetime has been related to bandgap and carrier concentration [61]. The difference in lifetime between impurity-doped and vacancy-doped HgCdTe has been studied [94]. The temperature dependence of lifetime has been used to determine the trap energy and density of bulk Shockley–Read centres [64, 95]. The most common methods of determining carrier lifetimes in HgCdTe include the following.

Photoconductive decay (PCD). In the photoconductive decay technique, lifetime is determined from the slope or 1/e point of the current or voltage decay following irradiation with a short laser pulse. The theory and measurement instrumentation is described in some detail in [81, 82, 95–97]. The pair of (ohmic) contacts required for measurement of lifetime by PCD has been obtained from simple circular dots, Hall devices [94], a multiprobe Hall bar with six sets of contacts spaced 5×10^{-2} cm apart down the length of the sample [81], and using a pair of plated electrodes, each covering about one-third of the wafer perimeter, allowing mapping of lifetime over a circular wafer [95]. The measurement can also be made on an MIS capacitor and ohmic contact, providing a measure of surface recombination velocity [98]. The measurement is dependent on the spacing and size of the contacts, which must be chosen to avoid minority carrier sweep-out [99]. Lifetimes measured by PCD and by optically modulated absorption have been compared [96], as well as lifetimes by the PCD, photoconductivity and PEM techniques [91].

Diode reverse-bias pulsed recovery technique (PRT). The pulsed recovery technique determines lifetime by the recovery of the current following an abrupt reversal of a junction from forward to reverse bias. The theory and instrumentation for HgCdTe photodiodes is summarized in Polla *et al* [64]. A simple interpretation of PRT measurements, developed for Si diodes without necessarily abrupt junctions [100], is applicable to HgCdTe [64]. Both p–n junction [64] and Schottky barrier [101] diodes have been used in the measurement.

Steady-state photoconductivity. For the steady-state photoconductivity measurement, the sample is illuminated with a laser or blackbody through a low-frequency chopper and the PC signal measured by a lock-in [47, 91, 94]. The measured photoconductive signal is proportional to $\mu_n \tau_n$. The technique is dependent on a separate measurement of minority carrier mobility. The light-modulated Hall effect has been used for this mobility measurement [90]. The steady-state photoconductivity measurement was then made with the same Hall devices.

Zero-bias resistance–area product. The determination of lifetime from the $R_0 A$ product of a p–n junction photodiode [53, 54, 79] is described in section 3.5.1.

Photoconductive frequency response (frequency domain or frequency roll-off). The lifetime of a semiconductor can be obtained from the short-circuit AC photocurrent as a function of light intensity modulation frequency response of a diode [102, 103]. Photocurrent (or responsivity of a photodiode) is plotted versus chopping frequency. The lifetime and fall-off frequency are related. The test structure is a photodiode or Schottky contact.

Photoelectromagnetic effect (PEM). A discussion of the technique and considerations for its application to HgCdTe is given in [90]. In the photoelectromagnetic effect, a magnetic field is applied perpendicular to a diffusion current of optically generated excess carriers. Analysis of the PEM current, I_{PEM}, versus magnetic field gives surface recombination velocity, carrier mobility and bulk lifetime. The test structure used is the Hall bar. By combining photoconductivity and PEM measurements, both bulk minority carrier lifetime and mobility can be obtained [91].

3.5.5. Metal–insulator–semiconductor (MIS) capacitors.
Metal–insulator–semiconductor capacitors can be fabricated along with photovoltaic detectors, as well as MIS photocapacitor detectors. The capacitors can be formed on all layers of an epitaxial process. Information about the semiconductor, the insulator, and the semiconductor-insulator interface can be obtained. The MIS test structure should incorporate a guard-ring gate, surrounding the primary MIS capacitor, to isolate the test structure from the surrounding surface [104].

The various insulators and passivation schemes used in infrared detectors have recently been reviewed [105]. Insulating layers for MIS capacitors on HgCdTe consist of either deposited dielectric films or thin native films with an overcoat of a deposited dielectric. Popular passivation materials for HgCdTe include: evaporated or sputter-deposited ZnS [90, 106–109], anodic (native) oxide (usually with an overcoating of ZnS) [104, 110, 111], anodic (native) sulphide (usually with an overcoating of ZnS) [90–92, 112–114], SiO$_2$ (deposited by several techniques) [115–117], evaporated Zn$_x$Pb$_{1-x}$S [118], SiN$_x$ [105], anodic (native) fluoride [119] and other II–VI compounds such as CdTe [120]. The MIS capacitor is the essential test structure for the evaluation and comparison of passivation and insulating layers of HgCdTe.

Like photovoltaic diodes, MIS photocapacitors have been their own most important test structure. Key parameters are the $R_0 A$ product and the storage time, τ_{st}. Storage time refers to the time required for minority carrier dark current to fill the potential well resulting from a voltage pulse of the MIS capacitor into deep depletion [52]:

$$\tau_{st} = C_{ox} V / J_d \qquad (6)$$

where C_{ox} is the insulator capacitance, V the voltage pulse, $C_{ox} V$ is the well capacity and J_d is the total minority carrier dark current density.

Beyond detector characterization, the MIS capacitor can be used for the determination and study of other material, interface and process parameters:

Capacitance, conductance, and current versus gate voltage. A large variety of standardized measurements developed for Si MOS capacitors, as detailed in [121], has been applied to MIS capacitors on HgCdTe. Primarily, these involve the measurement of the capacitance, conductance and DC current of the MIS capacitor as a function of gate bias, AC measurement frequency, temperature, time and illumination. Properties of the insulator that can be obtained include thickness, resistivity, breakdown electric field, insulator fixed charge and traps within the insulator. The doping level of the bulk semiconductor is obtainable from the change in capacitance from accumulation to inversion, but more importantly, the formation and dynamics of an inversion layer induced by the applied electric field can be studied [112]. This can provide insight into the minority carrier generation and recombination rates and mechanisms. At the interface, the properties of the fast and slow surface states can be obtained, as well as an indication of the metal–semiconductor work function [122] and the semiconductor–insulator barrier height. Interface states in HgCdTe MIS capacitors have often been quantified via the conductance method [112, 116, 123], or the high/low $C-V$ technique [117].

The $C-V$ of MIS capacitors has also been used to profile the carrier concentration of ion-implanted junctions in HgCdTe by fabricating an array of MIS capacitors, separated by 500 μm, on a wafer whose surface has been slant etched, resulting in a gentle grade in depth [91]. The properties of MIS structures fabricated on double-layer heterostructures, consisting of a 1 μm layer of wide-bandgap HgCdTe on top of a 5 μm layer of narrow-bandgap HgCdTe, have also been reported [124].

Unique concerns of MIS capacitors from HgCdTe. Interpretation of electrical measurements of HgCdTe MIS structures is not as straightforward as for an Si MOS [104, 112, 125, 126]. To adequately explain the observed behaviour of MIS capacitors on narrow-bandgap semiconductors, the following factors have to be considered:

  (i) the non-parabolic conduction band [104, 126];
  (ii) degeneracy in the occupancy of the free carriers [104, 126];
  (iii) compensation and partial ionization of impurities and defects [126];
  (iv) inversion layer quantization [104]; and
  (v) interband or Zener tunnelling [104, 125].

As a consequence of conduction band degeneracy, the most obvious effect on the measured $C-V$ characteristics is that the capacitance does not saturate in accumulation for n-type capacitors, or in the strong inversion for p-type capacitors in the low-frequency regime [104, 126]. Oscillations in $G-V$ response of MIS capacitors on p-type

HgCdTe are explained as arising from indirect (trap-assisted) tunnelling and inversion layer quantization effects [104, 127]. With the application of a magnetic field, the formation of Landau levels in the two-dimensional gas at the oxide/HgCdTe MIS interface has been observed at temperatures around 10 K [128]. The oscillations in the $C-V$ and $G-V$ response are shifted by an applied magnetic field in a manner consistent with tunnelling into the lowest Landau level associated with each electric subband [128]. Spicer has pointed out that due to the 'weak' Hg–Te bond, the bulk and surface properties of HgCdTe intercommunicate and are more closely related in HgCdTe than in III–Vs and Si [129].

Defect and damage characterization. An important sub-class of measurements concerns the determination of the effects of radiation damage on the MIS capacitor. Even low levels of short-wavelength visible light can create lateral non-uniformities in the fixed charge density of the HgCdTe–insulator interface [104]. Visual light exposure can result in a multiple flatband effect, though the effect can be removed by annealing. The MIS capacitor has also been used as a monitor of ion-milling damage [47, 130]. Dislocations and hillocks have been observed to affect the storage time and tunnelling currents of MIS capacitors on MBE-grown HgCdTe [110, 111].

3.5.6. Gated p–n junction diodes and MISFETs.
Gated diodes and metal–insulator–semiconductor field-effect transistors (MISFETs) are the most complex test structures in common usage. They require formation of p–n junctions, high-quality insulating layers and ohmic contacts.

Gated p–n junction diode. A gated p–n junction diode (GD) consists of a p–n junction with a concentric MIS gate surrounding and slightly overlapping the junction at the surface. A second, outer concentric gate is often employed to isolate the GD from the surface beyond the inner gate [115]. A gated diode is also formed by the gate and one source/drain region of a MISFET [131], though it is preferred that the gate completely surround the junction. The gate(s) of the GD offer the ability to precisely control the surface potential around the p–n junction. As a test structure applied to IR detectors, gated diodes have been used to localize and identify surface leakage effects and currents, as well as to provide an indication of surface recombination velocity and lifetime.

Typical characterization measurements include the reverse junction current (at a series of fixed diode reverse bias) and the R_0A product as a function of gate voltage. The outer guard gate (if it exists) would be held at a constant voltage, usually to accumulate the surface as determined from $C-V$ measurements. The R_0A product is also measured as a function of gate voltage and $1/T$. The GD has also been employed for $C-V$ dopant profiling of the region beneath the junction [66].

The well established interpretation of gated-diode reverse current versus gate voltage characteristics for Si GDs is described in [132]. As with the MIS capacitor, GDs in HgCdTe differ from those in Si; extensions of the

existing theory to cover GDs in HgCdTe are discussed in [51, 113, 115]. In narrow-bandgap material ($x \approx 0.22$) and temperatures of 77 K and below, gated diode behaviour is dominated by tunnelling currents [51, 66, 113, 114, 133]. The surface potential determines whether surface or bulk tunnelling prevails [113]. When the gate is biased to cause accumulation of the surface adjacent to the junction, surface tunnelling across the surface junction dominates. When the area adjacent to the junction has been inverted, tunnelling currents in the field-induced junction dominate.

For HgCdTe with a wider bandgap ($x \approx 0.45$ to 0.3) and at higher temperatures (145 K), gated diode characteristics are closer to those of Si GDs [115]. When the gate is biased to cause accumulation of the surface adjacent to the junction, the gated diode current is dominated by trap and band-to-band tunnelling. When the area adjacent to the junction is biased in depletion, generation current from interface states will contribute to the reverse-bias junction current. A measure of surface recombination velocity, S_0, at the intersection of the depletion region and the gate, can be obtained from the magnitude of the current in this region [115, 133]. The calculation is complicated due to uncertainties in the effective area of the induced junction [133]. When the area adjacent to the junction has been inverted, the effects of surface generation are suppressed and the effective area of the junction is increased by the field-induced junction. The magnitude of the current in this region is dependent on the minority carrier lifetime in the metallurgical and field-induced junction.

Gated diode studies of surface passivation. The gated diode, like the MIS capacitor, is a useful test structure with which to study surface effects. Measurements of noise and dark currents in gated diodes as a function of temperature, junction area and gate bias have been used to separate bulk and surface mechanisms contributing to $1/f$ noise [113, 134]. Gated diode characteristics have been used as a monitor of fixed charge and interface trapped charge density in long-wavelength infrared (LWIR) HgCdTe as a function of gamma radiation total dose [133].

MISFETs. Enhancement- and depletion-mode MISFETs in HgCdTe [107, 114, 131, 135–137] and a metal–semiconductor FET (MESFET) in CdTe [135], as well as simple digital circuits [106, 136, 138] have been reported. MISFETs in $Hg_{1-x}Cd_xTe$ offer some prospect for monolithic integration of signal processing functions with detectors [131]. The suitability of FETs for use in electronics circuits is commonly assessed from their DC characteristics (drain-to-source current as a function of drain-to-source voltage and gate voltage, threshold voltage, surface mobility, etc) and small-signal AC characteristics (drain–source resistance, amplification factor, transconductance, etc) [106, 136]. Simple MISFET digital invertor circuits on HgCdTe have been characterized at speeds to 1 MHz [106].

MISFETs in HgCdTe have been used as test structures to study quantum phenomena in reduced dimensions.

Subband spectroscopy, the observation of subbands due to inversion layer quantization effects, has been reported using gated diodes and MISFETs [107, 108]. MISFETs have been used as a test structure for the quantum Hall effect [139] and magnetotransport measurements [107]. By changing the gate voltage on an HgCdTe MISFET, the magnetotransport of the two-dimensional electron gas has been modulated from classical free electron behaviour to weak-localization behaviour [107].

3.5.7. Ohmic and Schottky contacts. Simple metal-to-semiconductor contacts are critical components of detectors, and their behaviour must be characterized. Ohmic and Schottky contacts are also employed as test structures in a number of different types of measurement. Theoretical models and experimental experience indicate that for $x < 0.4$, metal contacts are expected to be ohmic contacts on n-type and Schottky barriers on p-type $Hg_{1-x}Cd_xTe$ [140]. For $x > 0.4$, metal contacts are expected to be Schottky barriers on both n- and p-type material [140, 141].

Ohmic contacts. All detector structures require ohmic contacts. High-quality ohmic contacts are essential for photoconductive detectors. Ohmic contacts are characterized primarily by their resistance, which can be divided into components due to the semiconductor and to the contact resistance. Methods to determine the specific contact resistivity, the geometry-independent parameter which describes the ohmic metal-to-semiconductor contact, are described in the following sections.

Stable ohmic contacts have been used as test structures to measure minority carrier lifetime via the photoconductive decay technique, as well as for spreading resistance [62], resistivity and contact resistivity. Resistivity can be related to doping concentration and, at room temperature, to the x value of $Hg_{1-x}Cd_xTe$ [72, 142].

The defect structure and surface chemistry play an important part in determining the quality of an ohmic contact to HgCdTe [143, 144]. Ohmic contact test structures have been used to evaluate the effects of the contact formation process, surface preparation, intentional interfacial layer formation and annealing [144].

Schottky contacts. Schottky barriers to HgCdTe are themselves another class of photodiodes [101] and a critical component necessary before a MESFET can be fabricated [141]. Schottky contacts are commonly characterized by their current–voltage and capacitance–voltage responses. From the $I–V$ characteristic, the diode ideality factor, n, reverse leakage current and breakdown electric field can be determined. The Schottky metal-to-semiconductor contact is characterized by the barrier height, ϕ_B, which can be determined from $I–V$ or $C–V$ measurements. The barrier height has also been obtained from the activation energy of the variation of the saturation current with inverse temperature [101]. Dopant density profiles have also been obtained from $C–V$ measurements [145].
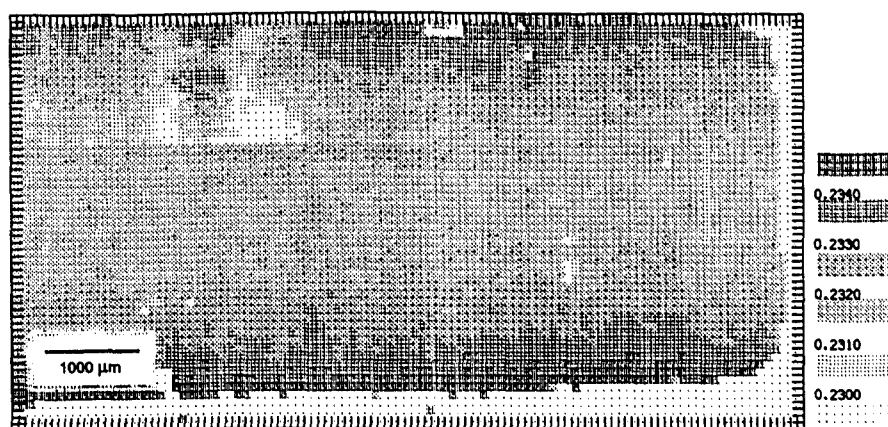
Figure 7. Magnified image of *x*-value variations in solid state recrystallized Hg$_{1-x}$Cd$_x$Te produced with a high spatial density of identical test structures and automated data collection. The region mapped is 0.5 by 1.0 cm. Each gray scale level represents a variation in *x* of 0.001.

Schottky contacts have been employed to study the process of their formation and to evaluate the effects of metal/HgCdTe chemical reactivity on contact properties [141]. In addition, Schottky barriers have been employed in DLTS studies of CdTe [145], for determination of minority carrier diffusion lengths by EBIC [101] and determination of minority carrier lifetimes by the reverse recovery technique [64].

Spreading resistance. Information about dopant variations and heterojunctions in HgCdTe has been obtained by the spreading resistance technique, implemented with mechanical point-pressure contacts along a wafer-level slant-etched surface [62]. Fine-scale variations in dopant as a function of depth is of growing concern for next-generation detector structures grown by MBE.

Spreading resistance measurements of HgCdTe can also be conducted using an array of lithographic ohmic contacts [142]. In concept, when combined with a wafer-level slant-etched technique, like that used by Fraenkel *et al* [91] with MIS capacitors, a contact array may also be used for spreading resistance dopant depth profiling.

Transmission line. The transmission line model (TLM) has been commonly applied for contact resistivity measurements of metal-to-HgCdTe contacts. The TLM can be implemented with the transmission line tap resistor, though simpler versions, like that described in [146], are in use. In essence, the transmission line consists of a series of metal contacts with varying spacing, often four metal rectangles with three different spacings are employed. Resistance between the contacts is plotted as a function of contact separation, with the contact resistance estimated as the resistance projected to zero contact separation. A measure of semiconductor sheet resistance can also be obtained.

The advantage of test structures based on TLM is their ease of fabrication: they can be realized by one photolithographic step and etch of a deposited metal layer. A disadvantage of transmission line-type test structures is that the total resistance is very sensitive to contact area variations and contains parasitic resistances due to current crowding effects. For low-resistance contacts on silicon ICs, test structures incorporating a single contact, such as a four-terminal contact resistor, have come to be preferred over TLM [16]. Contact resistivity and test structures for its determination have recently been reviewed [147].

Variable-area ohmic contacts. A set of variable area ohmic contacts has been used to determine the contact resistivity via the method of Cox and Strack [148], and to quantify the 1/*f* noise of the contact [143]. The range of areas of the ohmic contacts was used to determine a dependence of power spectral density of resistance fluctuations on contact diameter of $S_R \propto d^{-m}$, which can be related to the source of the 1/*f* noise [143].

Contact array. The structure consists of an array of contacts, precisely defined by photolithography through an insulating layer, and metal probe pads [142]. A contact diameter of 5 μm and a contact spacing of 40 μm have been used, though contact dimensions are limited only by photolithography. Two-probe spreading resistance, four-point probe resistivity and contact resistivity measurements can be made. Maps of HgCdTe resistivity variations with 120 μm spatial resolution have been produced by rapid measurement of many contact sites with an automatic probe station [142].

Resistivity variations are then related to *x*-value variations. The technique is illustrated in figure 7, in which the typically axial variations in *x* value, from a cross section of an HgCdTe crystal grown by solid state recrystallization, have been mapped.

Figure 7 represents another class of test structure applications, a refinement of the low-resolution wafer-scale maps shown in figures 2 to 5. Here, a high spatial

density of identical test structures and automated data collection are used to map variations in material parameters (resistivity and x value). The technique results in magnified images, such as would be obtained from a microscope sensitive to resistivity and x-value variations.

3.5.8. Miscellaneous test structures.

Variably spaced diodes. Variably spaced diodes are used to determine the minimum spacing at which adjacent diodes short, thus providing an estimate of junction spread. The same devices can be used to estimate diffusion length by injecting current at one diode and determining the change in leakage at an adjacent diode.

Deep-level characterization techniques. A variety of techniques, which make use of the depletion region of a p-n junction, Schottky barrier or MIS capacitor, has been employed to characterize deep levels in HgCdTe. These include deep-level transient spectroscopy (DLTS) [145, 149, 150], admittance spectroscopy (AS) [150] and thermally stimulated current (TSC) [150].

4. An expanded role for test structures?

This section contains suggestions for test structures with potential applications to IR detectors. Section 4.2 contains a discussion of how the silicon methodology can be applied to HgCdTe IR detectors, as well as some practices that the experience with silicon and GaAs test structures suggests would be beneficial if applied to IR detectors.

4.1. Test structures with potential applications to IR detectors

The devices discussed in section 3 form a relatively complete set of test structures for materials characterization, including some applications which are not usual for Si, such as magnetotransport measurements. One test structure that has been developed and useful in Si technology, is the *contact resistor* [16, 18]. The contact resistor is a single-contact, Kelvin-probe-type test structure used for the determination of contact resistance and contact resistivity. Contact resistors avoid the problems with some parasitics and sensitivity to material non-uniformity that plague TLMs.

In addition, some classes of test structures that are important in Si technology are scarcely mentioned in connection with HgCdTe. These are primarily test structures concerned with evaluation of photolithography and fabrication defect density, which can be important for yield prediction.

Linewidth. Numerous variations of bridge and van der Pauw structures for the measurement of sheet resistance and electrical linewidth have been developed [14, 23]. These are useful for evaluation of both the etching and photolithography processes used to define the different layers of the process. Linewidth test structures are very similar to photolithographic Hall bars.

Alignment. Variations of sheet resistors can also be applied as potentiometric electrical alignment test structures [21, 23]. The residual misalignment over a wafer, possibly due to wafer warpage and non-planarity, or misregistration, can be detected and quantified.

Meander contact chains. Contact chains are a series of contacts with tabs of metal connecting every other pair of contacts. These can be short chains of contacts, taking up a very small area, with probe pads every few contacts, to determine if the process to open and form contacts is functioning as desired. Larger, addressable arrays of contacts are also used to determine the yield of the contact process.

Step coverage. Step-coverage structures are simply two-terminal resistors designed to evaluate metal-overlayer electrical continuity [24, 29]. A typical step-coverage structure consists of a serpentine metallization line crossing a parallel array of epitaxial island lines at hundreds or thousands of steps. With the growing complexity and reduced dimensions projected in next-generation IRFPAs, some of these test structures may find application for evaluation of step coverage.

Gate dielectric integrity array. The fault density of gate insulators can be determined from an array of capacitors [151]. The leakage current, caused by photolithography-induced defects or dielectric breakdown of gate and passivation insulators, is determined as a function of capacitor array size. Along similar lines is the *random access fault* test structure, consisting of an array of individually addressable MISFETS.

4.2. Strategies for extending applications of test structures

The literature contains references to an abundance of test structures that have been applied to materials and process characterization for IR detectors. The techniques to fabricate the test structures and an understanding of the unique aspects of applying the test structures to HgCdTe have been developed. These test structures have been applied to a wide range of specific problems, most notably to the isolation and optimization of sources of dark current and noise in photodetectors. Major manufacturers of IR detectors have a range of test chips for their processes, which include some or many of the devices described above. However, information about specific instances of application of test structures for process control is harder to come by.

The central lesson from the experience of the Si and GaAs industries is that *yield improvement requires improved process control by means of the intelligent application of test structures.* The optimum test structure design and implementation for each application can only be achieved through an extensive effort as part of process

development, guided by the methodology that we have presented. The key elements of that methodology translate into the following specific areas demanding further study:

(i) Determine what information is needed from test structures by correlating detector performance and yield with material and process parameters.

(ii) Determine how that information will be obtained. Correlate the output from test structure measurements with relevant HgCdTe material and process parameters. Develop and document standard, well-characterized test structure designs as cells in a CAD library. Develop and document a detailed test plan.

(iii) The information from test structures should get to someone who can act upon it in a short period of time. Develop and document detailed data analysis procedures.

The experience of applying test structures to Si ICs and GaAs MMICs also indicates that changes in some current practices and trends in IR detector manufacture could produce positive results.

Low required product volume cannot justify a low-yield process. The relatively small numbers of devices required and the nature of the market have not demanded large yields to satisfy product demand or to ensure profitability. Even if production goals can be satisfied with a low-yield process, the quality and reliability of devices fabricated with a low-yield process could be compromised .

The substantial advantages of automated testing prior to packaging should motivate development and applications of cryogenic probe stations with low pressure or non-contact (i.e. non-damaging) probes. The need to test devices at low temperatures and as a function of illumination has often been most easily satisfied by packaging devices before any testing. Consequently, development and use of cryogenic automated probe stations to acquire statistically significant numbers of data at the wafer level and before packaging (a major application of Si and GaAs test structures) have not been vigorously pursued. Automated testing prior to packaging allows a statistically significant number of data to be rapidly acquired, and determination of the product functionality prior to the expensive packaging steps. Designated test chips, made to be compatible with automated probing, could be included on production substrates even if the final product were unsuited to prepackage probing. Probe measurements on these designated test chips will not compromise products.

An intelligently selected and applied set of test structures is more informative than finished product performance in the diagnosis of which specific process steps may be limiting detector performance or yield. A larger emphasis has been placed on the quality of detector performance rather than the direct measurement of specific material and process parameters with test structures. Instead of optimized test structure measurements, the electrical characteristics and figures-of-merit of detector elements have been used to deduce some

material parameters, and as a general indicator of device and process quality.

Low yield of a process justifies larger wafer area devoted to test structures. Early on, the poor quality of HgCdTe and resultant low yield of fabricated devices has, paradoxically, encouraged a reluctance to devote valuable HgCdTe surface area to test structures. Without test structures to verify process and material parameters, poor detector performance or unexplained failure of elements in an array is often attributed, without evidence, to low-quality starting material. Test vehicle (chip) design methodology facilitates judgment as to the appropriate number and kind of test structures, even for processes with very low yields.

Cooperation between users, and standardization of test structure designs and measurement methods, can result in gains in productivity beneficial to all. The experience of researchers at the National Institute of Standards and Technology (NIST) can play a part in extending the current applications of test structures to IR detectors. Potential areas of impact will be to augment the design and applications of the existing test structures, to develop new test structures aimed at specific process or material problems, and to develop comprehensive test structure implementation plans. Cooperation among the users can further increase the impact of test structures on IR detector manufacturability. NIST and industry should work together to develop common test structures and implementation approaches.

5. Summary

The experience of the silicon IC and GaAs MMIC industries has proved that the intelligent application of test structures will result in significant yield improvement and yield maintenance through improved process control. In these industries, test structures are commonly employed throughout the product cycle to determine and monitor process centring parameters, to measure critical device and circuit parameters, to identify and quantify yield limiting defects and to measure processing tool performance.

An abundance of test structures has also been applied to materials and process characterization for IR detectors. These test structures have been applied to a wide range of specific problems, most notably to the isolation and optimization of sources of dark current and noise in photodetectors. However, the IR detector industry does not appear to employ test structures for process control with the same discipline as the Si and GaAs industries.

We have described the uses of test structures, as well as a methodology for implementing user-specific applications of test structures. If these recommendations are observed in the manufacture of IR detectors, real gains in yield, in reliability and in performance can be expected.

References

[1] Buehler M G and Linholm L W 1981 *Proc. 2nd Cal. Tech. Conf. on VLSI*, *(Pasadena, CA, 19–21 Jan. 1981)* (Pasadena, CA: Caltech Computer Science Department) pp 135–51

[2] Fichtner W 1988 Process simulation *VLSI Technology* ed S M Sze (New York: McGraw-Hill) ch 10

[3] Murarka S P and Peckerar M C 1989 *Electronic Materials Science and Technology* (New York: Academic) pp 78–80

[4] Duncan W M and Westphal G H 1985 GaAs material preparation and characterization *VLSI Electronics Microstructure Science* vol 11, ed N G Einspruch and W R Wisseman (Orlando: Academic) pp 65–70

[5] Williams R E 1990 *Modern GaAs Processing Methods* (Boston: Artech House) pp 248–51

[6] Carver G P and Buehler M G 1980 *IEEE Trans. Electron Devices* **27** 2245

[7] Buehler M G 1980 *J. Electrochem. Soc.* **127** 2284

[8] Williams R E 1990 *Modern GaAs Processing Methods* (Boston: Artech House) pp 336–45

[9] Buehler M G 1980 *J. Electrochem. Soc.* **127** 701

[10] Palmer D W 1990 Characterization of semiconductors by capacitive methods *Growth and Characterization of Semiconductors* ed R A Stradling (Bristol: Adam Hilger) pp 187–224

[11] Stradling R A 1990 Hall, magnetoresistance and infrared conductivity measurements *Growth and Characterization of Semiconductors* ed R A Stradling (Bristol: Adam Hilger) pp 165–85

[12] Buehler M G 1983 Microelectronic test chips for VLSI electronics *VLSI Electronics Microstructure Science* vol 6, ed N G Einspruch (New York: Academic) pp 540–7

[13] van der Pauw L J 1958 *Philips Res. Rep.* **13** 1

[14] Buehler M G, Grant S D and Thurber W R 1978 *J. Electrochem. Soc.* **125** 650

[15] Buehler M G and Thurber W R 1978 *J. Electrochem. Soc.* **125** 645

[16] Mazer J A, Linholm L W and Saxena A N 1985 *J. Electrochem. Soc.* **132** 440

[17] Mazer J A and Linholm L W 1984 *IEEE Electron Dev. Lett.* **5** 347

[18] Proctor S J, Linholm L W and Mazer J A 1983 *IEEE Trans. Electron Devices* **30** 1535

[19] Carver G P, Mattis R L and Buehler M G 1982 *NBS Interagency Report* NBSIR 82-2548 (July)

[20] Yen D, Linholm L W and Buehler M G 1982 *J. Electrochem. Soc.* **129** 2313

[21] Carver G P, Linholm L W and Russell T J 1980 *Solid State Technol.* **23**(9) 85

[22] Russell T J and Maxwell D A 1979 *NBS Special Publication* 400-51

[23] Allen R A and Cresswell M W 1992 *Solid State Technol.* **35**(3) 435

[24] Linholm L W 1981 Semiconductor measurement technology: the design, testing, and analysis of a comprehensive test pattern for measuring CMOS/SOS process performance and control *NBS Special Publication* 400-66

[25] Williams R E 1990 *Modern GaAs Processing Methods* (Boston: Artech House) pp 345–55

[26] Buehler M G and Linholm L W 1981 *Proc. 1981 Custom Integrated Circuits Conf. (Rochester NY, 11–13 May, 1981)* (New York: IEEE) pp 142–6

[27] Linholm L W, Mazer J A and Galloway K F 1985 *Digest of the DoD/NBS Conf. on Microelectronic Electromagnetic Susceptibility (Gaithersburg MD 12–13 March 1985)* (Gaithersburg, MD: National Bureau of Standards) pp 16–18

[28] Radack D J and Linholm L W 1987 *Proc. IEEE 1987 Custom Integrated Circuits Conf. (Portland OR, 4–7 May 1987)* (New York: IEEE) pp 579–81

[29] Sayah H R and Buehler M G 1988 *IEEE Proc. Microelectronic Test Structures* **1** 23–8

[30] Schafft H A, Younkins C D and Grant T C 1984 *Proc. 1984 Reliability Physics Symp.* (New York: IEEE) pp 250–5

[31] Ipri A C and Sarace J C 1977 *RCA Rev.* **38** 323

[32] Hasan T F, Perloff D S and Mallory C L 1981 *Semiconductor Silicon/1981* ed H R Huff *et al* (Pennington, NJ: The Electrochemical Society) pp 868–81

[33] Yen D 1982 *Proc. Soc. Photo-Optical Instrum. Engrs., Integrated Circuit Metrology* **342** 73

[34] Perloff D S 1978 *IEEE J. Solid State Circuits* **13** 436

[35] Yen D and Linholm L W 1984 *Test & Measurement World* **4**(3) 48

[36] O'Keefe T W, Cresswell M W, Linholm L W and Radack D J 1986 *IEEE VLSI Workshop on Test Structures (Long Beach CA, 17–18 Feb. 1986)* (Redondo Beach, CA: All About Meetings) pp 82–94

[37] Russell T J, Maxwell D A, Reimann C T and Buehler M G 1979 *Solid State Technol.* **22**(2) 71

[38] Buehler M G and Sawyer D E 1976 *1976 Government Microcircuit Applications Conf. Digest of Papers (Orlando FL, 9–11 Nov. 1976)* (Fort Monmouth, NJ: US Army Electronics Command) pp 62–5

[39] Buehler M G 1977 *Proc. Symp. on Utilization of LSICs in Military Systems, (Arlington VA, 9–11 Aug. 1977)* pp III102–III117

[40] Schafft H A 1976 Semiconductor measurement technology: ARPA/NBS Workshop III, test patterns for integrated circuits. *NBS Special Publication* 400-15

[41] Buehler M G 1979 *Solid State Technol.* **22** 89

[42] Linholm L W, Mattis R L, Frisch R C and Reeve C P 1981 *Semiconductor Silicon/1981* ed H R Huff *et al* (Pennington, NJ: The Electrochemical Society) pp 906–20

[43] Cresswell M W, Khera D, Linholm L W and Schuster C E 1992 *IEEE Trans. Semicond. Manuf.* **5** 255

[44] Khera D, Zaghloul M E, Linholm L W and Wilson C L 1989 *Proc. ICMTS 1989, Int. Conf. on Microelectronic Test Structures (Edinburgh, Scotland, 13–14 March 1989)* (New York: IEEE) pp 201–4

[45] Linholm L W, Khera D, Reeve C P and Cresswell M W 1988 *Proc. 1988 IEEE Int. Conf. on Microelectronic Test Structures (Long Beach CA, 22–23 Feb. 1988)* (New York: IEEE) pp 160–3

[46] Schuster C E, Linholm L W and Gillespie J K 1991 *1991 Government Microcircuit Applications Conf. Digest of Papers (Orlando FL, 5–7 Nov. 1991)* (Fort Monmouth, NJ: US Army Labcom) pp 335–8

[47] Bahir G and Finkman E 1989 *J. Vac. Sci. Technol.* A **7** 348

[48] Balcerack R and Brown L 1992 *J. Vac. Sci. Technol.* B **10** 1353

[49] Tennant W E, Cockrum C A, Gilpin J B, Kinch M A, Reine M B and Ruth R P 1992 *J. Vac. Sci. Technol.* B **10** 1359

[50] Broudy R M and Mazurczyck V J 1981 (HgCd)Te photoconductive detectors *Semiconductors and Semimetals* vol 18, ed R K Willardson and A C Beer (New York: Academic) p 157

[51] Reine M B, Sood A K and Tredwell T J 1981 Photoconductive infrared detectors *Semiconductors and Semimetals* vol 18, ed R K Willardson and A C Beer (New York: Academic) p 201

[52] Kinch M A 1981 Metal–insulator–semiconductor infrared detectors *Semiconductors and Semimetals* vol 18, ed R K Willardson and A C Beer (New York: Academic) p 313

[53] Lanir M, Vanderwyck A H B and Wang C C 1978 *J. Appl. Phys.* **49** 6182

[54] Nemirovsky Y and Rosenfeld D 1988 *J. Appl. Phys.* **63** 2435

[55] Bajaj J, Williams, G M, Sheng N H, Hinnrichs M, Cheung D T, Rode J P and Tennant W E 1985 *J. Vac. Sci. Technol.* A **3** 192

[56] DeWames R E, Pasko J G, Yao E S, Vanderwyck A H B and Williams G M 1988 *J. Vac. Sci. Technol.* A **6** 2655

[57] Verdún H R, Tran D, Koechner W and Martinka M 1992 *Proc. 1992 Workshop on Mercury Cadmium Telluride (Boston MA, 23–25 Oct. 1992)* (Woodbury, NY: AIP Conference Proceedings)

[58] Price S L and Boyd P R 1993 *Semicond. Sci. Technol.* **8** 842

[59] Amirtharaj P M, Dinah J H, Kennedy J J and Boyd P R 1986 *J. Vac. Sci. Technol.* **4** 2028

[60] Bajaj J, Bubulac L O, Newman P R, Tennant W E and Raccah P M 1987 *J. Vac. Sci. Technol.* A **5** 3186

[61] Lopes V C, Syllaios A J and Chen M C 1993 *Semicond. Sci. Technol.* **8** 824

[62] Boukerche M, Yoo S S and Faurie J P 1990 *J. Vac. Sci. Technol.* A **8** 1233

[63] Norton P W and Erwin A P 1989 *J. Vac. Sci. Technol.* A **7** 503

[64] Polla D L, Tobin S P, Reine M B and Sood A K 1981 *J. Appl. Phys.* **52** 5182

[65] Scribner D A, Kruer M R and Killiany J M 1991 *Proc. IEEE* **79** 66

[66] Nemirovsky Y, Rosenfeld D, Adar R and Kornfeld A 1989 *J. Vac. Sci. Technol.* A **7** 528

[67] Tobin S P, Iwasa S and Tredwell T J 1980 *IEEE Trans. Electron Devices* **27** 43

[68] Nemirovsky Y and Unikovsky A 1992 *J. Vac. Sci. Technol.* B **10** 1602

[69] van der Ziel A, Handel P H, Wu X L and Anderson J B 1986 *J. Vac. Sci. Technol.* A **4** 2205

[70] Bajaj J, Blazejewski E R, Williams G M, DeWames R E and Brown M 1992 *J. Vac. Sci. Technol.* B **10** 1617

[71] van der Ziel A, Fang P, He L, Wu X L, van Rheenen A D and Handel P H 1989 *J. Vac. Sci. Technol.* A **7** 550

[72] Higgins W M, Pultz G N, Roy R G, Lancaster R A and Schmit J L 1989 *J. Vac. Sci. Technol.* A **7** 271

[73] Sood A K and Tobin S P 1980 *IEEE Electron Device Lett.* **1** 12

[74] Briggs R J, Marciniec J W, Zimmermann P H and Sood A K 1980 *Tech. Digest IEDM* **496**

[75] Krueger E E, Pultz G N, Norton P W and Mroczkowski J A 1990 *Proc. 1990 IRIS Detector Specialty Group (Gaithersburg MD, August 1990)*

[76] Pultz G N, Norton P W, Krueger E E and Reine M B 1991 *J. Vac. Sci. Technol.* B 1724

[77] Chung H K, Rosenberg M A and Zimmermann P H 1985 *J. Vac. Sci. Technol.* A **3** 189

[78] Kleinpenning T G M 1985 *J. Vac. Sci. Technol.* A **3** 176

[79] Lanir M and Riley K J 1982 *IEEE Trans. Electron Devices* **29** 274

[80] Kolodny A and Kidron I 1980 *IEEE Trans. Electron Devices* **27** 37

[81] Kinch M A, Brau M J and Simmons A 1973 *J. Appl. Phys.* **44** 1649

[82] Fastow R and Nemirovsky Y 1989 *J. Appl. Phys.* **66** 1705

[83] Look D C 1989 *Electrical Characterization of GaAs Materials and Devices* (Chichester: John Wiley) p 1–21

[84] Larrabee R D and Thurber W R 1980 *IEEE Trans. Electron Devices* **27** 32

[85] Meyer J R, Hoffman C A, Bartoli F J, Arnold D A, Sivananthan S and Faurie J P 1993 *Semicond. Sci. Technol.* **8** 805

[86] Gold M C and Nelson D A 1986 *J. Vac. Sci. Technol.* A **4** 2040

[87] Bartoli F J, Meyer J R, Allen R E and Hoffman C A 1982 *J. Vac. Sci. Technol.* **21** 241

[88] Meyer J R, Bartoli F J and Hoffman C A 1987 *J. Vac. Sci. Technol.* A **5** 3035

[89] Schacham S E and Finkman E 1986 *J. Appl. Phys.* **60** 2860

[90] Finkman E and Schacham S E 1989 *J. Vac. Sci. Technol.* A **7** 464

[91] Fraenkel A, Schacham S E, Bahir G and Finkman E 1986 *J. Appl. Phys.* **60** 3916

[92] Schacham S E and Finkman E 1990 *J. Vac. Sci. Technol.* A **8** 1171

[93] Seiler D G and Stephens A E 1991 The Shubnikov–de Haas effect in semiconductors: a comprehensive review of experimental aspects *Landau Level Spectroscopy* ed G Landwehr and E I Rashba (Amsterdam: Elsevier) p 1035

[94] Fastow R and Nemirovsky Y 1990 *J. Vac. Sci. Technol.* A **8** 1245

[95] Pratt R G, Hewett J, Capper P, Jones C L and Quelch M J 1983 *J. Appl. Phys.* **54** 5152

[96] Radford W A, Shanley J F and Doyle O L 1983 *J. Vac. Sci. Technol.* A **1** 1700

[97] Schacham S E and Finkman E 1985 *J. Appl. Phys.* **57** 2001

[98] Lopes V C, Wright W H and Syllaios A J 1990 *J. Vac. Sci. Technol.* A **8** 1167

[99] Baker I M, Capocci F A, Charlton D E and Wotherspoon J T M 1978 *Solid-State Electron.* **21** 1475

[100] Kuno H J 1964 *IEEE Trans. Electron Devices* **11** 8

[101] Polla D L and Sood A K 1980 *J. Appl. Phys.* **51** 4908

[102] Reichl H and Brent H 1975 *Solid-State Electron.* **18** 453

[103] Suzuki E and Hayashi Y 1992 *J. Electrochem. Soc.* **139** 1741

[104] Beck J D, Kinch M A, Esposito E J and Chapman R A 1982 *J. Vac. Sci. Technol.* **21** 172

[105] Nemirovsky Y and Bahir G 1989 *J. Vac. Sci. Technol.* A **7** 450

[106] Dreifus D L, Kolbas R M, Han J W, Cook J W and Schetzina J F 1990 *J. Vac. Sci. Technol.* A **8** 1221

[107] Palm E C, Szott W, Kobiela P S, Kirk W P, Schiebel R A and Reed M A 1988 *J. Vac. Sci. Technol.* A **6** 2716

[108] Schiebel R A 1991 *J. Vac. Sci. Technol.* A **9** 1759

[109] Zimmermann P H, Reine M B, Spignese K, Maschhoff K and Schirripa J 1990 *J. Vac. Sci. Technol.* A **8** 1182

[110] Chandra D, Tregilgas J H and Goodwin M W 1991 *J. Vac. Sci. Technol.* B **9** 1852

[111] Goodwin M W, Kinch M A and Koestner R J 1989 *J. Vac. Sci. Technol.* A **7** 523

[112] Nemirovsky Y and Bloom I 1988 *J. Vac. Sci. Technol.* A **6** 2710

[113] Nemirovsky Y and Rosenfeld D 1990 *J. Vac. Sci. Technol.* A **8** 1159

[114] Nemirovsky Y, Adar R, Kornfeld A and Kidron I 1986 *J. Vac. Sci. Technol.* A **4** 1986

[115] Rosbeck J P and Blazejewski E R 1985 *J. Vac. Sci. Technol.* A **3** 280

[116] Tsau G-H, Sher A, Madou M, Wilson J A, Cotton V A and Jones C E 1986 *J. Vac. Sci. Technol.* A **4** 1983

[117] Wilson J A and Cotton V A 1985 *J. Vac. Sci. Technol.* A **3** 199

[118] Orent T 1989 *J. Electrochem. Soc.* **136** 3057

[119] Weiss E and Mainzer N 1988 *J. Vac. Sci. Technol.* A **6** 2765

[120] Nemirovsky Y 1990 *J. Vac. Sci. Technol.* A **8** 1185

[121] Nichollian E H and Brews J R 1982 *MOS Physics and Technology* (New York: Wiley)

[122] Strong R L 1992 *J. Vac. Sci. Technol.* B **10** 1530

[123] Yang M J, Yang C H, Kinch M A and Beck J D 1989 *Appl. Phys. Lett.* **54** 265

[124] Goodwin M W, Kinch M A and Klestner R J 1990 *J. Vac. Sci. Technol.* A **8** 1226

[125] Bhan R K, Dhar V, Chaudhury P K, Gopal V and Chhabra K C 1990 *Semicond. Sci. Technol.* **5** 1093

[126] Bloom I and Nemirovsky Y 1988 *Solid-State Electron.* **31** 17

[127] Kinch M A, Beck J D and Zwirble W T 1980 *Tech. Digest IEDM* **508**

[128] Waterman J R, Wagner R J and Perez J M 1989 *J. Vac. Sci. Technol.* A **7** 381

[129] Spicer W E, Silberman J A, Morgan P and Lindau I 1982 *J. Vac. Sci. Technol.* **21** 149

[130] Elkind J L 1992 *J. Vac. Sci. Technol.* **10** 1460

[131] Kolodny A, Shacham-Diamand J and Kidron I 1980 *IEEE Trans. Electron Devices* **27** 591

[132] Grove A S 1967 *Physics and Technology of Semiconductor Devices* (New York: Wiley) pp 298–315

[133] Schirripa J J 1990 *Master's Thesis*, Massachusetts Institute of Technology

[134] Radford W A and Jones C E 1985 *J. Vac. Sci. Technol.* A **3** 183

[135] Dreifus D L, Kolbas R M, Tassitino J R, Harper R L, Bicknell R N and Schetzina J F 1988 *J. Vac. Sci. Technol.* A **6** 2722

[136] Schiebel R A 1987 *Tech. Digest IEDM* 132

[137] Nemirovsky Y, Margalit S and Kidron I 1980 *Appl. Phys. Lett.* **36** 466

[138] Schiebel R A, Dodge J and Gooch R 1989 *Electron. Lett.* **25** 530

[139] Kirk W P, Kobiela P S, Schiebel R A and Reed M A 1986 *J. Vac. Sci. Technol.* A **4** 2132

[140] Spicer W E, Friedman D J and Carey G P 1988 *J. Vac. Sci. Technol.* A **6** 2746

[141] Leech P W and Kibel M H 1991 *J. Vac. Sci. Technol.* A **9** 1770

[142] Kopanski J J, Lowney J R, Novotny D B, Seiler D G, Simmons A and Ramsey J 1992 *J. Vac. Sci. Technol.* B **10** 1553

[143] Beck W A, Davis G D and Goldberg A C 1990 *J. Appl. Phys.* **67** 6340

[144] Krishnamurthy V, Simmons A and Helms C R 1990 *J. Vac. Sci. Technol.* A **8** 1147

[145] Collins R T, Keech T F and McGill T C 1982 *J. Vac. Sci. Technol.* **21** 191

[146] Berger H H 1972 *J. Electrochem. Soc.* **119** 507

[147] Scorzoni A and Finetti M 1988 *Mater. Sci. Rep.* **3** 79

[148] Cox R H and Strack H 1967 *Solid-State Electron.* **10** 1213

[149] Jones C E, Nair V, Lindquist J and Polla D L 1982 *J. Vac. Sci. Technol.* **21** 187

[150] Polla D L and Jones C E 1981 *J. Appl. Phys.* **52** 5118

[151] Mitchell M A and Linholm L W 1981 Semiconductor measurement technology: test patterns NBS-28 and NBS-28A: random fault interconnect step coverage and other structures *NBS Special Publication* 400-65

APPENDIX C

INVITED PAPER

$Hg_{1-x}Cd_xTe$ characterization measurements: current practice and future needs*

D G Seiler, S Mayo and J R Lowney

Materials Technology Group, Semiconductor Electronics Division, National Institute of Standards and Technology, Gaithersburg, MD 20899, USA

Abstract. An extensive industrial survey of the importance and use of characterization measurements for HgCdTe materials, processes and devices has been completed. Seventy-two characterization/measurement techniques were considered and thirty-five responses were received. This information was sought for a study on materials characterization and measurement techniques of parameters and properties necessary to improve the manufacturing capabilities of HgCdTe infrared detectors. The nature of materials characterization is defined, and an overview is given of how it is related to improving IR detector manufacturing. Finally, we present a description of the characterization survey and a summary of the survey results. Major aspects of the results include: (1) ranking the 72 techniques by their importance and frequency of use, (2) listing the parameters or properties determined by each technique, (3) enumerating the most important properties that need to be measured, (4) indicating the key measurement techniques that most need to be developed, enhanced or improved, and (5) giving key overall comments.

1. Introduction

Mercury cadmium telluride, $Hg_{1-x}Cd_xTe$, where x is the Cd mole fraction of the semiconducting alloy, is the essential material for fabrication of intrinsic infrared detectors for a wide variety of military and space applications. The focus of the materials technology has evolved from small, bulk-grown wafer material to relatively large epitaxial wafers grown in special reactors with multiple capabilities. However, $Hg_{1-x}Cd_xTe$ is a complex material, and because of the large number of array elements used for imaging and the wide range of its uses, it may be ten times more complex than GaAs, and even more when compared with Si [1]. In addition, the cost and affordability of IR focal plane arrays are now of critical concern and must be addressed along with the quality and performance required [2]. It is our belief that, in order to attain high quality and top performance of IR detectors at affordable costs, enhanced understanding and use of key materials/process/device characterization methods are critical. The development of new or improved diagnostic and screening techniques will have an impact on device yields and lead to the establishment of empirical and physical models necessary for quantitative prediction of detector behaviour. Finally, we stress

that revolutionary new techniques might spring from the combination or revitalization of older ones.

Improved IR detector manufacturing may also come if US companies link their own R&D efforts involving characterization measurements more closely to the production side. As pointed out by Reich, most American technological firms draw a sharper distinction between R&D on the one side and production and marketing on the other than Japanese firms [3]. In Japan, research, product development and the design of manufacturing processes are carried out such that they are not isolated from each other. As a result, simultaneously, knowledge from one area can readily influence decisions made in other areas.

This paper attempts to describe the current importance and use of materials characterization methods now being utilized for $Hg_{1-x}Cd_xTe$ materials, processes and devices as well as to present future needs. The paper is based upon an extensive industrial survey (72 characterization/measurement techniques listed and 35 responses received) carried out over the past two years. First, in section 2, we describe the nature of materials characterization and related measurements by defining it in terms of its activities. Next, in section 3 and in three appendices, we present a description of the survey and its results. Major aspects of the survey results presented here include: (1) ranking the 72 techniques by their importance and frequency of use, (2) listing the parameters or properties

753

determined by each technique, (3) enumerating the most important properties that need to be measured, (4) indicating the key measurement techniques that most need to be developed, enhanced or improved, and (5) giving key overall comments.

2. Materials characterization—nature of, activities and definition

Materials characterization is an important subject. Many published papers, reports, activities and even organizational structures within industrial laboratories use these words readily. Unfortunately, materials characterization is a rather complex area, and many types of definitions and common usage, often assumed, have evolved. It is the purpose of this section to review the activities and nature of materials characterization, as well as to come up with the best overall definition that encompasses all aspects of this topic.

Over the years, many people have adopted the definition developed in 1967 by the Committee on Characterization of Materials, Materials Advisory Board, National Research Council: 'Characterization describes those features of composition and structure (including defects) of a material that are significant for a particular preparation, study of properties or use, and suffice for reproduction of the material' [4]. Hannay also seems to have adopted this approach in 1967—'In simple terms our definition of characterization means what atoms are present and where they are. This is all that is required in principle, for characterization.... Eventually, however, one hopes to understand properties in terms of composition and structure, and to eliminate the need for a description of properties, as well as the method of preparation, in characterization' [5]. Unfortunately, these definitions limit the characterization methods to those that provide information about composition, structure and defects, and exclude those methods that yield information primarily related to materials properties, such as thermal, electrical, optical, mechanical, etc. Also, some workers use on a less frequent basis the terminology 'analysis of materials' in an interrelated way. For example, Meieran *et al* (1987) in defining this subject say, 'The intent of analysis of materials is to understand material properties in order to modify them to make more usable, useful, economical objects' [6].

We give here what we feel is the broadest (and perhaps best) possible definition for materials characterization that includes its incorporation as an integral part of the manufacturing process: Activities that 'determine the structure and composition, properties, and performance of materials, and the interrelationships among these elements.' Specific subcomponents relate to: '(1) structure and composition, including the development of instrumentation and its application to determine chemical and geometric descriptions of materials, from atomic to macro scales; (2) properties, involving the measurement of properties and their relationship to structure and composition; and

(3) performance, involving analysis of the behaviour of materials in simulated or actual use' [7].

In most industrial laboratories, materials characterization measurements reflect an exceptionally diverse, multi- and interdisciplinary set of activities. The background and skills required to achieve enhanced yields of $Hg_{1-x}Cd_xTe$ IR focal plane arrays at low costs do not coincide with those of the ordinary disciplines. The scope of materials characterization in device production covers a wide range of activities—quality assurance of incoming materials, wafer screening methods, proper control and monitoring of manufacturing processes, diagnostic and failure analyses, and in playing the essential role of determining how a manufactured device differs from its intended design and function. Consequently, its importance is well established in the semiconductor industry; e.g. 'a key to the continued progress in VLSI technology is the refinement and development of new materials characterization tools.... The coupling of characterization methods to the fabrication process permits proper control of the resultant product and the tailoring of material properties to specific physical requirements, for practical applications or for fundamental studies' [8]. 'Materials characterization and device development have evolved in a synergistic partnership which has been fundamental to the semiconductor industry' [9].

The materials characterization/measurement techniques for HgCdTe materials, processes and devices listed in the survey involve three major areas of characterization: chemical and physical (or structural), electrical and optical. Figure 1 shows a simple overview of these areas, showing some representative examples, what the techniques determine and some general comments. In most cases there exists a strong interrelationship between these areas or techniques. For example, the composition of $Hg_{1-x}Cd_xTe$ greatly affects the electrical and optical properties, as well as the chemical and physical. Consequently, relevant measurements in any of the three categories of techniques shown in figure 1 can provide a determination of the composition. Obviously, intercomparisons of techniques must be carried out by correlating all the results.

3. Description of characterization survey

The survey was designed to measure the importance and use of various characterization/measurement techniques for $Hg_{1-x}Cd_xTe$ materials, processes and IR detector devices by industrial laboratories. An extensive list of 72 techniques that cover the vast majority of methods used to characterize semiconductors was assembled. Note that the authors realized that this list would not be exhaustive and so asked a general question in the survey as to what measurement techniques have been inadvertently omitted from the list. In addition, for each technique, the respondent was asked to list the key parameters or properties determined. Finally, four questions were asked at the end of the survey as shown below. The format of

the survey given out was thus as follows:

Characterization/ Measurement Technique	Technique Importance				Use of Technique					Should Use More	Key Parameters or Properties Measured By
	Don't Know	Not Imp.	Imp.	Very Imp.	Daily	Weekly	Monthly	Seldom	Never		
1. Admittance Spectroscopy											
2. Atomic Absorption Spectroscopy											
3. Atomic Emission Spectroscopy											
4. Auger Electron Spectroscopy											
: :											
72. Surface Topography											

CHEMICAL AND PHYSICAL

Examples: TEM, SIMS, neutron diffraction/scattering, X-ray topography, photoemission, SEM, STM, AES, EBIC, ESCA, WDX, EDX, XRF, XRD, EXAFS, mass spectrometry

Comments: High spatial resolution (atomic)
Ability to identify elements and compounds
Rather complex equipment used
Interpretation of data frequently difficult
Generally lower sensitivity
Usually performed by specialists

Determines: Atomic coordination, composition, chemical bonding, elements, stoichiometry, surface topography

ELECTRICAL

Examples: Hall, resistivity, mobility, lifetime, C-V, DLTS, spreading resistance, admittance spectroscopy, quantum magnetotransport

Comments: Very prevalent
Both contacting and non-contacting methods

Determines: Carrier concentrations, lifetime, mobility, resistivity (for profiles and maps), carrier type, contact resistance

OPTICAL

Examples: Optical microscopy, ellipsometry, FTIR, PL, Raman, PR, reflectance, modulation spectroscopy, photoconductivity, LBIC, OMA, Faraday rotation, PEM, magnetoabsorption, photothermal spectroscopy

Comments: Contactless, high sensitivity
Some used routinely by nonspecialists

Determines: Optical constants; epitaxial layer and insulator thickness; optical images of surfaces; impurity and defect type and size; composition; stress/strain; damage/structural imperfections; wafer cleanliness; carrier lifetimes

Figure 1. Some simple examples of materials characterization techniques representing chemical and physical, electrical and optical measurements. Also shown are some of the properties they determine along with some general comments. The acronyms are as follows: TEM (transmission electron microscopy), SIMS (secondary ion mass spectroscopy), SEM (scanning electron microscopy), STM (scanning tunnelling microscopy), AES (Auger electron spectroscopy), EBIC (electron beam induced current), ESCA (electron spectroscopy for chemical analysis), WDX (wavelength dispersive x-ray analysis), EDX (energy dispersive x-ray analysis), XRF (x-ray fluorescence), XRD (x-ray diffraction), EXAFS (extended x-ray absorption fine structure), C-V (capacitance–voltage), DLTS (deep level transient spectroscopy), FTIR (Fourier transform infrared spectroscopy), PL (photoluminescence spectroscopy). PR (photoreflectance spectroscopy), LBIC (laser beam induced current), OMA (optical modulation absorption), PEM (photoelectromagnetic effect).

Table 1. Top twenty characterization measurements for $Hg_{1-x}Cd_xTe$ and their scores ranked in order of their importance and their use.

Imp. rank	Characterization measurement	Imp. score	Use rank	Characterization measurement	Use score
1	29. Fourier transform infrared spectroscopy	60	1	26. Etching for defects	544
2	30. Hall effect	60	2	29. Fourier transform infrared spectroscopy	537
3	11. Current–voltage	53	3	30. Hall effect	510
4	26. Etching for defects	51	4	45. Optical microscopy	483
5	45. Optical microscopy	51	5	11. Current–voltage	452
6	7. Capacitance–voltage	49	6	58. Resistivity	368
7	62. Secondary ion mass spectrometry	48	7	24. Ellipsometry	296
8	16. Double crystal x-ray rocking curve	45	8	7. Capacitance–voltage	278
9	49. Photoconductivity	40	9	16. Double crystal x-ray rocking curve	250
10	58. Resistivity	40	10	6. Breakdown voltage	241
11	60. Scanning electron microscopy	39	11	43. MOS capacitance	193
12	24. Ellipsometry	38	12	49. Photoconductivity	191
13	6. Breakdown voltage	34	13	72. Surface topography: optical interferometry, stylus, scanning tunnelling microscopy	174
14	43. MOS capacitance	32	14	60. Scanning electron microscopy	128
15	72. Surface topography: optical interferometry, stylus, scanning tunnelling microscopy	32	15	31. Laser beam induced current	88
16	4. Auger electron spectroscopy	31	16	41. Microwave impedance	80
17	15. Double crystal x-ray topography	31	17	25. Energy dispersive x-ray analysis	74
18	19. Electron beam induced current	30	18	46. Optical modulation absorption	72
19	20. Electron spectroscopy for chemical analysis	28	19	62. Secondary ion mass spectrometry	66
20	53. Photoluminescence	28	20	71. Electron diffraction	65

Questions asked:

1. What are the most important (2–4) properties or parameters to measure or determine? Why?

2. What measurement techniques most need to be developed, enhanced or improved? Why?

3. Any additional helpful, constructive comments?

4. What measurement techniques have been inadvertently omitted from this listing?

4. Survey results

The survey was distributed to numerous representatives from industry and to several key personnel at the US Army Night Vision and Electro-Optics Directorate. Two anonymous responses were also received. Among the 35 responses received, eight companies were represented. Of these company responses, the vast majority came from four major HgCdTe focal plane array producers and research laboratories. Multiple responses received from the four companies accounted for about two-thirds of the total responses received. No one company was 'over represented' in the sense that the number of respondents from each of these companies was 8, 6, 6 and 5. Consequently, the authors believe that the survey results are representative of the state-of-the-art characterization practices used in manufacturing HgCdTe infrared detectors.

The details of the survey results are presented in three appendices. Appendix 1 reports the ranking of each chracterization measurement by its importance. It was decided to weight a response that was checked 'very important' with a '2', 'important' with a '1' and 'not important' with a '0.' The top 20 techniques and their scores are listed in order of importance in table 1. In compiling the use ranking, the weight for techniques used daily was 20, weekly 4, and monthly 1. The top 20 techniques and their use score are also listed in table 1, with all the results tabulated in appendix 1.

We note the high correlation between daily or weekly usage and the importance of the technique. In some cases such as secondary ion mass spectrometry, the complexity of the technique precludes daily usage, and thus the importance rank of 7th is much greater than its use rank of 19.

Figure 2(*a*) shows a histogram of the number of techniques for the response for importance. If eight or more respondents said a technique was in a given category, then it was counted in that category. We note that the respondents were not familiar with a sizable portion of techniques. More strikingly, of all the rest of the techniques they were familiar with, very few (fewer than 10%) were marked 'not important'. Figure 2(*b*) shows a histogram of the number of techniques for the response for usage. Note that almost half are never used by more than eight of the respondents and that about 20% are used daily.

In appendix 2 are listed the respondents' comments to the key parameters or properties measured for each
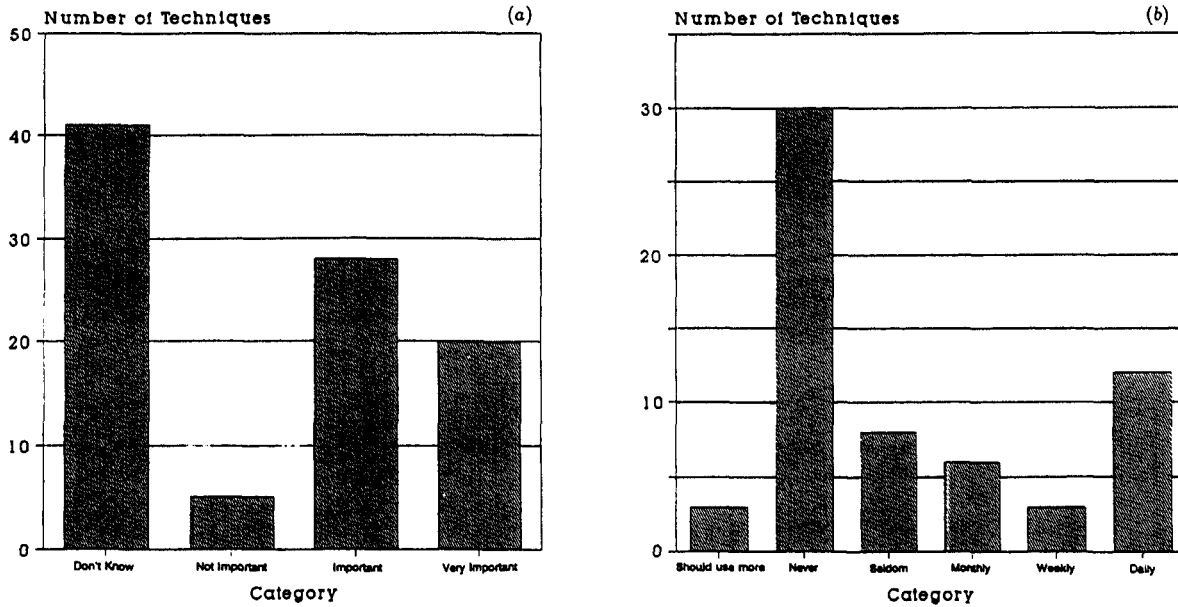
Figure 2. (*a*) Importance histogram for characterization techniques. (*b*) Usage histogram for characterization techniques. In each case a minimum of eight respondents is needed to include the technique in the category.

technique. Each respondent has been identified by a separate letter of the alphabet. Since there were 35 respondents, double letters had to be used. As can be seen from these results, the responses for each technique ranged from 0 to 25, a greater number of responses usually indicating an important or frequently used technique.

Answers to the four questions in the survey from each respondent are presented in Appendix 3. We give summaries of these answers in figures 3–6.

5. Summary and conclusions

To our knowledge, this is the first time such a characterization survey has been done for HgCdTe. We believe that results of this survey of the importance and prevalence of characterization techniques in the HgCdTe IR detector industry are important. We hope that they will stimulate and challenge existing concepts and practices and even lead to the development or application of new characterization techniques for the HgCdTe industry.

Properties/Parameters	Needs for Improvement
• alloy composition (E_g, λ_c) • carrier concentration • mobility • lifetime (minority carrier) • impurities (trace, etc.) • breakdown voltage • R_oA • quantum efficiency • tellurium (second phase, precipitates) • crystalline quality • individual layer properties • interface/surface structure and chemistry • dark currents • 1/f noise • impurity content in starting materials • defects (dislocations, etc.)	• NEED TO MEASURE PROPERTIES ON SURFACE AND PROFILE IN TO DEPTH OF SAMPLE. • NEED TO KNOW NONUNIFORMITY AND SPATIAL VARIATIONS. • NEED SUFFICIENT KNOWLEDGE TO ACCURATELY PREDICT PERFORMANCE OF REAL DETECTORS.

Figure 3. Summary of most important properties or parameters to measure for HgCdTe.

- anything related to device performance (defects, impurities)
- starting material analysis
- processing characterization
- device parameter measurements
- nondestructive techniques
- noncontact techniques
- techniques that cover large areas
- spatially resolved methods
- scanning methods
- mapping (of defects, concentration, composition of thickness, lifetime)
- in situ monitoring of growth processes
- characterization of multilayer structures
- material screening after growth and during processing
- defect mapping, by DLTS or scanning photoluminescence
- Te cluster detection and identification
- defect detection

- detection of p-type micro islands in n-type matrix
- dark-current detection and identification
- dopant nonuniformities (sensitivity 10^{14} cm^{-3})
- surface analysis techniques - surface passivation still limits performance
- both qualitative and quantitative techniques to determine impurities or control trace amounts very early in overall process
- differential Hall effect
- Faraday rotation for nondestructive mapping of carrier concentration
- laser scanning mass spectroscopy - a good impurity survey technique?
- optical probes (PL, OMA, LBIC, etc.)
- junction location, quality, and profiling techniques

Figure 4. Summary of measurement techniques that most need to be developed, enhanced or improved.

- HgCdTe analysis is a very difficult problem. Most important question: Why do I see what I see, and what does this mean physically? Answer by carefully designing experiments combining several analytical techniques and proper controls. Focus combined efforts of materials growth, test device (or structure fab), and materials and device analysis. Multiorganizational effort is highly desirable.
- Often, materials characterization techniques and device characterization tools are developed separately. Closed loop needed between materials parameters and device-performance parameters.
- Process-control test features used in Si and GaAs industries could be transferred and/or modified for use in HgCdTe processing.
- Develop techniques for better analyses of defect states in MCT, use as more routine characterization tools.

- Establish clearinghouse of data correlated to absolute (or, if secrecy requires, relative) performance parameters.
- Establish agreed measurement standards and cross-lab correlation (as was done by NATO composition exercise in 1980).
- Standardization of surface preparation and ambient during measurements generally lacking.
- Any technique requiring >$100K investment likely to be confined to occasional research and corroboration of cheaper, less accurate techniques needed in production.
- Need to improve detection limits of various analytical techniques such as SIMS.
- Needed a column entitled, "Relative Knowledge of Technique."

Figure 5. Summary of general comments.

- Laser reflectance
- Laser microscopy
- Residual stress measurements in processed devices
- Positron annihilation
- Atomic force microscopy or scanning capacitance microscopy
- Quantum efficiency measurements
- Contact resistance (especially for p-type samples)
- Contact and surface recombination velocity

- Open-circuit photovoltage decay
- Transmission line measurements for contact, sheet resistance
- Variable-area-diode measurements
- RHEED analysis
- Electrochemical analysis
- IR microscopy to image precipates
- X-ray Laue back-reflection to determine single crystal orientation
- X-ray topography techniques other than double crystal
- Imaging SIMS

Figure 6. Summary of measurement techniques omitted from list.

CHARACTERIZATION OF HgCdTe MATERIAL
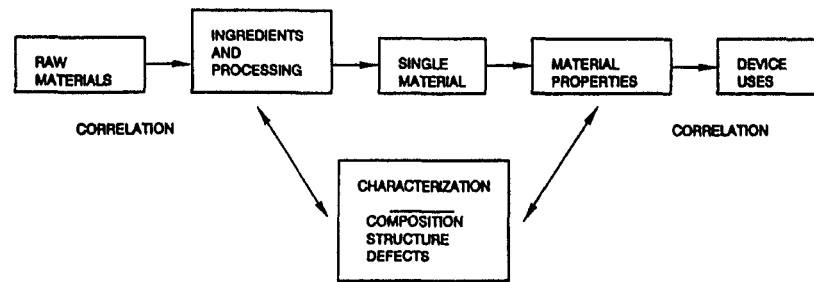
OUTPUTS OF ABOVE CYCLE BECOME INPUTS FOR CYCLE BELOW
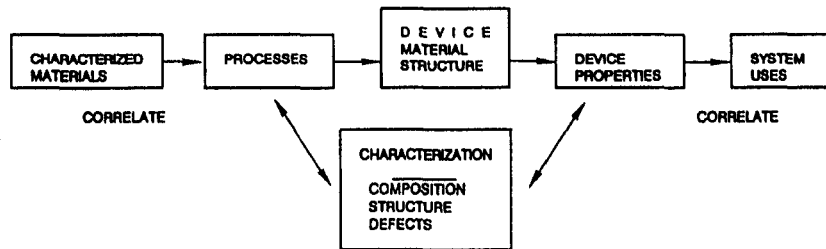
CHARACTERIZATION OF HgCdTe MATERIAL SYSTEM

Figure 7. Diagram of the characterization activities for a single material and a material system (see [10]). Note the strong role of characterization measurements and the need for correlation activites.

The appendices contain all the detailed results from the survey. Thus each person can individually interpret and arrive at his/her own conclusions. However, the key to success may be the *adequate use and proper combination* of many of the techniques on the list. It is worthwhile to remember that relationships exist among the structure, properties, synthesis, processing and performance of HgCdTe materials and devices as shown in figure 7 [10]. Once the material properties are characterized satisfactorily in the first part of the cycle, they become inputs for the device cycle. Important questions need to be raised and answered: how are the HgCdTe composition, structure, defects and electrical/optical properties

determined by the fabrication processes, and how, in turn, does this characterization determine the useful properties of the electronic devices? Both scientific and technological issues and practices need to be thoroughly understood. Only then: (1) will HgCdTe processes and devices be capable of being controlled and continually improved, (2) can we hope to understand the physical mechanisms that affect all aspects of producing HgCdTe IR focal plane arrays, and (3) can we hope to meet the cost and reliability requirements for HgCdTe systems.

The top five measurements in order of importance are (1) Fourier transform infrared spectroscopy, (2) Hall effect, (3) current–voltage, (4) etching for defects and

(5) optical microscopy. The top five measurements in order of usage are exactly the same as for the importance ranking, but with a redistribution: (1) etching for defects, (2) Fourier transform infrared spectroscopy, (3) Hall effect, (4) optical microscopy and (5) current–voltage. The reasons for their high ranking can be ascertained from the key parameters or properties they measure, as tabulated in appendix 2. We summarize the information obtainable from them and the reasons for their high ranking.

For $Hg_{1-x}Cd_xTe$ materials, the x-value is a very important parameter to determine because, in addition to the temperature, it affects the energy band structure. The energy band structure, in turn, directly affects the cut-off wavelength, intrinsic carrier concentration, carrier mobilities, etc. The technique used more than any other is infrared transmission, most often called FTIR for Fourier transform infrared spectroscopy. The FTIR measurement has numerous advantages: it has mapping capability, it is contactless and non-destructive, and it accurately predicts cut-off wavelengths, determines layer thicknesses, and is thus capable of determining the x-value and other compositional information of epitaxial layers [11].

The Hall effect is one of the most important characterization methods because of its wide application in the determination of semiconductor resistivity, carrier concentration and mobility. Discussions of the Hall effect can be found in many solid-state and semiconductor textbooks. It has become an excellent process monitor for crystal growth with the purity, doping and homogeneity able to be correlated with growth conditions. In addition to bulk electron and hole densities and mobilities, one can determine inversion and accumulation layer properties, acceptor binding energies and compensation ratios from the low-temperature freeze-out of free holes, and energy gaps from the temperature dependence of the intrinsic carrier concentration [12].

Current–voltage measurements to determine the behaviour of diodes are very important for characterizing diode parameters. Two types of diodes may be distinguished: p–n junction diodes and metal–insulator–semiconductor (MIS) diodes. For modern-day infrared detection the p–n junction photodiode is the more important. Surface and geometrical effects become increasingly important as the detector size shrinks. Bulk defects can have impact on the operation of large arrays. Variable-area diode data analysis is an essential tool in the characterization of HgCdTe infrared detectors [13]. Measurement of the zero-bias resistance–area product (R_0A) and its perimeter/area dependence provides critical information useful in separating surface and bulk effects and evaluating the quality of the surface passivation. The junction quality can be ascertained and the diffusion,

generation–recombination and tunnelling mechanisms found. Leakage or dark currents, as well as breakdown voltages, are also important parameters that can be measured by this technique.

The physical characterization of HgCdTe crystals by etching for defects is one of the major techniques for measuring the deviation from perfection of the crystal lattice. The rate of reaction of a solution with a solid surface depends distinctly on the crystallographic orientation. The rate is also significantly affected by local stress caused by defects. Chemical etching proceeds more rapidly in regions near dislocations or any other physical defect than in perfect regions. As a result, etch pits are often formed on the surface. Etch hillocks may also form and can often be confused with pits in an optical microscope. Use of a Normarski microscope in conjunction with preferential chemical etching and optical microscopy is thus one of the easiest and least expensive techniques for the determination of crystal defects in HgCdTe. Extended crystallographic defects such as dislocations, stacking faults, precipitates, voids and subgrain boundaries can have a major impact on the performance of focal plane arrays.

Finally, we note that this paper provides a reference for the importance and use of characterization techniques in the HgCdTe community. It should be a 'handy' document for scientists or engineers who want to know what techniques are available, what they are used for, how important they are and how often they are used.

Acknowledgments

Appendix 1. Importance and usage ranking of characterization measurements

In this appendix the 72 characterization measurements are ranked by their importance (table A1) and their usage (table A2). Note that there is generally (but not always) a correlation between the importance rank and the usage rank.

Table A1. Ranking of characterization measurements by their importance.

Imp. rank	Characterization measurement	Technique importance		Imp. score $I + 2VI$	Use of technique			Use score $20D + 4W + M$
		Imp. I	V. Imp. VI		Daily D	Weekly W	Monthly M	
1	29. Fourier transform infrared spectroscopy	6	27	60	26	4	1	537
2	30. Hall effect	4	28	60	25	2	2	510
3	11. Current–voltage	3	25	53	22	3		452
4	26. Etching for defects	9	21	51	26	4	8	544
5	45. Optical microscopy	3	24	51	24		3	483
6	7. Capacitance–voltage	11	19	49	12	9	2	278
7	62. Secondary ion mass spectrometry	10	19	48	1	9	10	66
8	16. Double crystal x-ray rocking curve	11	17	45	11	6	6	250
9	49. Photoconductivity	14	13	40	8	7	3	191
10	58. Resistivity	10	15	40	18	2		368
11	60. Scanning electron microscopy	15	12	39	4	10	8	128
12	24. Ellipsometry	12	13	38	14	3	4	296
13	6. Breakdown voltage	10	12	34	11	5	1	241
14	43. MOS capacitance	6	13	32	8	8	1	193
15	72. Surface topography: optical interferometry, stylus, scanning tunnelling microscopy	14	9	32	8	3	2	174
16	4. Auger electron spectroscopy	13	9	31	2	2	1	49
17	15. Double crystal x-ray topography	15	8	31	2		4	44
18	19. Electron beam induced current	12	9	30	1	3	3	35
19	20. Electron spectroscopy for chemical analysis	10	9	28	2	1	5	49
20	53. Photoluminescence	12	8	28		5	5	25
21	67. Transmission electron microscopy	12	8	28	1	1	8	32
22	2. Atomic absorption spectroscopy	15	6	27		1	5	9
23	25. Energy dispersive x-ray analysis	14	6	26	2	7	6	74
24	31. Laser beam induced current	16	5	26	3	6	4	88
25	14. Deep level transient spectroscopy	15	4	23			3	3
26	61. Scanning transmission electron microscopy	11	6	23	1		2	22
27	46. Optical modulation absorption	11	5	21	3	3		72
28	40. Mass spectrometry	12	4	20	1	1	7	31
29	12. Diode reverse recovery	11	4	19	2	2		48
30	13. Deep level optical spectroscopy	10	3	16		2	1	9
31	47. Photo Hall effect	10	3	16			3	3
32	64. Spreading resistance	7	4	15	1	1	3	27
33	8. Cathodoluminescence	14		14			3	3
34	71. Electron diffraction	6	4	14	3	1	1	65
35	54. Photoreflectivity	4	4	12	2		1	41
36	44. Neutron activation analysis	5	3	11	1			20
37	33. Low energy electron diffraction	4	3	10	1	1		24
38	69. X-ray photoelectron microscopy	6	2	10		1	1	5
39	70. Electron channelling	8	1	10		2	3	11
40	42. Microwave reflection	5	2	9	2	1	1	45
41	56. Raman scattering spectroscopy	7	1	9				0
42	57. Reflectometry	1	4	9	3	1		64
43	59. Rutherford backscattering spectroscopy	9		9			2	2
44	1. Admittance spectroscopy	4	2	8	2			40
45	3. Atomic emission spectroscopy	8		8			1	1
46	5. Beta-ray absorption/backscatter	4	2	8	2	0	1	41
47	21. Electroreflectance	4	2	8		1	1	5
48	41. Microwave impedance	2	3	8	4			80
49	17. Drift mobility	1	3	7	1	1	1	25
50	18. Eddy current	5	1	7	2	1	1	45
51	48. Photocapacitance	3	2	7	1			20
52	10. Current transient spectroscopy	6		6		2	1	9
53	65. Surface photovoltage	4	1	6				0
54	22. Electron energy loss spectroscopy	5		5			1	1
55	28. Faraday effect	5		5	1	1		24
56	32. Laser ionization mass analysis	4		4				0
57	37. Magneto-optics	2	1	4		1	1	5
58	68. X-ray fluorescence analysis	4		4			1	1
59	23. Electroluminescnce	3		3				0
60	34. Magnetoabsorption	2		2				0

Table A1. (*Continued*)

Imp. rank	Characterization measurement	Technique importance		Imp. score I + 2VI	Use of technique			Use score 20D + 4W + M
		Imp. I	V. Imp. VI		Daily D	Weekly W	Monthly M	
61	38. Magnetoresistance	2		2				0
62	50. Photoelectromagnetic effect	2		2			1	1
63	51. Photoemission spectroscopy	2		2				0
64	27. Extended x-ray absorption fine structure	1		1				0
65	35. Magnetoconductivity	1		1				0
66	39. Magnetophonon spectroscopy	1		1				0
67	52. Photoinduced transient spectroscopy	1		1				0
68	63. Shubnikov–de Haas effect	1		1				0
69	66. Thermal wave microscopy	1		1				0
70	9. Charged particle activation analysis	0						0
71	36. Magnetoreflectivity	0						0
72	55. Photothermal spectroscopy	0						0

Table A2. Ranking of characterization measurements by their usage.

Use rank	Characterization measurement	Technique importance		Use score I + 2VI	Use of technique			Use score 20D + 4W + M
		Imp. I	V. Imp. VI		Daily D	Weekly W	Monthly M	
1	26. Etching for defects	9	21	51	26	4	8	544
2	29. Fourier transform infrared spectroscopy	6	27	60	26	4	1	537
3	30. Hall effect	4	28	60	25	2	2	510
4	45. Optical microscopy	3	24	51	24		3	483
5	11. Current–voltage	3	25	53	22	3		452
6	58. Resistivity	10	15	40	18	2		368
7	24. Ellipsometry	12	13	38	14	3	4	296
8	7. Capacitance–voltage	11	19	49	12	9	2	278
9	16. Double crystal x-ray rocking curve	11	17	45	11	6	6	250
10	6. Breakdown voltage	10	12	34	11	5	1	241
11	43. MOS capacitance	6	13	32	8	8	1	193
12	49. Photoconductivity	14	13	40	8	7	3	191
13	72. Surface topography: optical interferometry, stylus, scanning tunnelling microscopy	14	9	32	8	3	2	174
14	60. Scanning electron microscopy	15	12	39	4	10	8	128
15	31. Laser beam induced current	16	5	26	3	6	4	88
16	41. Microwave impedance	2	3	8	4			80
17	25. Energy dispersive x-ray analysis	14	6	26	2	7	6	74
18	46. Optical modulation absorption	11	5	21	3	3		72
19	62. Secondary ion mass spectrometry	10	19	48	1	9	10	66
20	71. Electron diffraction	6	4	14	3	1	1	65
21	57. Reflectometry	1	4	9	3	1		64
22	20. Electron spectroscopy for chemical analysis	10	9	28	2	1	5	49
23	4. Auger electron spectroscopy	13	9	31	2	2	1	49
24	12. Diode reverse recovery	11	4	19	2	2		48
25	42. Microwave reflection	5	2	9	2	1	1	45
26	18. Eddy current	5	1	7	2	1	1	45
27	15. Double crystal x-ray topography	15	8	31	2		4	44
28	5. Beta-ray absorption/backscatter	4	2	8	2		1	41
29	54. Photoreflectivity	4	4	12	2		1	41
30	1. Admittance spectroscopy	4	2	8	2			40
31	19. Electron beam induced current	12	9	30	1	3	3	35
32	67. Transmission electron microscopy	12	8	28	1	1	8	32
33	40. Mass spectrometry	12	4	20	1	1	7	31
34	64. Spreading resistance	7	4	15	1	1	3	27
35	53. Photoluminescence	12	8	28		5	5	25
36	17. Drift mobility	1	3	7	1	1	1	25
37	33. Low energy electron diffraction	4	3	10	1	1		24
38	28. Faraday effect	5		5	1	1		24
39	61. Scanning transmission electron microscopy	11	6	23	1		2	22

Table A2. (*continued*)

Use rank	Characterization measurement	Technique importance		Use score I + 2VI	Use of technique			Use score 20D + 4W + M
		Imp. I	V. Imp. VI		Daily D	Weekly W	Monthly M	
40	44. Neutron activation analysis	5	3	11	1			20
41	48. Photocapacitance	3	2	7	1			20
42	70. Electron channelling	8	1	10		2	3	11
43	2. Atomic absorption spectroscopy	15	6	27	1	5		9
44	13. Deep level optical spectroscopy	10	3	16	2	1		9
45	10. Current transient spectroscopy	6		6	2	1		9
46	69. X-ray photoelectron microscopy	6	2	10	1	1		5
47	21. Electroreflectance	4	2	8	1	1		5
48	37. Magneto-optics	2	1	4	1	1		5
49	14. Deep level transient spectroscopy	15	4	23			3	3
50	47. Photo Hall effect	10	3	16			3	3
51	8. Cathodoluminescence	14		14			3	3
52	59. Rutherford backscattering spectroscopy	9		9			2	2
53	3. Atomic emission spectroscopy	8		8			1	1
54	22. Electron energy loss spectroscopy	5		5			1	1
55	50. Photoelectromagnetic effect	2		2			1	1
56	68. X-ray fluorescence analysis	4		4			1	1
57	56. Raman scattering spectroscopy	7	1	9				0
58	65. Surface photovoltage	4	1	6				0
59	32. Laser ionization mass analysis	4		4				0
60	23. Electroluminescence	3		3				0
61	34. Magnetoabsorption	2		2				0
62	38. Magnetoresistance	2		2				0
63	51. Photoemission spectroscopy	2		2				0
64	27. Extended x-ray absorption fine structure	1		1				0
65	35. Magnetoconductivity	1		1				0
66	39. Magnetophonon spectroscopy	1		1				0
67	52. Photoinduced transient spectroscopy	1		1				0
68	63. Shubnikov–de Haas effect	1		1				0
69	66. Thermal wave microscopy	1		1				0
70	9. Charged particle activation analysis	0		0				0
71	36. Magnetoreflectivity	0		0				0
72	55. Photothermal spectroscopy	0		0				0

Appendix 2. Key parameters or properties measured

In this appendix the key parameters or properties measured by each characterization/measurement technique are given. Each letter of the alphabet refers to a specific respondent throughout. The more important and highly used the technique, the more the responses received.

1. *Admittance spectroscopy*

   t. (On MIS) N_{ss}, flatband voltage
   w. Conductance
   dd. Deep level analysis
   ff. Interface state density
   hh. Lifetimes, activation energies, transition rates
   ii. Dark current mechanisms, activation energy

2. *Atomic absorption spectroscopy*

   d. Impurities
   f. Cu concentration in Te matrix, etc. Other impurites
   g. Used to measure impurities in raw materials and substrates. Buying instrument
   j. Fe, Cu impurity concentrations in bulk CdTe

k. Dopant concentrations—typically In, masked by ^{115}Cd in mass spectrometry
n. Characterization of starting materials
o. Trace level impurities
p. Impurities, material and source materials & gases (MOCVD)
r. Trace element analysis, we have a contract with VHG to improve technology
s. Impurity survey in starting materials, including organometallics using ICP
t. Low levels of impurities, good for impurities hard to detect by SIMS
u. Cu detection in substrates; other impurities: Si, Na, Li, etc.
v. Zeeman corrected. Impurities in films and substrates
w. II–VI material purity
y. Composition
aa. Composition, impurity concentration
cc. *Trace impurities* in starting materials, substrates and epilayers. Use ZCGFAAS technique
dd. Trace element analysis of raw materials and semiconductor materials
ee. Impurity levels. Need more sensitive technique

Continued

Appendix 2 (*Continued*)

3. *Atomic emission spectroscopy*

   d. Impurities
   f. Survey elemental impurities
   y. Composition
   aa. Impurity concentration
   dd. Trace element analysis of raw materials and semiconductor materials
   ff. Impurity concentrations

4. *Auger electron spectroscopy*
   d. Composition profiles
   f. Surface analysis and passivation profiles and compositions
   g. Occasionally used during array fabrication process development
   j. Profiles of host elements
   l. HgCdTe material composition and quality
   m. Surface analysis
   n. Surface impurities
   o. Surface composition, interface chemistry
   p. Spatial resolution high, useful in device surface analysis, passivation, metallization, interface
   r. Surface element analysis and bonding
   s. Surface contaminants, test of substrate cleaning
   t. Composition, Te precipitates, high levels of impurities
   u. Surface composition
   w. Surface composition
   y. Composition, especially surfaces
   z. Surface chemical composition
   aa. Surface composition, depth profile
   cc. Surface deposits, precipitates. Use scanning AES technique
   dd. Surface analysis with good spatial sensitivity—surface contaminants
   ee. Surface contamination
   ff. Concentrations of elements on surfaces, in films or in bulk

5. *Beta-ray absorption/backscatter*

   j. Layer thickness (production line)
   s. Thickness measurements when surface morphology rough
   t. Nondestructive thickness determination
   w. Heterojunction profiles
   dd. Contactless layer thickness, metallization thickness
   ee. Thickness of films on reference surface

6. *Breakdown voltage*

   d. Empirical αc factor
   f. Breakdown voltage in MIS
   g. Measure of device/junction quality
   h. Used mostly for MIS HgCdTe detectors
   j. Some indication of diode quality—part of *I V* analysis
   s. Indicates presence of defects that will enhance tunnelling currents; also test passivation
   t. (On diodes) carrier concentration
   u. Breakdown field
   v. Routine characterization for MIS devices
   w. Breakdown field
   dd. p–n junction quality
   ee. Breakdown voltage usually higher than requirement. *I–V* measurements more useful
   ff. Insulator breakdown strength
   hh. Material quality (tunnelling or bandgap states)
   ii. Dark current mecanisms, material defects

7. *Capacitance–voltage*

   d. Process control/doping
   f. MIS properties, capacitance
   g. Determine surface parameters—MIS. Determine junction profile—photodiodes
   h. Junction doping for p–n junctions
   i. Diode carrier concentration
   j. Near junction concentration, interface states, V_{FB}, other MIS properties (versus temperature)
   l. Material doping estimate
   m. Fixed charge, interface state density, doping profile
   n. Well capacity, carrier concentration
   p. MIS device characteristics, passivation
   s. Good technique for measuring carrier concentration in wide bandgap material
   t. (On MIS, diodes) carrier concentration near the junction, flatband voltage, N_{ss}
   u. Fixed charge density, carrier concentration
   v. Routine characterization for MIS devices
   w. Threshold voltage; carrier concentration
   aa. Carrier concentration
   cc. Electrical conductivity, carrier concentration
   dd. Carrier concentration, quality of passivation layer (flatband, hysteresis, etc)
   ee. Base layer doping extrapolate from *C–V*, capacitance itself
   ff. Carrier concentration, flatband voltage, hysteresis, high/low frequency characteristics
   hh. Material quality, surface passivation quality
   ii. Carrier concentration

8. *Cathodoluminescence*

   f. Defects in substrates
   g. We're going to try some measurements
   j. Some indication of CdTe or wide band MCT dislocations and impurity properties
   m. Structural quality of CdTe films
   o. Subsurface defect density, carrier concentration variations
   r. We have used in past, may again in future
   s. Indicates presence of electrically active defects but limited to MWIR or wide bandgaps
   u. Electrical activity of defects such as dislocations and p/n junctions
   w. CdZnTe substrate uniformity
   aa. Structural defects in substrate material (CdTe, CdZnTe, etc)
   cc. There is no commercial source of CL service in CdTe or CdZnTe so far as we know. *HELP*
   dd. Imaging of defects of CdZnTe, have not yet used it for HgCdTe
   ee. Lifetime too long to precisely locate junction (diffusion length too long)

9. *Charged particle activation analysis*

10. *Current transient spectroscopy*

    d. Lifetime and junction (R_0A) product
    dd. Deep level analysis
    ii. Dark current mechanisms, activation energy

11. *Current–voltage*

    d. R_0A
    f. MIS properties, *G–V*, dark current versus bias
    h. p–n junction characterization
    i. Many diode parameters

Continued

Appendix 2 (*Continued*)

j. Provides key insight both into diode performance and mechanisms (versus temperature)
l. Diode quality
m. Leakage current, dark current in photodiodes
p. Key device performance parameters, R_0A etc for photovoltaic diode
r. Diode *IV* characteristics
s. R_0A, breakdown voltage, photocurrent
t. (On diodes) origin of leakage currents
u. R_0A
w. R_0A
aa. Diode properties
dd. Junction quality
ee. R_0, $R_d(V)$, R_{series}. Model diffusion, *G–R*, and tunnelling mechanisms
ff. R_0A, leakage current
hh. Dark current mechanisms, breakdown properties
ii. Dark current mechanisms, activation energy

12. *Diode reverse recovery*

d. Lifetime after diode processing
g. OMA and PC-rolloff to determine lifetime
h. Carrier lifetime
i. Minority carrier lifetime
j. Some idea of minority carrier lifetime near junction (*versus temperature*)
l. Diode lifetime
m. Minority carrier lifetime
t. Lifetime in depletion region
aa. Diode properties
dd. Recombination lifetime in diode; difficult for thin-base diodes
ee. Lifetime
ii. Lifetime, activation energy

13. *Deep level optical spectroscopy*

d. Check on process, deep levels, not routine (simpler than DLTS)
m. Defect density, energy level and capture cross section
r. Optical determination of impurity levels
s. Midgap states
t. Deep levels
cc. Nature of traps
dd. Deep level analysis
ee. E_T
ff. Energy of trap levels
ii. Activation energy

14. *Deep level transient spectroscopy*

d. Check on process, deep levels, not routine
f. Au in Si and GaAs
m. Defect density, energy level and capture cross section
n. Impurity levels
r. Looks at impurity, vacancy levels. Seems problematic for HCT
s. Midgap states, levels and concentrations
t. Deep levels
v. Desirable to correlate with device performance
w. Traps in wide bandgap II–VI materials
dd. Deep level analysis
ee. Trap levels, cross sections (expensive to use)
ff. Energy of trap levels
gg. Defect levels
ii. Activation energy

15. *Double crystal x-ray topography*

d. Defects—much too time-consuming
i. Defects
j. Some insight into defects and strain
k. Cd(Zn)Te(Se) substrate quality (substructure, inclusions, precipitates)
m. Structural quality over large areas
n. Crystalline perfection
p. Crystal quality bulk substrates
r. Surface topograph
s. Spatial variations in crystal quality
t. Spatial structural uniformity, defect structure
u. Crystalline perfection, precipitates, dislocation types and arrangement
v. Crystal perfection—films and substrates
w. Structural perfection of II–VI materials
y. Surface roughness
cc. Crystal perfection, defect topography
dd. High resolution imaging of defect strain field
ee. Surface crystal lattice quality

16. *Double crystal x-ray rocking curve*

d. FWHM of epilayers and substrates
g. Determine quality of layer, crystallinity and lattice matching with substrates
i. Crystal quality
j. Basic crystal quality of epi
l. Substrate quality; substructure, dislocations
m. Structural quality of CdTe and HgCdTe layers
n. Subject to interpretation
p. X-tal quality of epi
r. We have a Brimrose X-ray mapper. It produces both topographs and RWHM rocking curve maps
s. Crystalline quality of epilayers, tilt, strain, composition, dislocation density
t. Crystallinity
u. Microstructures/grain boundaries, etc.
v. Crystal perfection—films and substrates
w. Structural perfection of II–VI materials
y. Structural perfection
z. Crystal lattice perfection
aa. Structural properties/crystal quality
cc. Gives number related to crystal perfection. Must be in conjunction with x-ray topography or etch pitting
dd. Crystal quality, FWHM of substrates and epitaxial layers, lattice mismatch
ee. Crystal quality
ff. Linewidth, crystalline perfection
gg. Crystalline defects
hh. Epilayer quality, substrate quality

17. *Drift mobility*

j. Basic to assessing materials electrical properties (versus temperature and field)
m. Minority carrier mobility for photoconductors
ee. Mobility

18. *Eddy current*

f. Electrical conductivity
v. Non-destructive measurement of conductivity in films
w. Measure LPE liquidus
cc. Electrical resistivity
ee. Resistivity (no instrumentation readily available)
ii. Carrier concentration

Continued

Appendix 2 (*Continued*)

19. *Electron beam induced current*

    d. Investigation of junction location; check on BAD devices on FPAs in certain configurations

    f. Diffusion lengths, electrically active defects, mapping, junction depths

    g. Location of electrical versus metallurgical junction

    i. Junction position

    j. Junction depth, hidden junctions

    m. Diode junction location, diffusion length

    o. Subsurface defect structure, junction depth

    s. Indicates junction location and electrically active defects

    t. Junction depth in diodes

    u. p/n junction depth

    w. Type variations in HgCdTe

    dd. p–n junction location on cleaved diodes

    ee. Electrically active defect mapping, junction location, *x*-value, limited spatial resolution

    hh. Diode contours, junction profiles

    ii. Electrically active defect

20. *Electron spectroscopy for chemical analysis*

    f. Passivation compositions

    g. Used during process development to obtain chemical information (residue after etching, etc.)

    j. Helps assess surface contamination and processes

    l. HgCdTe material

    n. Material analysis

    o. Surface and interface chemistry

    p. Chemical surface and interface information. Compound formation during epi growth, metallization, etc, non-destructive depth profile MBE interface, electronic parameters

    r. Use along with Auger

    t. Surface chemistry

    w. Surface analysis—cleanups, passivations

    z. Surface chemical constituents

    cc. Surface chemistry, surface deposits

    dd. Surface analysis of insulators; HgCdTe composition depth profile, interface between insulator/semiconductor

    ee. Surface contamination

    ff. Chemical composition of surfaces and films

21. *Electroreflectance*

    j. Tells something about surface composition and properties, but not too clear how useful

    l. HgCdTe composition

    n. Results questionable

    s. X profile with depth

    t. Composition, E_1, E_2, Δ_0, crystallinity

    aa. Composition, bandgap

    dd. Composition, carrier concentration if calibrated. Requires ohmic contact to sample

    ee. MCT *x*-value

    ff. Bulk composition from E_1, material quality from linewith Γ

    ii. Composition, maybe carrier concentration

22. *Electron energy loss spectroscopy*

    o. Low *Z* element surface analysis, electronic states and chemical bonding

    s. Bonding of surface atoms

    dd. Used in TEM analysis to determine composition

    ee. Surface crystal diffraction patterns

    ff. Vibrational energies of phonons and adsorbates (high resolution mode)

23. *Electroluminescence*

    d. Check on junction quality

    t. (p–n junctions) radiative quantum efficiency

    ee. More useful in other material systems

24. *Ellipsometry*

    g. Thin film thicknesses and index. MCT surface state

    h. Surface preparation monitor for various parts of processes

    j. Tells surface condition, composition, film structures

    m. Film quality in detector. Passivation

    n. Film thickness and uniformity

    p. Non-destructive MBE growth control

    r. Optical constants, film thickness

    s. X profile with depth, measure dielectric layers

    t. Surface conditions, bandgap

    u. Index of refraction for insulators. (Not useful for MCT?)

    w. Surface cleanliness, film thickness

    y. ψ and Δ, *n*, film thickness

    z. Substrate surface contamination

    dd. Excellent measure of surface cleanliness

    ee. Surface cleanliness, film thickness

    ff. Film thickness and refractive index

    hh. Surface quality, surface contamination

25. *Energy dispersive x-ray analysis*

    f. LPE compositional profiles

    g. Occasionally used during process development. Would use more if had a good in-house one

    j. Gives gross confirmation of compositional profiles

    m. Determination of *X*-value in HgCdTe layers

    o. *X*-value, compositional uniformity

    p. Film composition average, e.g. *X*-value

    r. Maps of wafer *X*-value, impurity maps

    s. Composition analysis in thick films

    t. Compositions and their depth profile

    w. Chemical mapping on devices

    y. Composition

    z. Layer composition

    aa. Composition

    cc. Chemical nature of precipitates, Zn % CZT, chemistry of deposits

    dd. Destructive measure of composition; routine for failure analysis of processing problems

    ee. 'Bulk' composition and impurities

    ff. Bulk composition of $Hg_{1-x}Cd_xTe$

26. *Etching for defects*

    d. Defects

    f. Dislocation and Te precipitate density

    g. Qualify substrates and check growth process

    i. Defects

    j. Tells dislocation density of layer—essential to materials improvement

    k. Te precipitates, dislocations, substructure (orientation A/B)

    m. Indirect assessment of crystalline quality

    o. Etch pit density

    p. Defect measure, substrate film

    r. We don't do this, but others use a lot for material dislocation density

    s. Dislocation density

    t. Defect structure, EPD

    u. Dislocations, Te precipitates

Continued

Appendix 2 (*Continued*)

v. Dislocations—pits—inclusions in films and substrates
w. Dislocation density in HgCdTe and CdZnTe. Damage
y. Etch pit density, A–B face (111)
z. Crystal lattice perfection
aa. Defects (structural)
cc. Defect densities, dislocation nature and distribution
dd. Best technique available for determining dislocation density
ee. Correlation of etch defects with device performance
ff. Dislocation density, substructure
hh. Material quality, dislocations and other defects
ii. Dislocations, microstructure

---

27. *Extended x-ray absorption fine structure*

---

28. *Faraday effect*

f. Local carrier concentration
u. Is this rotation?
w. Carrier concentration in HgCdTe
ff. Carrier concentration
gg. Carrier concentration (under development)
hh. Material uniformity, $N_D - N_A$
ii. Carrier concentration

---

29. *Fourier transform infrared spectroscopy*

d. Cutoff, thickness
f. Cutoff measurements
g. Measure transmittance of substrates, films, determine X-value, device spectral response
h. Film cut-off and thickness from IR transmission spectrum. Device cut-off wavelengths and spectral response
i. Composition
j. Gives composition of film, spectral response (temperature dependence important)
k. Composition determination, IR transmission
l. Diode spectral response
m. X-value, thickness. We use double beam IR grating spectrophotometer
n. Composition, uniformity
p. Key performance parameters, absorption α
s. Composition and thickness mapping
t. Composition, gradients, thickness, far IR for transport
u. Composition (from bandgap), thickness, scattering
v. Cut-off wavelength and thickness in MCT films
w. Epilayer thickness, cut-off wavelength
y. Molecular (group) vibrational modes
aa. Cut-on λ, thickness, free-carrier absorption
cc. IR transmission, impurity effects or stoichiometric deviations
dd. Accurate, nondestructive mapping of MCT composition
ee. X-value, λ_{co}, transmission
ff. Cutoff wavelength/composition uniformity
gg. Composition
hh. Energy gap for grown material
ii. Composition, carrier type? (below bandgap absorption)

---

30. *Hall effect*

d. Transport properties
f. Material type and carrier concentration, mobility
g. Process monitor for crystal growth. Carrier density and mobility

---

h. Versus magnetic field is ESSENTIAL!! Versus temperature is desirable. With resistivity, gives carrier concentration and mobility. Multiple carrier effects must be taken into account in many cases
i. Carrier concentration/mobilities
j. Gives essential layer electrical properties (profile and versus B and T)
k. Electrical parameters—purity, doping, homogeneity
l. Material doping
m. μ, n, R_H, resistivity
n. Carrier concentration, mobility
p. Type determination, doping, carrier behaviour
r. Carrier type, concentration mobility. Use depends on facilities and demand
s. Carrier concentration and mobility
t. n, μ, p
u. N_d, mobility, type
v. Electrical properties in MCT films
w. Carrier concentration, mobility, type
aa. Carrier concentration, mobility, resistivity
cc. Bulk chemistry effects, impurities, process variations
dd. Destructive measurement of carrier concentration, mobility, resistivity
ee. μ, N_A, N_D (versus T and versus H)
ff. Carrier concentration, mobility
gg. Carrier concentration (mobility)
hh. Material type, carrier concentration, mobility; homogeneity indicator
ii. Carrier concentration

---

31. *Laser beam induced current*

d. Use on FPC diodes restricted to certain configurations. Can only evaluate drastic failure
f. Variations in electrically active defects
g. Identify active areas and location of 'breakdown'
i. Electrical uniformity
j. Helps assess material quality, junction location, optical area, etc
m. Diode junction location, diffusion length
o. Defect features
s. Junction location, electrically active defects
t. Electrically active defects, QE of diodes
u. p–n junctions in uniform MCT
w. Uniformity of HgCdTe, junction profiles
dd. Difficult to interpret results on n-type material—requires contacts to sample
ee. Defect mapping
ff. Implant uniformity, carrier inhomogeneity, diode junction position
gg. Electrically active (charged) defects, inhomogeneities
hh. Homogeneity of type of material; diode contours
ii. Electrically active defect, minority carrier diffusion length

---

32. *Laser ionization mass analysis*

f. Impurity analysis
j. Possibly better than SIMS for certain elements
s. Microanalysis of precipitates
z. Impurity concentrations
aa. Impurity
cc. Specialized impurity analysis. Might offer some lower detection limits
dd. Quantitative trace-level analysis
ee. Use SIMS instead

(*Continued*)

Appendix 2 *(Continued)*

33. *Low energy electron diffraction*

    i. *In situ* monitoring of MBE growth
    s. Surface crystalline structure
    t. Surface chemistry, lattice spacing
    y. Surface atomic order or disorder
    dd. Used as a measure of surface cleanliness and crystallinity primarily in MBE
    ee. Surface crystal quality and lattice parameters, good for MBE

34. *Magnetoabsorption*

    h. Research technique to obtain fundamental material properties
    r. Good technique for looking at impurity levels, carrier lifetime. We have no facilities for this now
    s. Fine structure
    w. Defect and impurity states in HgCdTe
    dd. NIST accurate determination of MCT bandgap versus composition and temperature

35. *Magnetoconductivity*

    h. Research technique to obtain fundamental material properties
    r. Good technique for looking at impurity levels, carrier lifetime. We have no facilities for this now
    s. Fine structure

36. *Magnetoreflectivity*

    h. Research technique to obtain fundamental material properties
    r. Good technique for looking at impurity levels, carrier lifetime. We have no facilities for this now
    s. Fine structure

37. *Magneto-optics*

    h. Research technique to obtain fundamental material properties
    r. Good technique for looking at impurity levels, carrier lifetime. We have no facilities for this now
    hh. Bandgap states investigations. Spectroscopy, transition rates
    ii. Activation energy

38. *Magnetoresistance*

    h. Research technique to obtain fundamental material properties
    r. Good technique for looking at impurity levels, carrier lifetime. We have no facilities for this now
    ii. Carrier type

39. *Magnetophonon spectroscopy*

    h. Research technique to obtain fundamental material properties
    r. Good technique for looking at impurity levels, carrier lifetime. We have no facilities for this now
    s. Coordination and short-range ordering in alloy

40. *Mass spectrometry*

    f. Impurities, dopant profiles
    g. Monitoring high vacuum processes
    j. Gives basic purity information on solid source material
    k. Low discharge mass spectrometry is routine purity control
    n. Chemical analysis
    o. Major constituent and impurity analysis

    p. Impurities of source materials
    r. Regularly used to look at film junctions, interdiffusion, impurities
    s. GCMS of starting materials can analyse for organic impurities
    t. Very important with SIMS
    w. II–VI material purity
    y. Trace elements
    z. Impurity concentrations
    aa. Trace impurity
    cc. Glow discharge MS and spark source MS are good impurity screening techniques but do not give low enough DLS. ICPMS has proved very poor in CT and CZT matrices
    dd. Trace impurity analysis
    ee. Impurity levels
    ff. Background gas composition, primary gas composition

41. *Microwave impedance*

    f. Conductivity
    u. Minority carrier lifetime
    w. Lifetime
    dd. Contactless resistivity measurement
    ee. Lifetime
    hh. Carrier lifetime

42. *Microwave reflection*

    d. Lifetime
    f. Lifetime measurements
    g. Tried some measurements with inconclusive results
    t. Minority carrier lifetime
    v. Minority carrier lifetime in MCT films
    dd. Contactless measurement of carrier lifetime
    ee. Lifetime
    ff. Minority carrier lifetime
    hh. Carrier lifetime

43. *MOS capacitance*

    f. Carrier concentration, cut-off, storage time, breakdown voltage, etc
    g. Surface passivation quality; fixed charge and surface states
    h. Monitor fixed charge at interface; measure dopant concentration
    i. Surface
    j. Basic information on flat band—important to understanding surface properties
    l. ZnS/HgCdTe passivation quality and material doping
    m. Insulator thickness
    s. Storage capacity of MIS devices or persistent currents in diodes
    t. Carrier concentration, flatband voltage, N_{ss}
    w. Carrier concentration
    dd. Surface passivation quality, carrier concentration
    ee. Surface states, surface charge: process monitor for passivation
    ff. Insulator thickness and uniformity
    hh. Material quality, surface quality
    ii. Carrier concentration—activation energy (DLTS)

44. *Neutron activaton analysis*

    f. Residual impurity analysis
    k. Special (im)purity analyses

Continued

Appendix 2 (Continued)

m. Impurity determination
n. For tellurium and cadmium analysis
w. Impurities in II–VI materials
cc. Good for a very few impurities in CT/CZT materials, but it has excellent DLS when applicable
dd. Trace impurity analysis
ee. Impurity determination (level)
ff. Elemental composition

45. Optical microscopy

d. Need automated scanning of morphology with macro–micro resolution (sampling micro)
f. Dislocation and precipitate densities, micro-structure of bulk MCT, defects, morphology
i. Morphology
j. Essential to observation of defects, layer thickness, crystal morphology and growth features
k. Surface quality
l. Fabrication and material defects
m. Surface morphology, defect determination, thickness
p. General structure of materials and devices
r. Inspection of devices and materials, IR microscope is also useful
s. Surface morphology, macro-defect density
t. Surface roughness, macro-defects
u. Surface morphology
y. Surface features
z. Surface morphology
cc. Many features of surfaces, cleaved cross sections, damage features
dd. Surface inspection/characterization
ff. Defect density

46. Optical modulation absorption

d. Accurate low temperature cut-off; contactless lifetime measurements; measure of junction R_0A in LWIR
g. Lifetime measurements, cut-off measurements, wafer level screening
h. Lifetime; device cut-off wavelength; film quality
j. For τ
l. Heterojunction material cut-off, response time
m. X-value
o. Carrier lifetime
t. Minority carrier lifetime, defect levels
w. Lifetime
dd. Contactless carrier lifetime measurement and mapping
ee. Bandgap, lifetime
ff. Carrier concentration
hh. Carrier lifetimes
ii. Lifetime

47. Photo Hall effect

i. Properties of minority carriers
j. For minority τ, μ
m. Influence of compensation on mobility
s. Surface states
t. N_A, N_D
u. Type, donor and acceptor concentration, mobility
hh. Lifetime measurements, transport data versus temperature, etc
ii. Activation energy, trap levels

48. Photocapacitance

s. Surface states
t. Defect levels

w. Detectors
ee. Used in the past with MIS structure to screen wafers for λ_{co}
ii. Quantum efficiency, responsivity

49. Photoconductivity

f. Lifetime
g. Photoconductive devices
h. Carrier lifetime
i. Transients for minority carrier lifetime
j. Lifetime and essential to materials/device understanding
k. Predictor of PC response—used on bulk CMT and epi EMT
m. Lifetime
p. Lifetime measurements
r. Pulse decay lifetime measurements for material lifetime and surface recombination
s. Minority carrier lifetime
t. Minority carrier lifetime, PC decay on diodes gives R_0A
w. Detectors, lifetime
cc. Might correlate to purity and stoichiometry
dd. Carrier lifetime measurement (transient)
ee. Lifetime PC device
ff. PC lifetime
gg. Lifetime
hh. Material quality, spectral response, lifetimes
ii. Lifetime, surface recombination velocity

50. Photoelectromagnetic effect

ee. Device parameters
hh. Minority carrier versus majority carrier effects

51. Photoemission spectroscopy

s. Bonding of dopants and impurities
w. Surface analysis
ff. UPS—measures valence electron energies; XPS—see ESCA

52. Photoinduced transient spectroscopy

cc. Traps and defects, impurities, and the way they are tied up in materials
dd. Needs development work

53. Photoluminescence

d. Compositions/lifetimes (77 K)—this technique is definitely underutilized in epilayer. Also substrate evaluation of low temperature 4 K
g. Compositional measurement
h. Carrier lifetime; surface quality
j. Provides some useful information on CdTe substrate quality
m. Measure crystalline quality of CdTe epi
n. Characterization of substrates
p. Non-destructive electronic characteristics measurements
s. Important for wide bandgap (defects, impurities, etc)
t. Non-radiative centres (distribution), shallow levels, Te precipitates
u. Very useful for substrates (Cd, Zn)Te. Acceptor levels/donor levels/E_g/[Zn] concentration
w. Wide-gap II–VI materials purity and defects
z. Impurities
aa. Impurities, composition, crystal quality
cc. Optically active impurity and defect states; effect of various annealing treatments

Continued

769

Appendix 2 (*Continued*)

dd. Primarily used to determine composition of
CdZnTe (77 K meas. temp.)
ff. CdTe perfection
hh. Material quality, defect bands, particularly
epilayers

54. *Photoreflectivity*

d. More accurate surface X-values. Also surface state
evaluation
p. Film composition, X-value, non-destructive MBE
growth control
r. HCT X-value at the surface; formerly used frequently,
equipment currently down
s. Alloy composition
t. Composition, E_1, E_2, Δ_0, crystallinity
aa. Surface composition
dd. Contactless compared with electroreflectance
ff. Composition (X-value)
ii. Composition—carrier concentration?

55. *Photothermal spectroscopy*

56. *Raman scattering spectroscopy*

j. Tried to get surface information (not sensitive).
Bulk information not clear as to importance
p. Crystal lattice quality and imperfections
t. Te precipitates, composition
w. Clustering in II–VI materials
y. Molecular species, group vibrations
dd. Surface ordering, not much work done for HCT
ff. Vibrational modes of compounds
ii. Phonon energies, defects? (anti-site)

57. *Reflectometry*

g. UV–vis reflectance used to determine X-value
h. Reflectance spectrum near the E_1 and $E_1 + \Delta_1$
transitions. Gives x at the surface
s. Alloy composition
dd. UV reflectance (E_1 transition) used to map surface
composition of MCT (300 K meas.)
ee. Surface X-value

58. *Resistivity*

d. Part of Hall process
f. Hall measurements, determination of p-type
material
g. Part of Hall measurement
i. With Hall for cc and μ
j. With Hall, gives mobility—essential to materials,
understanding and device modelling
k. Electrical parameters (with Hall)—purity,
doping, etc
m. Carrier concentration, contact resistance
s. Deduce mobility in conjunction with Hall
measurements, contact resistance
t. Product of carrier concentration and mobility
w. HgCdTe for photoconductors
cc. Impurities, defects, stoichiometry, annealing effects
and effectiveness
dd. Integral part of Hall effect measurements: not
separately measured
ee. Done in conjunction with Hall effect
ff. Resistivity of metal film or semiconductor
gg. Mobility
hh. Material type, carrier concentration mobility;
homogeneity indicator

59. *Rutherford backscattering spectrometry*

f. Passivation characterization and implant profiling
j. Provides information on near-surface composition
and damage
m. Chemical analysis, crystal perfection
s. Composition depth profiles, crystallinity and strain
y. Atom %
dd. Crystallinity of epitaxial layers, ion implantation
damage, etc
ee. Passivation layer purity (hard to use for MCT)
ff. Film composition, density

60. *Scanning electron microscopy*

d. Morphology
g. Important for process development
j. Key to detailed morphology examination
l. Fabrication/material analysis, especially defects
m. Surface imaging, defects
n. Defects
o. Morphology, crystalline quality, chemical
composition, etc
p. Surface features
r. Used for materials and device inspection
s. Morphology, layer thickness
t. Morphology
u. Surface morphology, composition by WDX, EDAX
v. Surface defects and other features
w. Device examination
y. Microstructure
z. Surface morphology, crystallinity, thickness
cc. Surface damage, surface features, surface deposits
dd. Routine characterization of materials and devices
ee. Structural micro-features
ff. Step coverage, surface morphology

61. *Scanning transmission electron microscopy*

f. TEM of defects
g. Locating inclusion, dislocations, etc
m. Dislocation density
n. Defects
p. Interface structure
t. Defect structure
y. Defect structure
dd. Presently use TEM only
ee. Defects. Difficult to use
ff. Presence of dislocations, twinning
hh. Defect quality of material, interfaces

62. *Secondary ion mass spectrometry*

d. Impurities
f. Chemical analysis of dopant profiles and
impurities
g. Determine impurity locations, dopant versus
X-value profiles
h. LPE film composition and impurity profiles
i. Impurities
j. Key to materials purity and composition and
interface control
l. HgCdTe heterostructure material composition,
impurities
m. Impurity determination
n. Analysis of impurity clusters
p. Impurity doping profiles
r. Regularly used to look at film junctions,
interdiffusion, impurities
s. Impurity analysis and depth profiles
t. Impurity concentration (profiles), composition

Continued

Appendix 2 (Continued)

u. Measure concentration of various impurities in MCT and (Cd, Zn)Te
w. Impurities in II—VI materials
y. Trace elemental analysis
z. Impurity concentration
cc. Depth profiling of trace impurity and dopant concentrations, interface or surface pile-ups, segregation effects
dd. Trace level analysis, doping profiles
ee. Impurity levels
ff. Elemental composition, implant depth
gg. Profiling of impurities, and composition

63. Shubnikov–de Haas effect

s. Interface states and band bending

64. Spreading resistance

g. Important for FPA (staring)
h. Gives contact resistance
j. Spatial information
l. Use trans. line method → contact resistance
s. Sheet resistance
t. Transport, $n\mu$ product
w. Conductivity uniformity
dd. 77 K spreading resistance technique to profile p–n junctions needs development!
ee. Use to analyse contact resistance

65. Surface photovoltage

d. Carrier concentration; R_0A
r. We have used optical scanning technique in conjunction with electrical contacts to see photovoltaic and photoconductivity response
dd. Not yet developed for MCT, requires contacts on samples
ii. Carrier type changes (inhomogeneity)

66. Thermal wave microscopy

j. Tried, but found nothing after a casual look
m. Defect imaging

67. Transmission electron microscopy

f. Defect analysis and microstructural analysis
j. Key insight into materials defects
m. Dislocation density determination
n. Defects, dislocations
p. Interface structure local phases
s. Analysis of defects
t. Defect structure
v. Defect analysis
w. Precipitates, dislocation structure, interface in II–VIs
y. Defect structure
z. Defect structure
cc. High magnification defect and dislocation analysis, damage structure
dd. Imaging of structural quality of thin-film interfaces in cross section
ee. Defects, structure. Difficult to use
ff. Crystalline quality
hh. Defect quality of material interfaces

68. X-ray fluorescence analysis

m. Impurity determination
t. Composition

u. Not very sensitive
y. Atom %
dd. Composition measurement of large-area samples

69. X-ray photoelectron microscopy

f. Surface contamination on thin film profiles
l. HgCdTe material composition, impurities
p. Local device chemistry; information on films and interfaces
r. SEM in this mode gives greater sensitivity for elemental analysis
s. Analysis of impurity bonding
y. Composition
dd. Surface composition analysis; combined with sputtering can be used for comp. depth profiling, interface chemical composition

70. Electron channelling

d. Orientation; surface preparation
o. Orientation, near surface crystalline quality
p. Rough orientation of crystal films
s. Crystallinity of thin layers
y. Structural symmetry
z. Crystal orientation and perfection
dd. Rapid surface sensitive measurement of crystallinity (qualitative)

71. Electron diffraction

f. MBE growth, crystal quality and orientation
j. Essential to good MBE
p. Assume RHEED, growth monitor MBE
s. In conjunction with TEM for analysis of defects
t. Lattice spacing, crystallinity
u. Crystalline quality, orientation, Burger's vector
y. Order/disorder
dd. Useful in high-vacuum environments such as MBE
ff. Surface perfection in MBE

72. Surface topography: optical interferometry, stylus, scanning tunnelling microscopy

d. Topography; defects
f. Nomarski interference microscopy, to see shallow etch pit defects
g. Thin film process measurements, grown LPE film surface morphology
j. Helps get film thicknesses, wafer depths
n. Uniformity
p. Topography to calibrate film thickness, roughness, device structures, depth analysis craters, atomic resolution structure, electronics of surface and interface, epi films, non-destructive device testing
r. Make interferometric topographs. May use to measure thickness of films by looking at bevelled edge of multilayer structure, and detecting transitions by phase change
s. Measurement of surface topography, height and period
w. Wafer flatness
y. Roughness at various levels of scrutiny to atomic resolution
cc. Surface flatness of substrates
dd. Fizeau—flatness; Stylus—etch depths, surface roughness, etc; STM—not widely used in MCT (need clean surfaces)
ff. Film thickness; stress from bow measurement

Appendix 3. Results from questions asked

In this appendix we tabulate the answers given by the respondents to four questions asked. Again each letter of the alphabet refers to a specific respondent throughout this appendix, as in appendix 2.

Questions

1. **What are the most important (2–4) properties or parameters to measure or determine? Why?**

   a. Bandgap, carrier concentration, Hall mobility, dislocation density, lifetime

   c. Carrier concentration, λ_c, uniformity, charge storage

   d. Cut-off/composition, carrier concentration, lifetime, R_0A

   e. Diode $I-V$, Hall, spectral response

   f. Voltage past threshold (breakdown voltage), storage time, cut-off wavelength, Hall carrier concentration and mobility, dislocation density. MIS performance

   g. Where are the leakage currents? Surface or bulk? Are they localized defect: Substrate related?
   Properties of the individual layers of heterostructure material

   h. $Hg_{1-x}Cd_xTe$ alloy composition, carrier concentration, carrier lifetimes, carrier mobilities. These *directly* determine device performance

   i. Composition and composition variations on surface and in depth; same for carrier concentration and mobilities; transport properties of minority carriers; deep levels

   j. Nature of point defects, spatially resolved extended defects, spatially resolved surface/interface flaws. These are the perceived causes of non-ideal device behaviour

   k. • composition (absolute and variation)—governs $\Delta\lambda$ of arrays—D^* uniformity (a) bulk, (b) epilayers. *NON-DESTRUCTIVE
   • non-destructive defect mapping—Te ppts, dislocations, mosaic substructure
   • quick-check predictor of responsivity and detectivity on relatively unprocessed substrates

   l. Hard to choose

   m. X-value, n, p, μ—screen material for processing; minority carrier lifetime

   n. Mobility—crystal perfection and purity; minority carrier lifetime—same as above; tellurium second phase—*ALL* MCT materials are plagued with tellurium as a second-phase problem

   o. Composition, carrier concentration, junction position (diodes), crystalline quality and minority carrier lifetime

   p. Materials—crystal quality, defect concentration, carrier concentration, profile of impurities and activity. Interface/surface structure chemistry and electronic property
   Device—QE, R_0A, lifetime, carrier concentration and profile, D^*

   r. Depends on the use. Substrates: crystalline perfection, trace element analysis; HgCdTe films: X-value, mobility

   s. Composition (cut-off wavelength), carrier concentration, lifetime, dopant profiles. Most fundamental to operation of IR detector

   t. Minority carrier lifetime, N_A, N_D—directly affect device performance. Lifetime good indicator of material quality
   Dislocation density, electrically active defects, Te precipitates
   Surface state density (MIS): $I-V$ characteristics, quantum efficiency

   u. Carrier concentration, mobility, lifetime, composition, crystalline defects concentration. If we know these values accurately, then we can predict the performance. These parameters uniquely determine the quality of the material

   v. For screening MCT material: spectral cut-off, carrier concentration, mobility, lifetime
   For improving MCT material: defect levels (dislocations, etc), dopant uniformity

   w. Breakdown field, carrier concentration, lifetime, cut-off wavelength, dark current—these five properties determine detector performance. Need non-destructive means for mapping HgCdTe wafers for uniformity of these five properties

   x. Electrical transport (Hall), composition (transmission), crystallinity (x-ray)

   y. (1) Stoichiometry, (2) trace impurities, (3) oxidation state, (4) dislocation density, (5) most important—atomic structural order at surfaces and at interfaces

   z. Defect structure and purity—strongest influence on device performance

   bb. Composition, grading, thickness and Hall coefficient and mobility

   cc. (1) Impurity content in Cd, Zn, Te and Se starting materials—must control these or have no chance for downstream quality. (2) Impurities in substrates—must control as in (1). (3) EPDs—must control in order to assume epilayer quality yields. (4) Precipitate type, size and distribution—somehow affects epilayer and device quality and yield

   dd. (1) Absolute composition and compositional uniformity—determines wavelength cut-off; strongly affects device quality. (2) Carrier concentration and mobility—strongly affects device properties; control of carrier concentration is essential. (3) Minority carrier lifetime—directly affects device quality

   ff. Carrier concentration, cut-off wavelength,

minority carrier lifetime, dark current—they are the factors which most directly affect device performance

gg. Composition, carrier concentration, lifetime, deep-level defects and their spatial distribution

hh. ● Diode/MIS dark current—depends on lifetime, bandgap states, surface passivation

● Diode/MIS breakdown voltage—depends on doping concentration, density and position of bandgap states

● Diode/MIS 1/f noise—depends entirely on surface passivation

ii. Composition, carrier concentration, material defects—these material properties determine the device performance

2. What measurement techniques most need to be developed, enhanced or improved? Why?

a. Imaging SIMS, defect etching

c. C-V, c-t, Hall effect, FTS

d. ● Optical probing (OMA, PL, thickness mapping by absorption—non-destructive, fast and cheap, one set-up, large area

● Detailed morphology mapping/pattern recognition—present R&D, future process control

f. Position annihilation—its limits and usefulness are not understood very well. It could provide a means for measuring defects which we have difficulty in observing (i.e., Te vacancy concentration in HgCdTe, CdZnTe, etc)

Photoluminescence—We do not have sufficient understanding of what point defects or impurities contribute to which peaks

● Non-destructive, non-contact, screening techniques

● Non-contact MIS; fast qualification of production materials

● Current MIS device fabrication takes too long

g. ● Ability to determine junction location versus alloy composition for heterostructure material—potentially a combination of cold stage Ebic in a SEM

● Wafer level screening techniques for junction quality—OMA response time (at low backgrounds) has potential

h. ● *Non-contact* measurement of junction quality (e.g., R_0A, quantum efficiency, ...) would have enormous impact on array costs

● Junction (heterojunction) profiling techniques would greatly facilitate control and diagnostics of advanced device structures

● *In situ* monitoring of VPE film growth of HgCdTe multilayer devices

i. ● Characterization of multilayer structures

● Diode reverse recovery for measurement of minority carrier lifetimes on actual device

(after processing may have changed the properties of the material)

j. All spatially resolved materials analytical techniques which provide specific, interpretable information. NDE and *in situ* materials and device characterization follow close behind. Priorities should be set by the relevance of the technique to solving the most important problems

k. ● above; for layers f (x, y, depth) in scanning mode

● above; but correlated with device (PC and PV types) performance to permit reasonable specification of parameters and screening

● above; mobility, carriers and lifetime are commonly spec'd to prescreen for performance. $\Delta R/\Delta$ flux has been tested and found effective, but is little used

l. We badly need a cheap, reliable optical standard (detector, probably) for the 10–12 μm region

We also need better in-process characterization of our HgCdTe diodes, which are too fragile to be probed directly and also need to be measured at low T ($\sim$ 80 K) and low optical background

m. Non-destructive techniques would be very useful. X-ray techniques that correlate substrate defects to HgCdTe epi defects, and device performance

n. Starting material analysis—no suitable technique exists for PPB or less analysis; tellurium cluster detection and identification—in my opinion, Te clustering is the dominant cause of low detector yields

p. Non-destructive growth and device parameter measurement and control

q. Defect etches/EPD counts; defect detection (non-destructive if possible)

r. We need a way to map on pixel size level the carrier type, concentration and mobility. N-type HCT seems to have p-type micro-islands through it. We need to see these and figure a way to remove them

s. In general, techniques that are capable of mapping critical wafer properties that impact the variability of diode performance. For structural imperfections, x-ray topography and long wavelength cathodoluminescence or photoluminescence could be developed. Basic properties such as carrier concentration and lifetime also need to be mapped routinely. Another area of weakness is compositional inhomogeneities

t. Spatially scanning techniques LBIC; electrically active defects ought to be important for electro-optical devices techniques that are non-destructive and can be applied at different states of processing—this will help identify processing steps that limit performance

Surface analysis techniques—surface passivation still limits performance for many applications

u. Mapping techniques for carrier concentration need to be developed or improved.

Optical techniques utilized to probe the gap—needs to be enhanced and brought into more laboratories in industry

v. Techniques to measure dopant non-uniformities with sensitivity of 10^{14} cm^{-3}. This may be the limiting factor in charge storage in MIS devices on MCT

Non-destructive characterization of defects—needed to improve hetero-interfaces in films

w. Current/field, pulse, decay (J/E curves). Great potential for studying field dependence of dark current in HgCdTe. Shape variations in J/E curves yield strong clues about the source of the dark current

x. Low-level impurity identification ($<1 \times 10^{14}$ cm^{-3})

y. *In situ* surface chemistry (properties 1–3, Question 1, y) during wet *and* dry processing

z. Techniques to determine impurities—both qualitative and quantitative. LCMS—Laser Scanning Mass Spectroscopy—good impurity survey technique?

bb. Differential Hall effect

cc. ● Impurity analysis so that we can control trace impurities *very early* in the overall process rather than when the epilayer is characterized or the device is made and tested

● II–VI incorporated and the whole industry will significantly benefit from the development of ZCGFAAS under the now active US Army SBIR contract at VHG Labs

dd. ● Techniques for trace level impurity measurement at $<10^{15}$ cm^{-3} level. Ultimately correlate with deep level analysis and device properties

● 77 K p–n junction profiling technique—i.e., measure actual profile as opposed to SIMS, S–R measurements (currently use taper-etch C–V which is time-consuming)

● 77 K carrier concentration mapping (as being pursued by NIST)—will not be used routinely, but is helpful for development of materials

ee. ● It certainly would be nice to profile alloy concentration and junction location to better resolution to determine just where the junction occurs in heterostructure devices

● Anything related to device performance (defects, impurities)

ff. Non-contact techniques need to be developed/enhanced/improved to allow material screening quickly after growth and during processing. The time required to build, bond and test electrical devices hampers all aspects of material, process and device development

gg. Faraday rotation for non-destructive mapping of carrier concentration; defect mapping,

e.g., by DLTS or scanning photoluminescence; and scanning double crystal x-ray rocking curves

hh. ● Contactless techniques for determining material parameters relevant to the above device properties

● Rapid turnaround device data at 77 K for diodes/MIS devices

ii. ● Localized mapping techniques need to be developed to characterize the material. (Ideally, these techniques should be non-contact)

● Techniques need to be developed to identify microscopic material defects which may cause carrier-type inhomogeneity, compositional non-uniformity, etc.

3. Any additional helpful, constructive comments?

d. I do not think the Consortium approach will work. Best approach to long-range problems is to fund Government Labs (MIT, NIST, CNVEOL, etc) which can subcontract to industry

f. Too much weight is put on x-ray rocking curve half-width and it is not reflective of the overall crystal quality. Defect etching is much better

h. NIST should actively get involved in HgCdTe infrared detector technology, probably in the area of materials/process characterization

j. MCT analysis is a *very* tough problem. It will not be solved by the magical application of an overlooked technique. The most important questions to answer are: Why do I see what I see and what does this mean physically? These questions will have to be answered by carefully designing experiments combining (often) several analytical techniques and proper controls. The issues cannot adequately be addressed without the focused combined efforts of materials growth, test device (or structure fab) and materials and device analysis. A multi-organizational effort is highly desirable

k. ● A clearing house of data correlated to absolute (or, if secrecy requires, relative) performance parameters. Agreed measurement standards and cross-lab correlation (as was done by NATO composition exercise in 1980)

● Standardization of surface preparation and ambience during measurements is generally lacking

l. I have a feeling that there are many process-control test features used in the Si and GaAs industries which could be transferred and/or modified for use in HgCdTe processing—and some new features which should be developed for the special HgCdTe diode case where there are a lot of new things such as In bumps

s. I am unclear of the applicability of some of these techniques to MCT (such as charged particle activation analysis, deep level optical spectroscopy, etc). There is a need to develop some of these techniques so that better analyses can be made of defect states in MCT and to bring them to the point where they can be used as more routine characterization tools by the crystal grower

t. Quite often, materials characterization techniques and device characterization tools are developed separately, and very little effort is made to close the loop between materials parameters and device performance parameters

Any defect-detecting technique will show defects in HgCdTe. The trick is to isolate 'bad' defects from 'good' defects

y. Should have had a column entitled 'Relative knowledge of the technique' (i.e., knowledge possessed by person filling out form) for cases where 'don't know' is inappropriate. Last column should *not* have had the word 'by' in it (thought, at first, that you meant 'how' property is measured)

z. NIST should establish impurity characterization capability, including LSMS (not currently available in US—Brian Easton at Philips in UK has it)

cc. Correlation between EPDs and device performance are coming along well; now we have got to learn how to lower EPDs in substrates and epilayers

dd. Keep up the good work to measure fundamental properties such as E_g, N_i versus composition that NIST has already done

ff. I have been exposed to many of these techniques. I am aware that certain techniques are in use with which I have no experience, so I cannot say what key parameters are determined by every technique. There should be a middle ground of minor importance for techniques which are highly specialized and useful, but not used on an everyday basis. I would have placed magneto-absorption in this class, but instead I was forced to select 'not important' because the information it provides is more fundamental and less practical

gg. Need to improve detection limits of various analysis techniques such as SIMS, etc.

4. What measurement techniques have been inadvertently omitted from this listing?

a. Lifetime
d. Laser microscopy
f. Residual stress measurements in processed

devices; x-ray diffraction for crystal orientation; positron annihilation

h. Atomic force microscopy, scanning capacitance microscopy; quantum efficiency; contact resistance (especially important for p-type samples); contact and surface recombination velocity; far infrared transmission; variable-area photodiode test arrays; open-circuit photovoltage decay

j. Nothing strikes me offhand. The key is adequate use and *proper combination* of many of the techniques on the list. Many techniques should be applied versus temperature and magnetic field (in some cases). Spectroscopy should include spectral responses versus T. Depth and spatial profiles are very desirable for many techniques

k. Any technique requiring > \$100 K investment will likely be confined to occasional research and corroboration of cheaper, grosser techniques which are needed in production (my feelings after 25 years in the business)

l. ● Transmission line measurements for contact, sheet resistance (we use for p contacts on our p–n diodes)

● Variable-area-diode measurements → material optical response, diffusion (R_0A), and lateral optical collection effects, perimeter g–r effects

n. Photon backscattering

s. *In situ* measurement for MOCVD such as laser reflectance

w. Current/field, pulse, decay (J/E curves). Great potential for studying field dependence of dark current in HgCdTe. Shape variations in J/E curves yield strong clues about the source of the dark current

y. (1) Atomic force microscopy, (2) reflection high energy electron diffraction, (3) electrochemical techniques (as done by Arthur Hubbard, Manuel Soriaga and J Stickney), (4) ADAM (Angular Distribution Auger Microscopy—*Science*, in January 1990, **247** 182–8) (by Hubbard and Doug Frank)

z. LSMS

bb. Microscopic etch pit and dislocation density

cc. None that I can cite

dd. (1) UV–NIR surface reflectance to measure surface composition from E_1 transition (comments under reflectometry). (2) X-ray topography techniques other than double-crystal (not a serious omission). (3) IR microscopy to image precipitates in substrates and layers. (4) X-ray lattice constant measurements. (5) X-ray Laue back-reflection to determine single crystal orientation; powder diffraction and other specialized techniques

ee. Imaging SIMS

ff. MIS reverse recovery lifetime, MIS storage time

References

[1] Tennant W E, Cockrum C A, Gilpin J B, Kinch M A, Reine M B and Ruth R P 1992 *J. Vac. Sci. Technol.* **B 10** 1359
[2] Balcerak R and Brown L 1992 *J. Vac. Sci. Technol.* **B 10** 1353
[3] Reich R B 1989 *Sci. Am.* **261** 41
[4] The Committee on Characterization of Materials, Materials Advisory Board, National Research Council, MAB-229-M, March 1967
[5] Hannay N B 1967 *Trace Characterization, Chemical and Physical* NBS Monograph 100 ed W W Meinke and B F Scribner (Washington, DC: US Government) p 1
[6] Meieran E S, Flinn P A and Carruthers J R 1987 *Proc. IEEE* **75** 908

[7] *Advanced Materials and Processing: Fiscal Year 1993 Program* 1992 (Office of Science and Technology Policy) p 10
[8] Materials Research Advisory Committee, in *Trends and Opportunities in Materials Research* (Washington, DC: National Science Foundation, 1984) pp 2, 22
[9] Schaffner T J 1987 *Scanning Electron Microscopy* (AMF O'Hare, IL: SEM) p 11
[10] Adapted from *Materials and Processes for Electron Devices* (National Academy of Sciences, 1972) p 7
[11] Price S L and Boyd P R 1993 *Semicond. Sci. Technol.* **8**
[12] Meyer J R, Hoffman C A, Bartoli F J, Arnold D A, Sivananthan S and Faurie J P *Semicond. Sci. Technol.* **8** 805
[13] McLevige W V, Williams G M, DeWarmes R E, Bajaj J, Gergis I S, Vanderwyck A H and Blazejewski E R *Semicond. Sci. Technol.* **8** 946

NIST Technical Publications

Periodical

Journal of Research of the National Institute of Standards and Technology—Reports NIST research and development in those disciplines of the physical and engineering sciences in which the Institute is active. These include physics, chemistry, engineering, mathematics, and computer sciences. Papers cover a broad range of subjects, with major emphasis on measurement methodology and the basic technology underlying standardization. Also included from time to time are survey articles on topics closely related to the Institute's technical and scientific programs. Issued six times a year.

Nonperiodicals

Monographs—Major contributions to the technical literature on various subjects related to the Institute's scientific and technical activities.

Handbooks—Recommended codes of engineering and industrial practice (including safety codes) developed in cooperation with interested industries, professional organizations, and regulatory bodies.

Special Publications—Include proceedings of conferences sponsored by NIST, NIST annual reports, and other special publications appropriate to this grouping such as wall charts, pocket cards, and bibliographies.

Applied Mathematics Series—Mathematical tables, manuals, and studies of special interest to physicists, engineers, chemists, biologists, mathematicians, computer programmers, and others engaged in scientific and technical work.

National Standard Reference Data Series—Provides quantitative data on the physical and chemical properties of materials, compiled from the world's literature and critically evaluated. Developed under a worldwide program coordinated by NIST under the authority of the National Standard Data Act (Public Law 90-396). NOTE: The Journal of Physical and Chemical Reference Data (JPCRD) is published bimonthly for NIST by the American Chemical Society (ACS) and the American Institute of Physics (AIP). Subscriptions, reprints, and supplements are available from ACS, 1155 Sixteenth St., NW, Washington, DC 20056.

Building Science Series—Disseminates technical information developed at the Institute on building materials, components, systems, and whole structures. The series presents research results, test methods, and performance criteria related to the structural and environmental functions and the durability and safety characteristics of building elements and systems.

Technical Notes—Studies or reports which are complete in themselves but restrictive in their treatment of a subject. Analogous to monographs but not so comprehensive in scope or definitive in treatment of the subject area. Often serve as a vehicle for final reports of work performed at NIST under the sponsorship of other government agencies.

Voluntary Product Standards—Developed under procedures published by the Department of Commerce in Part 10, Title 15, of the Code of Federal Regulations. The standards establish nationally recognized requirements for products, and provide all concerned interests with a basis for common understanding of the characteristics of the products. NIST administers this program in support of the efforts of private-sector standardizing organizations.

Consumer Information Series—Practical information, based on NIST research and experience, covering areas of interest to the consumer. Easily understandable language and illustrations provide useful background knowledge for shopping in today's technological marketplace.
Order the above NIST publications from: Superintendent of Documents, Government Printing Office, Washington, DC 20402.
Order the following NIST publications—FIPS and NISTIRs—from the National Technical Information Service, Springfield, VA 22161.

Federal Information Processing Standards Publications (FIPS PUB)—Publications in this series collectively constitute the Federal Information Processing Standards Register. The Register serves as the official source of information in the Federal Government regarding standards issued by NIST pursuant to the Federal Property and Administrative Services Act of 1949 as amended, Public Law 89-306 (79 Stat. 1127), and as implemented by Executive Order 11717 (38 FR 12315, dated May 11, 1973) and Part 6 of Title 15 CFR (Code of Federal Regulations).

NIST Interagency Reports (NISTIR)—A special series of interim or final reports on work performed by NIST for outside sponsors (both government and non-government). In general, initial distribution is handled by the sponsor; public distribution is by the National Technical Information Service, Springfield, VA 22161, in paper copy or microfiche form.

U.S. Department of Commerce
National Institute of Standards and Technology
Gaithersburg, MD 20899

Official Business
Penalty for Private Use $300